Development of a high pressure xenon gas time projection chamber with a unique cellular readout structure to search for neutrinoless double beta decay

Department of Physics, Graduate School of Science, Kyoto University
Sei Ban (Sheng Pan)

March 13, 2020

Abstract

An observation of neutrinoless double beta ($0\nu\beta\beta$) decay would prove the existance of Majorana components of neutrinos. This is an essential feature to explain light neutrino masses by introducing a right-handed Majorana neutrinos to the standard model. It would also be an important step to understand the origin of the matter-antimatter asymmetry in the universe. Experiments so far put lower limits of the half life of $0\nu\beta\beta$ decay such as 10^{26} years for ^{136}Xe.

A Xenon ElectroLuminescence (AXEL) detector is proposed for $0\nu\beta\beta$ decay search. It is a high pressure xenon gas time projection chamber (TPC) and uses the electroluminescence (EL) process to measure ionization signal. It has an unique cellular structure, called electroluminescence light collection cell (ELCC), to induce and measure EL photons. A TPC with ELCC would provide good energy resolution and three-dimensional track pattern reconstruction. The target energy resolution at the ^{136}Xe $0\nu\beta\beta$ decay Q-value, 2458 keV, is 0.5% (FWHM). The track pattern can be used to distinguish signals from backgrounds. ELCC is a new concept and proof-of-principle is demanded. Hence, we constructed two prototypes and their performances were evaluated using gamma-ray sources.

A prototype with 10 L size pressure vessel was constructed to demonstrate the principle of the ELCC. We succeeded in observing the clear photo peaks of 122 keV and 356 keV gamma-rays and achieved energy resolutions are 4.16±0.30% for 122 keV peak at 4 bar and 2.54±0.20% for 356 keV at 8 bar. However, these results do not reach the target value. Detailed studies and simulations have shown that the performance of the ELCC depends significantly on its dimensions.

A prototype with the 180 L pressure vessel is being developed to acquire a know-how to build larger detectors and to evaluate the performance at the energy region around the Q-value. The dimensions of ELCC are optimized and designed to achieve the energy resolution of 0.35% (FWHM) at the Q-value at 8 bar. As the first phase, the TPC with the volume of 2.1 L and 168 channels was installed and a stable operation was achieved. The performance was evaluated with 511 keV gamma-ray at 4 bar and the energy resolution is obtained as 1.49±0.004% (FWHM). This value is comparable to the best energy resolution in the $0\nu\beta\beta$ decay search experiments using xenon. Clear track patterns were also observed. However, again, the obtained result does not achieve our target energy resolution.

The reasons why the energy resolution does not reach the target value are investigated. Then, future prospects and plan to further sensitivity are discussed.

Acknowledgement

First of all, I would like to denote that this thesis is the product of years with the tremendous supports. I greatly appreciate all the people who have contributed to this thesis and my research life.

I would express the deepest appreciation to my supervisor, Prof. Atsuko K. Ichikawa. She has ardent love and spirit of inquiry to physics and experiments. I really respect her attitude to physics and research. She has taught me various things and guided me to the correct way when I was lost in my work. The advice that she gave me, “Think deeply and do quickly”, is a motto of my research life. I would like to express my gratitude to Prof. Tsuyoshi Nakaya for giving me great opportunities to start the first step as a researcher. He also gave me a lot of insightful advices and warm encouragements and they were helpful for writing this thesis. Special thanks to Dr. Tatsuya Kikawa for a lot of advices for writing this thesis. This thesis had been brushed up thanks to his comments.

I express a deep gratitude to the AXEL collaborators. I am deeply grateful to Dr. Kiseki Nakamura. I have seen him doing many works such as development of the detectors and construction of simulation as a early member of the AXEL experiment. I greatly respect him and learned a lot from him. He also always cared my research progress and helped me many times. I am indebt to Dr. Shuhei Obara for his essential works in the AXEL. He was like an engine of our team and the progress of our experiment was impelled forward thanks to his leadership. Mr. Kazuhiro Nakamura and Mr. Masashi Yoshida played very important roles and supported my work. The result in this thesis was significantly improved by Mr. Kazuhiro Nakamura with his measurement of MPPC recovery times. I wonder why he has so much knowledge in a lot of fields. The stoic works by Mr. Masashi Yoshida were indispensable to our group. He contributed to deepen our understanding of discharges and to construct the field shaper as a master of high voltages. I also want to thank Mr. Bungo Sugashima for his help of data taking. I expect him to become a central person in the AXEL experiment in the future.

I express a lot of thanks to Mrs. Saori Yanagita (Yamaguchi), Mr. Syunsuke Tanaka, and Mr. Yuki Ishiyama, who are graduated members of the AXEL project. Mrs. Saori Yanagita (Yamaguchi) was my colleague in the same period, and we had been researching together while encouraging each other (sometimes, until midnight). Mr. Syunsuke Tanaka had greatly contributed to the development of the FEB and the study using deep learning. The work in this thesis would not have been achieved without the FEB he developed. I remember learning together with Mr. Yuki Ishiyama in a seminar (zisyu-semi) during my undergraduate years and it gave me the foundation of my current knowledge.

I also appreciate the other AXEL collaborators for giving me various advices about constructing and evaluating the detectors.

I would like to thank all the members involving me in the High Energy Physics laboratory and secretaries in the department of physics in Kyoto University. Especially, I express thank to Mr. Satoshi Shinohara, Mrs. Saori Yanagita (Yamaguchi), Mr. Ryutaro Monden, Mrs. Mika Yamamoto (Numakura), Mr. Keisuke Kondo, and Mr. Kento Haneda as my colleague in the same sachool year. It was joyful time that we studied together and spent many times together in the laboratory for the preparation of KEK summer challenge.

I also appreciate my wife, Moeko. She did housework and parenting without any complaint while I was doing research and in busy days. This thesis would not be completed without your kind supports. My dear son, Sosuke, has always excited our daily life. You are my healing during the tough days. It will be a great pressure if someday you understand this thesis and discuss together.

Finally, I express the greatest appreciation to my parents and family, Pan Li Rui, Chen Yan, and Shin Ban. They always believed and supported me, and that encouraged me a lot.

Sei Ban
Kyoto, Japan
April, 2020

Contents

Chapter 1

Introduction

1.1 Standard Model

The standard model (SM) is the most successful model to explain various phenomena in our universe from the view point of elementary particles. It consists of fermions with three generations and some symmetries: Translational, Rotational, Time translational symmetry ("global symmetry") and

$$SU(3) \times SU(2) \times U(1) \tag{1.1}$$

local gauge symmetry, and a scalar boson so-called Higgs particle. Gauge bosons are introduced automatically by the gauge symmetries of Equation (1.1). Figure 1.1 summarizes the elementary particles in the SM.

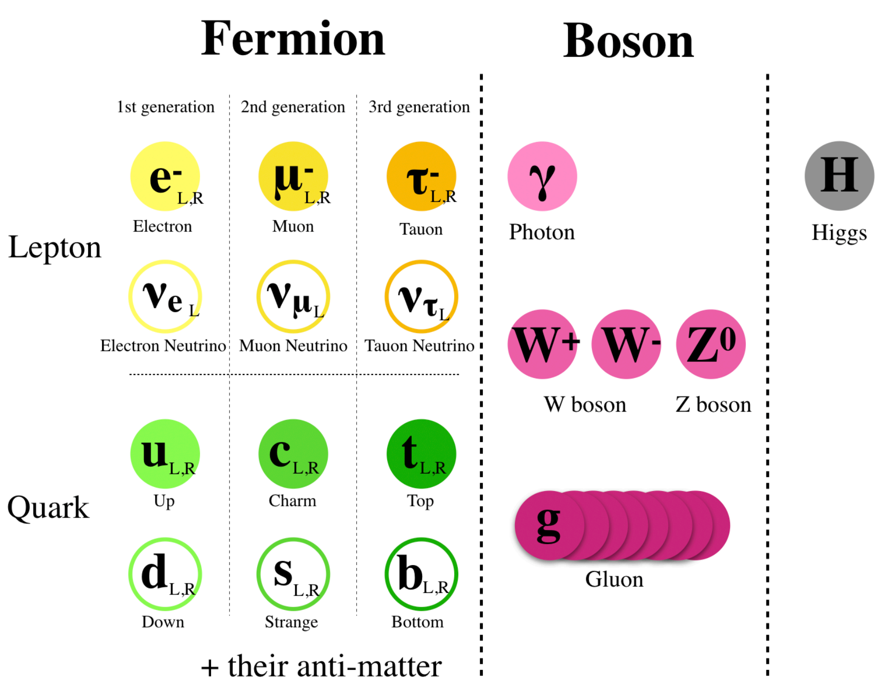

Figure 1.1: Particles in the standard model. It consists of three generations of fermions and their anti-matters, gauge bosons, and Higgs particle. Right-handed (R) and left-handed (L) chirality states exist for fermions except for neutrinos. In the SM, right handed neutrino ν_{R} does not exist.

The equation of motion of the field in the standard model is often described in a Lagrangian format and introduced automatically by the symmetries, renormalizability and Brout-Englert-Higgs (BEH) mechanism mentioned later. The standard model Lagrangian ($\mathcal{L}_{\mathrm{SM}}$) is expressed as

$$\begin{aligned}
\mathcal{L}_{\mathrm{SM}} \;=\;& -\frac{1}{4}\sum_{a=1}^{8} G^a_{\mu\nu}G^{a\ \mu\nu} - \frac{1}{4}\sum_{a=1}^{3} W^a_{\mu\nu}W^{a\ \mu\nu} - \frac{1}{4}B_{\mu\nu}B^{\mu\nu} \\
& +\overline{Q_l}i\gamma^\mu D_\mu Q_l + \overline{L_l}i\gamma^\mu D_\mu L_l \\
& +\overline{u_{lR}}i\gamma^\mu D_\mu u_R + \overline{d_{lR}}i\gamma^\mu D_\mu d_{lR} + \overline{e_{lR}}i\gamma^\mu D_\mu e_{lR} \\
& +(D^\mu\Phi)^\dagger(D_\mu\Phi) - \lambda(\Phi^\dagger\Phi - \frac{1}{2}v^2)^2 \\
& +\left\{y_{lu}\overline{Q_l}\Phi u_{lR} + y_{ld}\overline{Q_l}\Phi d_{lR} + y_{le}\overline{L_l}\Phi e_{lR} + h.c.\right\} \\
& (l = 1, 2, 3),
\end{aligned} \tag{1.2}$$

where γ^μ is so-called gamma matrix. and D_μ is covariance derivative

$$D_\mu = \partial_\mu + ig_s\sum_{a=1}^{8}\frac{\lambda^a}{2}G^a_s + ig\sum_{a=1}^{3}\frac{\sigma^a}{2}W^a_\mu + ig_Y Y B_\mu \tag{1.3}$$

which is required by local gauge symmetry. Its physical interpretation is a kinetic term of fermions (the first term) and interaction terms with gauge bosons (the remain three terms). Left-handed fermions constitute $SU(2)$ doublets represented by

$$Q_l = \begin{pmatrix} u_L \\ d_L \end{pmatrix}, \begin{pmatrix} c_L \\ s_L \end{pmatrix}, \begin{pmatrix} t_L \\ b_L \end{pmatrix} \tag{1.4}$$

$$L_l = \begin{pmatrix} \nu_{eL} \\ e_L \end{pmatrix}, \begin{pmatrix} \nu_{\mu L} \\ \mu_L \end{pmatrix}, \begin{pmatrix} \nu_{\tau L} \\ \tau_L \end{pmatrix} \tag{1.5}$$

and right-handed fermions

$$u_{lR} = u_R, c_R, t_R,\ d_{lR} = d_R, s_R, b_R,\ e_{lR} = e_R, \mu_R, \tau_R \tag{1.6}$$

are $SU(2)$ singlets. The difference of representations between the left-handed and right-handed fermions are based on the experimental facts that weak interaction described by the $SU(2)$ gauge translation violates parity symmetry in maximum and couples only to the left-handed fermions. The meaning of fourth and fifth lines in Equation (1.2) is explained in Section 1.1.2.

1.1.1 Masses of Fermions

The difference of the representations of fermions between left handed and right handed indicates that the SM is a chiral gauge theory and prohibits introducing mass term

$$m_D(l_L\overline{l_R} + l_R\overline{l_L}) \tag{1.7}$$

in $\mathcal{L}_{\mathrm{SM}}$ directory by hand. It means all fermions cannot have masses anymore. However, fermions actually have finite masses. The problem described above was solved by introducing the Higgs particle and Brout-Englert-Higgs (BEH) mechanism.

1.1.2 Brout-Englert-Higgs Mechanism

A chiral invariant term is introduced as:

$$\mathcal{L}_{\text{Yukawa}} = y_{lu}\overline{Q_l}\Phi u_{lR} + y_{ld}\overline{Q_l}\Phi d_{lR} + y_{le}\overline{L_l}\Phi e_{lR} + h.c. \quad (l = 1, 2, 3), \tag{1.8}$$

where y_{lu}, y_{ld}, y_{le} are constants so-called "Yukawa coupling", Φ is a scalar field which is a doublet under the $SU(2)$ transformation and a singlet under the $SU(3)$ transformation, and $h.c.$ represents the Hermitian conjugate. The potential of the scalar field Φ is expressed as

$$V(\Phi) = \lambda(\Phi^*\Phi - \frac{1}{2}v^2)^2. \tag{1.9}$$

If $\lambda > 0$, it can take the minimum value at $\Phi^*\Phi = v^2/2$ and the scalar field can have a vacuum expectation value:

$$\langle\Phi\rangle = \frac{1}{\sqrt{2}}\begin{pmatrix} 0 \\ v \end{pmatrix} \tag{1.10}$$

with the expression of unitary gauge. Then Equation (1.9) can be written as

$$\begin{aligned} \mathcal{L}_{\text{Yukawa}} \quad = \quad & -\frac{y_u v}{\sqrt{2}}(\overline{u_L}u_R + \overline{u_R}u_L) - \frac{y_d v}{\sqrt{2}}(\overline{d_L}d_R + \overline{d_R}d_L) - \frac{y_e v}{\sqrt{2}}(\overline{e_L}e_R + \overline{e_R}e_L) \\ & +(\text{2nd generations}) \\ & +(\text{3rd generations}) \end{aligned} \tag{1.11}$$

These terms have the same form as the mass term of Equation (1.7), thus fermions can acquire their mass by coupling to the scalar field condensed in the vacuum. The gauge bosons are also given masses through the coupling to the scalar field. The scalar field Φ is called the "Higgs field" and the process that gauge bosons and fermions have masses in such way is called the "Brout-Englert-Higgs mechanism". The fermion mass obtained in this mechanism is conventionally called "Dirac mass".

1.2 Neutrino in Standard Model

Neutrino is one of the elementary particles. Its existence was predicted by W. Pauli in 1930 in order to explain the continuous energy spectrum of electrons from beta decays [1]. In 1934 E. Fermi formulated the beta decay as [2]:

$$n \to p + e^- + \bar{\nu}_e. \tag{1.12}$$

In 1956, F. Reines and C. Cowan observed the interaction between protons and (electron) antineutrinos generated from a reactor, proving the existence of neutrinos [3]. Subsequently, L. M. Lederman, M. Schwartz, and J. Steinberger discovered muon neutrinos using the AGS proton accelerator at the BNL, USA in 1962 [4]. The third species of neutrinos, tau neutrino, was discovered by the DONUT collaboration at Fermilab using nuclear emulsion in 2000 [5]. The number of light active neutrinos was measured to be 2.984 ± 0.008 from the decay width of the Z boson by accelerator experiments in 2006 [6].

In the standard model, neutrinos are introduced as electrically neutral and purely left-handed, hence, massless lepton with spin 1/2 and anti-neutrinos as purely right-handed. In the SM, neutrinos and anti-neutrinos are distinguishable.

1.3 Neutrino Beyond the Standard Model

Direct neutrino mass measurements have not shown any indications of non-zero neutrino mass. In 1976, a solar neutrino observation showed an anomaly that the measured rate was only one third of the theoretical expectation based on the standard solar model [7]. An anomaly was also shown by observations of atmospheric neutrinos by Kamiokande [8]. Neutrino oscillation was a candidate as a solution of their problems.

1.3.1 Neutrino Oscillation

Z. Maki, M. Nakagawa, and S. Sakata proposed that flavor eigenstates of neutrinos $|\nu_f\rangle$ $(f = e, \mu, \tau)$ can be expressed as mixings of mass eigenstates $|\nu_i\rangle$ $(i = 1, 2, 3)$:

$$|\nu_f\rangle = \sum_{i=1}^{3} U_{fi}|\nu_i\rangle, \tag{1.13}$$

where U_{fi} is the mixing matrix so called "Pontecorvo-Maki-Nakagawa-Sakata matrix" (PMNS matrix). The PMNS matrix is a 3×3 unitary matrix and is described as:

$$\begin{aligned} U_{\mathrm{PMNS}} &= \begin{pmatrix} U_{e1} & U_{e2} & U_{e3} \\ U_{\mu 1} & U_{\mu 2} & U_{\mu 3} \\ U_{\tau 1} & U_{\tau 2} & U_{\tau 3} \end{pmatrix} \\ &= \begin{pmatrix} c_{12}c_{13} & s_{12}c_{13} & s_{13}e^{-i\delta} \\ -s_{12}c_{23} - c_{12}s_{23}s_{13}e^{i\delta} & c_{12}c_{23} - s_{12}s_{23}s_{13}e^{i\delta} & s_{23}c_{13} \\ s_{12}c_{23} - c_{12}s_{23}s_{13}e^{i\delta} & -c_{12}c_{23} - s_{12}s_{23}s_{13}e^{i\delta} & c_{23}c_{13} \end{pmatrix}, \end{aligned} \tag{1.14}$$

where $s_{ij} = \sin\theta_{ij}$, $c_{ij} = \cos\theta_{ij}$ $(i, j = 1, 2, 3)$, θ_{ij} are mixing angles, and δ is CP phase. A probability of a flavor transition $P(\nu_\alpha \to \nu_\beta)$ is calculated as

$$\begin{aligned} P(\nu_\alpha \to \nu_\beta) = \delta_{\alpha\beta} &- 4\sum_{i>j} \mathrm{Re}(U^*_{\alpha i}U_{\beta i}U^*_{\alpha j}U^*_{\beta j}) \sin^2\left(\frac{\Delta m^2_{ij}}{4E}L\right) \\ &+ 2\sum_{i>j} \mathrm{Im}(U^*_{\alpha i}U_{\beta i}U^*_{\alpha j}U^*_{\beta j}) \sin^2\left(\frac{\Delta m^2_{ij}}{2E}L\right), \end{aligned} \tag{1.15}$$

where $\delta_{\alpha\beta}$ is Kronecker's delta which equals to 1 when $\alpha = \beta$ and 0 when $\alpha \neq \beta$, E is the energy of neutrino, L is the propagating distance, and Δm^2_{ij} is mass-squared difference defined as

$$\Delta m^2_{ij} = m^2_i - m^2_j. \tag{1.16}$$

As shown in Equation 1.15, neutrino changes its flavor in propagation only if neutrinos have finite masses.

The non-zero neutrino mass is established in 1998 by the observation of neutrino oscillation in atmospheric neutrinos by SuperKamiokande [9]. And then, the SNO experiment established that the solar neutrino anomaly is due to the neutrino oscillation [10]. Nowadays, the neutrino oscillation is measured by using various neutrino sources such as atmospheric, solar, reactor, and accelerator. Table 1.1 summarizes the neutrino oscillation parameters obtained by a global fit of the current neutrino oscillation data [11].

What can be measured by neutrino oscillation is squared difference of the masses, insensitive to absolute mass. The order of m_2 and m_3 are also not determined. If $\Delta m^2_{32} > 0$, the ordering of neutrino masses is $m_3 > m_2 > m_1$ and is called "Normal Ordering (NO)", and if $\Delta m^2_{32} < 0$, $m_2 > m_1 > m_3$ called "Inverted Ordering (IO)".

Table 1.1: Neutrino oscillation parameters from PDG2018 [11]

Oscillation Parameter	Best fit value
$\sin^2\theta_{12}$	0.307 ± 0.013
$\sin^2\theta_{23}$ (NO, Octant I)	$0.417^{+0.025}_{-0.028}$
$\sin^2\theta_{23}$ (NO, Octant II)	$0.597^{+0.024}_{-0.030}$
$\sin^2\theta_{23}$ (IO, Octant I)	$0.421^{+0.033}_{-0.025}$
$\sin^2\theta_{23}$ (IO, Octant II)	$0.592^{+0.023}_{-0.030}$
$\sin^2\theta_{13}$	$(2.12 \pm 0.08) \times 10^{-2}$
Δm^2_{12}	$(7.53 \pm 0.18) \times 10^{-5}$ eV^2
Δm^2_{32} (NO)	$(2.51 \pm 0.05) \times 10^{-3}$ eV^2
Δm^2_{32} (IO)	$(-2.56 \pm 0.04) \times 10^{-3}$ eV^2

1.3.2 Mass Ordering of Neutrinos

Measurement of neutrino oscillation also has a sensitivity to determine the mass ordering via the matter effect during the oscillation of $\nu_\mu \to \nu_e$. The matter effect is a change of the probabilities of the neutrino oscillation when traveling in dense mediums such as the Earth. In a dense medium, ν_μ and ν_τ interact with electrons via neutral current and ν_e interacts via both charged and neutral current. Therefore, an electron neutrino feels different potential from the other species of neutrino resulting in the change of the oscillation probabilities depending on the scale and sign of the squared difference of the masses. The long baseline neutrino oscillation experiments, T2K experiment and NOνA experiment, are suitable for measuring the effect of the matter effect because of the fixed well-known flight distance. Because the baseline of the NOνA experiment (L$\sim$810 km) is longer than that of the T2K experiment (L$\sim$295 km), the matter effect is more significant in NOνA and it is more sensitive to the mass ordering of the neutrinos. SuperKamiokande also tries to determine the mass ordering by measuring atmospheric neutrinos [12]. Although the significance is not yet conclusive, recent results from oscillation experiments prefer the normal ordering by 99.7% [13].

1.3.3 Limit on the Mass of Neutrino

The absolute scale of the neutrino masses is still unknown. It is only known that they are very light, less than about 0.1 eV. This is seven or more orders of magnitude lighter than other fermions. This unnaturalness may be solved by another mechanism from the BEH mechanism as will be described in Section 1.5.2.

Constraint from Direct Mass Measurement

The direct neutrino mass measurement is based on the kinematics of beta decay. The maximum energy of the beta rays is decreased by the neutrino mass as shown in Figure 1.2. The neutrino mass measured by beta decay is the averaged electron neutrino mass $\langle m_{\nu_e} \rangle$ defined as

$$\langle m_{\nu_e} \rangle \equiv \sqrt{\sum_{i=1}^{3} |U_{ei}^2| m_i^2}. \tag{1.17}$$

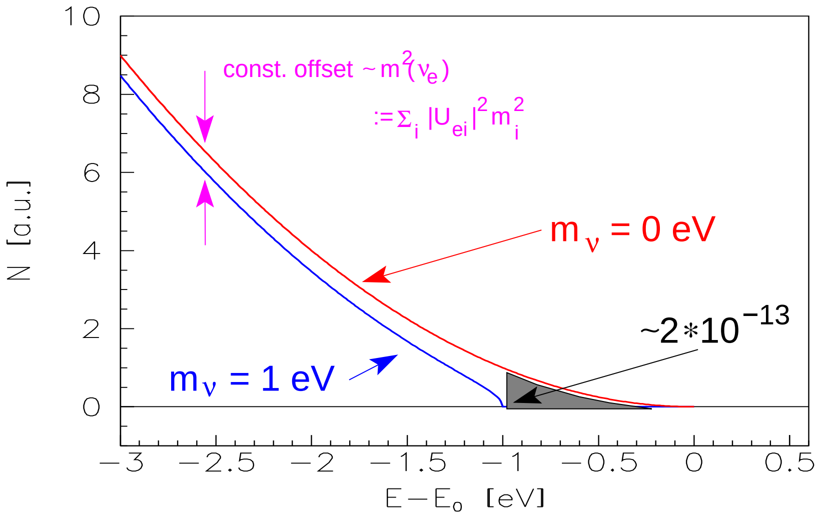

Figure 1.2: Schematic electron energy spectrum of ^{3}H beta decay around the end point. The horizontal axis represents the energy of beta rays (E) subtracted by the maximum electron energy in case of zero neutrino mass (E_0). The red line represents the spectrum with $\langle m_{\nu_e} \rangle = 0$ eV and the blue line represents $\langle m_{\nu_e} \rangle = 1$ eV. The gray-shaded area corresponds to a fraction of 2×10^{-13} of all tritium beta decays. The figure is taken from [14].

The most strict limit of the neutrino mass is given by the KATRIN experiment measuring tritium β-decays. With 4-week measurement in 2019, they obtained

$$\langle m_{\nu_e} \rangle < 1.1 \text{ eV (90\% C.L.) [15]}. \tag{1.18}$$

The statistic error is dominant in the result and will be improved with 1,000-day measurement. The target sensitivity is $\langle m_{\nu_e} \rangle < 0.2$ eV (90% C.L.).

Constraint from Cosmology

The neutrino masses are also constrained from cosmological observations. The obtained value depends on the cosmological model and the combinations of various measurements such as CMB, weak lensing, and Hubble constant. In 2018, the Planck collaboration reported the limit for the total neutrino masses (m_{total}) using *planck* TT, TE, EE+lowE+lensing+baryon acoustic oscillation, and Hubble constant [16]:

$$m_{\text{total}} = \sum m_\nu < 0.12 \text{ eV (95\% C.L.)}. \tag{1.19}$$

Since the mass differences of neutrinos are small compared to the upper limit of the total mass, 0.12 eV, the mass of the lightest neutrino is estimated by

$$m_{\text{lightest}} \simeq m_{\text{total}}/3 < 0.04 \text{ eV (95\% C.L.)}. \tag{1.20}$$

Constraint from Neutrinoless Double Beta Decay

The measurement of neutrinoless double beta decay ($0\nu\beta\beta$ decay) also constraints the neutrino effective mass. The detail of the neutrinoless double beta decay and the neutrino effective mass are explained in Section 1.5.3. The most strict constraint of the effective neutrino mass $\langle m_{\beta\beta}\rangle$ is given by the KamLAND-Zen experiment [17]. The obtained half life of ^{136}Xe $0\nu\beta\beta$ decay is $T^{0\nu}_{1/2} = 1.07 \times 10^{26}$ years and this corresponds to the upper limit of the effective neutrino mass of

$$\langle m_{\beta\beta}\rangle < 61 - 165 \text{ meV} \ \ (90\% \text{ C.L.}). \tag{1.21}$$

1.4 Matter-Antimatter Asymmetry in Universe

The universe today mostly consists of matter and little anti-matter exists. It indicates that in the early universe a small asymmetry between the baryon number and the anti-baryon number existed. Then almost baryons and anti-baryons annihilate to be photons and slightly excessive baryons remained. The degree of asymmetry is expressed as the ratio of the baryon asymmetry ($\Delta n_B = n_B - n_{\bar{B}}$) divided by photon number density (n_γ) [18]:

$$\eta \equiv \frac{\Delta n_B}{n_\gamma} = (6.21 \pm 0.16) \times 10^{-10}. \tag{1.22}$$

It is convenient to rewrite the expression using entropy density (s) instead of the photon number density because s almost represents the same meanings as the photon number density and it conserves during the early universe with the generation and annihilation of photons:

$$\eta_s \equiv \frac{\Delta n_B}{s} = (8.75 \pm 0.23) \times 10^{-11}. \tag{1.23}$$

1.4.1 Sakharov's Conditions

In order to generate the matter-antimatter asymmetry in the universe, A. Sakharov gave three requirements [19]:

- Baryon number violating processes
- Violation of C-symmetry and CP-symmetry
- Interaction out of thermal equilibrium

Actually, the first condition, baryon number violation, is not sufficient. Even if the baryon number is violated, the generated baryon number vanishes via sphaleron process, which is a process possible within the framework of the standard model and conserves $B - L$, where B is baryon number and L is lepton number. Therefore, the first condition should be replaced by

- Existence of processes violating $B - L$.

As scenarios which meet the conditions, "Baryogenesis" and "Leptogenesis" were proposed.

1.4.2 Baryogenesis

An attempt to explain the baryon number generation within the framework of the standard model had been made and is called "electroweak baryogenesis". However, in this scenario, the mass of the Higgs particle is constrained below 73 GeV [20], which contradicts with the observed Higgs mass $m_H = 126$ GeV [11]. The degree of CP violation by the CKM mechanism is not enough to generate the asymmetry of the universe today [21]. Supersymmetry (SUSY) might give another explanation to electroweak baryogenesis beyond the standard model, however, it requires a light scalar top quark ($\tilde{t}$) which is almost excluded by the experiments at the LHC [22] [23].

1.4.3 Leptogenesis

The idea that the baryon number generation is originated from the lepton number generation was proposed. The lepton number is generated, for instance, by a decay of heavy right-handed Majorana neutrino. Majorana neutrino is explained in Section 1.5.1. The decay process itself can violate CP-symmetry and can be out of equilibrium. The generated lepton number is converted into baryon number via the sphaleron process. This scenario is called "leptogenesis" originally proposed by M. Fukugita and T. Yanagida (thermal leptogenesis) [24]. Nowadays, various scenarios based on the leptogenesis have been proposed and studied such as leptogenesis from inflaton decay [25], Affleck-Dine leptogenesis [26] [27] [28], leptogenesis via right handed neutrino oscillation [29], and so on. In any cases, right handed Majorana neutrino plays an important role. Thus, confirmation of the existence of Majorana neutrino is essential for the understanding of the matter-antimatter asymmetry in universe.

1.5 Neutrinoless Double Beta Decay

1.5.1 Majorana Mass

Dirac mass term consists of left- and right-handed fermions as described in Section 1.1.2. E. Majorana showed that it is possible to construct a mass term with left-handed only or right-handed only if the fermion ψ satisfies the condition

$$\psi^C = \psi, \tag{1.24}$$

where ψ^C is the charge conjugation of ψ [30]. Such fermion is called "Majorana fermion". The condition can be rewritten using the left- and right-handed components, ψ_L and ψ_R, as

$$\psi = \begin{pmatrix} \psi_L \\ \psi_R \end{pmatrix} = \psi^C = \begin{pmatrix} \psi_R^C \\ \psi_L^C \end{pmatrix}. \tag{1.25}$$

and can be satisfied only by neutral fermions. In the standard model, only neutrino is a candidate of the Majorana fermion.

The mass term of left-handed Majorana neutrino is represented as

$$\mathcal{L}^L_{\text{neutrino mass}} = -M_L \overline{\nu_L} \nu_L = -\frac{M_L}{2}(\overline{\nu_R^C}\nu_L + \overline{\nu_L}\nu_R^C) \tag{1.26}$$

and right-handed Majorana neutrino as

$$\mathcal{L}^R_{\text{neutrino mass}} = -M_R \overline{\nu_R} \nu_R = -\frac{M_R}{2}(\overline{\nu_L^C}\nu_R + \overline{\nu_R}\nu_L^C). \tag{1.27}$$

Unlike the Dirac fermions, in the case of the Majorana fermion, different masses are permitted for the left handed and right handed states.

1.5.2 See-Saw Mechanism

The scenario that neutrinos acquire their mass via the BEH mechanism is possible by introducing right handed neutrinos which do not contribute to the weak interaction.

$$\mathcal{L}^{D}_{\text{neutrino mass}} = -m_D\overline{\nu}\nu = -m_D(\overline{\nu_L}\nu_R + \overline{\nu_R}\nu_L) \tag{1.28}$$

However, in this case the unnaturalness of the very light neutrino masses remains. Introducing right handed heavy Majorana neutrinos to the SM may provide a natural explanation for the neutrino mass [24]. With an assumption of the Majorana neutrino, the neutrino mass term in Lagrangean is written as

$$\begin{aligned} -\mathcal{L}_{\text{neutrino mass}} &= -\mathcal{L}^{D}_{\text{neutrino mass}} - \mathcal{L}^{L}_{\text{neutrino mass}} - \mathcal{L}^{R}_{\text{neutrino mass}} \\ &= m_D(\overline{\nu_L}\nu_R + \overline{\nu_R}\nu_L) + \frac{M_L}{2}(\overline{\nu^C_R}\nu_L + \overline{\nu_L}\nu^C_R) + \frac{M_R}{2}(\overline{\nu^C_L}\nu_R + \overline{\nu_R}\nu^C_L) \\ &= \frac{1}{2}(\overline{\nu_L}, \overline{\nu^C_L}) \begin{pmatrix} M_L & m_D \\ m_D & M_R \end{pmatrix} \begin{pmatrix} \nu^C_R \\ \nu_R \end{pmatrix}, \end{aligned} \tag{1.29}$$

where $\hat{M} = \begin{pmatrix} M_L & m_D \\ m_D & M_R \end{pmatrix}$ is so-called "neutrino mass matrix". Diagonalization of the mass matrix by unitary matrix U is needed to find the fields of massive neutrinos.

$$M_{\text{diag}} = U^T\hat{M}U = \begin{pmatrix} M_1 & 0 \\ 0 & M_2 \end{pmatrix}, \tag{1.30}$$

where M_1 and M_2 are the observable of neutrino masses and are given as:

$$M_1, M_2 = \frac{M_L + M_R}{2} \pm \sqrt{\frac{(M_R - M_L)^2}{4} + m_D^2}. \tag{1.31}$$

Let us consider the situation:

$$M_L = 0, \quad M_R \gg m_D, \tag{1.32}$$

which corresponds to "type-I seesaw". Under this condition, the diagonalized masses can be approximated as

$$M_1 \simeq \frac{m_D^2}{M_R}, \quad M_2 \simeq M_R. \tag{1.33}$$

If the Dirac mass m_D is chosen as the same scale as other fermions, ∼100 GeV and the Majorana mass is set to much higher scale, for instance, 10^{15} GeV, which corresponds to the energy scale of the grand unified theory (GUT), the observed neutrino mass M_1 is very small (<1 eV) and another neutrino remains very heavy ($M_2 \simeq M_R = 10^{15}$ GeV). This is the seesaw mechanism which can explain smallness of the neutrino mass naturally.

1.5.3 Neutrinoless Double Beta Decay

Double beta decay is a phenomenon in which beta decay occurs twice at the same time. It occurs if single beta decay is forbidden due to energy conservation or large spin difference with the daughter nucleus. In the double beta decay, two neutrons transform into two protons in the nucleus, and two electrons and two anti-neutrinos are emitted. This decay mode is called "$2\nu\beta\beta$ decay" and occurs in the framework of the standard model. The Feynman diagram of the $2\nu\beta\beta$ decay is shown in Figure 1.3a.

If the neutrino has a Majorana mass term, a decay that does not emit neutrinos may occur. This mode is called neutrinoless double beta decay ($0\nu\beta\beta$ decay). The Feynman diagram of $0\nu\beta\beta$ decay mode is shown in Figure 1.3b. This process violates lepton number conservation ($\Delta L = +2$). The half life of the $0\nu\beta\beta$ decay, $T^{0\nu}_{1/2}$, is expressed as follows:

$$(T^{0\nu}_{1/2})^{-1} = G_{0\nu}|M^{0\nu}|^2\langle m_{\beta\beta}\rangle^2, \tag{1.34}$$

where $G_{0\nu}$ is a phase space factor, $M^{0\nu}$ is a nuclear matrix element of the $0\nu\beta\beta$ decay, and $\langle m_{\beta\beta}\rangle$ is an effective neutrino mass defined as

$$\langle m_{\beta\beta}\rangle \equiv |\Sigma_i U^2_{ei} m_{\nu_i}|. \tag{1.35}$$

The phase space factor $G^{0\nu}$ is calculated from the initial and final state of the decay. The nuclear matrix element is calculated from the structure of the nucleus however it depends much on the nuclear models. Thus, the values of the nuclear matrix element have a significant uncertainty with factor of 2–3. Because of the large uncertainty of the value of the nuclear matrix element, the effective neutrino mass derived from the life time using Equation (1.34) also has a large uncertainty. Figure 1.4 shows the calculated values of the nuclear matrix element in various models.

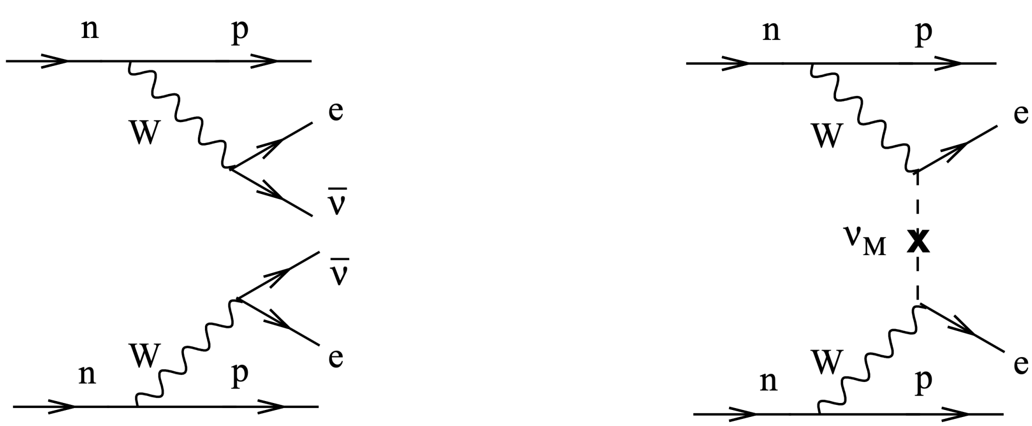

(a) $2\nu\beta\beta$ decay.

(b) $0\nu\beta\beta$ decay.

Figure 1.3: Feynman diagrams of double beta decay. Pictures are taken from [31].

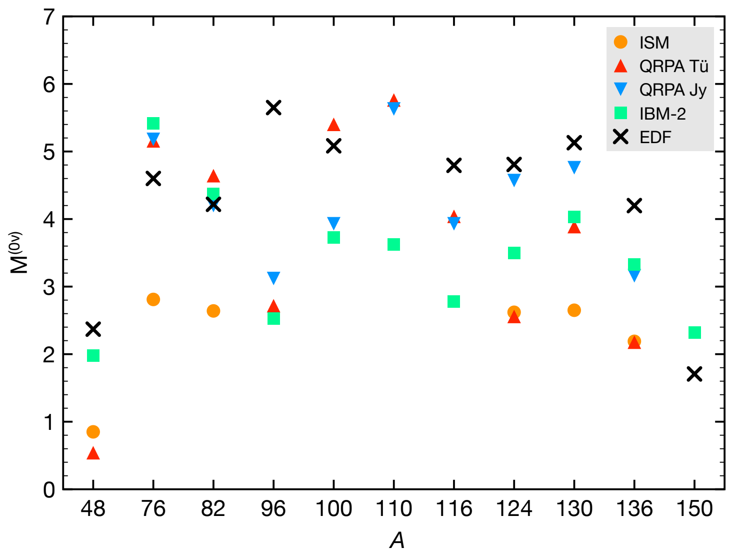

Figure 1.4: Nuclear matrix elements for various nuclei with various nuclear models [32]. The horizontal axis, A, is mass number of atoms.

Since neutrinos have an extremely small cross section, only two beta rays can be observed in both decay mode. Figure 1.5 shows a schematic spectrum of the energy sum of the two electrons emitted from double beta decay. The $2\nu\beta\beta$ decay spectrum is continuous distribution because the two neutrinos take off kinetic energies. On the other hand, the energy spectrum has a sharp peak structure for the $0\nu\beta\beta$ decay. In principle, the peak is a mono-energetic, but is smeared by the detector resolution. These two modes can be distinguished if a detector has sufficient energy resolution.

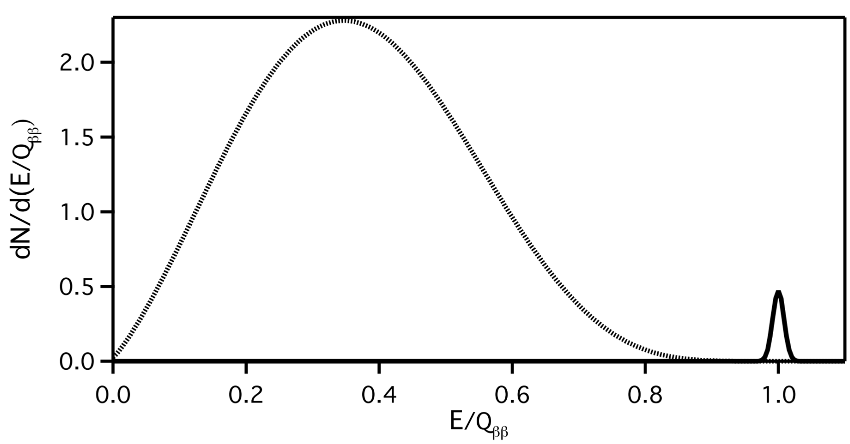

Figure 1.5: Schematic spectrum of the energy sum of the two electrons from double beta decay normalized by the Q-value of $0\nu\beta\beta$ decay. The left dotted spectrum is for $2\nu\beta\beta$ and the right solid curve corresponds to $0\nu\beta\beta$ decay smeared by a detector energy resolution. Redrawn from [31].

The rate of the $0\nu\beta\beta$ decay is largely affected by the mass ordering of neutrinos. The relation between the effective neutrino mass and the lightest neutrino mass, m_1 for the normal hierarchy or m_3 for the inverted hierarchy, is shown in Figure 1.6. The limit in the horizontal axis comes from cosmological observations as mentioned in Section 1.3.3. Measurements of the $0\nu\beta\beta$ decay constrain the vertical direction.

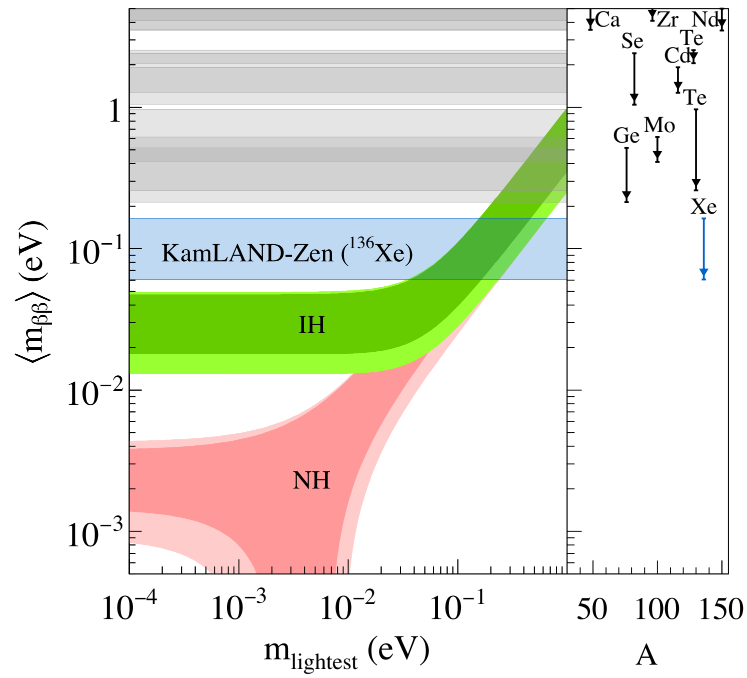

Figure 1.6: Allowed region of the effective neutrino mass as a function of the lightest neutrino mass. Redrawn from [17]. The blue band represents the current best limit for the neutrino effective mass given by the KamLAND-Zen experiment. The arrows shown in right represent constraints obtained by various isotopes. Note that the limits of Ge and Te are currently updated. Here, IH (NH) means inverted (normal) ordering.

Searching for the $0\nu\beta\beta$ decay has essential importance for particle physics and cosmology because it can potentially determine the absolute mass scale of neutrinos, the mass ordering, and whether neutrino is Dirac or Majorana particle.

1.5.4 Requirements for Experiments Searching for Neutrinoless Double Beta Decay

Since the $0\nu\beta\beta$ decay is a very rare process even if it occurs, following requirements should be satisfied.

- Large target mass
  To fully cover the inverted hierarchy region, ton-scale $\beta\beta$-decay isotopes are required.
- Good energy resolution
  Only a good energy resolution can distinguish the $2\nu\beta\beta$ decay background.
- Low background
  Extremely low background environment is required. Very radiopure materials and good background rejection methods using, for example, track pattern are required.

1.5.5 Experiments to Search for Neutrinoless Double Beta Decay

A lot of $0\nu\beta\beta$ decay search experiments are ongoing and planned. Among those, three experiments which recorded the most strict limit for ^{136}Xe, ^{76}Ge, and ^{133}Te are introduced here. In addition, two experiments using xenon time projection chamber (TPC), EXO experiment and NEXT experiment, are introduced.

KamLAND-Zen

The KamLAND ZEro Neutrino double-beta decay (KamLAND-Zen) experiment searches for the $0\nu\beta\beta$ decay using 91% enriched ^{136}Xe loaded to liquid scintillator (LS). The xenon loaded LS is filled in a nylon film balloon with 25 μm thickness (so called "mini-balloon") suspended in the KamLAND detector. The KamLAND detector is located at the Kamioka mine, which is underground site with 2,700 meter water equivalent (m.w.e.) rocks on top of it. In the first phase (Phase-I) of KamLAND-Zen, 320 kg of ^{136}Xe enriched xenon were loaded and a measurement was done with a total live time of 270.3 days and in total exposure of 89.5 kg·year. Unexpected backgrounds were found in the KamLAND-Zen Phase-I at the region around the Q-value. After purification, KamLAND-Zen Phase-II with 380 kg ^{136}Xe enriched xenon started in 2013. The total exposure of Phase-II was 504 kg·year with 534.5 days measurement. By combining the data of Phase-I and Phase-II, the lower limit for the half life of ^{136}Xe is obtained as

$$T^{0\nu}_{1/2}(^{136}\text{Xe}) > 1.07 \times 10^{26} \text{ year} \quad (90\% \text{ C.L.}) \text{ [17]}, \tag{1.36}$$

which corresponds to the effective neutrino mass of

$$\langle m_{\beta\beta} \rangle < 61 - 165 \text{ meV}. \tag{1.37}$$

This result is the most strict constraint of neutrino effective mass currently (March 2020). The KamLAND-Zen Phase-I and Phase-II are collectively called KamLAND-Zen 400.

In KamLAND-Zen 400, backgrounds from the mini-balloon surface or mini-balloon itself restricted the sensitivity. A new mini-balloon was introduced with very careful control of contamination of impurities. The diameter of the new mini-balloon was extended from $R = 1.54$ m (for KamLAND-Zen 400) to $R = 1.90$ m. In total, about 800 kg of ^{136}Xe enriched xenon was installed into the new mini-balloon. The experimental phase using the new mini-balloon and about 800 kg enriched xenon is named KamLAND-Zen 800. Currently, a measurement of KamLAND-Zen 800 is ongoing.

The contamination of $2\nu\beta\beta$ decay is one of the most serious backgrounds because the energy resolution of KamLAND-zen is not so good, and limits the sensitivity. The achieved energy resolution is 9.6% (FWHM) at the Q-value [17]. To improve the energy resolution, KamLAND2 zen is planned. The light yield will be improved by 10 times by introducing high Q.E. PMT, new brighter LS, and light collecting mirrors.

GERDA

The GERmanium Detector Array (GERDA) experiment searches for $0\nu\beta\beta$ decay using 86% ^{76}Ge-enriched high purity Ge (HPGe) detector arrays. The experimental site is Laboratori Nazionali del Gran Sasso (LNGS) in Italy, which locates underground with 3,500 m.w.e., and the cosmic muon rate is reduced to 1.2 $\mu/\text{m}^{-2}\text{h}^{-1}$. The feature of the germanium detector is its excellent energy resolution. They achieved the energy resolution of 0.147% FWHM at the ^{76}Ge Q-value, 2039 keV. The germanium detector arrays are immersed directly in the cryogen, 64 m^3 liquid argon (LAr), and cooled to the operating temperature of about 90 K. The LAr also works as an active veto with its scintillation lights to eliminate multi-site events, which are caused by a gamma-ray with Compton scattering. The LAr cryostat is surrounded by 590 m^3 ultra-pure water which acts as a passive veto for external backgrounds. A pulse shape discrimination (PSD) method was developed to remove surface β-ray backgrounds. They started the Phase-I measurement in 2011 and collected data with 21.6 kg·year exposure. The Phase-II measurement was started in December 2015 and 58.9 kg·year exposure has been collected by April 2018. Combining the Phase-I and Phase-II data, a limit for the half life of ^{76}Ge $0\nu\beta\beta$ decay,

$$T^{0\nu}_{1/2}(^{76}\text{Ge}) > 0.9 \times 10^{26} \text{ year} \quad (90\% \text{ C.L.}), \tag{1.38}$$

was obtained [33]. It corresponds to the neutrino effective mass of $\langle m_{\beta\beta} \rangle < 100 - 230$ meV.

They achieved a background free measurement and only the statistics limits the sensitivity.

CUORE and CUPID

The Cryogenic Underground Observatory for Rare Events (CUORE) experiment searches for $0\nu\beta\beta$ decay using TeO_2 crystals operated as a bolometric detector. The $0\nu\beta\beta$ decay source is ^{133}Te in TeO_2 crystals with a natural abundance of 33.8%. Crystals with the total mass of 742 kg were installed in a cryostat surrounded by lead, steel, and radiation shields. The total mass of the source is 206 kg. The crystals are connected to copper holders via weak thermal couplings and kept under 10 mK. A neutron transmutation doped germanium sensor (NTD Ge sensor) detects the temperature rise in a detector. CUORE achieved good energy resolution, 0.30 ± 0.02 keV (FWHM), at the ^{133}Te $0\nu\beta\beta$ decay Q-value, 2527.5 keV [34].

They reported the first result of $0\nu\beta\beta$ decay search with 86.3 kg·year exposure. The obtained lower limit of the $0\nu\beta\beta$ decay half life is

$$T^{0\nu}_{1/2}(^{133}\text{Te}) > 1.5 \times 10^{25} \text{ year} \quad (90\% \text{ C.L.}) \tag{1.39}$$

by combining the results from the previous experiments, Cuoricino [35] and CUORE-0 [36]. This yields the effective mass as

$$\langle m_{\beta\beta} \rangle < 110 - 520 \text{ meV} \quad (90\% \text{ C.L.}) \text{ [34]}. \tag{1.40}$$

The data taking of CUORE is ongoing and their target discovery sensitivity is $T^{0\nu}_{1/2} = 4.0 \times 10^{25}$ year with five-year measurement.

As the future project, CUORE Upgrade with Particle IDentification (CUPID) is proposed and the first demonstrator, CUPID-0 has been constructed. CUPID-0 uses ZnSe crystals as a bolometer and a scintillator. The double beta source is ^{82}Se whose Q-value is 2998 keV. Combination of two kinds of signals, heat signal and light signal, makes it possible to distinguish β/γ events from α events because of the quenching effect to α events. The first phase physics run started in 2017 and the total exposure of 9.95 kg·year data were collected. No evidence for $0\nu\beta\beta$ decay is seen and they set a lower limit for the half-life of ^{82}Se $0\nu\beta\beta$ decay as

$$T^{0\nu}_{1/2}(^{82}\text{Se}) > 3.5 \times 10^{24} \text{ year} \quad (90\% \text{ C.L.}) \text{ [37]}. \tag{1.41}$$

EXO-200 and nEXO

Enriched Xenon Observatory (EXO) was conducted in Waste Isolation Pilot Plant (WIPP) with an overburden of 1,624 m.w.e. near Carlsbad New Mexico, USA. It uses two identical back-to-back time projection chambers (TPC) filled with ^{136}Xe enriched liquid xenon. The ionization signal is read out by the cathodes made of crossed wire planes at both ends of the chamber. The scintillation signals are also acquired by avalanche photo-diodes (APDs) placed behind the cathodes. Three-dimensional position reconstruction is achieved using the timing information of scintillation signal and hit pattern at the cathode wires. The energy information is reconstructed from both the ionization signal and the scintillation signal. Combination of these two kinds of signals improves the energy resolution and their achieved energy resolution is 2.7±0.05% (FWHM) at the ^{136}Xe $0\nu\beta\beta$ decay Q-value. EXO-200 started data taking in 2011 and finished in December, 2019 with the total exposure of 234.1 kg·year. No statistically significant $0\nu\beta\beta$ decay signal was observed and a lower limit is set as

$$T^{0\nu}_{1/2}(^{136}\mathrm{Xe}) > 3.5 \times 10^{25} \text{ year} \quad (90\% \text{ C.L.}), \ [38]. \tag{1.42}$$

which corresponds to the effective neutrino mass of $\langle m_{\beta\beta} \rangle = 93 - 286$ meV.

As a future program, the nEXO experiment is proposed using single side TPC and 5 tons of enriched liquid xenon. The target sensitivity is $T^{0\nu}_{1/2}(^{136}\mathrm{Xe}) = 9.2 \times 10^{27}$ year (90% C.L.) with ten-year running [39]. A signal identification by tagging Ba^{++} ion, which is double beta decay daughter of ^{136}Xe, is also proposed and being studied.

NEXT

The Neutrino Experiment with a Xenon TPC (NEXT) is a pioneer of $0\nu\beta\beta$ decay search using high pressure xenon gas TPC and electroluminescence (EL) process to read out ionization signals. Ionization electrons generate EL photons by high electric field after drifting to the anode. Generated EL lights are detected by SiPMs for tracking purpose and by PMTs placed at the cathode side for energy measurement. The EL process makes it possible to achieve high energy resolution, less than 1% at the Q-value. Powerful background rejection is possible using track information, in particular, backgrounds from external γ-rays.

The proof of the concept was done by two small prototypes and the energy resolution of 1.75% (FWHM) was achieved at 511 keV corresponding to 0.8% (FWHM) at the ^{136}Xe $0\nu\beta\beta$ decay Q-value extrapolated by $1/\sqrt{E}$ [40].

Currently, they have developed and are operating a large size demonstrator, NEXT-White, for background studies and a measurement of $2\nu\beta\beta$ decay. By a calibration using ^{208}Tl, energy resolution of 0.91±0.07% was achieved at 1614.5 keV, which is the best energy resolution in $0\nu\beta\beta$ decay search experiment using xenon [41]. Backgrounds were measured using xenon depleted in ^{136}Xe in 2018 [42] and observation of $2\nu\beta\beta$ decay using ^{136}Xe enriched xenon is ongoing.

As future plans, NEXT-100 using about 100 kg of ^{136}Xe enriched xenon gas will be constructed and a search for $0\nu\beta\beta$ decay will start with a target sensitivity of $\langle m_{\beta\beta} \rangle < 70 - 130$ meV (90% C.L.) with 5 years of data [43].

1.6 AXEL Detector

The AXEL (A Xe ElectroLuminescence) detector is a high pressure xenon gas TPC to search for $0\nu\beta\beta$ decay. It is designed to meet the fundamental requirements described in Section 1.5.4. We choose ^{136}Xe as an isotope of $\beta\beta$-decay source. High pressure gas makes it easier to achieve ton-scale target mass. The EL process is used to convert ionization electrons into photons to measure a deposit energy with very high energy resolution: our target is 0.5% FWHM at 2458 keV, Q-value of $0\nu\beta\beta$ decay of ^{136}Xe. The readout part consists of PTFE body sandwiched by electrodes and has a cellular structure. We can also reconstruct an event topology using information from the TPC. With obtained track pattern, backgrounds of α-rays and γ-rays with Compton scattering are easily distinguished (see Section 2.2.3). Backgrounds of γ-ray with photoelectric absorption are also distinguishable using the information of endpoint of a track as described in Section 2.2.3. Detailed experimental principle is explained in Section 2.1.

Our detector concept is similar to the NEXT experiment in that both experiments use high pressure xenon gas TPC and EL process. However, our detection scheme has rigid structure making it easier to enlarge the detector compared to a detection scheme that consists of two faced meshes as the NEXT experiment. In addition, the cellular readout system has less event position dependence because the generated ionization electrons are collected into the cells and the acceptance to the photo-detectors are almost uniform as mentioned in Section 2.3.

To sweep out all the region of the inverted mass ordering (corresponding to $\langle m_{\beta\beta}\rangle = 20$ meV) is a milestone of many $0\nu\beta\beta$ decay search experiments today. The AXEL experiment also aims at the sensitivity of $\langle m_{\beta\beta}\rangle = 20$ meV with one ton of xenon gas. On the other hand, as explained in section 1.3.2, recent oscillation measurements indicate the normal mass ordering. Therefore, $0\nu\beta\beta$ decay search experiments in the next generations should aim to reach far below $\langle m_{\beta\beta}\rangle = 20$ meV. We, the AXEL experiment, also consider a sensitivity to $\langle m_{\beta\beta}\rangle = 1$ meV as an ultimate goal. Some ideas to achieve this are described in Chapter 7.

The project is now in R&D phase. We have constructed prototypes for proof of the concept and evaluated the detector performance.

1.7 Outline of This Thesis

The purpose of this thesis is to describe technical difficulties and solutions in the construction of the unique high pressure xenon gas TPC with cellular readout structure and to demonstrate the performance for $0\nu\beta\beta$ decay search experiment. In Chapter 2, overview of the AXEL experiment is described. Design and construction of a small size prototype are summarized in Chapter 3 and their performances are described in Chapter 4. Based on the experience of small prototype, we have constructed a larger prototype. Design of the large prototype is described in Chapter 5 and the obtained performance is explained in Chapter 6. In Chapter 7, the results are discussed. The future prospects are mentioned in this chapter. Finally, this thesis is summarized in Chapter 8.

Chapter 2

AXEL Detector

The AXEL detector is a high pressure xenon gas time projection chamber (TPC) for neutrinoless double beta ($0\nu\beta\beta$) decay search. In this chapter, the concept of the AXEL detector is explained.

2.1 Overview

A schematic of the AXEL detector is shown in Figure 2.1.

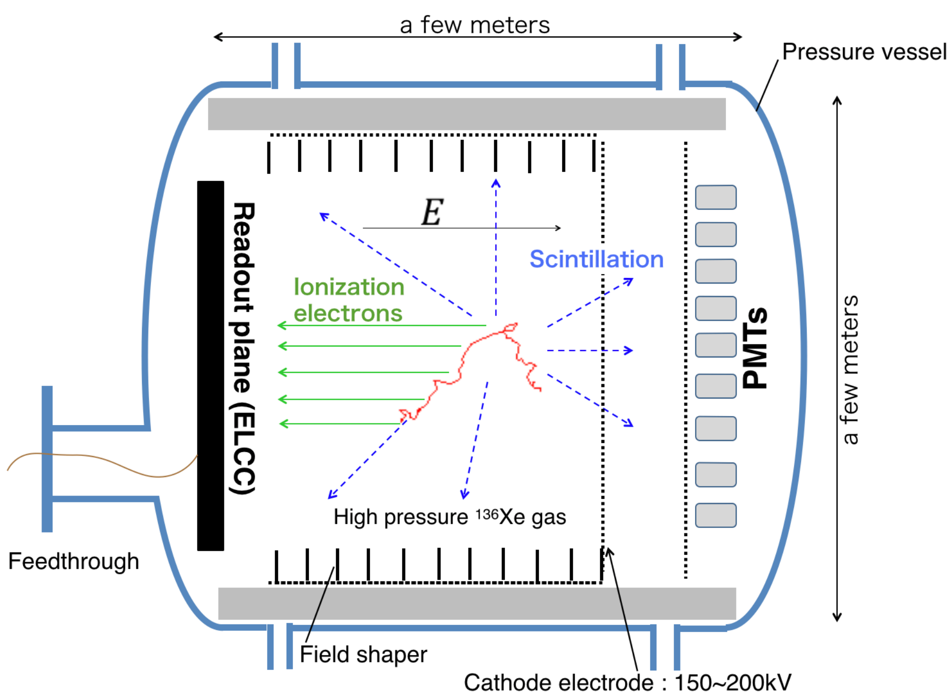

Figure 2.1: Schematic of the AXEL detector.

Most of the detector components and xenon gas are contained in a cylindrical pressure vessel. Sensitive region is formed between the cathode electrode and the plane to detect ionization electrons, which also acts as the anode. We have developed a unique readout structure called ELCC which utilizes electroluminescence process. Details of ELCC are explained in Section 2.3.2. A field shaper is located between anode and cathode electrodes to form a uniform electric field in the drift region of ionization electrons. Photomultiplier tubes (PMTs) are placed behind the cathode to detect scintillation light.

The detection principle is as follows. When charged particles are produced in xenon gas by various processes such as double beta decay, photoelectric absorption or Compton scattering of a gamma-ray, alpha decay, and beta decay, they lose their energy via interaction with surrounding xenon atoms and excite or ionize them. Excited atoms emit scintillation lights and they are detected by PMTs. Ionization electrons are drifted toward the ELCC plane by electric field and then further accelerated by strong electric field to generate electroluminescence (EL) lights in cells of the ELCC. The EL lights are detected by SiPMs (Silicon photomultipliers) in the cell. The energy deposition is reconstructed from the total amount of detected EL photons. The event topology is also reconstructed from the hit pattern of ionization signals at the ELCC and the time interval between the scintillation signal and ionization signal. The reconstructed event topology is used to distinguish $0\nu\beta\beta$ decay signals from backgrounds.

2.1.1 Interactions of Gamma-ray

A gamma-ray interacts with matter through one of the following three processes

- Photoelectric absorption
- Compton scattering
- Pair production

Photoelectric absorption is a process in which an orbital electron with some energies (called "photoelectron") jumps out after a photon interacts with an atom and disappears. The energy of a photoelectron E_e is given as

$$E_e = h\nu - E_\mathrm{b}, \tag{2.1}$$

where $h\nu$ is the energy of the initial gamma-ray and E_b is the binding energy of the shell where the photoelectron existed. Table 2.1 shows the main energy levels of xenon atom [44]. The energies of $\mathrm{K}_{\alpha1}$ and $\mathrm{K}_{\alpha2}$ are too close to distinguish with our detector, thus it is described as $\mathrm{K}_\alpha = 29.78$ keV hereafter.

Table 2.1: Binding energies of xenon atom [44].

Shell	Energy [keV]
$\mathrm{K}_{\alpha1}$	29.782
$\mathrm{K}_{\alpha2}$	29.461
K_{β}	33.642
$\mathrm{L}_{\alpha1}$	4.106

In the case of xenon, in approximately 87% of photoelectric absorption events, an electron in the K-shell is emitted. In the course of filling the vacancy of the K-shell, an X-ray (called "characteristic X-ray") is emitted for 87.5% and an Auger electron for 12.5% in the case of xenon. In case of the former, the X-ray sometime escapes from the sensitive region, and the observed energy is smaller by ∼30 keV than the initial energy making the escape peak. If the X-ray interacts again in the sensitive region or an Auger electron is emitted, the observed energy is the same with the initial energy of the incident gamma-ray (full peak). If the initial gamma-ray interacts out of the sensitive region and the characteristic X-ray interacts in the sensitive region, the observed energy is ∼30 keV and they make up characteristic X-ray peak. About 14% events of the photoelectric absorption are not involved in the K-shell, and the X-ray does not escape to outside of the sensitive region since the energy of a characteristic X-ray is small (a few keV). Thus, such an event looks as a single-site event instead of a multi-site event, that is, it looks as a single track event not accompanied by a characteristic X-ray.

The Compton scattering is a process, where an incident photon interacts with an orbital electron and both the photon and electron are scattered out. The relation of the energy of incident photons $h\nu$ and scattered photon $h\nu'$ is represented as follows

$$h\nu' = \frac{h\nu}{1 + \frac{h\nu}{m_e c^2}(1 - \cos\theta)}, \tag{2.2}$$

where θ is the angle of scattered photon and $m_e c^2$ is the rest mass of an electron (511 keV).

The pair production is a process in which a gamma ray is replaced with an electron-positron pair caused by the coulomb potential of a nuclear in matter. It can only occur with a gamma ray exceeding the threshold of 1022 keV, which is the sum of the rest masses of an electron and a positron.

Figure 2.2 shows the mass attenuation length of gamma-ray in xenon. At 122 keV, the photoelectric absorption process is dominant compared to the Compton scattering process. At 511 keV, the rate of the Compton scattering is higher than that of the photoelectric absorption.

Figure 2.3 shows the Continuous Slowing Down Approximation (CSDA) range normalized by the density of matters in xenon. The CSDA range means the range of an electron obtained by integrating the reciprocal of the stopping power (dE/dx) of matter from $E = 0$ to the initial energy of the electron. For instance, the CSDA range of an electron having the energy of 125 keV is 0.03827 g/cm^2 corresponding to 1.628 cm in 4 bar xenon.

2.1.2 Detector Coordinate

In this thesis, the detector coordinates are defined as follows. The x and y axes are parallel in the Cu-electrode of the ELCC plane. The central axis of field shapers of the drift region is taken as the z axis. (see Figure 2.4)

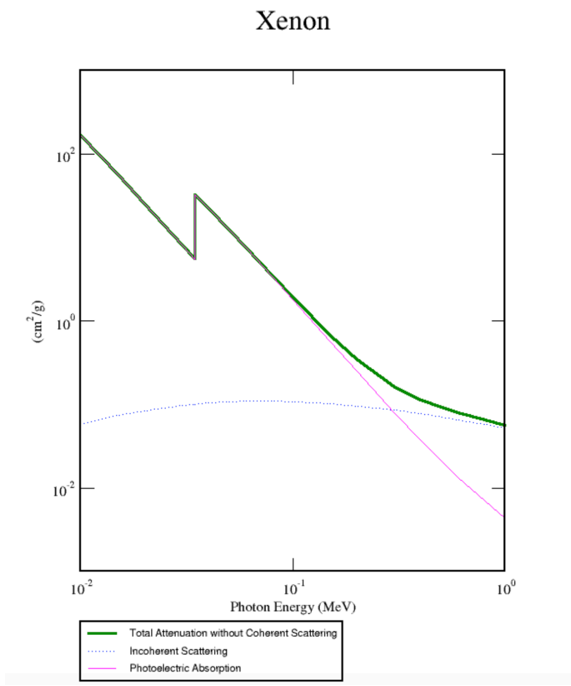

Figure 2.2: Mass attenuation length of gamma-ray in xenon [45]. In the energy range shown here, pair creation does not occur.

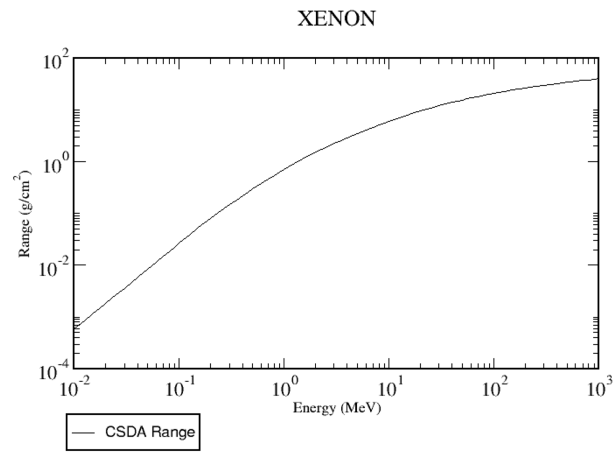

Figure 2.3: CSDA range of electron normalized by the density of matter [45].

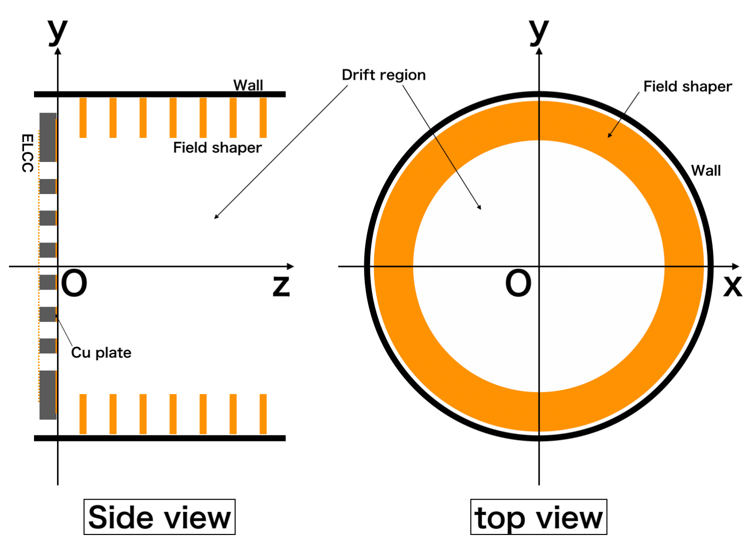

Figure 2.4: Definition of the detector coordinate.

2.2 Road Map and Expected Sensitivity of the AXEL Project

2.2.1 Road Map of the AXEL Project

Figure 2.5 shows the road map of the AXEL project. We have constructed two prototypes, "HP10L" and "HP180L". The main purposes of HP10L are to acquire the knowledge for constructing and operating a high pressure gas TPC, to observe the first signal from the ELCC, to evaluate the performance of the ELCC, and to achieve an good energy resolution. The targets of HP180L are to get the techniques to construct larger detector, to operate the detector for long term such as a week stably, to evaluate the performance at higher energy region, and to observe track pattern of gamma-rays. In addition, background studies are also a purpose of this prototype. "AXEL 1000 L" and "AXEL 1 ton" are future detectors for physics run. The target sensitivity of AXEL 1 ton is $\langle m_{\beta\beta}\rangle = 20$ meV covering all the region of the inverted ordering of the neutrino mass. Details and the results of evaluation of the two prototypes are described in Chapters 3 and 4 (HP10L) and Chapters 5 and 6 (HP180L).

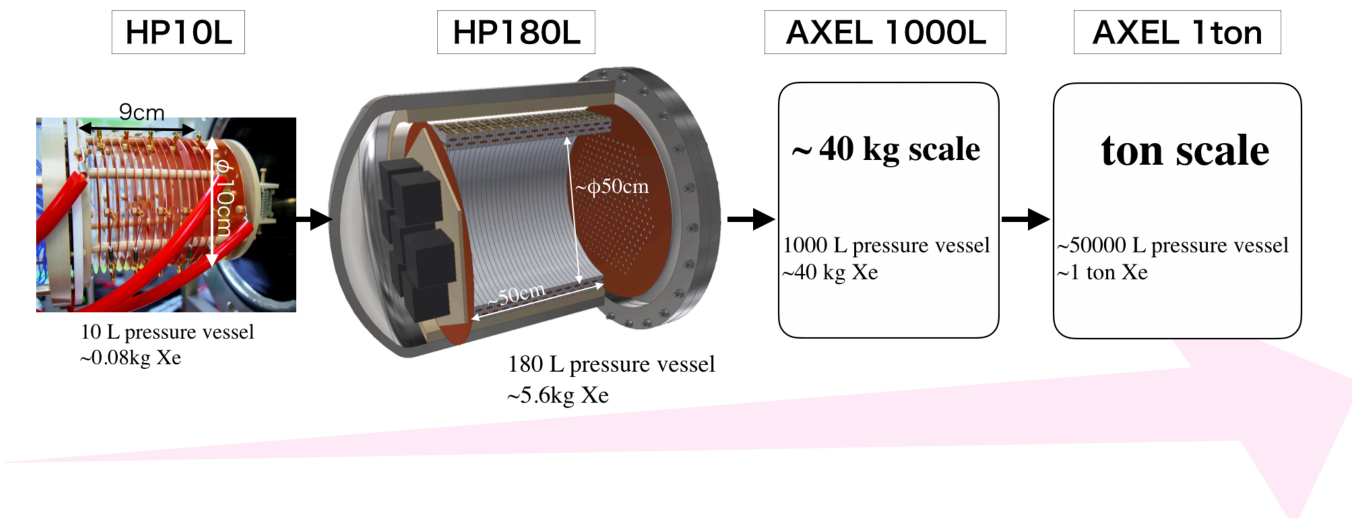

Figure 2.5: Road map of the AXEL project. HP10L and HP180L are prototypes to evaluate the performance of the AXEL detector. Physics run will be done with AXEL 1000 L aiming to a sensitivity of $\langle m_{\beta\beta}\rangle$ =60 meV, which is a world record of $0\nu\beta\beta$ decay search and the AXEL 1 ton aiming to sweep out all the region of the inverted ordering.

2.2.2 Contamination of $2\nu\beta\beta$ Decay Background

The $2\nu\beta\beta$ decay is irremovable intrinsic background for $0\nu\beta\beta$ decay search. The only way to distinguish this decay mode is using energy information. At the endpoint energy of the $2\nu\beta\beta$ decay spectrum, it has very little strength. However, the effect of finite energy resolution (ΔE) should be considered. The fraction (F) of the $2\nu\beta\beta$ events in the $0\nu\beta\beta$ peak region (Q$\pm\Delta E$) is approximated by

$$F = \frac{a(\delta)Q\delta^6}{m_e}, \tag{2.3}$$

where Q is the endpoint energy of $2\nu\beta\beta$ decay and almost same with the Q-value, δ $(= \Delta E/Q)$ is the energy resolution in FWHM, and m_e is the mass of electron (511 keV) [46]. The coefficient $a(\delta)$ depends moderately on the energy resolution and is 8.50 for the energy resolution of 1%.

2.2.3 Background Rejection Using Track Pattern

The track of beta-ray in xenon gas is twisty due to multiple scatterings. Thus the track pattern is further blurred to be observed by the diffusion of ionization electrons during drift. Still, the track pattern has useful information to discriminate signal and background. Figure 2.6 shows an example reconstructed track pattern of a $0\nu\beta\beta$ decay event generated by a simulation using GEANT4 [47]. All the events hereafter in this sub-section were also generated by the simulation. The $0\nu\beta\beta$ decay events are characterized by two large energy losses (blob) at the end points of the beta-rays. The pixel size of the display corresponds to the cell pitch for the xy plane, and the sampling rate of the digitizer for the z axis. In Figure 2.6, those are set to be 10 mm.

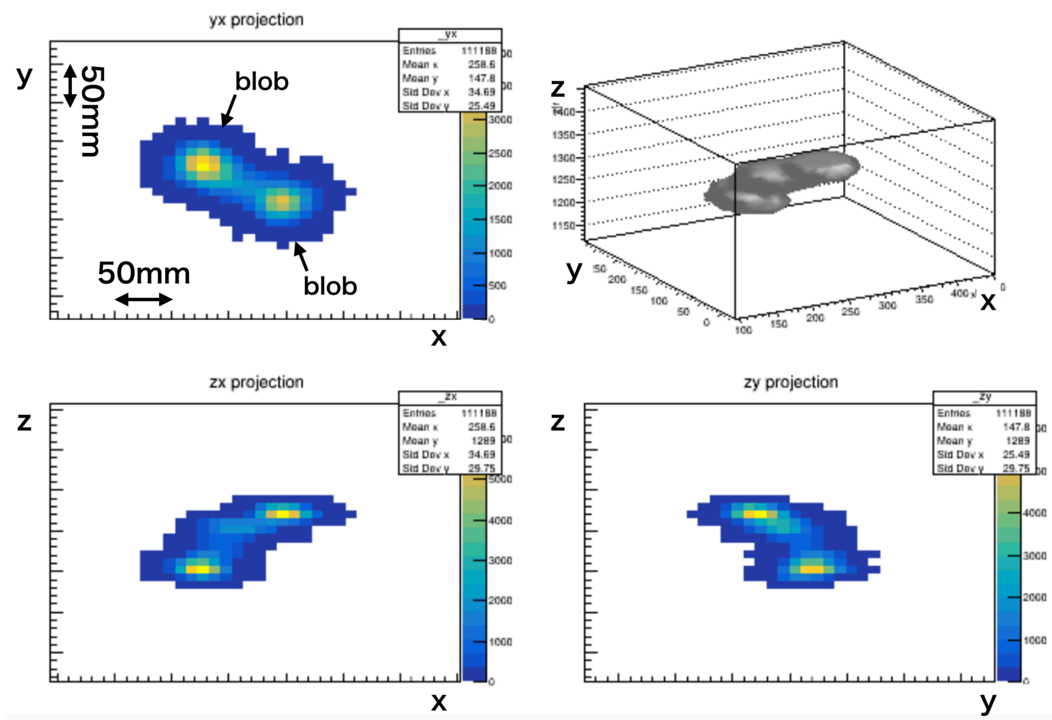

Figure 2.6: Reconstructed track pattern of a simulated $0\nu\beta\beta$ signal. Two blobs are seen at the end points of the two beta-rays. Here, pixel size of the ELCC is 10 mm.

Figures 2.7 and 2.8 show reconstructed track patterns of an alpha-decay event and a gamma-ray Compton scattering event, respectively. Both types of the events are easily distinguishable from the $0\nu\beta\beta$ decay signal since the alpha-decay event gives a point-like reconstructed image due to very short track of the alpha-ray and the Compton scattering gives a multi-site reconstructed track. The 98% of the interactions of 2.5 MeV gamma-rays with xenon gas are Compton scattering. Therefore majority of the gamma-ray events can be easily rejected as backgrounds.

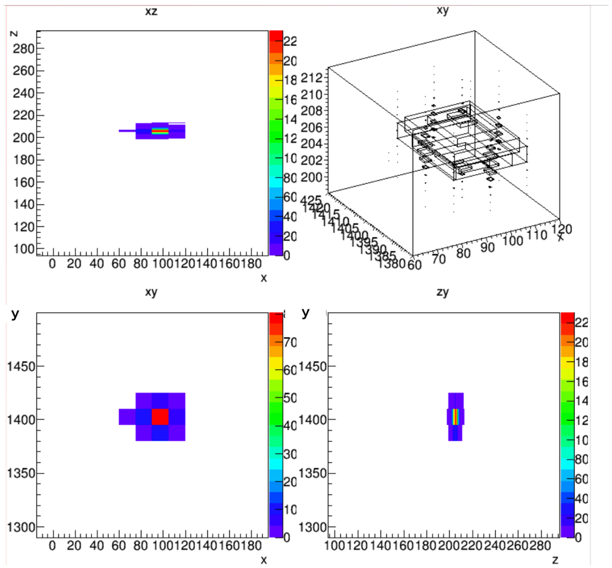

Figure 2.7: Reconstructed track pattern of a simulated alpha-decay event. The track has a point-like shape. The fineness of these pictures are 15 mm-pitch.

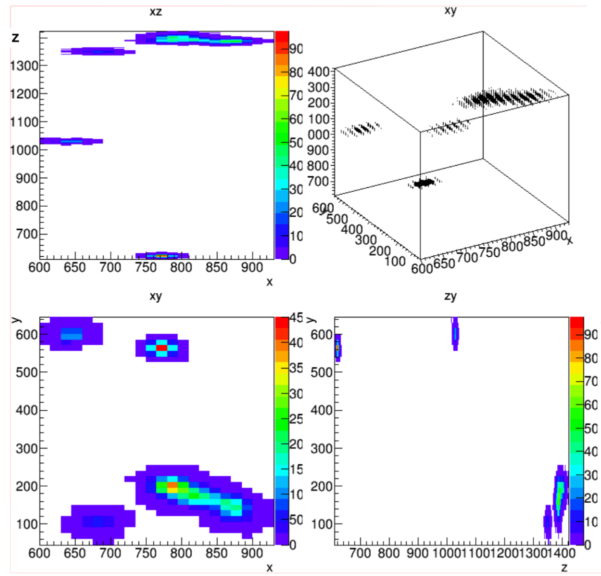

Figure 2.8: Reconstructed track pattern when a single gamma-ray incidents and interacts via Compton scattering. The fineness of these pictures are 15 mm-pitch

Figures 2.9 and 2.10 show gamma-ray photoelectric absorption events. Events with only a single blob, like the one in Figure 2.9, are distinguishable from a $0\nu\beta\beta$ decay events, however events that appear to have two blobs as in Figure 2.10 are difficult to reject.

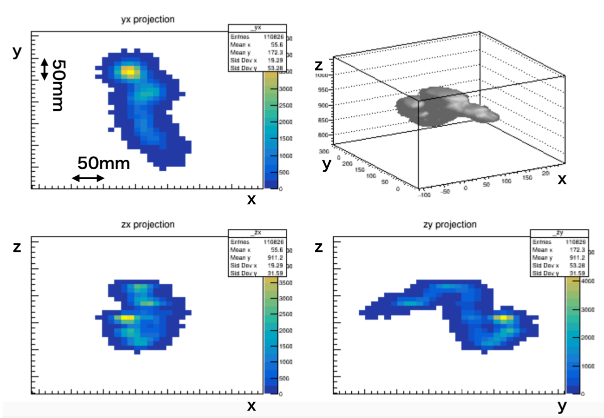

Figure 2.9: Reconstructed track pattern of a simulated gamma-ray photoelectric absorption event which seems to have only one blob.

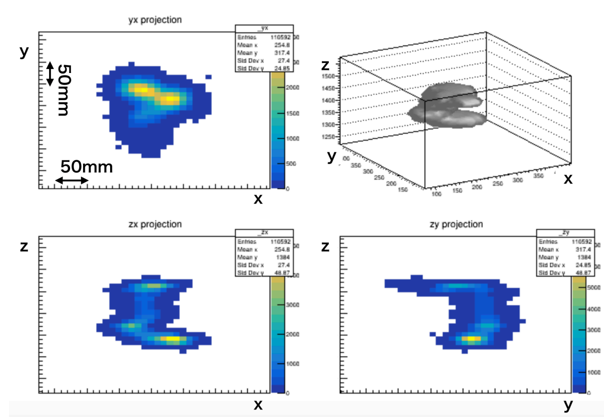

Figure 2.10: Reconstructed track pattern of a simulated gamma-ray photoelectric absorption event which has two blobs-like structure.

Event Discrimination by Deep Learning

In order to distinguish $0\nu\beta\beta$ decay events from photoelectric absorption of gamma-ray, an algorithm using three dimensional convolutional neural network (3D-CNN) [48], a kind of a deep learning, has been studied. The conditions at this study are summarized in Table 2.2. Only the pressure vessel made of oxygen-free copper which contains ^{214}Po is considered because that would be the dominant background source. The ^{214}Po undergoes beta-ray and becomes ^{214}Bi, which produces a 2448 keV gamma-ray. Figure 2.11 shows the output of the algorithm. The output is a scalar between 0: background-like and 1: signal-like and is called "signal likelihood". For signal and background, 6000 events are used for learning respectively, and another 960 events are used to evaluate the performance.

2.2.4 Expected Sensitivity

Before application of the deep learning (DL) selection, fully-contained event selection and energy ROI (region of interest) cut are applied to select the appropriate events. The energy ROI is set to be 2458 keV $\pm 0.5\%$. Because of PC memory limitations, only the events that fit in $36\times36\times36$ pixels (correspond 36 cm$\times$ 36 cm$\times$ 36 cm) are selected to apply the DL selection. With these selections, gamma-ray events are reduced to 0.05% while keeping the signal acceptance at 50%. After that, the DL selection is applied. By setting a threshold for signal likelihood to 0.9, gamma-ray events are reduced to approximately 1/100 while the signal reduction is 50%, therefore, by combining all the selections, gamma-ray events are reduced to 0.0004% with the signal acceptance of 27%.

Table 2.2: Condition of the simulation.

Gas	90% enriched ^{136}Xe
Gas pressure	10 bar
Sensitive volume	ϕ 3 m, 2.5 m-long
(Target mass)	1 ton
Cell pattern	Square, 10 mm-pitch
Pressure vessel	10 tons, Oxygen-free copper

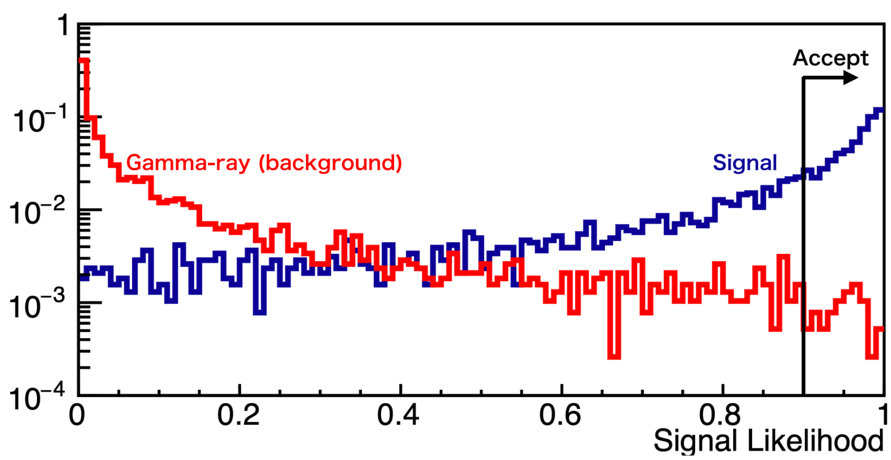

Figure 2.11: Output of the algorithm based on the 3D-CNN method. Output is a scalar between 0 (background-like) and 1 (signal-like).

With this background rejection method, the background rate of gamma-ray around the signal region (2458 keV) is expected to be 0.8 counts/year assuming 10 tons of the pressure vessel made of oxygen-free copper. The expected 90% confidence level sensitivity of the AXEL 1 ton is $T_{0\nu}^{1/2} = 1.0 \times 10^{27}$ years, which corresponds to $\langle m_{\nu_{ee}} \rangle$ =19.7–53.5 meV, with the background rate of 0.8 counts/year, the signal acceptance of 27% and six-year measurement.

2.3 Detection of Ionization Signal

2.3.1 Electroluminescence Process

With an electric field applied in gas, ionization electrons are accelerated and collide with molecules around them. Electrons excite molecules in collision and generate electroluminescence (EL) lights. The process occurs with lower electric field than that required for the ionization process. The EL process in normal pressure noble gas is described as [49],

$$\begin{aligned} e + A &\rightarrow e + A^* && (2.4)\\ A^* + 2A &\rightarrow A_2^* + A && (2.5)\\ A_2^* &\rightarrow 2A + \gamma, && (2.6) \end{aligned}$$

where A^* represents the excitation state of the noble gas atom A. The process of Equation (2.5) and hence the whole processes occur at gas densities higher than 10^{10} cm^{-3}. The spectrum of the photons emitted by this process is similar to that of scintillation light, which are shown in Figure 2.12 [49] . In the case of xenon, the peak wavelength is around 170 nm lying in the vacuum ultraviolet (VUV) region. Since the EL processes described in Equations (2.4)$-$(2.6) do not accompany avalanche multiplication process and a subject of less fluctuation, a detector which uses the EL process can potentially achieve good energy resolution. It is known that the reduced

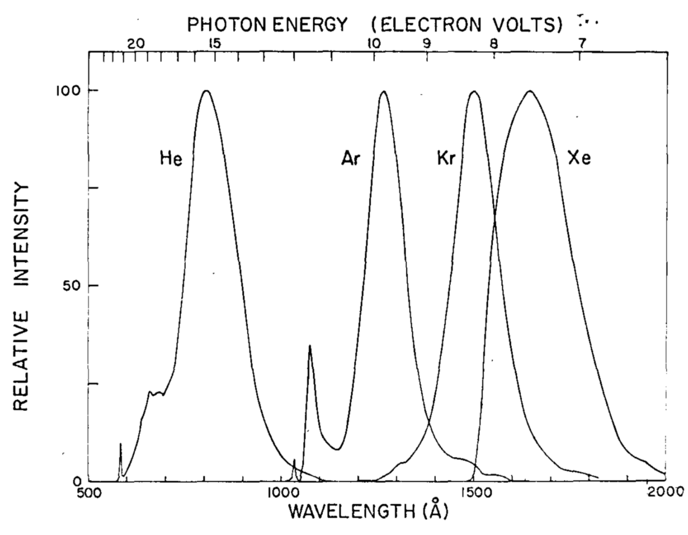

Figure 2.12: Spectra of scintillation photons (molecular continua) emitted from various noble gases normalized to the same intensity at the maximum [50]. Xenon emits lights at the wavelength around 170 nm.

light yield of EL process from a single electron, Y/p [photons/electron/cm/bar], is proportional to the reduced electric field strength, E/p [kV/cm/bar] over a threshold, and represented by the empirical equation:

$$Y/p = 140E/p - 116 \tag{2.7}$$

at room temperature, 20°C and 1.52 bar [51].

In the case of heavy noble gas such as xenon, atoms form dimers or clusters with increasing density and decreasing temperature. When the density is more than 10^{21} cm^{-3} (corresponding to 41.4 bar at 300 K), atoms begin to form dimers, A_2 and the following process starts to occur [49],

$$\begin{aligned} e + A &\rightarrow e + A^* && (2.8)\\ e + A_2 &\rightarrow e + A_2^* && (2.9)\\ A^* + A_2 &\rightarrow A_2^* + A && (2.10)\\ A_2^* &\rightarrow 2A + \gamma. && (2.11) \end{aligned}$$

This additional channel increases the yield of EL photons. On the other hand, presence of dimers A_2 causes a photon attenuation due to resonant absorption and makes the energy resolution of the detector worse.

If the energy of drifting electrons exceeds the ionization threshold, an avalanche multiplication process occurs:

$$e + A \rightarrow A^+ + e + e. \tag{2.12}$$

This multiplication process opens an additional recombination channel to increase EL light output [49]:

$$\begin{aligned} e + A &\rightarrow A^+ + e + e && (2.13)\\ A^+ + 2A &\rightarrow A_2^+ + A && (2.14)\\ A_2^+ + e &\rightarrow A_2^* && (2.15)\\ A_2^* &\rightarrow 2A + \gamma, && (2.16) \end{aligned}$$

but at the same time, the avalanche multiplication process introduces significant fluctuation and degrades the energy resolution of the detector.

2.3.2 Electroluminescence Light Collection Cell

As described above, the EL process well preserves the information of the number of ionization electrons, thus it is important to measure EL light precisely and uniformly for all electrons in order to achieve good energy resolution. If photo-detectors are, for example, placed just behind the EL region consisting of two plane meshes, the solid angle to the photo-detectors differs event by event and this makes the energy resolution of the detector worse (see Figure 2.13).

To solve this problem, we have developed a new configuration with a cellular structure, called "Electroluminescence Light Collection Cell (ELCC)". Figure 2.14 depicts the schematic of the ELCC. The EL region is made of a Cu-plate electrode, a PTFE structure with holes to make cells, and a mesh plane. Negative high voltage is applied to the Cu electrode, regarded as "anode electrode" to the drift field, and the mesh is connected to the ground electrically, thus a strong electric field is generated in each cell. The region above the Cu plate is the sensitive region and electric field to drift ionization electrons is applied. Since the electric field in the EL region (inside

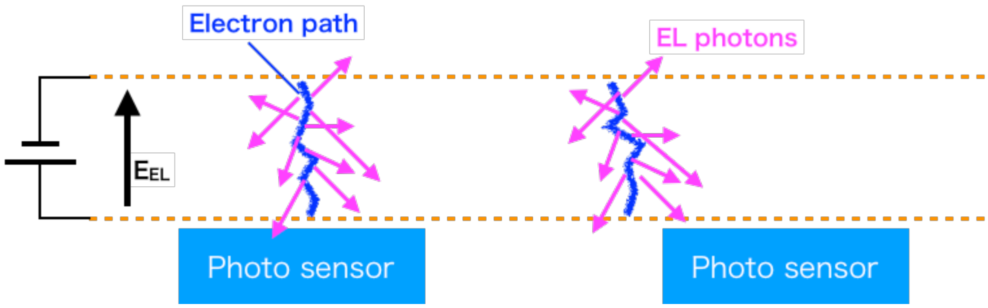

Figure 2.13: Schematic view of an EL detector with two meshes to generate EL electric field. The solid angle to photo-detectors differs if the position of an electron differs as described in this picture.

cells) is much stronger than that in the drift region, the lines of electric field are pulled into cells, thus drifted electrons are collected into cells along the lines and then produce EL photons, which are detected by SiPM photo-detectors placed behind the GND mesh. With this configuration, the acceptance of the photo-detectors to EL light is less affected by event position. The cell wall made of PTFE reflects VUV light, increases the light detected by the photo-detectors, and improves the uniformity of ionization electron measurement. Pitch and thickness of cells are adjustable and needed to be optimized. In particular, to exhibit satisfied performance, optimization of the electric field for given cell pitch and thickness is needed to guarantee 100% collection efficiency and uniform EL gain independently on event-position. Details are discussed in Sections 3.3.2 and 5.3.1 for the configuration of prototype detectors.

Pixelated image of the track of a charged particle is reconstructed in the xy plane, corresponding to the pixelated ELCC cells. Finer cell pitch enables to reconstruct a finer image of the original track, however, as will be mentioned in Section 2.3.4, ionization electrons diffuse during drift to have a spread of typically 10 mm. Therefore, a cell pitch much smaller than 10 mm less affects the performance of the track reconstruction.

Another advantage of ELCC is extendability to large areas in the xy plane thanks to the rigid structure of its components. In the case of two mesh planes, the meshes could be non-flat when extending the detector. To prevent the mesh to ripple, introducing supports is an effective method, however the area of supports will be dead regions for detection.

Cell Pattern

We have two options of the cell pattern, square pattern (Figure 2.15) and hexagonal pattern (Figure 2.16). Originally, a prototype has an ELCC plane with the square pattern. As will be explained in Section 3.3.1, we had changed the design of ELCC from the square pattern to the hexagonal pattern. Larger pitch can be adopted for the hexagonal pattern with same high voltage because the distances to all neighboring cells are the same.

Electric Field in Electroluminescence Region

Since the EL process is a threshold process, it is necessary to apply an electric field above the threshold, ~ 1 kV/cm/bar. As explained in Section 2.3.1, the energy resolution is degraded when it enters an avalanche amplification region. Generally, the threshold of the avalanche process is approximately 10 kV/cm/bar. Therefore, our detector should be operated in the range between

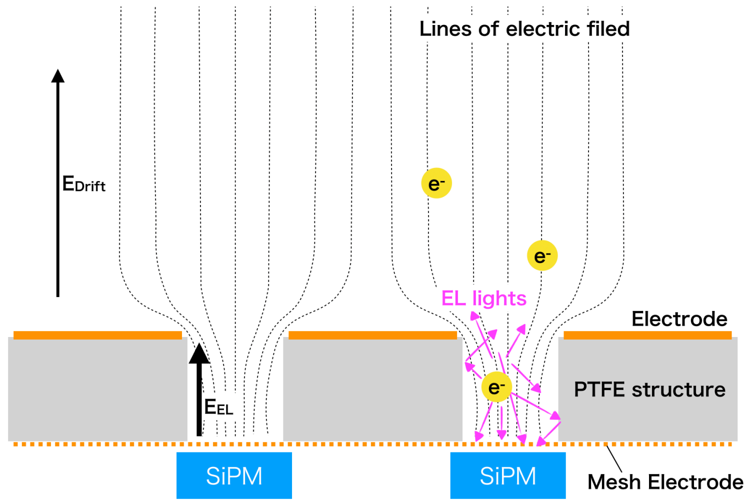

Figure 2.14: Schematic view of the ELCC. Ionization electrons are drifted along electric field lines, collected into cells and produce EL lights. The EL photons are detected by a photo detector, SiPM, placed behind each cell. The PTFE wall of the cell reflects photons.

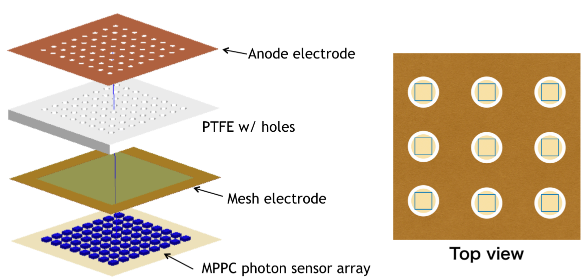

Figure 2.15: ELCC with square pattern.

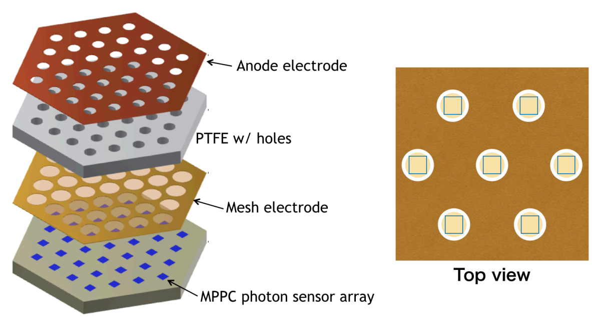

Figure 2.16: ELCC with hexagonal pattern.

EL threshold ($\sim$ 1 kV/cm/bar) and avalanche threshold ($\sim$ 10 kV/cm/bar). Within this range, the stronger the electric field, the higher the collection efficiency of electrons to the cell, and the EL light quantity increases. However, too strong electric field causes signal saturation of SiPMs due to too much light outputs and increases a risk of discharge. Optimum operating point of the EL electric field will be around 3 kV/cm/bar.

Simulation of the Electric Field and Paths of Electrons

A method has been developed to estimate the performance of the ELCC. The flow of the method is shown in Figure 2.17 and explained below:

- Geometry is modeled by Gmsh [52].
- Electric field is calculated with the finite element method by Elmer [53].
- Electron is tracked with the effect of diffusion. The values of the diffusion coefficients are shown in Figure 2.26b and Figure 2.26c. The initial position of an electron is random for xy plane and $z = 2$ cm to account for the effect of diffusion during the drift.

- EL photons are generated according to the strength of the electric field along the electron path and transported with the effect of reflection at the PTFE wall.
- The number of photons which reach the sensitive area of an SiPM, 3×3 mm^2 area, is counted and is converted into the number of detected photons with the aperture of the ground mesh of 0.5 and the photon detection efficiency (PDE) of a SiPM of 50% taken in to account.

The collection efficiency of the electric field line and drift electron are evaluated in this simulation. Uniformity of EL gain is also estimated by this simulation.

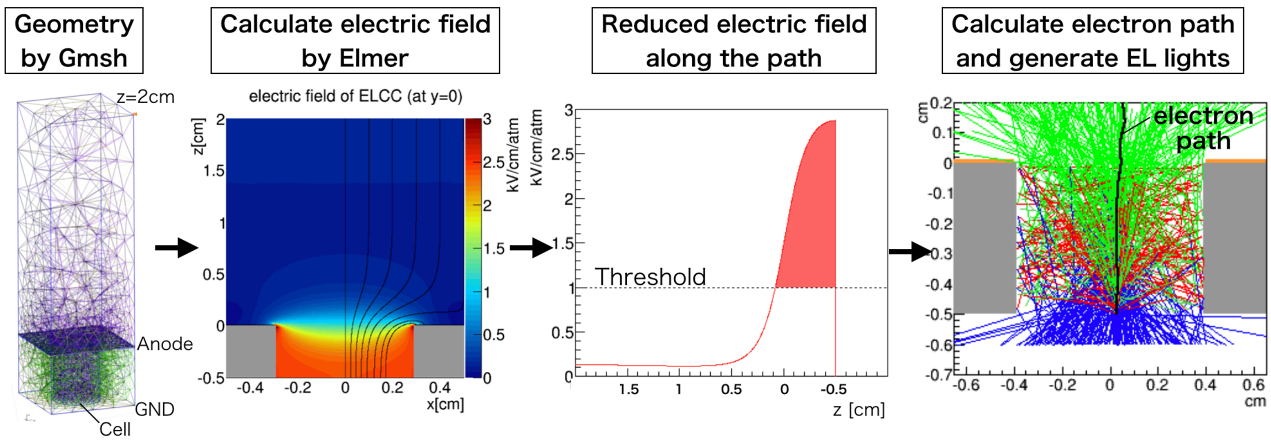

Figure 2.17: Schematic of the flow of simulation.

Figure 2.18 shows an example result of the electric field simulated by Elmer [53]. The condition of the simulation is $E_{\text{drift}} = 100$ V/cm/bar, $E_{\text{EL}} = 3$ kV/cm/bar, and with the ELCC with 7.5 mm-pitch square cell pattern and 5 mm-thickness. The diameter of a cell is 6 mm for this simulation. Figure 2.19 shows the trajectories of an electron simulated by Garfield++ [54]. One can see that electric lines and electrons are collected into the cells. As a result of the simulation, it is found that not all ionization electrons can be collected in the cell unless the electric field in the cell is sufficiently strong or the cell diameter is large enough. Specific simulations and performance evaluation for the configuration of the prototype detectors are described in Sections 3.3.1 and 5.3.1.

2.3.3 Silicon Photo Multiplier (SiPM)

SiPM has a great flexibility to equip to detector systems because it is compact (smaller than 1 cm^3) and can be operated with comparatively low voltages (below 60 V). It also can be used under an electromagnetic field. SiPM has high-sensitivity to a single photon. For the AXEL detector, Multi-Pixel Photon Counter (MPPC), a kind of SiPM, made by Hamamatsu Photonics K.K. is used as the photo detector of the ELCC. The performance of MPPC is important to achieve good energy resolution in the ELCC. In this section, we describe the basic properties of MPPC.

Principle of Photon Detection

An MPPC consists of multiple avalanche photo diodes (APDs) connected electrically in parallel (see Figure 2.20). A bias voltage is applied so that those APDs work in the Geiger mode. The

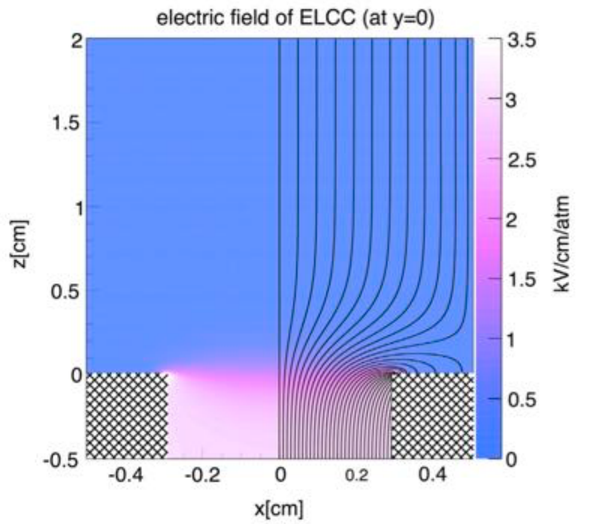

Figure 2.18: Electric field strength simulated by Elmer when voltage is applied at 100 V/cm/bar to the drift region and at 3 kV/cm/bar to the EL region. The configuration of the ELCC is 7.5 mm-pitch, 6 mm-diameter, and 5 mm-thickness.

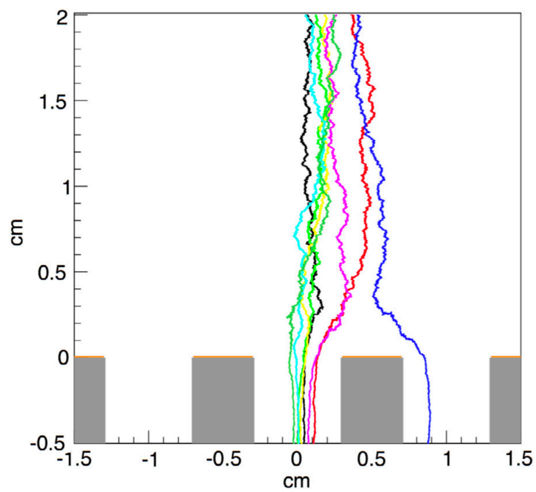

Figure 2.19: Examples of the trajectories of drifting electrons to the ELCC. Gray region corresponds to PTFE insulator. One can see the drifting electrons are pulled into the cells.

voltage at which Geiger mode starts is called breakdown voltage and the over voltage is defined as the bias voltage subtracted by the breakdown voltage. Schematic of MPPC is shown in Figure 2.21. The incident photon produces photoelectron (p.e.) at the absorption layer in an APD and the generated electron is drifted to the cathode by an electric field. Then, the electron causes avalanche amplification by the strong electric field. Increasing electric currents induce voltage drop at a register inserted in each pixel serially and then the avalanche process is quenched. The output charge from a single pixel is constant independently from the number of incident photons in the pixel due to the Geiger avalanche process. The observed charge is the sum of each pixel's output charge. When the number of photons is much less than the number of pixels of the MPPC, the output charge is proportional to the number of entering photons. However, when the number of incident photons is close to the number of pixels of the MPPC, the output signal saturates because the multiple photons having entered one pixel at the same timing is counted as one p.e..

Photon Detection Efficiency

The probability of actually detecting a single photon when it is incident on the MPPC surface is called Photon Detection Efficiency (PDE). Generally, the higher the over voltage, the higher the PDE of an MPPC. This is because the absorption layer at which a photon interacts in an APD becomes thicker and comes closer to the surface of the MPPC with higher over voltage then the efficiency to generate photoelectron increases.

PDE also depends on the wavelength of the incident photon. Conventional MPPCs are only sensitive to visible lights. However, in our experiments it is necessary to use MPPCs with a sufficient PDE for VUV lights, that is, the emission wavelength of xenon. An MPPC sensitive to VUV lights originally developed for the MEG experiment is used in our experiment. The catalog

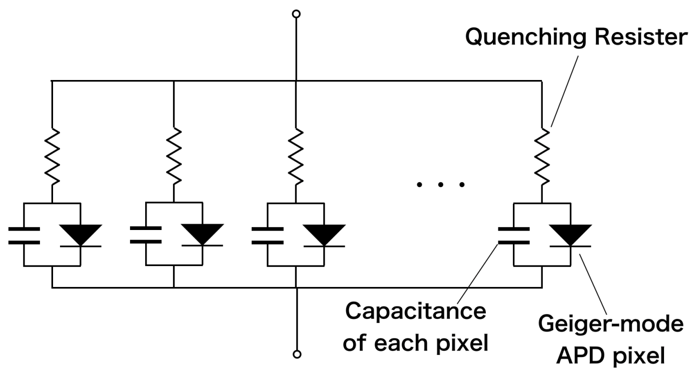

Figure 2.20: Equivalent circuit of an MPPC. Each pixel consists of an APD and a quench resister. An APD has a capacitance. The picture is from [55]

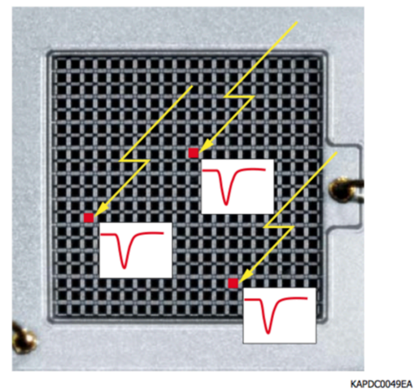

Figure 2.21: When photons enter multiple pixels, the output is the sum of outputs from pixels. The picture is from [55]

value of a VUV-sensitive MPPC with the type number of S13370 is shown in Figure 2.23 [56]. We uses the MPPC with the type number of S13370-4870 and S13370-3050CN.

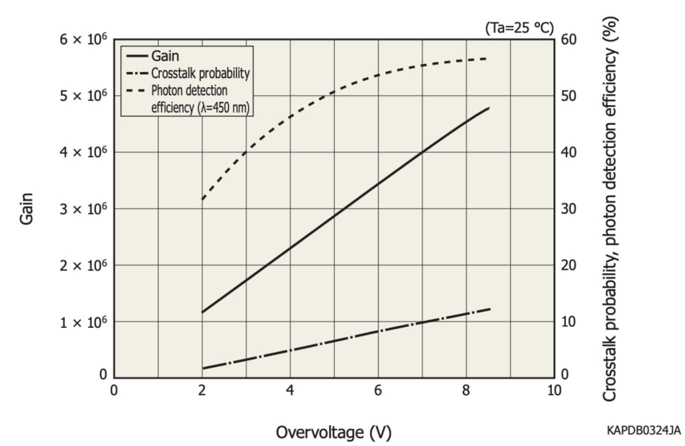

Figure 2.22: Over voltage specifications of gain, crosstalk probability and PDE (Typical value) [57]. All items increase as the over voltage increases.

Dark Current

An output that is not attributable to externally incident photons is called a “dark current”. Thermal excitation and tunneling of electrons in the crystal are considered as the main origin of dark current. In the case of dark current derived from thermal excitation, the dark current rate increases as the temperature rises, following the function:

$$r(T) = CT^{3/2} \exp\left(-\frac{E_g}{kT}\right), \tag{2.17}$$

where C is a constant, T is the temperature, E_g is the band gap energy of a semiconductor, k is the Boltzmann constant [58].

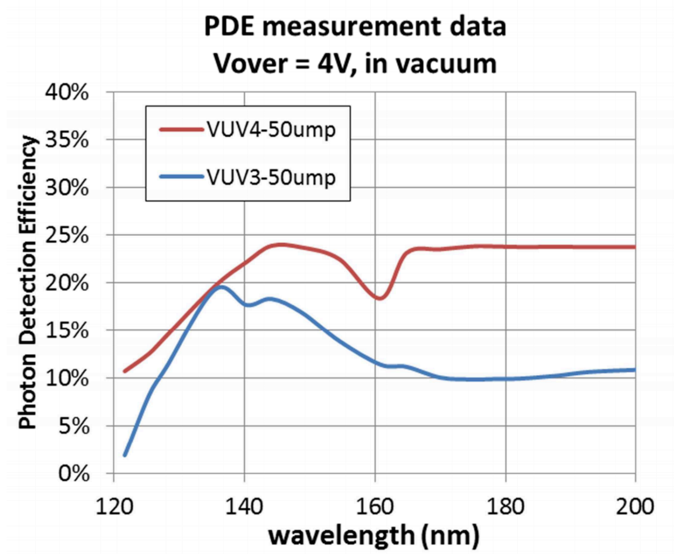

Figure 2.23: Waveform dependence of PDE for a VUV sensitive MPPC (S13370 series) [56].

On the other hand, in the case of the tunneling effect, the electrons in the valence band cause tunneling effect and transition to the conduction band by applying a reverse bias voltage to the diode[1], therefore the generation rate does not depend on the temperature. It becomes larger depending on the bias voltage applied to an MPPC and the area of the APD elements [58].

Crosstalk and After Pulse

During avalanche amplification in a pixel of the MPPC, secondary photons may be generated through the process of bremsstrahlung and recombination of electrons. When this secondary photon penetrates another pixel to generate an electron-hole pair, the Geiger amplification occurs also in that pixel. Such a phenomenon is called (optical) crosstalk. The probability of occurrence of crosstalk is known to increase depending on the over voltage, ΔV. In addition, if secondary photons generate new electron-hole pairs in the depletion layer in the same pixel, after a short time from the first Geiger discharge, the next Geiger discharge is observed. This is called after pulse. Typical crosstalk rate is $5 \sim 15\%$ [57].

Gain

The charge released as the signal when a photon is detected is given as

$$Q = C\Delta V, \tag{2.18}$$

where C is the capacitance of one pixel of MPPC and ΔV is an over voltage. Thus, the gain is calculated as

$$\mathrm{Gain} = \frac{\mathrm{C}}{\mathrm{e}}\Delta \mathrm{V}. \tag{2.19}$$

[1] By applying a reverse bias voltage to the diode, the valence band level becomes higher than the conduction band level. Therefore, such a transition can occur

Typical value of the capacitance is 10–100 fF and the over voltage is a few volts, resulting in the gain of 10^5-10^6. The gain also changes depending on the temperature because the break down voltage changes as temperature changes.

As explained above (Section 2.3.3 Crosstalk and After Pulse), even if a single photon is detected by an MPPC, the output charge sometimes becomes more than 1 p.e. equivalent due to crosstalk and after pulse. Hereafter, we call a gain containing the effects of crosstalk and after pulse "effective gain". On the other hand, the gain represented by Equation (2.19) is called "1 p.e. gain".

Determination of the effective gain using "threshold method" Dark currents of the MPPC can be used to measure the gain. Typical waveform of dark currents is shown in Figure 2.24. The difference from the baseline is integrated for each pulse whose height exceeds a

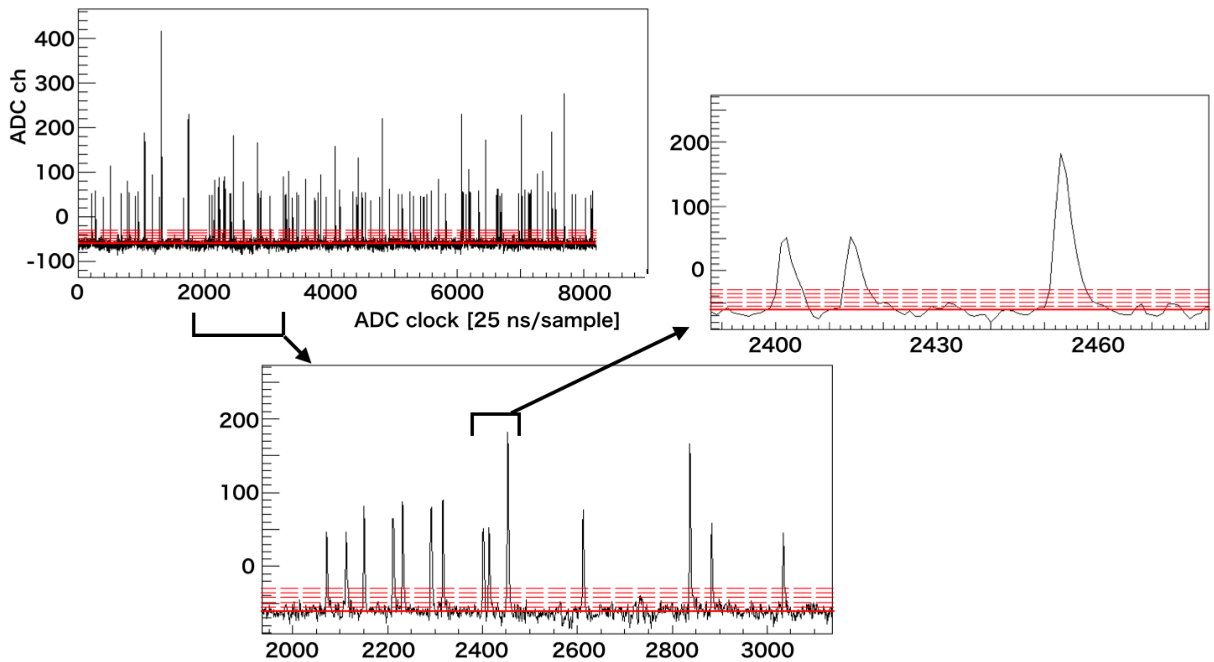

Figure 2.24: Typical waveform of dark current taken by a 12 bit, 40 MSps ADC. The waveform is amplified by 165 times by two preamplifiers. A solid line represents calculated baseline and dotted lines represent baseline fluctuation in one sigma, two sigmas ... from the bottom.

certain threshold. Figure 2.25 is a typical distribution of integral of dark currents with threshold of 3.5 sigma level from the baseline. Peaks of 2 p.e. and 3 p.e. are from the crosstalk, and a continuous component between each peak is due to the after pulse. The mean of charges above 0.5 p.e. is regarded as effective gain, which corresponds to the gain after the crosstalk and after pulse effects are taken into account. We define the procedure to find the gain in this way as the "threshold method".

Determination of the effective gain using "Random window method" In the threshold method, the dark current accompanied by after pulses may be regarded as two independent dark currents, and the effective gain may be underestimated.

To avoid this problem, a method called "random trigger method" which utilizes the nature of the Poisson statistics is used. A time window with a certain width is randomly set for acquired

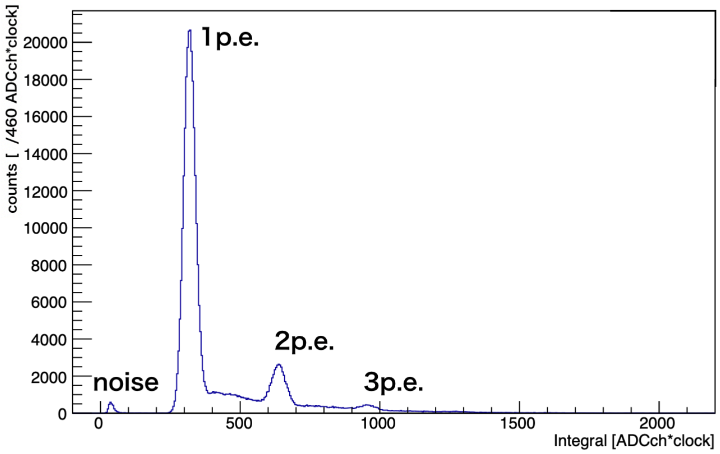

Figure 2.25: Typical distribution of dark current charge. The MPPC signal was amplified with preamplifiers by 165 times and read out by a 12 bit, 40 MS/s ADC.

waveform data including dark current, and the mean of the integration of the waveform after subtracting the baseline in the window is calculated. The number of events that do not exceed the threshold is counted and the zero probability of the Poisson distribution is obtained. By comparing the mean value obtained from dark current charges with the mean value calculated using the Poisson distribution, the effective gain is obtained.

Non-linearity and Recovery Time

Since the signal output of an MPPC is a release of the charge accumulated in the capacitance of each pixel, the hit pixel then begins the re-charging process. The time required for the re-charging is called "recovery time". Naively, the recovery time is determined by the capacitance of the pixel and the quenching resistance. When another photon enters during the re-charging, the signal becomes smaller than the normal signal output. Therefore, in case photons are incident at a rate higher than the recovery time, the output signal exhibits non-linearity. According to our previous research [59], it is shown that the nonlinearity of an MPPC signal is well expressed by the following equation.

$$N_{\mathrm{observe}} = \frac{N_{\mathrm{true}}}{1 + \tau/(N_{\mathrm{pixel}} \cdot \Delta t) N_{\mathrm{true}}}, \tag{2.20}$$

where N_{observe} is the reconstructed number of photons from the observed signal output, N_{true} is actual number of hit photons in Δt period, τ is the recovery time, and N_{pixel} is the number of pixels of the MPPC. With this expression, recovery time τ represents the time required to recover the gain once zeroed to $1/e$ times. If the recovery time τ of each MPPC is measured in advance, N_{true} can be reconstructed from N_{observed} using Equation (2.20). This is very important to achieve high energy resolution with our detector.

2.3.4 Drift Field

The strength of the drift field affects the velocity, diffusion, recombination, and attachment of ionized electrons. Drift velocity and diffusion constants are calculated with MAGBOLTZ [60] which has an extensive table of molecular collision cross section and shown in Figures 2.26a, 2.26b and 2.26c. Since a xenon atom is heavy, the recoil angle of an electron due to collisions is large, and thus, the diffusion coefficient is large. Electrons diffuse with a spread of typically ∼10 mm in the transverse plane and ∼2.5 mm longitudinally at 100 V/cm/bar for the drift distance of 100 cm.

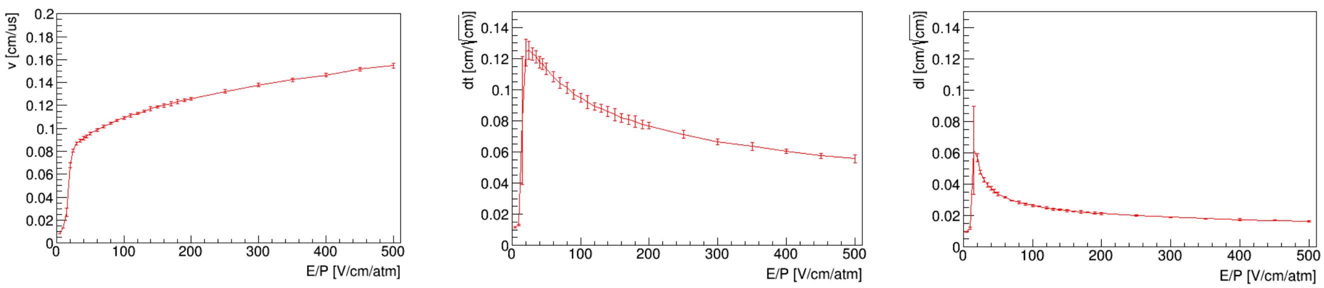

(a) Drift velocity. (b) Transverse diffusion const. (c) Longitudinal diffusion const.

Figure 2.26: Parameters representing behaviour during drift calculated by MAGBOLTZ [60].

Dependence of the recombination rate on the electric field is shown in Figure 2.27, which was measured by the NEXT experiment group [61] and Figure 2.28 by our group [62]. In these figures, the effect of the recombination is seen as an increase in the number of scintillation photons and a decrease of ionization signals.

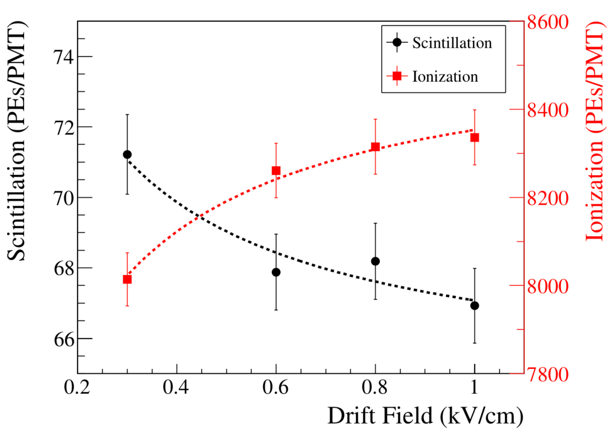

Figure 2.27: Average scintillation and ionization signals in 10 bar xenon for ^{222}Rn alpha candidate events, as a function of drift field.[61]

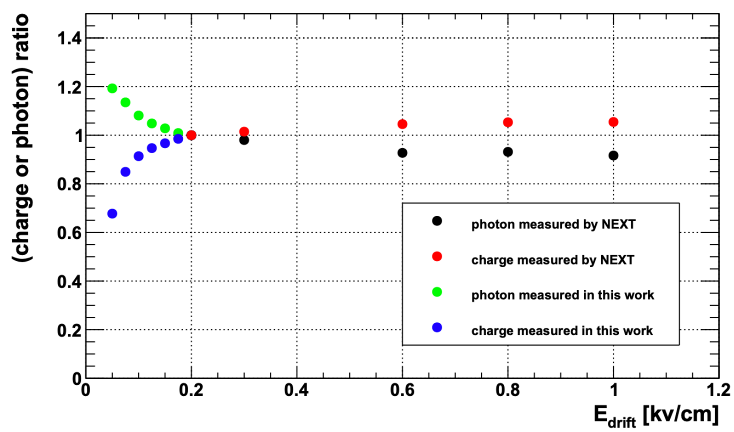

Figure 2.28: Average scintillation and ionization signals for ^{241}Am alpha candidate events as a function of drift field in low strength region. Measured values by the NEXT group are also shown in this plot.

At around 100 V/cm/bar, the changes in ionization signal and scintillation light are small, and the influence of recombination is regarded as small. Therefore, we choose around 100 V/cm/bar as an operating condition. These are measured with alpha-rays and the ionization electron density is higher than the case of beta-rays, thus, the effect of recombination should be much smaller for the case of double beta decay events.

2.4 Detection of Scintillation Signal

2.4.1 Scintillation Process

The excitation and de-excitation processes which produce scintillation in xenon gas are the same processes in Equations (2.4)–(2.6) for gas densities between 10^{10} cm^{-3} and 10^{21} cm^{-3}. Our measurement conditions are in this range. The dimer Xe_2^* has two kinds of decay life, 4.6 ns and 99 ns [63]. In addition, slow scintillation lights over tens microseconds are generated due to recombination process [64]. The W-value, which is defined as the average energy required for production of single scintillation photon, is 22.1 eV [49].

2.4.2 Photomultiplier Tube (PMT)

We use Photomultiplier Tubes (PMT) to detect primary scintillation lights as the time-zero signal of the TPC. Requirements to PMT in our project are as follows:

- To have a sensitivity to the emission wavelength from xenon gas, ∼170 nm.
- To have pressure tolerance up to 10 bar.
- Radiopure.
- Low outgas.

As a photo-detector to satisfy these requirements, we have chosen PMT, R8520-406MPDASSY produced by Hamamatsu Photonics. The window of photo-cathode is made of quartz so that VUV light can penetrate. Figure 2.29 shows a picture of PMT, R8520-406MPDASSY. The basic

Figure 2.29: R8520-406MPDASSY produced by Hamamatsu photonics K.K. which is sensitive to VUV-lights and can stand up to 10 bar.

properties of the PMT is shown in table 2.3.

PMTs are equipped at the opposite side of the ELCC. Configuration of PMTs for two prototypes is described in Section 3.5 and Section 5.5 respectively.

Table 2.3: Basic properties of R8520-406MPDASSY

Model ID	R8520-406MPDASSY
Sensitive Area	$20.5 \times 20.5\text{mm}^2$
High voltage	-800 V
Gain	10^6
QE	30%

2.5 Gas for TPC

2.5.1 Gas Pressure

Choice of the gas pressure is one of very important component to achieve the goal of the AXEL detector. Higher pressure increases the amount of the $\beta\beta$-decay source in a sensitive region. However, higher gas pressure does not always improve the sensitivity because, as shown in Figure 2.30, the intrinsic energy resolution becomes worse above a pressure of 0.6 g/cm^3 (approximately 100 bar). This is considered to be due to the formation of clusters of xenon atoms [49]. Furthermore, resolution of the reconstructed track of β-rays gets worse because track length becomes shorter. This makes it difficult to reject backgrounds using track pattern and, hence, makes the sensitivity worse.

With the reasons above, we have chosen the gas pressure of 6 bar (0.036 g/cm^3) or 8 bar (0.048 g/cm^3).

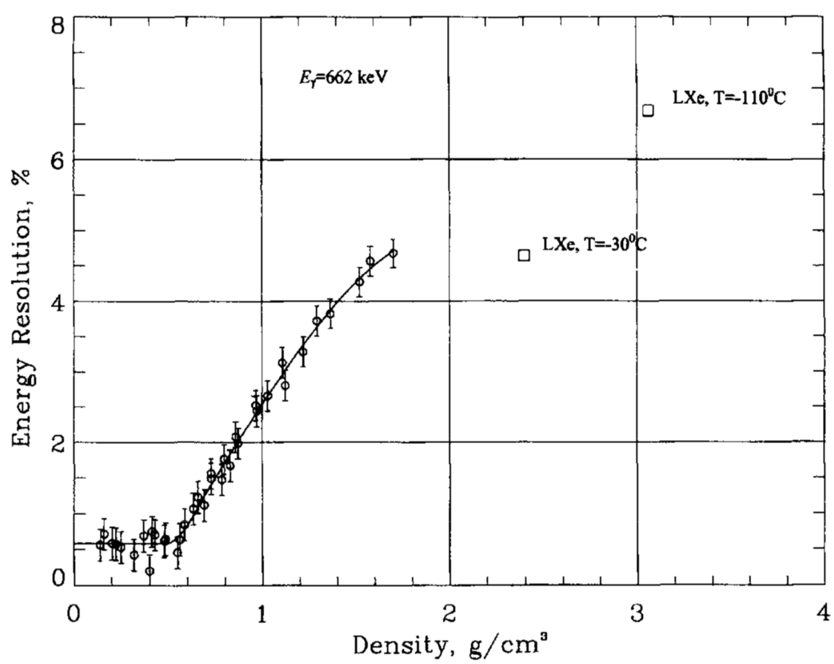

Figure 2.30: Density dependence of the intrinsic energy resolution of xenon (% FWHM) measured for 662 keV gamma-rays[65]. Energy resolution dramatically degrades above 0.6 g/cm^3.

2.5.2 Gas System

Our gas system mainly consists of xenon storage, pumps and filters to purify xenon gases. The actual gas system diagram differs depending on the stage of the prototype and is explained in Sections 3.7 and 5.7. We use swagelok® joints for gas introduction lines, VCR joints for gas circulation and purification lines, and NW joints for vacuum part for connection of gas pipes. The schematic of our gas system is shown in Figure 2.31.

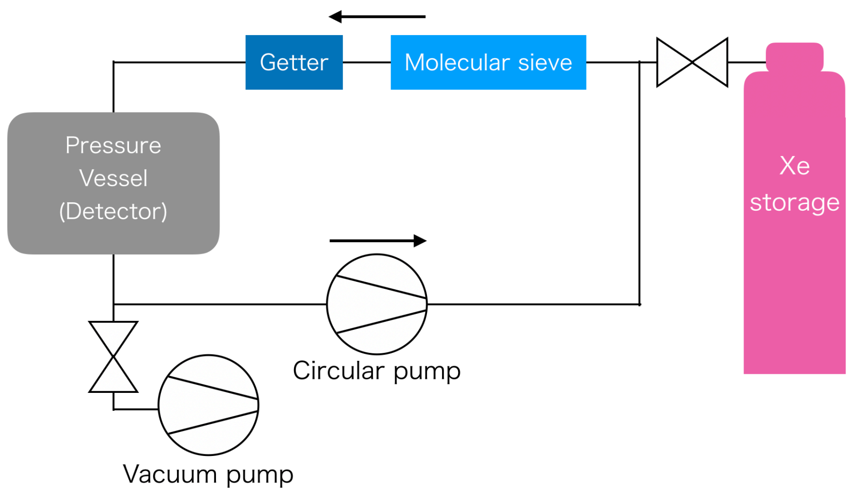

Figure 2.31: Schematics of a gas system of the AXEL experiment.

Molecular sieve

A molecular sieve filter can remove various impurities such as O_2, H_2O, CO, CO_2, acids, bases, and organics. However, Nitrogen cannot be removed by a molecular sieve, therefore, a getter is used to remove nitrogen. We use SAES micro torr MC1-902FV as a molecular sieve.

Getter

A getter is used to remove mainly Nitrogen from xenon gases. The getter is located behind the molecular sieve in order not to introduce Oxygen into the getter. We use API-GETTER-I -RE (produced by API inc.) which can operate at 10 bar.

Chapter 3

Design and Construction of a 10 L Size Prototype

3.1 Overview and Purpose

To demonstrate the ELCC concept, we have developed a small size ($\sim$ 10 cm scale) prototype detector. This prototype detector is housed in a 10 L volume vessel which can contain high pressure gas up to 10 bar, thus, we call this prototype "HP10L" (high pressure 10 L) or "10 L prototype detector". Due to the detector size limitations, the performance of this prototype detector is evaluated using relatively low energy gamma rays (up to 400 keV). Since the purpose of this detector is to demonstrate the performance in particular the energy resolution, we do not care about radioactive impurities yet, thus the components of the HP10L are not radio pure. The experimental site is the third floor of the Kyoto University Science Building 5, which is not underground low background facility. To maximize the performance of the detector, we have to care about outgases which decrease EL gain or absorb drift electrons. Therefore, low outgas materials such as Poly Ether Ether Ketone (PEEK), poly Tetra Fluoro Ethylene (PTFE), and metals are mainly used to construct the HP10L. This chapter describes the development of each component of the 10 L prototype detector and the obtained performance is described in the next chapter.

3.1.1 Versions of the 10 L Prototype Detector

The detector has been developed and improved in stages. The summary of the detector at each stage is listed below.

Version 1

As a first phase of HP10L, we developed the detector with 32 ch ELCC with square pattern and a field shaper of 9 cm in inner-diameter and 6 cm in length. MPPCs in this version were not sensitive to VUV light, thus a plate coated with wave-length shifter (WLS) is placed in front of the MPPC array. Detail and performance of this version are described in Appendix A.

Version 2

The number of ELCC channel is 64. MPPCs which is not sensitive to VUV lights are used also in this version, thus a plate coated with WLS is placed in front of the MPPC array again. In addition, MPPCs whose surface is directly coated with WLS are also used in this version. PMTs to detect scintillation lights are installed since this version. Detail and performance of this version are also described in Appendix A.

Version 3

MPPCs are replaced to VUV-sensitive ones. Field shaper is enlarged to 9 cm in inner-diameter, 9 cm in length. The gas system is upgraded to enable purification during data acquisition in the middle of the commissioning of this version. We evaluated the performance at 4 bar using a ^{57}Co gamma-ray source (mainly 122 keV) and at 8 bar using a ^{133}Ba gamma ray source (mainly 81, 302, and 356 keV). The results are described in Section 4.2 and Section 4.3, respectively.

Version 4

As described in Section 2.3.2, the cell arrangement of the ELCC was changed from square to hexagonal to improve the uniformity of the EL gain. In addition, in order to increase the volume of the sensitive region, pitch of cells is increased from 7.5 mm to 13 mm. The structure of the ELCC is changed from one-piece style to prefabricated style. The field shaper was changed to the one with a strip electrode embedded in a PTFE structure, from the copper ring electrodes used in previous versions. The size of the field shaper is 15 cm in inner-diameter and 10 cm in length. The results obtained with this version is explained in Section 4.4.

Versions of HP10L are summarized in Table 3.1

Table 3.1: Summary of versions of the 10 L prototype detector.

Ver	#ch	MPPC type	Cell pattern	Field shaper	Others
1	32	non VUV-sensitive	square, 7.5 mm-pitch	ϕ9 cm, 6 cm-long	No PMTs
2	64	non VUV-sensitive	square, 7.5 mm-pitch	ϕ9 cm, 6 cm-long	
3	64	VUV-sensitive	square, 7.5 mm-pitch	ϕ9 cm, 9 cm-long	
4	64	VUV-sensitive	hexagonal, 13 mm-pitch	ϕ15 cm, 10 cm-long	

3.2 Pressure Vessel

The pressure vessel for housing the 10 L prototype detector is made of stainless steel, SUS304. Figure 3.1 shows a picture of the pressure vessel. It consists of a cylindrical part made of a JIS 200A-sch10 pipe and two JIS 10K200A flanges attached to the both ends of the cylindrical part. The inner (outer) diameter of the cylindrical part is 208.3 mm (216.3 mm), that is, the wall thickness is 4 mm. The length is 340 mm. Both ends of the vessel are closed by blank JIS 10K200A flanges. One of them has feedthroughs described in Section 3.2.1. Two half-inch nipples with VCR joints are welded to the cylindrical body for gas introduction, disposal and circulation. This pressure vessel is designed to tolerate high pressure up to 10 bar. To maintain air tightness, an O-ring made of Viton is sandwiched between flanges for vacuum. The vessel is supported by a frame made of stainless steel. The lid, blank flange with the feedthrough, can be smoothly opened and closed thanks to the rail on the frame. The pressure vessel and frame are commonly used in all versions of the 10 L prototype.

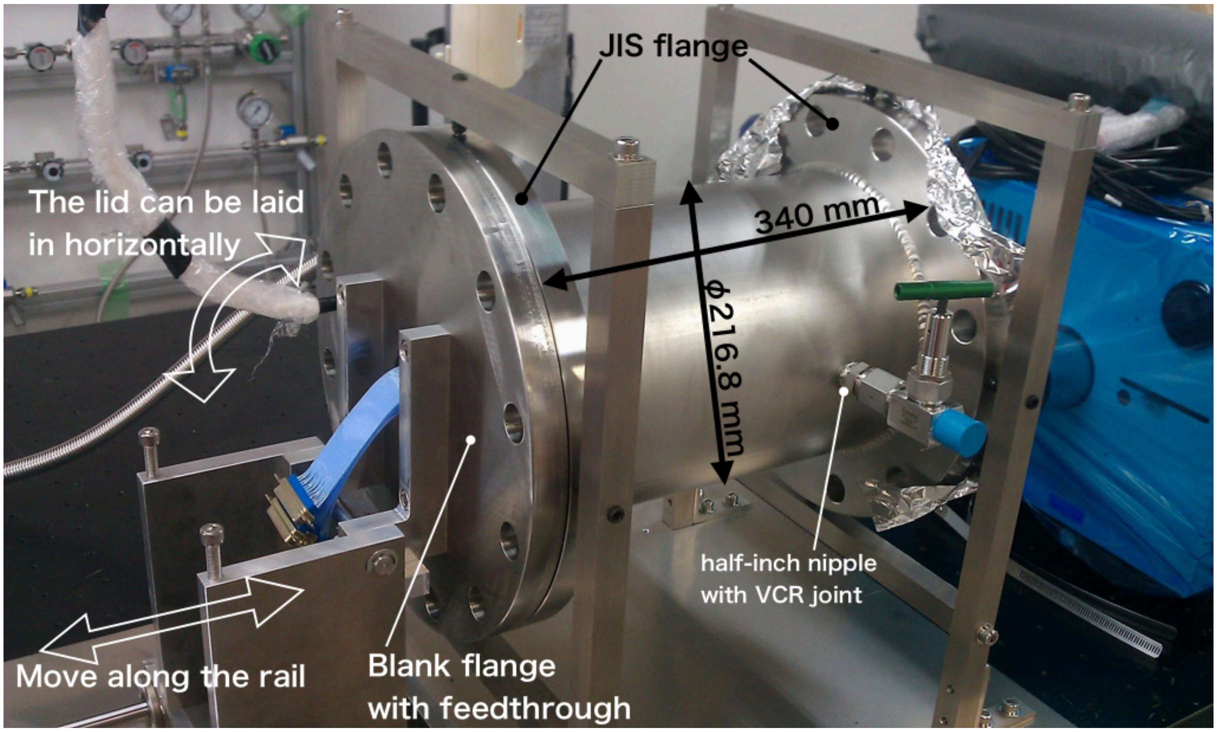

Figure 3.1: Pressure vessel for HP10L. The feedthrough flange on this picture is version 1.

3.2.1 Feedthrough

The application of high voltages into the pressure vessel and the readout of the signals are performed through hermetic feedthroughs. Apart from the HP10L versions, there are also three versions of the feedthrough. All versions of the feedthrough are processed on a JIS 10K200A flange as already mentioned.

Feedthrough version 1

This version is for the Version 1 of HP10L. It has ribbon cables for 32-channel signal readout and no coaxial cables for PMTs. Detail is described in Appendix A.

Feedthrough version 2

This version is designed for the Version 2 and a part of Version 3 of the HP10L, which have 64 channels and two PMTs. The picture of the feedthrough version 2 is shown in Figure 3.2 . Nine Teflon® sealed 25-bundles-ribbon-cables (RF28#25) and five silicon-sleeved cables (SIL12#15F) which can withstand up to 30 kVDC are passed through two separate feedthroughs. Both cables are high vacuum compatible and expected to have low outgassing. Eight ribbon cables are used for bias voltage application to MPPCs and as signal readout lines of MPPCs. The remaining one ribbon cable is used as a signal readout line of PMTs. Two of the five Silicon sleeved cables are used to apply high voltage to PMTs. The remaining three are used to apply an electric potential to the cathode electrode, the anode electrode, and the ground mesh of the ELCC, respectively. As shown in Figure 3.2, because five cables are densely packed in a narrow area, the distance between the core of the Silicon sleeved cables and the blank flange is very short. This causes a serious discharge at the feedthrough as explained in the next section.

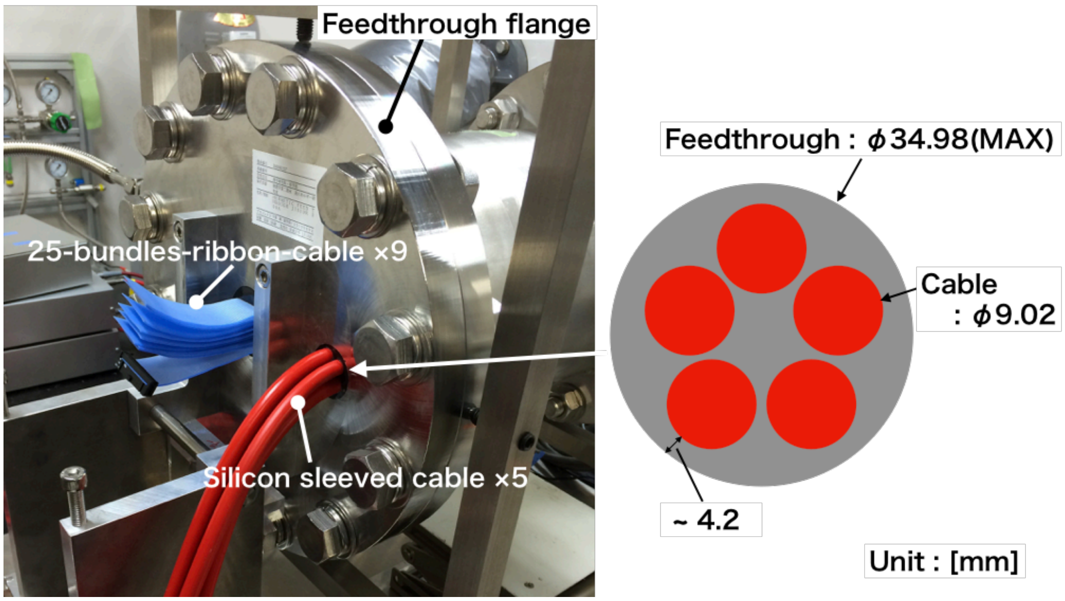

Figure 3.2: Picture of the feedthrough version 2 of HP10L and schematics view of the feedthrough of Silicon sleeved cables.

Discharge at a feedthrough version 2

Discharge occurred in the feedthrough part of the silicon-sleeved cables during operation of the HP10L Version 3. The discharge occurred when the cathode electrode was applied to be $\sim$11 kV at 5.6 bar. After that, the breakdown voltage of discharge gradually decreased, and finally, 9.5 kV could not be applied. This discharge is monitored by sounds of sparks and count rate by PMTs. It should be noted that the discharge at feedthrough did not occur immediately after the start of use of the feedthrough version2, but occurred about 21 months after the start of use, and that the discharge occurred at many other places during that time. This indicates that the cause of this discharge is not necessarily a design problem. Figure 3.3 shows the picture of a discharge at the feedthrough of silicon-sleeved cable which was taken in the air and with the blank flange of opposite side of the feedthrough flange removed. Figure 3.4 shows a possible discharge path; creeping discharge may occur between the core wire of the cable and the blank flange. As mentioned above, although it is not necessarily a problem of design, it is conceivable that the closeness of the distance between the core of cables and the flange may lower the discharge resistance. Based on this observation, the next version of the feedthrough was designed.

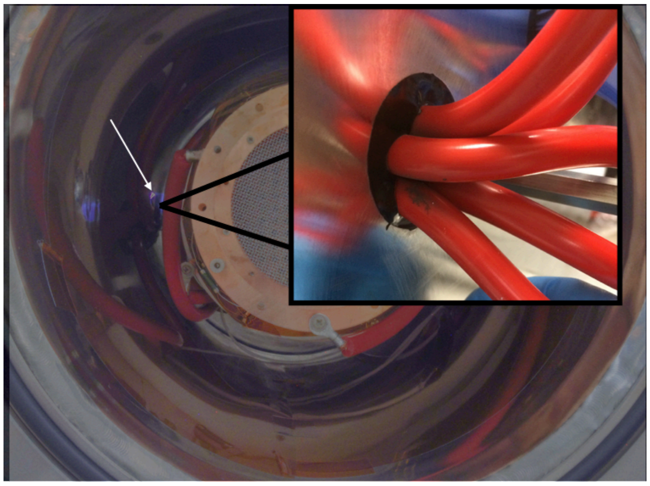

Figure 3.3: Picture of surface discharge at the feedthrough. You can see a lightning at the edge of the feedthrough (indicated by the white arrow).

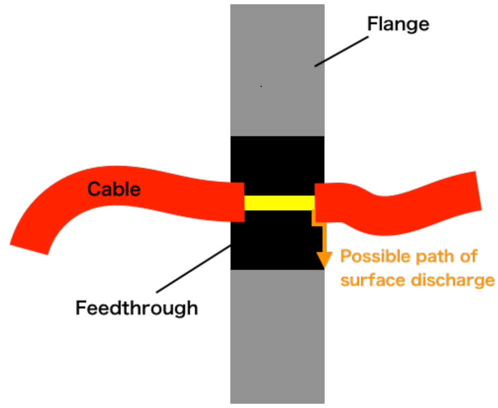

Figure 3.4: Schematics cross section view of a feedthrough flange for high voltage line. Possible path of a surface discharge is also illustrated.

Feedthrough version 3

This version is used in a part of the Version 3 and Version 4 of the HP10L. Reflecting on the failure of the discharge in the previous version, we improved the withstand voltage at the feedthrough through silicon-sleeved cables. The number of silicon-sleeved cables passing through the feedthrough is reduced from five to three, thus the distance between the core of cables and the flange increases. Furthermore the feedthrough resin is thickened more than the flange to extend the path of surface discharge and improve the discharge resistance. These three silicon-sleeved cables are used to apply high voltages to the cathode electrode, anode electrode, and ground mesh of the ELCC, respectively. Two more feedthroughs are added in this feedthrough version. One feedthrough has six Kapton® -coated coaxial cables which are highly vacuum compatible (CX26#I), and the other feedthrough has one coaxial cable with the same Kapton® -coated coaxial cable. Also nine Teflon® sealed 25-bundles-ribbon-cables are passed through the feedthrough at the center of the flange. The high voltage application and signal readout of PMTs are done through Kapton® sleeved coaxial cables in this feedthrough version. Thanks to the coaxial cables, it becomes possible to transmit fast signals of PMTs with less noise. Crosstalk between PMT signals and MPPC signals can be suppressed by separating feedthroughs. Figure 3.5 shows the schematic drawing of the feedthrough version 3.

3.3 ELCC

3.3.1 Configuration of the ELCC

Two cell-patterns of the ELCC were designed for the HP10L.

Square Cell-Pattern with 7.5 mm Pitch

Originally, square cell-pattern with 7.5 mm-pitch was adopted and installed to the HP10L Versions 1 to 3. The thickness of the cell is 5 mm. Figure 3.6 shows the configuration of cell-pattern of the

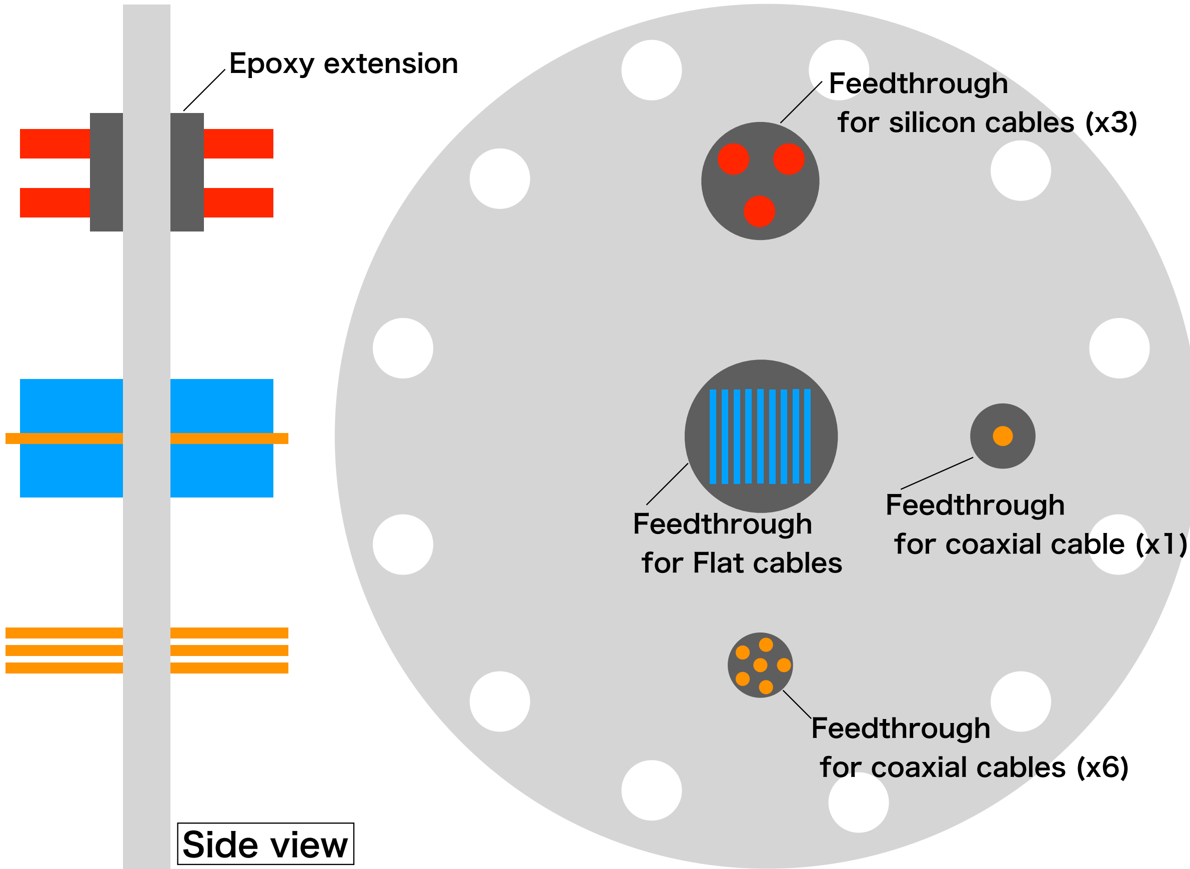

Figure 3.5: Schematic drawing of the feedthrough version 3.

square version. The cells are arranged in 8×8 with a pitch of 7.5 mm, thus the detection area is 36 cm^2. Since the outermost cells are used as veto channels, the fiducial area is 20.25 cm^2. The diameter of holes in the anode electrode is 4 mm. The diameter of the PTFE holes is 3.8 mm, slightly smaller than that of the anode electrode. This is to prevent creeping discharge by forming a detour in the path between the ground mesh and the triple point (the anode electrode, PTFE, and the gas), which is a weak point for discharge (see Figure 3.7). The diameter of the anode electrode determines the electric field structure. The diameter of PTFE holes affects the light yield via reflection on the wall. Therefore both diameters are important parameters for the performance of the ELCC.

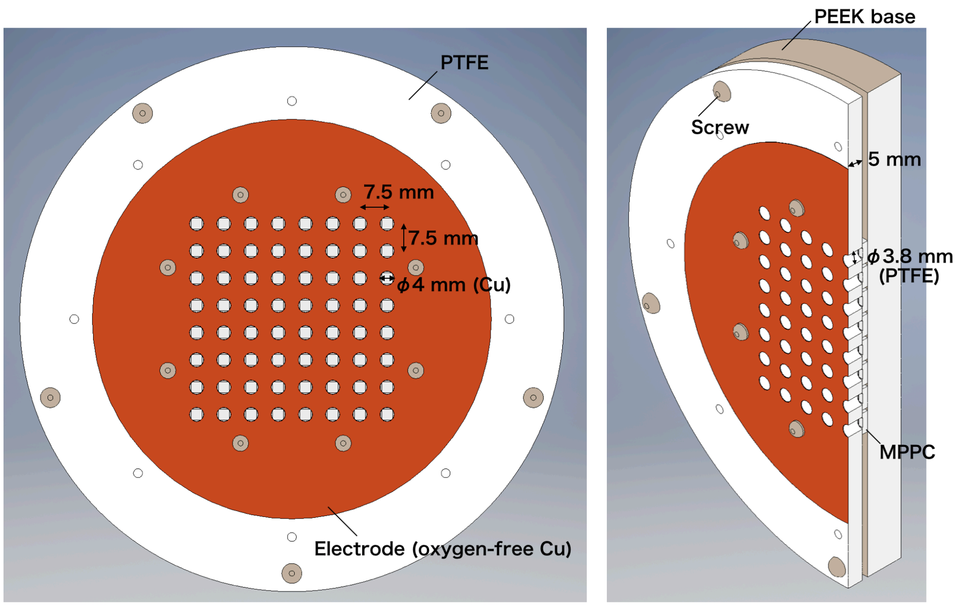

Figure 3.6: Schematic view of the ELCC of a square cell-pattern with 7.5 mm-pitch. Top view (left) and cross sectional view (right).

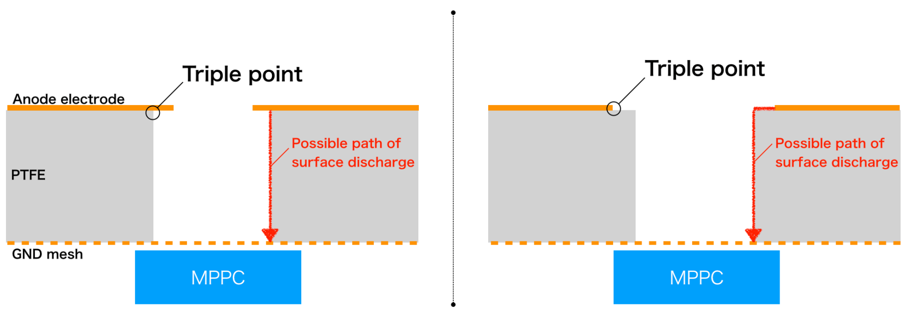

Figure 3.7: Relation of diameters of an anode electrode and a PTFE holes. Left : In the case that the diameter of the PTFE cell hole is larger than the anode electrode, a triple point which consists of anode electrode (Oxygen-free copper), PTFE cell, and xenon gases directly faces the ground mesh. Right : In the case that the diameter of the PTFE cell holes is smaller than that of the anode electrode, the path between the triple point and the ground mesh has a detour and a vertical corner.

Hexagonal Cell-Pattern with 13 mm Pitch

In order to increase the detection area with the same number of channels, an ELCC with 13 mm-pitch hexagonal cells was designed and installed in the HP10L Version 4. Figure 3.8 shows the schematic view of the hexagonal version. The MPPCs were not installed in the top and bottom line cells because of the limitation of the number of readout channels of the FADC as will be explain in Section 3.8.1. Thus, the number of channels is still 64. The sensitive area is calculated to be 93.67 cm^2, and since the outermost cells are used as veto channels the fiducial area is 57.08 cm^2, approximately twice as that of the square pattern with 7.5 mm-pitch. The diameter of a cell hole of the anode electrode is 7 mm and that of the PTFE cell is 6 mm. As mentioned later, after being designed, it was found by a simulation that this cell arrangement does not exhibit sufficient performance.

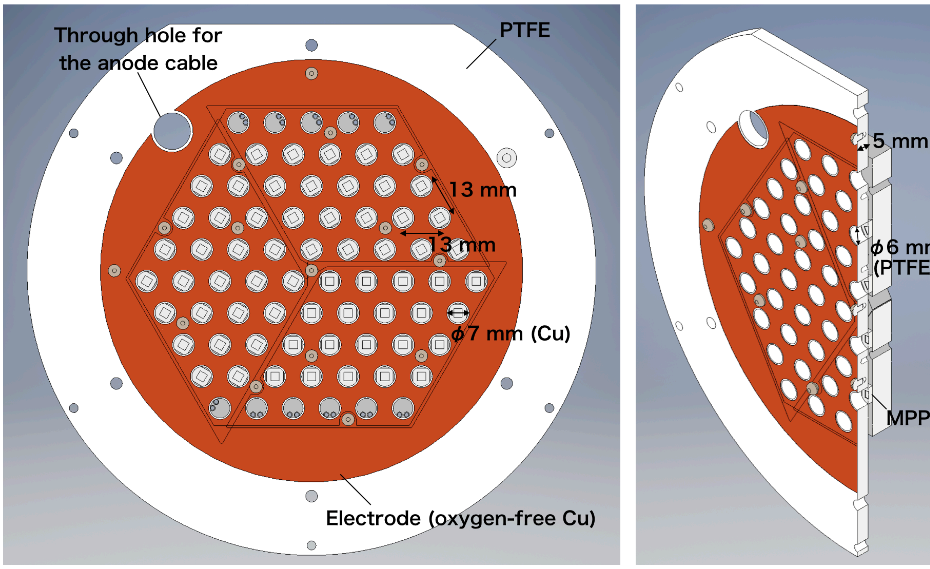

Figure 3.8: Schematics of the ELCC of a hexagonal cell pattern with 13 mm-pitch. Top view (left) and cross sectional view (right).

3.3.2 Simulation of an Electric Field

Simulations are performed to estimate the performance of the ELCC according to the method described in Section 2.3.2.

Square Cell Pattern with 7.5 mm Pitch

The simulation of the ELCC with square, 7.5 mm-pitch cell pattern is done for two different conditions. One is the condition of E_{drift} = 100 V/cm/bar, E_{EL} = 2.7 kV/cm/bar and, 4 bar xenon gas, corresponds to the measurement described in Section 4.2 and the others is E_{drift} = 83 V/cm/bar, E_{EL} = 2.375 kV/cm/bar and, 8 bar xenon gas, for the measurement in Section 4.3. These values are less than the target values, that is, $E_{\mathrm{EL}} = 3$ kV/cm/bar, $E_{\mathrm{drift}} = 100$ V/cm/bar. This is due to discharges at the cathode electrode as will be mentioned in Section 3.4.1. The geometry in this simulation is shown in Figure 3.9. A boundary condition is imposed that this unit geometry is repeated in mirror image.

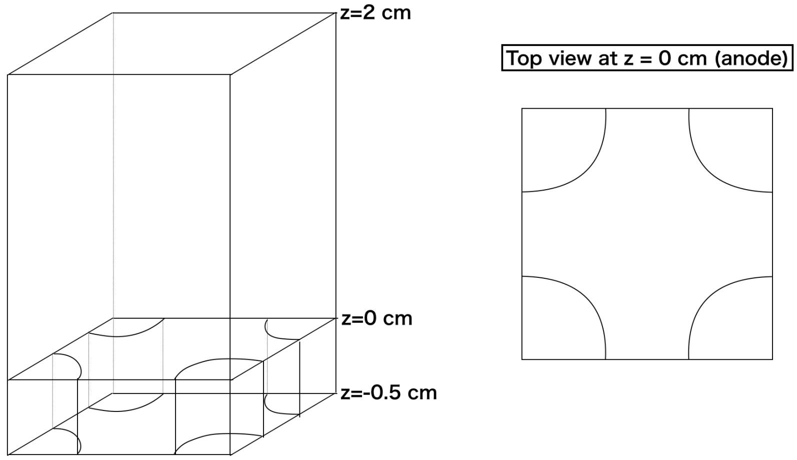

Figure 3.9: Geometry of the square cell pattern with 7.5 mm-pitch, thickness of 5 mm inputted in the simulation.

Simulation for 4 bar xenon Figure 3.10a and Figure 3.10b show the calculated electric field strength and electric potential of the ELCC for 2.7 kV/cm/bar for the EL region, 100 V/cm/bar for the drift region. As can be seen in the figure, the electric field strength in the cell is not completely uniform and the drift field is leaking into the cell.

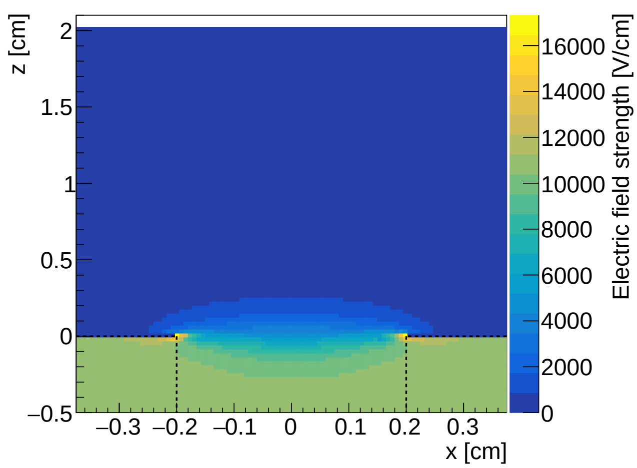

(a) Electric field strength

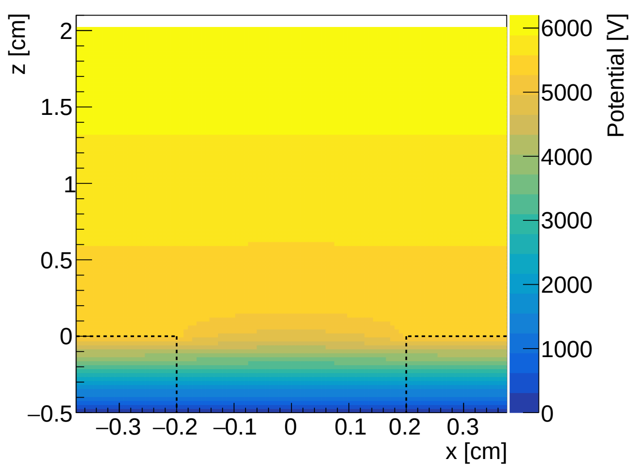

(b) Electric potential

Figure 3.10: Calculated electric field strength and electric potential at 2.7 kV/cm/bar for the EL region and 100 V/cm/bar for the drift region

Figure 3.11a shows the map of the calculated EL gain for each initial electron position and Figure 3.11b shows its projection to the one dimensional histogram. The non-uniformity of the EL gain reflecting the shape of the cell can be seen. The gain at the center of the cell tends to be small. This may be because the integrated field strength along the path is larger at the peripheral of the cell. Although this non-uniformity is likely to deteriorate the energy resolution, in fact, the ionizing electrons generated in a single event range over multiple cells, thus in the energy distribution consisting of multiple events the effect of this non-uniformity becomes mitigated. The effect of this non-uniformity on the energy resolution is discussed and comparisons with data from the prototype detectors are given in Section 4.2.

In this simulation, 651 out of 10,000 electrons hit the electrode and are not drawn into the cell. That is, the collection efficiency of electrons to the cell is 93.49%. This may make the performance of the ELCC worse.

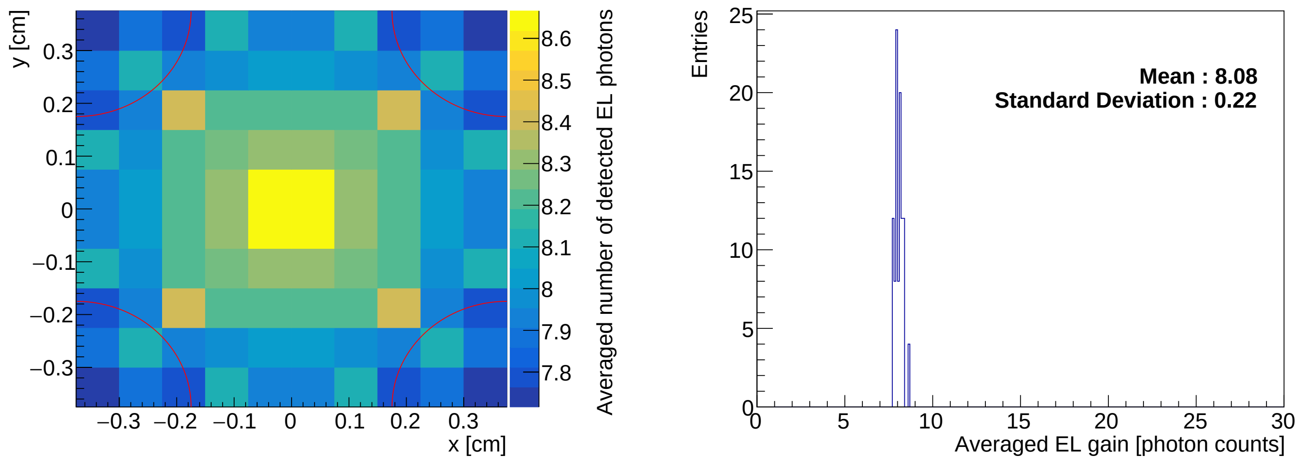

(a) EL gain map for each initial electron position

(b) Distribution of EL gain

Figure 3.11: Calculated electron's initial position dependence of EL gain and its distribution

Simulation for 8 bar xenon Figure 3.12a and Figure 3.12b show the calculated electric field strength and electric potential of the ELCC for 8 bar xenon. The input conditions of the electric field are $E_{\text{drift}} = 83$ V/cm/bar, $E_{\text{EL}} = 2.375$ kV/cm/bar, as mentioned above.

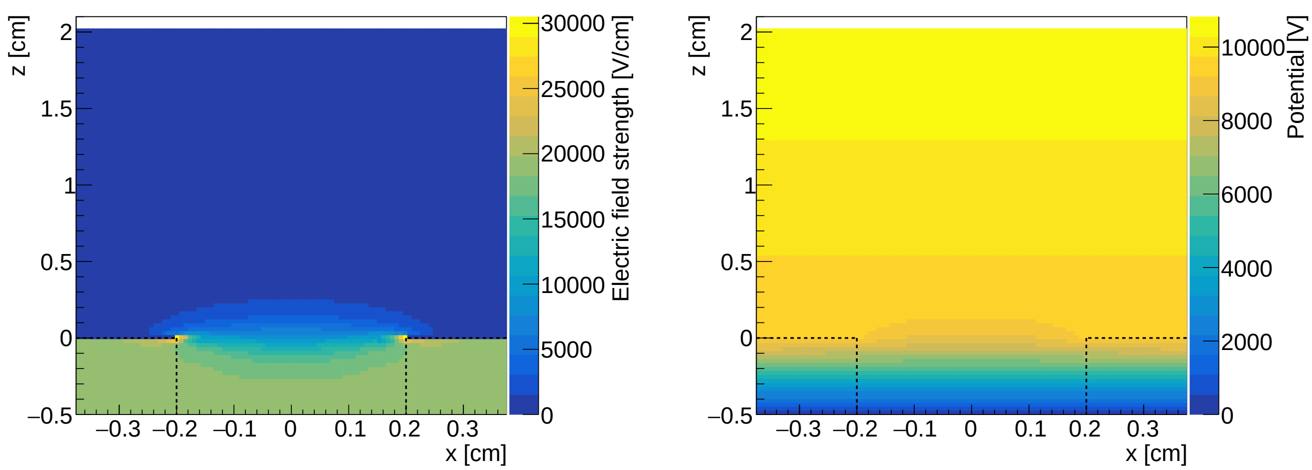

(a) Electric field strength

(b) Electric potential

Figure 3.12: Calculated electric field strength and electric potential at 2.375 kV/cm/bar for the EL region and 83 V/cm/bar for the drift region

Figure 3.13a shows the map of the calculated EL gain for each initial electron position and Figure 3.13b shows its projection to the one dimension histogram. The non-uniformity of the EL gain is seen even more clearly in this condition. In this simulation, 331 out of 10,000 electrons cannot go through the anode cell and vanish in the electrode.

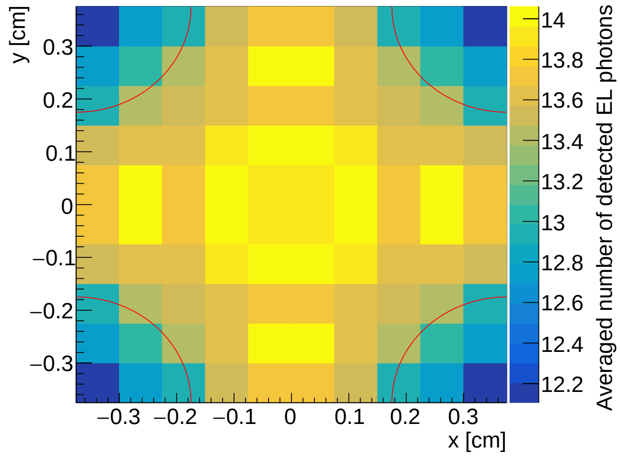

(a) EL gain map for each initial electron position

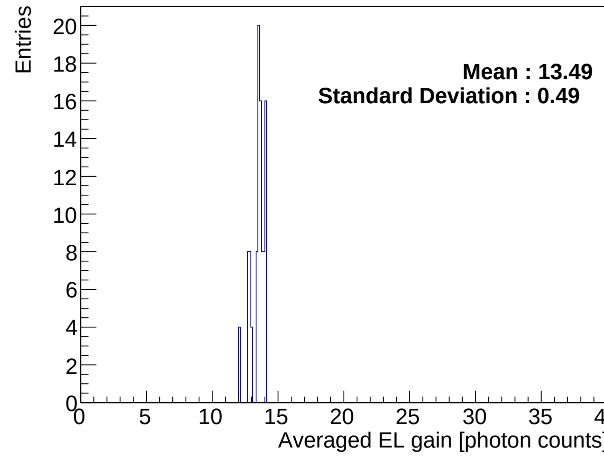

(b) Distribution of EL gain

Figure 3.13: Calculated electron's initial position dependence of EL gain and its distribution

Hexagonal Cell Pattern with 13 mm Pitch

Figure 3.14 shows the geometry for the simulation of the ELCC with hexagonal, 13 mm-pitch cell-pattern. The simulation is done with the condition of $E_{\mathrm{drift}} = 72$ V/cm/bar and $E_{\mathrm{EL}} = 3$ kV/cm/bar and 6 bar xenon, which corresponds to measurement with the 10 L prototype detector Version 4. The drift field could not reach to 100 V/cm/bar due to discharge limitation, resulting in measurement at 72 V/cm/bar. Figure 3.15a and Figure 3.15b show the calculated electric field strength and electric potential of the ELCC.

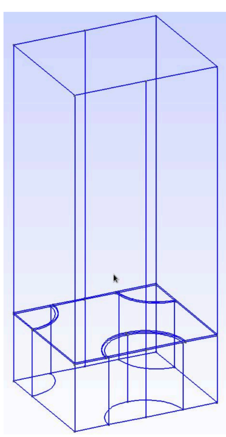

Figure 3.14: Geometry of the hexagonal cell pattern with 13 mm-pitch, thickness of 5 mm inputted in the simulation.

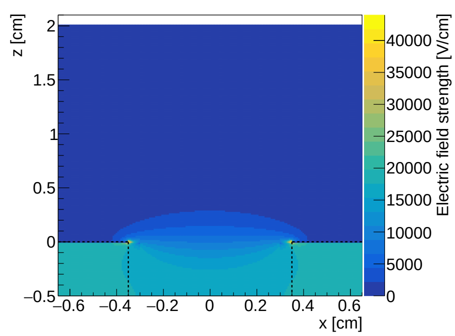

(a) Electric field strength

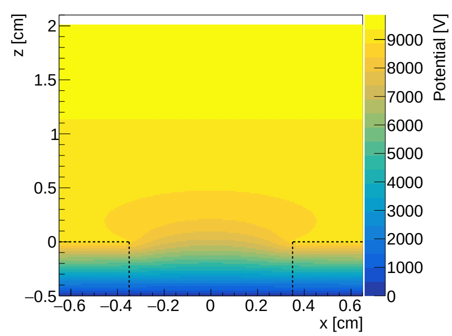

(b) Electric potential

Figure 3.15: Calculated electric field strength and electric potential at 3.0 kV/cm/bar for the EL region and 72 V/cm/bar for the drift region

Figure 3.16a shows the map of the calculated EL gain for each initial electron position and

Figure 3.16b shows its projection to the 1-D histogram. The non-uniformity of the EL gain reflecting the shape of the cell again is seen in this condition. In this simulation, all the 10,000 electrons are pulled into the cell.

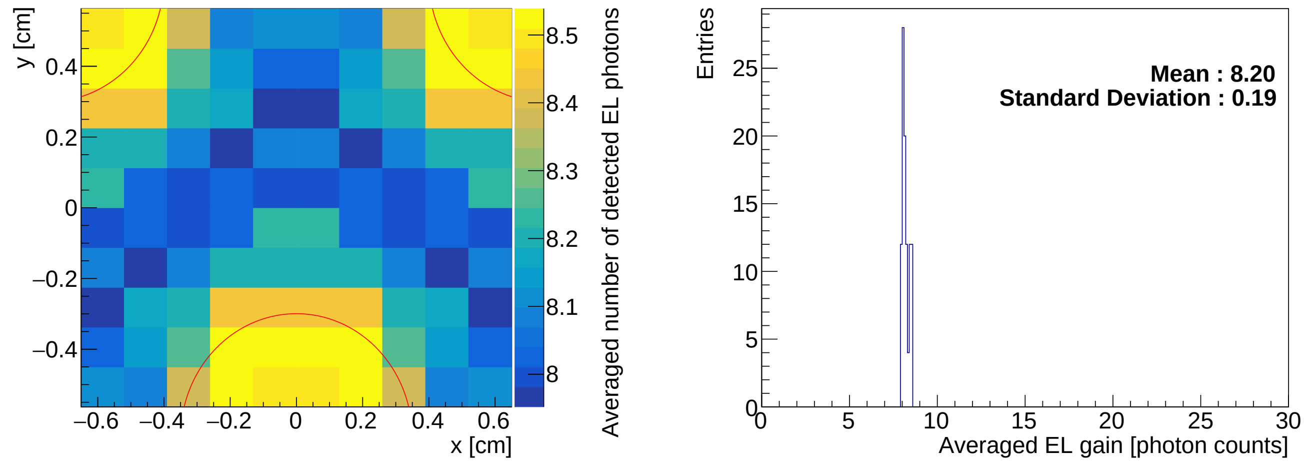

(a) EL gain map for each initial electron position

(b) Distribution of EL gain

Figure 3.16: Calculated electron's initial position dependence of EL gain and its distribution

3.3.3 SiPMs

S17740-4830 (VUV3) for the HP10L Version 3

MPPCs with type number S17740-4830 are used for the HP10L Version 3. This type belongs to the series called "VUV3", since it is the third generation of the MPPC, which has low dark current, low crosstalk, and low after pulse type. The pixel pitch of this MPPC is 50 μm, and the sensitive area is 3 mm square, that is, it is composed of $60 \times 60 = 3{,}600$ pixels of APDs. Unlike normal (non-VUV sensitive) MPPCs, the sensitive surface is not coated with epoxy resin to avoid VUV light absorption, thus, very thin lead wires on the surface of an MPPC are exposed. Therefore, very careful treatment is needed.

The PDE of VUV-3 measured by Hamamatsu photonics K.K. with $\Delta V = 4$ V is already shown in Figure 2.23 and the value at wavelength of 170 nm is about 10%.

S17740-3050CN (VUV4) for the HP10L Version 4

MPPCs are replaced from S13370-4870 (VUV3) to model number : S13370-3050CN, which is called "VUV4", for the HP10L Version 4. In this model, PDE is improved by restraining a reflection of VUV lights at the MPPC surface, thinning down the insensitive area near the surface, and increasing the aperture ratio. The PDE of VUV-4 measured by Hamamatsu photonics K.K. with $\Delta V = 4$ V is shown in Figure 2.23. The PDE at wavelength of 170 nm is 23%, improved compared to that of VUV-3.

3.3.4 Construction of the ELCC of the 10 L Prototype Detector

ELCC with Square Pattern

The ELCC with 7.5 mm-pitch square pattern has a small number of channels (only 64 channels) and a small sensitive area, therefore the base part to which the MPPCs are attached and the cell part are made as a single unit for simplicity. Socket-pins (PD-10 provided by MAC8 inc.) for fixing MPPC legs are inserted into the base, and the base is fixed to the feedthrough flange by pillars (Figure 3.17-①). Then, MPPCs are attached on the base (Figure 3.17-②).

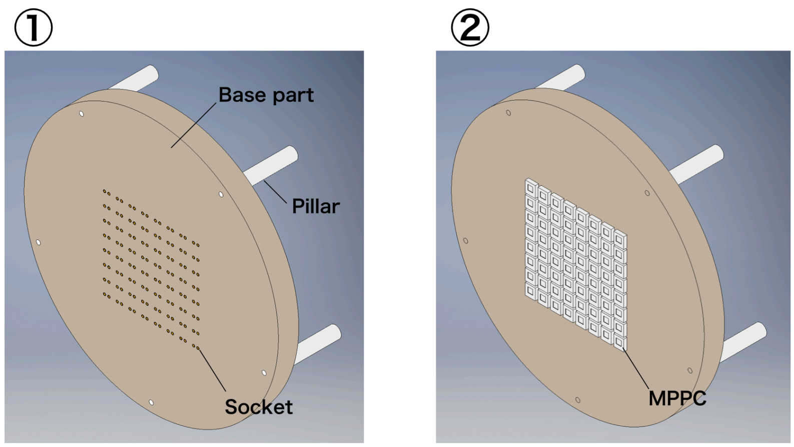

Figure 3.17: Installation of the base and MPPCs. ① : the base is fixed to the feedthrough flange by pillars. Socket-pins to fix MPPCs are inserted to the base. ② : MPPCs are installed to the base.

The ground mesh is attached to the PTFE cell body and fixed by the ring at the edge (Figure 3.18 -③, ④). Gold-plated tungsten mesh with 100 mesh/inch dealt by NILACO inc. is used as the ground mesh. The wire diameter of the mesh is 0.03 mm, thus the aperture is 78%. This fineness of the mesh prevents the EL electric field from leaking to an MPPC surface, and prevents the effect on the operation of the MPPCs. The anode electrode, an oxygen-free 0.5 mm-thick copper is processed by etching to make holes. This is attached to the opposite side of the PTFE body (Figure 3.18 -⑤, ⑥).

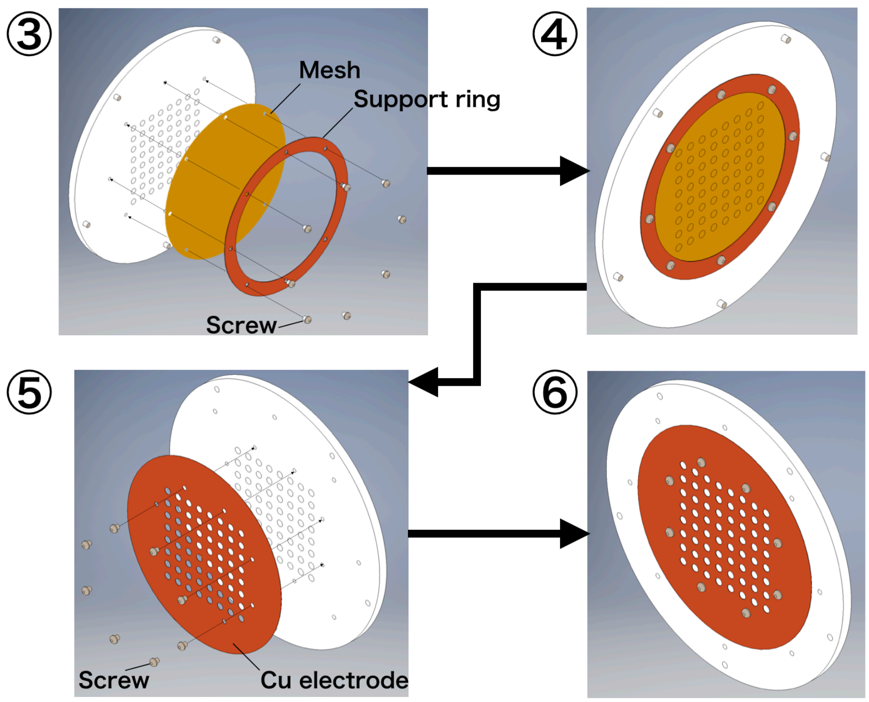

Figure 3.18: Ground mesh is attached to the PTFE cell body (③, ④) . Anode electrode is attached to the opposite side of the PTFE body by screws (⑤, ⑥).

The cell body and the MPPC base are assembled by screws and form the ELCC (Figure 3.19 - ⑦, ⑧).

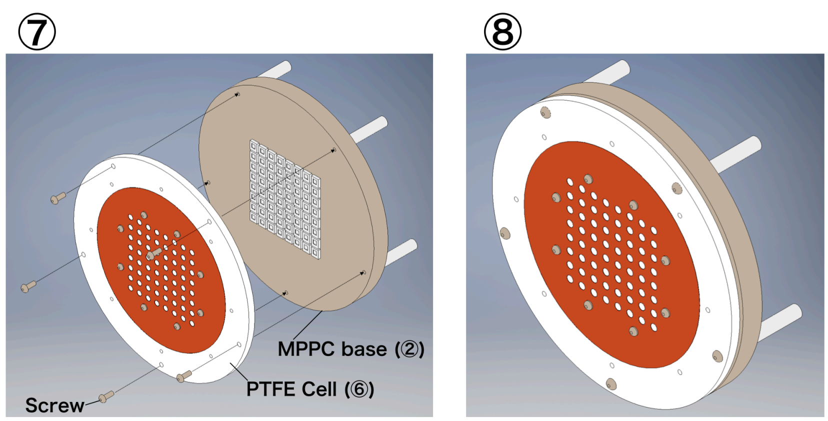

Figure 3.19: PEFE cell body and MPPC base are assembled to form the ELCC.

A small copper thin plate is attached to each of the ground mesh and the anode electrode. The plate extends to the outside of the outer periphery of the ELCC, and is connected to the high voltage cable there using a crimp terminal.

A socket (RS-3-1-P provided by MAC8 inc.) is attached to each tip of the ribbon cables (RF28#25) for voltage application and signal readout of the MPPCs as mentioned in Section 3.2.1. Then they are connected to MPPCs through the socket-pins by inserting these from the back side of the base (Figure 3.20).

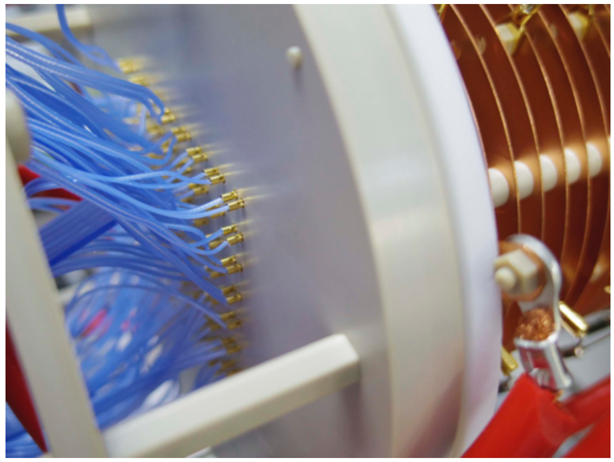

Figure 3.20: Connection of the ribbon cables to the MPPCs. Sockets (RS-3-1-P provided by MAC8 inc.) are crimped at the tip of ribbon cables and inserted into the socket-pins (PD-10) in the base.

ELCC with Hexagonal Pattern

For the 13 mm-pitch ELCC, the modular style is adopted to prepare for future extension. In this version, MPPC base and anode plate are designed in module and a PTFE cell body is made as a single unit.

The MPPC base is made of PEEK and has a parallelogram shape, with a total of 25 MPPCs in five rows and five columns in one unit. Again, socket-pins (PD-10) are inserted into the base, then, MPPCs are attached on the base (Figure 3.21). As shown in this figure, the neighboring MPPC bases are rotated by 120°.

The ground meshes are cut into the same parallelogram shape as the MPPC base and attached to the PTFE cell body with oxygen-free copper frames (Figure 3.22 -②, ③). Gold-plated tungsten meshes with 100 mesh/inch, 0.03 mm of the wire diameter, and 78% of aperture are again used as the ground meshes.

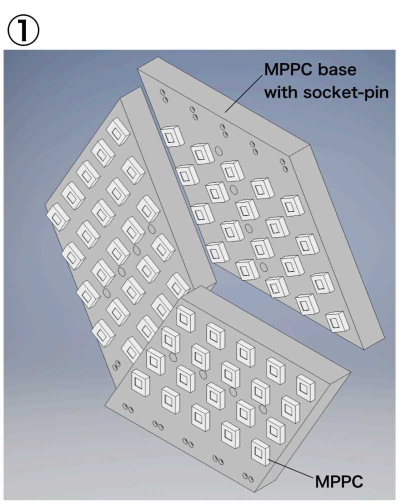

Figure 3.21: MPPC base.

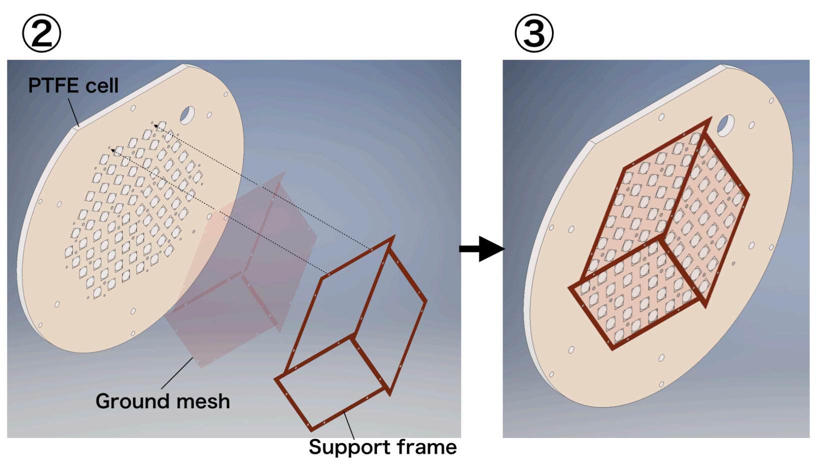

Figure 3.22: MPPC base.

On the anode side, the outer peripheral electrode is attached first (Figure 3.23-④), and then parallelogram electrodes that match the shape of the MPPC base unit are screwed to attach (Figure 3.23-⑤-⑦).

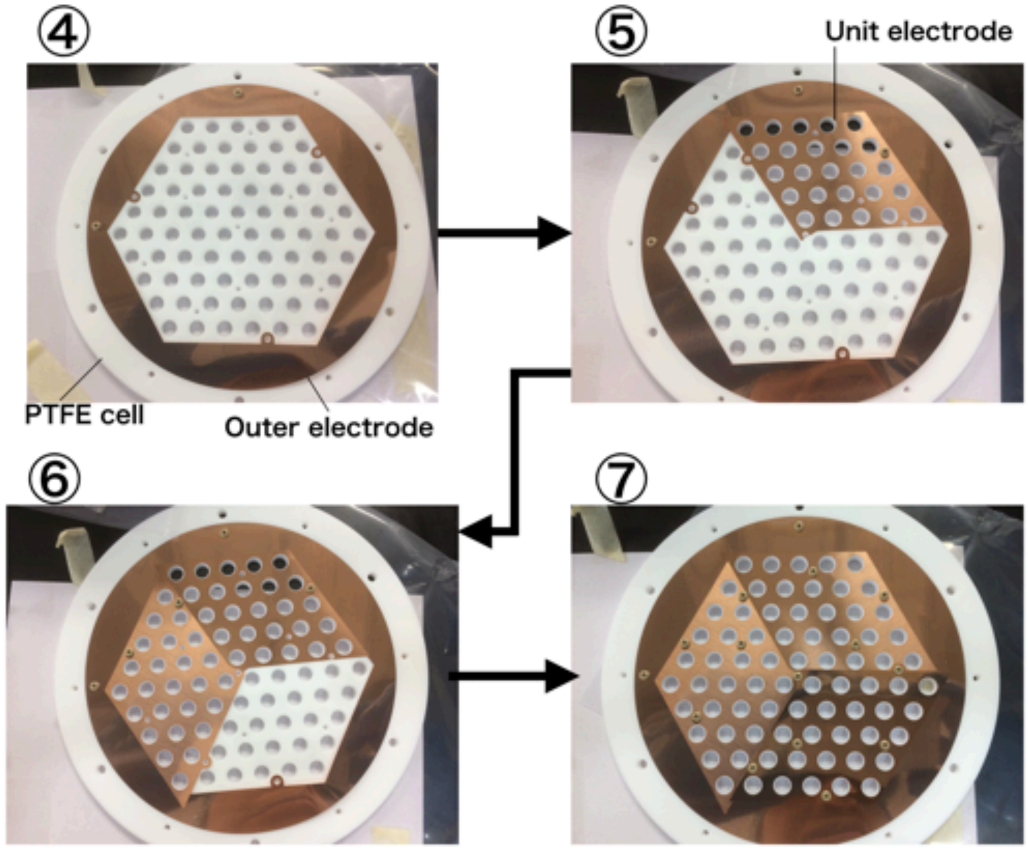

Figure 3.23: Anode electrode.

The MPPC bases are attached to PTFE body from the ground mesh side with screws (Figure 3.24). Then the constructed ELCC is fixed to the feedthrough flange by pillars.

Cable connections are done in the same way as Version 3.

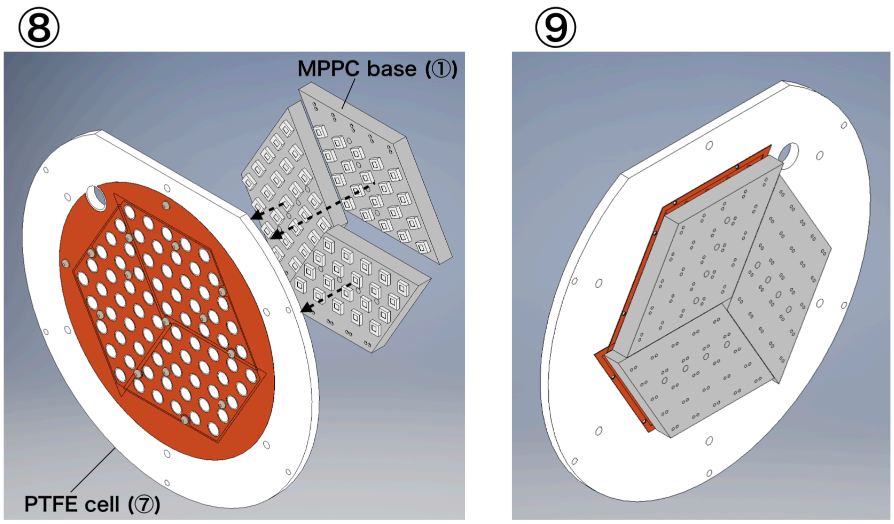

Figure 3.24: Assembling the MPPC bases to the PTFE cell body.

3.4 Field Shaper

In the 10 L detector, the field shaper that produces the electric field at the drift region is categorized into two versions, "ring field shaper" and "strip field shaper". Originally, a ring field shaper is designed and used for the HP10L Version 1-3. Later, a strip field shaper designed for stronger discharge resistance is used for the HP10L Version 4.

3.4.1 Ring Field Shaper

Oxygen-free copper ring-electrodes are concentrically stacked to construct a field shaper. The electrode at the top of the field shaper (cathode electrode) is composed of rings sandwiching a mesh plate so that scintillation lights can be transmitted towards PMTs. The inner diameter and outer diameter of the ring field shaper are 90 mm and 110 mm, respectively. The inner diameter of 90 mm is large enough to cover a 7.5 mm-pitch, 8×8 channels sensitive area of the ELCC. Spacers made of PEEK are inserted between the ring electrodes, and the rings are kept at an interval of 6 mm. The length of the ring field cage (in other words, the length of the sensitive region) is determined by the number of stacked stages. In the HP10L Version 1 and Version 2, the length of the field cage is 60 mm, and in the HP10L Version 3, it is extended to 90 mm. The rings are electrically connected in series with 100 MΩ resistances. We use a very low outgassing type resistor (RG1S, produced by Japan Finechem Inc.). The resistor at the bottom stage (at $z = 0$ cm) is connected to the anode electrode. To reduce outgases, a crimped terminal instead of soldering is used to connect a resister with a ring electrode until the middle of the HP10L Version 3. Then crimp terminals are removed to prevent corona discharges and each resister is directly connected with a screw as explained below. The high voltage applied to the cathode is equally divided to the respective electrodes by the resistances with respect to the anode. Figure 3.25 shows the 3D CAD model of the ring field shaper with the length of 60 mm and a picture of the field shaper used in HP10L version 2 is shown in Figure 3.26.

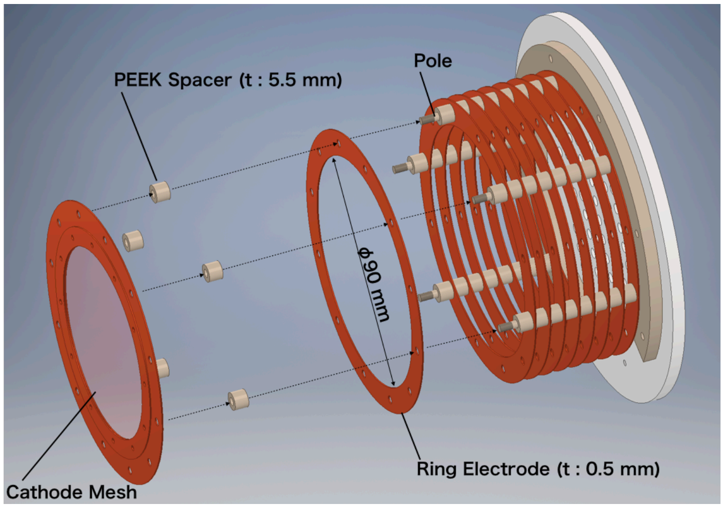

Figure 3.25: 3D CAD drawing of a ring field shaper. Ring electrodes (t0.5 mm) and spacers (t5.5 mm) are alternately stacked to form a field shaper. The top electrode is tightened by PEEK nuts.

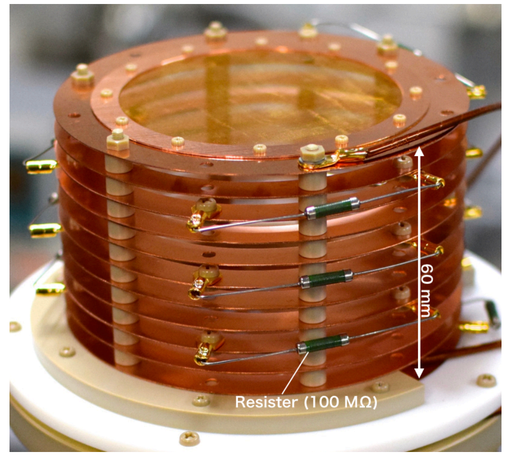

Figure 3.26: Ring field shaper with 6 cm-length which is used in the HP10L Version 1 and Version 2. Each electrode is connected electronically by a 100 MΩ resister.

Simulation of the Electric Field by Ring Field Shaper

A simulation of the electric field at the sensitive region is done to check the uniformity of the drift field and the discharge tolerance. Finite Element Method (FEM) is used to simulate the electric field. We use "Finite Element Method Magnetics (FEMM)", which is a free software to simulate with FEM [66]. The simulation is done under the condition of axial symmetry around the central axis of the field shaper. The boundary conditions are set such that the potential becomes ground at $R = 104.15$ mm which corresponds to the inner wall of the vessel. The gas region is assumed to be air at 1 bar, and -2100 V was applied to the cathode electrode and -1500 V to the anode electrode which correspond to 100 V/cm for the drift electric field, and 3 kV/cm for the EL electric field, respectively.

Figure 3.27 shows the calculated electric field strength for the ring field shaper of 6 cm in length (10 stages) and indicates that the electric field is uniform in the region inside the field shaper (∼100 V/cm). Also, it can be seen that the electric field at the edge of the cathode electrode is very strong, approximately 4500 V/cm.

Figure 3.28 and Figure 3.29 show the graph of the electric field strength along the central axis and the line at $R = 80$ mm, respectively. These results indicate that the residuals of electric field are within 2% from the designed value of 100 V/cm even at $R = 80$ mm from the center. The drift electric field in the detection area is sufficiently uniform since the 64 cells are within the radius of 80 mm.

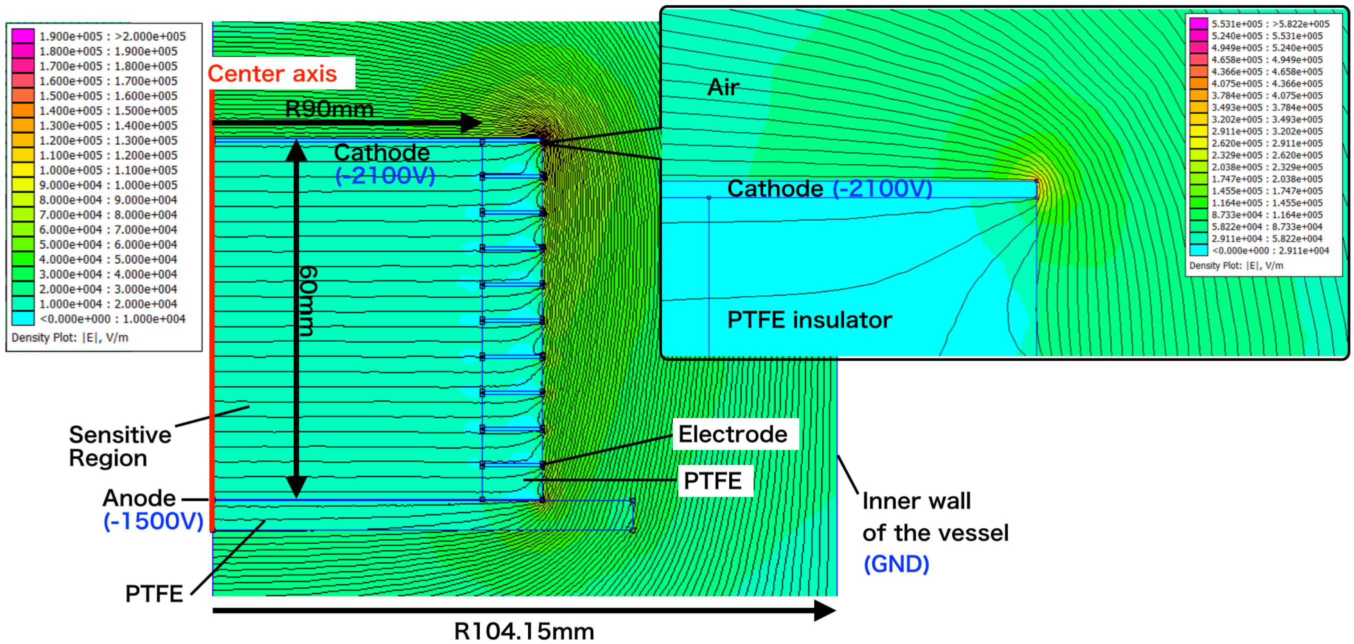

Figure 3.27: Simulated potential and equipotential surface by FEM.

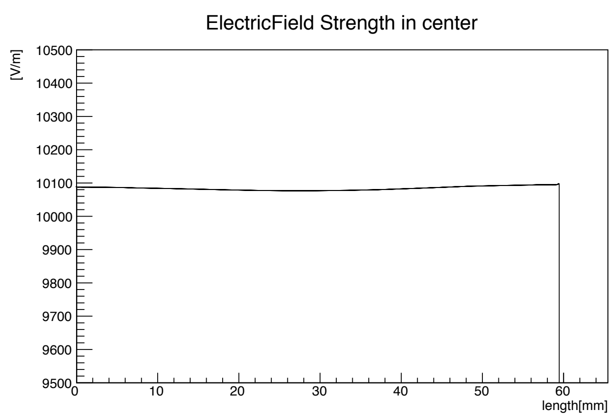

Figure 3.28: Electric field strength along the central axis of the field shaper.

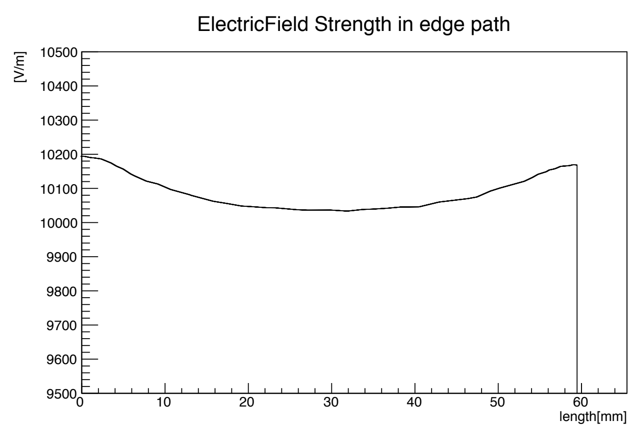

Figure 3.29: Electric field strength along the line at radius of 80mm.

Corona Discharge of the Ring Field Shaper and Countermeasure

During the operation, a corona discharge occurred at a cramped terminal which connects a field shaper electrode with a resister. Figure 3.30 shows a picture of the corona discharge. Since the potential difference between the crimp terminal near the cathode and the wall of the vessel is large, it is considered that the electric field at the sharp edge of the crimp terminal is very strong, thus a corona discharge has occurred. It is necessary to remove the sharp edge in order to prevent this discharge, hence, we stopped using crimp terminals and resistances are directly attached to the ring electrodes with screws (see Figure 3.31). In addition, Kapton® sheets with 0.5 mm thickness are stuck on the inner wall of the pressure vessel to prevent sparks between the field shaper and the wall (see Figure 3.32). However, as described in Section 3.3.2, since a discharge at the cathode electrodes occurred despite these countermeasures, we could not apply the electric field at the target value, $E_{\rm EL} = 3$ kV/cm/bar, $E_{\rm drift} = 100$ V/cm/bar, i.e. $V_{\rm cathode} = 19.2$ kV, in 8 bar xenon. The evaluation was done under the condition of $E_{\rm EL} = 2.375$ kV/cm/bar, $E_{\rm drift} = 72$ V/cm/bar.

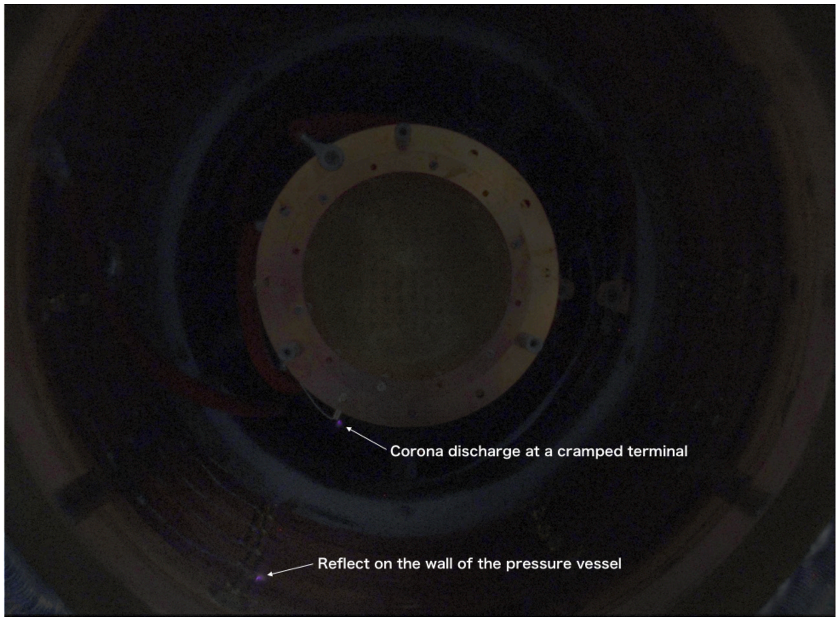

Figure 3.30: Corona discharge at a cramped terminal in air. The blank flange of the opposite side of the feedthrough flange is removed to inspect sparks by eyes. Approximately 17 kV is applied at the cathode electrode.

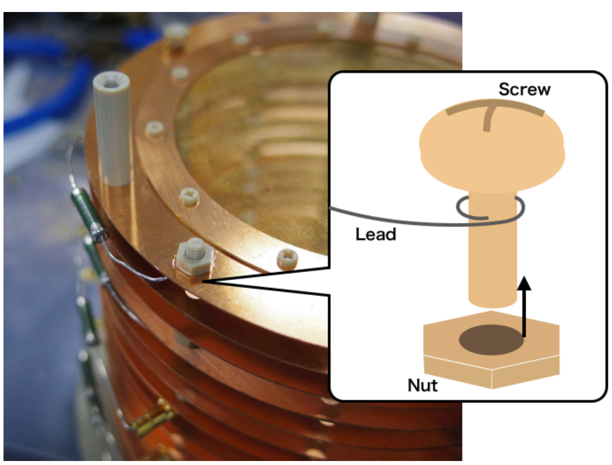

Figure 3.31: Ring field shaper without cramped terminals.

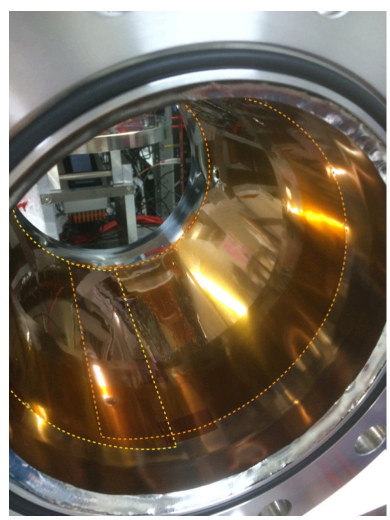

Figure 3.32: Kapton® sheets stuck on the pressure vessel. Dotted lines represent the edge of the Kapton® sheets.

3.4.2 Strip Field Shaper

Since a ring field shaper put flat plate perpendicular to the vessel wall, the distance between electrodes and the wall is short, and the edges of electrodes face the wall, the electric field there becomes very strong, thus discharges could occur at these points. Therefore, we designed a new field shaper whose electrodes are parallel to the wall of the vessel. Figure 3.33 shows a 3D CAD model view of the strip field shaper. An oxygen-free copper strip-electrode is embedded in the groove in an insulator made of PTFE. The radii of electrodes are 95.5 mm and 98.5 mm, stacked alternately. The width of an electrode is 12 mm, and the spacing of electrodes is 8 mm, thus an inner layer one and an outer one have an overlap of 1 mm. The PTFE insulator is 10 mm thick and its outer diameter is 208 mm, almost matches the inner wall of the pressure vessel. Thus, it is the inner wall of the pressure vessel that supports the weight of the field shaper. The inner diameter of the insulator is 164 mm, which is expanded from the previous version to accommodate the extended ELCC with 13 mm-pitch as explained in Section 3.3.1. The insulator is not entirely circular, but is partially flat to pass cables or attach resistors. It is expected to suppress discharge between the electrodes and the wall of the pressure vessel by embedding electrodes in insulators. The inner wall reflects scintillation lights from xenon and increases the number of incident photons to PMTs. Figure 3.34 shows a picture of the strip field shaper for the HP10L Version 4. The PTFE insulator of the top stage is removed in this picture to make the internal structure visible. Each electrode has a terminal for voltage supply taken out of the PTFE insulator through a stainless steel screw. Again in this field shaper, the high voltage applied to the cathode is equally divided to the respective electrodes with respect to the anode electrode by the resistances. Originally, it was planned to use resistances surface-mounted on a flexible printed cable (FPC) by solder for vacuum use. However, since discharge occurred in the FPC as described below, they were replaced to normal lead resistances (100 MΩ). A 0.05 mm thick Kapton® sheet is wrapped around the field shaper as an insulator.

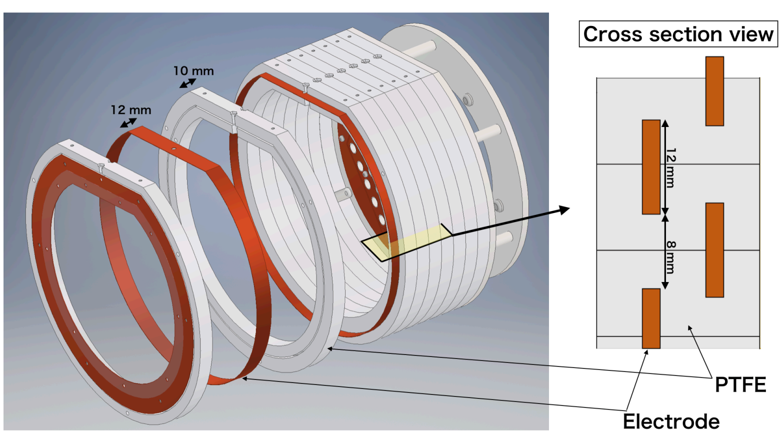

Figure 3.33: 3D CAD model view of the strip field shaper. The 12 mm-wide strip electrodes are embedded in PTFE insulators and they are stacked to form the strip field shaper. The field shaper has a straight part to pass cables and attach resistances.

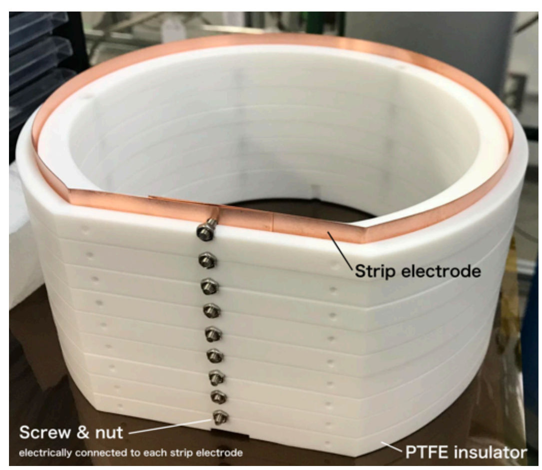

Figure 3.34: Strip field shaper installed in the HP10L Version 4. The top insulator is removed in this picture.

Simulation of the Electric Field by Strip Field Shape

Again, a simulation of the electric field for this field shaper is done with FEMM. The boundary condition of the simulation is the same with that of the ring field shaper. Figure 3.35 shows the result of the calculation by FEMM. The strength of the electric fields at the peripheral region are not significantly different from the ring field shaper, but the strip field shaper was expected to have high discharge resistance because the PTFE insulators exist between the electrodes and the wall of the vessel.

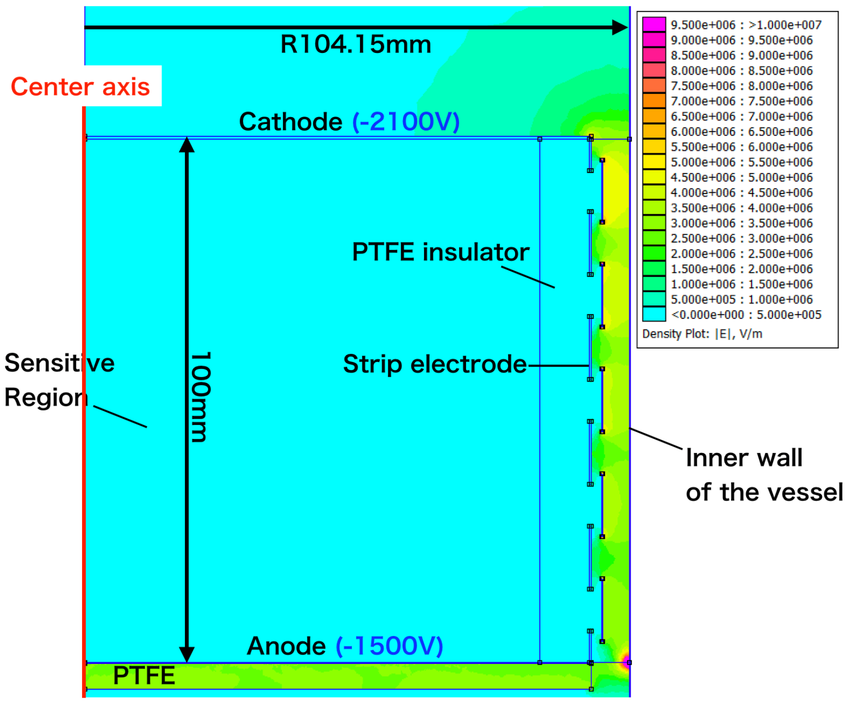

Figure 3.35: Calculated electric field by the strip field shaper by FEMM.

Discharges and countermeasures at strip field shaper

Discharges occurred when rising high voltage to the cathode electrode in 8 bar xenon gas. When a voltage around 13 kV was applied to the cathode and 9 kV to the anode, discharge accompanied by spark noise occurred. As shown in Figure 3.36, traces of discharges were left on the PTFE insulators. We considered that this is because charge-up occurs between the PTFE insulators and the Kapton sheet wound around the insulators, and the potential difference between the outer periphery of the PTFE insulators and an electrode is increased (see Figure 3.36).

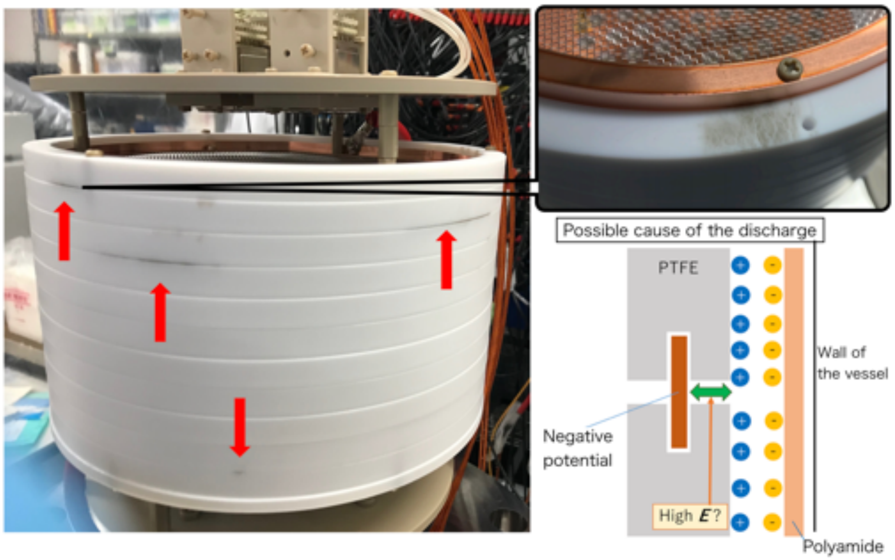

Figure 3.36: Discharge traces at the strip field shaper (left and top right figures). Interpretation of discharge mechanism is also shown in bottom right.

As a countermeasure to this discharge, we attached a Kapton tape tightly to a gap at the seam of the PTFE insulators, expecting that charge-up is positively induced between the Kapton tape and the surrounding Kapton sheet to weaken the electric field in the gap region (see Figure 3.37).

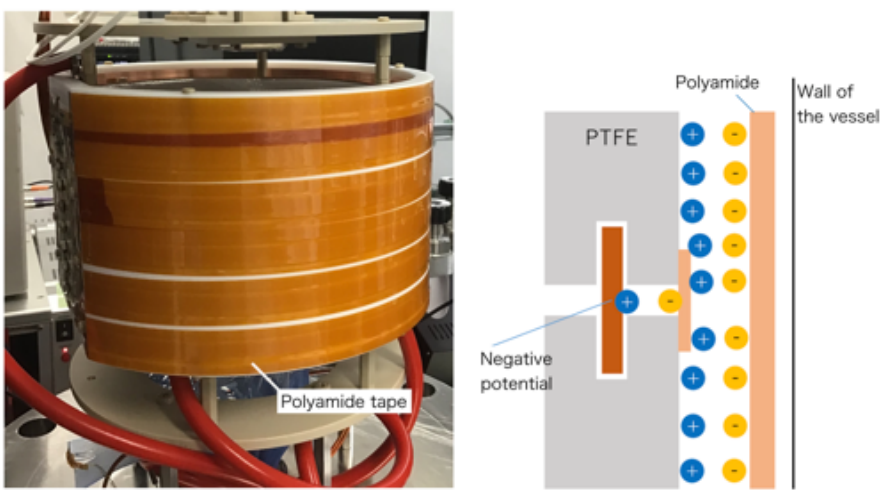

Figure 3.37: Picture of field shaper wrapped by Kapton tape (left) and schematics of a strategy for preventing sparks.

Even with this countermeasure, discharge occurred again in 8 bar xenon gas at around 12 kV applied to the cathode electrode. This time, it turned out that it is creeping discharges inside the FPC mounting resistances. Figure 3.38 shows the FPC with traces of the creeping discharges. As can be seen from this figure, the discharge mainly occurs between sharp edges and other part of the patterns at short distance. Therefore, it has been found design improvement is necessary for the pattern. As a short-time countermeasure of this creeping discharge, the FPC was removed, and normal lead resistances are used by attaching between adjacent electrodes. The evaluation of the HP10L Version 4 described in Section 4.4 was done with this "first aided" strip field shaper.

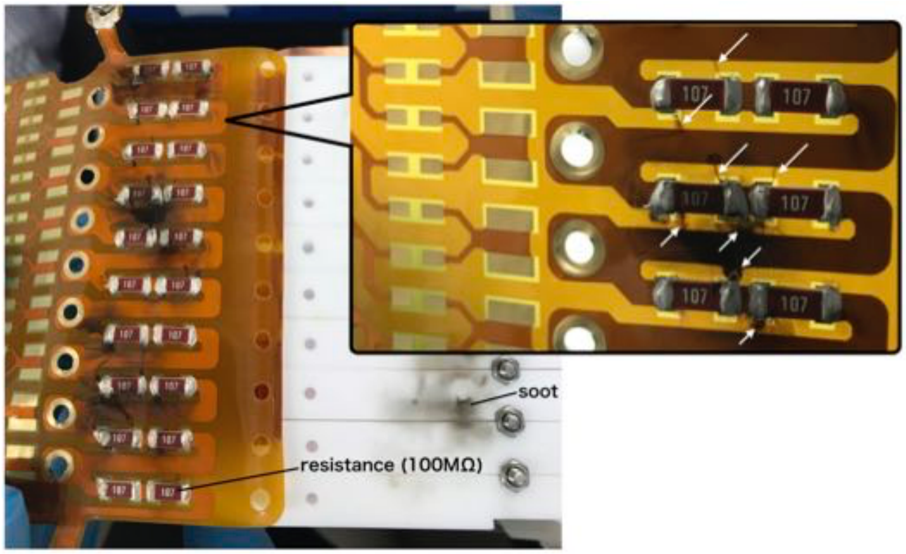

Figure 3.38: Traces of creeping discharge on the FPC.

3.5 PMT

Two PMTs mentioned in Section 2.4.2 are installed in the HP10L Version 3 and Version 4 as shown in Figure 3.39. The PMTs are fixed by a support made of PEEK at a distance of 22.3 mm from the cathode. As mentioned in Section 3.2.1, in version 3, high voltages to the PMTs are applied by the silicon sleeved cables and signals are read out through the ribbon cables. In version 4, both voltage application and signal readout are performed by Kapton sleeved coaxial cables.

3.5.1 Calibration of 1 p.e. Gain

Gains of the PMTs are calculated using an LED light. The light quantity of the LED is adjusted to the level of photoelectron, thus the distribution of the number of photoelectrons by a PMT will obey a Poisson distribution. The distribution of integrated charge is shown in Figure 3.40. The left peak is the pedestal which is considered as 0 p.e. events. From the 0 p.e. entries, the PMT gain is calculated using Poisson distribution. The obtained gain is 7.05×10^7, consistent to the specification value.

3.6 Peripherals

3.6.1 High Voltage Application to the Anode and Cathode Electrodes

For Cathode Electrode

The high voltage to the cathode electrode is applied by a 30 kVDC power supply with negative polarity (HFR10-30N, manufactured by Matsusada inc.).

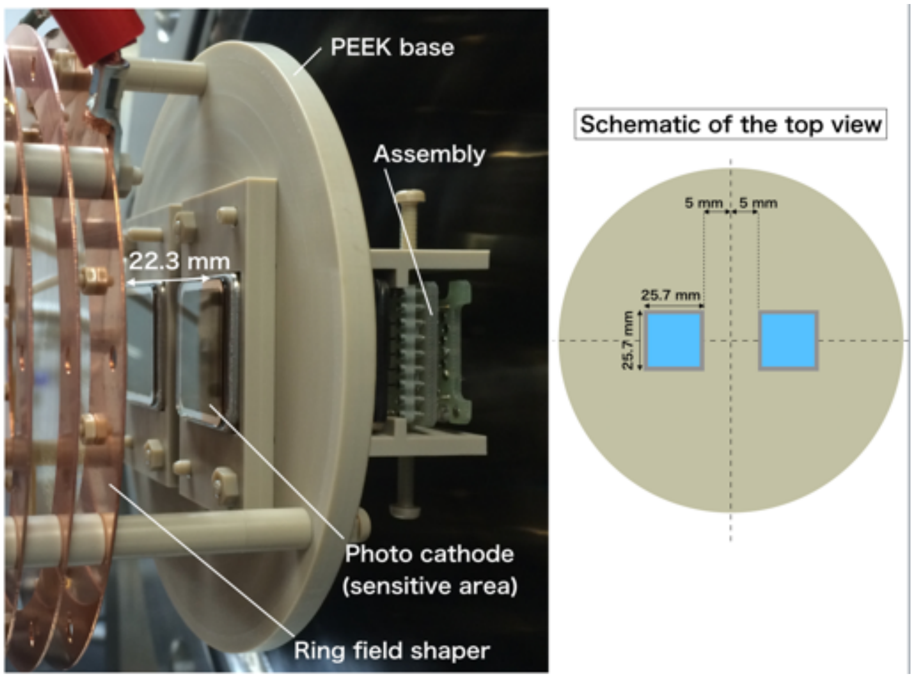

Figure 3.39: PMTs installed in the HP10L (left) and the schematics of the top view of the PMT mount.

For Anode Electrode

The high voltage to the anode electrode is applied by a 20 kVDC power supply with negative polarity (HFR10-20N, manufactured by Matsusada inc.). The ripple of these modules is less than 0.003% thus the output is very stable.

Protection Circuit Against Reverse Currents

To prevent reverse currents to the power supplies, protection circuits are inserted between the power supplies and each electrode. Figure 3.41 shows the schematic of the protection circuit and the power supplies. Due to these protection circuits, even if the cathode voltage is raised to the maximum output (-30 kV) while keeping the anode voltage at 0 V, no reverse current flows to the power supply for the anode electrode (HFR10-20N). Likewise, even if the anode voltage is raised up to -10 kV while keeping the cathode voltage at 0 V, no reverse current flows to the power supply for the cathode electrode (HFR10-30N). A resistor connected in parallel to each power supply provides escape path of reverse current.

3.6.2 Bias Voltage Supply to the MPPCs

At the delivery from the manufacturer, MPPCs having similar break down voltage within $\pm$ 1 V were selected. So a common bias voltage is applied to 64 channels with a single DC power supply (PL-0.6-120 produced by Matsusada inc.).

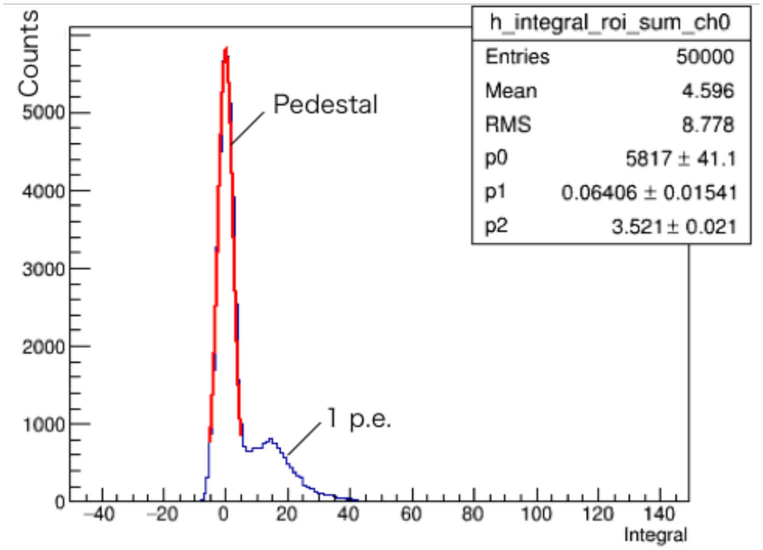

Figure 3.40: Distribution of integrated charge of a PMT.

Low Pass Filter for MPPC Bias Line

As mentioned above, the bias voltage for all MPPCs is applied by a single power supply module, therefore a low pass filter (LPF) shown in Figure 3.42 is needed to be inserted between the power supply and each MPPC to make each MPPC independent for fast pulses. It also suppresses noise from the power source. To accommodate EL signals with a large light intensity (maximum 10^5 photons/sec) and a long duration (typically ten to several tens micro seconds), the time constant of the LPF is set to be $\sim$15 ms, and the capacitors have a large capacitance of 1 μF.

3.7 Gas System

Figure 3.43 is the gas system diagram for the HP10L. The part surrounded by the dotted line is the gas line for circulation, which is introduced from the middle of the HP10L Version 3. The result of the evaluation in Section 4.2 is obtained before the introduction of the dotted line region, and the result after Section 4.3 is with the circulation. The gas flow is monitored by a mass flow meter (F-111CM-40K-AAD-88-K, BRONKHORST) during gas circulation. When the detector is not operated, xenon is stored in a solidified state in the restoration cylinder. It is liquefied by liquid nitrogen and collected into the restoration cylinder while the pressure is reduced to 2 bar or less using the reducing valve. For operation, the cylinder is warmed up and gas is transferred into the vessel using a compressor. In either case, the inlet of the cylinder is heated up to 170 K to avoid freezing and clogging.

3.8 Data Acquisition System

3.8.1 Flash ADC

The MPPC and PMT signal waveforms are acquired using flash analog to digital converter (FADC) modules. Two digitizers with 32-channel readout, 12 bit (2 Vp-p), and 62.5 MS/s (DT5740 pro-

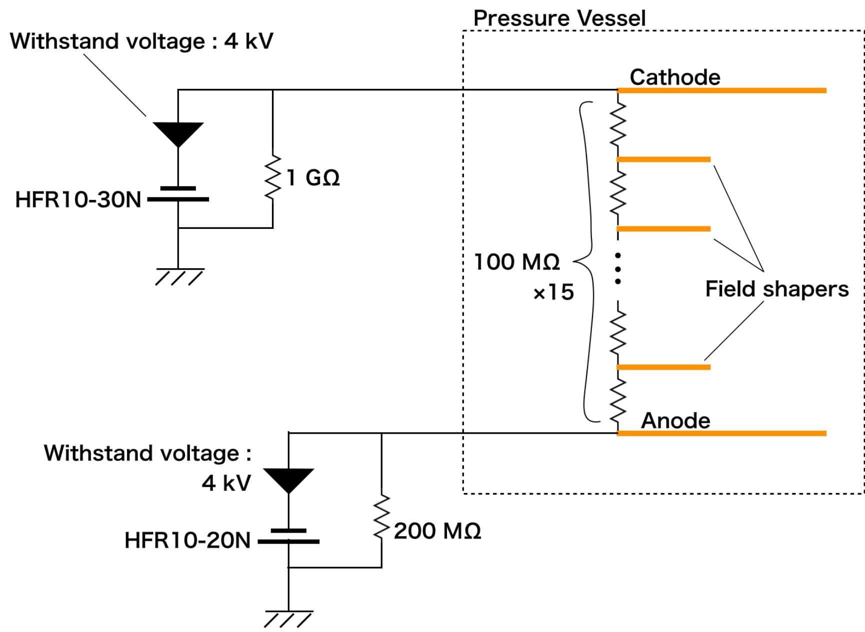

Figure 3.41: Schematic of the protection circuits and the power supplies.

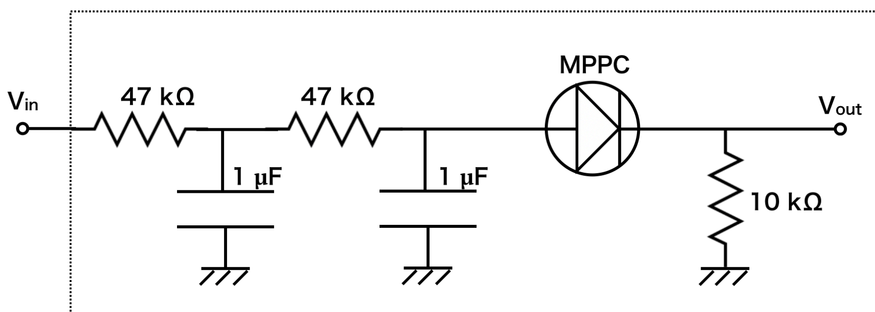

Figure 3.42: Circuit diagram of the low pass filter inserted between the power supply and MPPCs. The part enclosed by the dotted line is connected in parallel for 64 channels.

duced by CAEN inc.) are used to acquire MPPC signals. PMT signals are acquired using a digitizer with 8-channel readout, 14 bit (2.25 Vp-p), and 100 MS/s (v1724 produced by CAEN inc.). Figure 3.44 and Figure 3.45 show examples of waveform of an MPPC and a PMT respectively obtained by FADCs above.

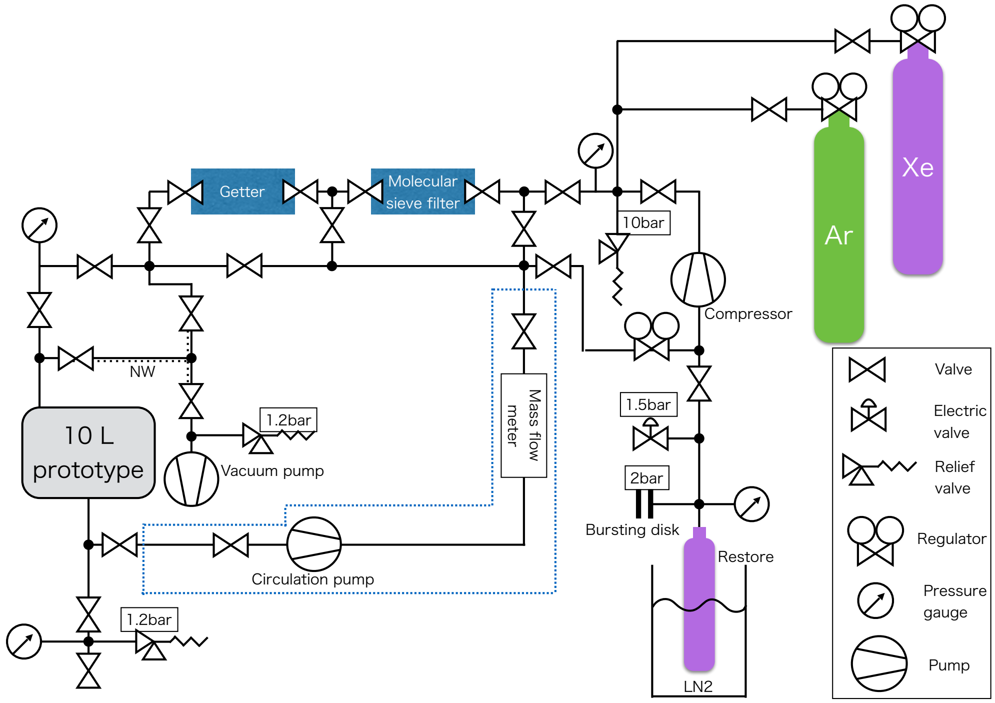

Figure 3.43: Gas system for the HP10L.

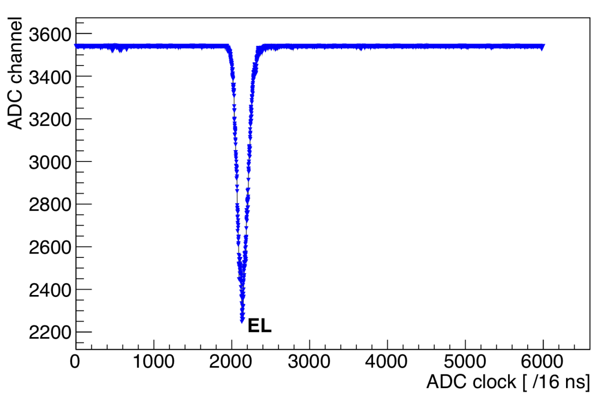

Figure 3.44: Example waveform of an MPPC signal.

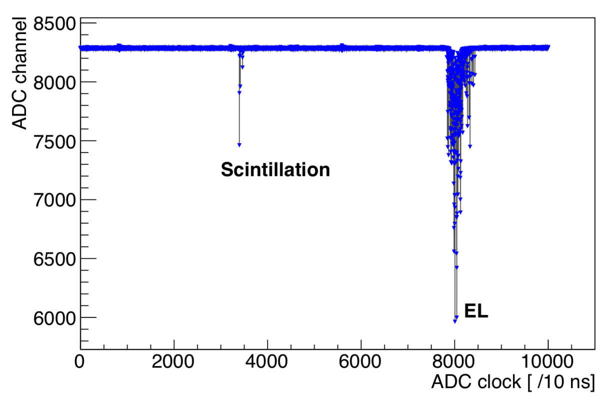

Figure 3.45: Example waveform of a PMT signal.

3.8.2 Band Pass Filter

The trigger is generated from the analog sum signal of MPPC. However, since the rate of dark noise of MPPC is high, they may generate fake triggers. A band pass filter (BPF) is used to eliminate dark current pulses from the MPPCs but allow acquisition of the EL waveform for signals to generate DAQ triggers. Figure 3.46 shows the circuit diagram of the BPF. The BPF's frequency range is between 10^3 and 10^6 Hz.

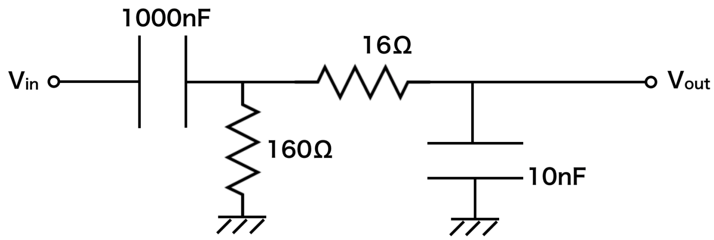

Figure 3.46: Circuit diagram of the band pass filter. The frequency range is set between 10^3 and 10^6 Hz which is adjusted to the EL signals.

3.8.3 Block Diagram

Figure 3.47 shows the block diagram for data acquisition. The MPPC signal is amplified 10 times by a PM amplifier and then input to the FADC with an external trigger. The external trigger is generated from the signal sum of fiducial channels by linear fan-in fan-out modules passing through the band-pass-filter. Specific diagrams for trigger generation are shown in Section 4.2.3, Section 4.3.3, and Section 4.4.3. PMT signals are input into FADC with the same external trigger.

Waveform data are recorded at 6,000 samples (96 μs) for the MPPC signals and 10,000 samples (100 μs) for the PMT signals. The post-trigger rates are set to 93% for the MPPC signals and 20% for the PMT signals. The three FADC modules are linked with optical cables and controlled by a PC.

A pulse generator is used to acquire dark current data for the MPPC gain.

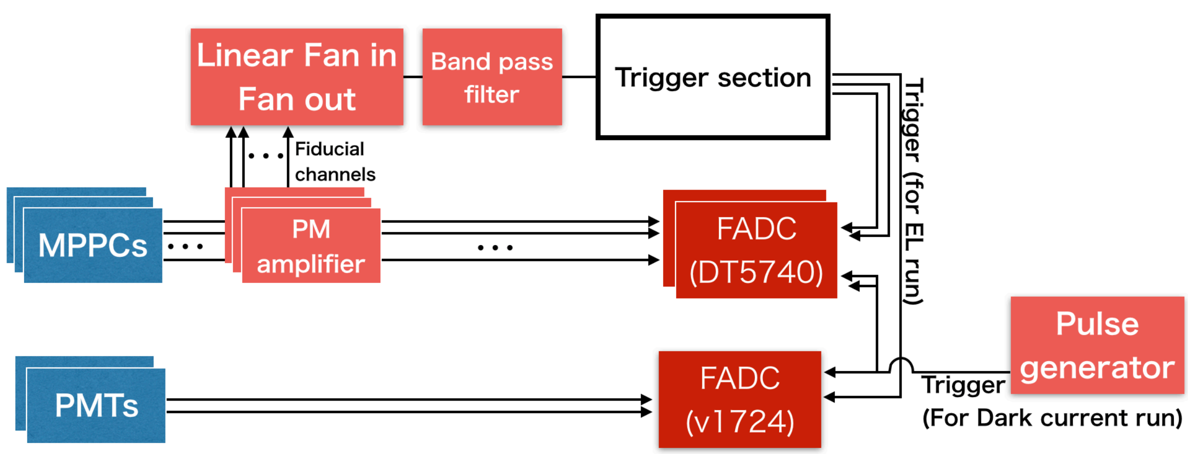

Figure 3.47: Block diagram for DAQ.

Chapter 4

Performance of the 10 L Size Prototype

The performance of the 10 L prototype was evaluated at 4 bar and 8 bar for the square cell pattern ELCC and at 6 bar for the hexagonal cell pattern ELCC. The 4 bar pressure was chosen for easier operation with lower cathode and anode voltages. It was sufficient to measure 122 keV events. Then, in order to evaluate with higher energy (356 keV), the pressure was increased to 8 bar. The cell arrangement was changed to hexagonal pattern with a larger pitch as a preparation of future expansion. Due to the larger detection area, the pressure was reduced to 6 bar to allow operation with lower voltages.

4.1 Purpose and Target

As mentioned in Section 2.2.1, the purposes of analysis of the 10 L prototype are as follows:

- observing the first signal from the ELCC
- to understand the behavior of the ELCC
- evaluation of the performance of the ELCC
- to achieve the energy resolution of 0.5% (FWHM) extrapolated to the Q-value.

The first one was achieved with HP10L Version 1, as described in Appendix A.

4.2 Evaluation of Performance at 4 bar

The performance of the prototype Version 3 was evaluated with 4 bar xenon gas and 122 keV gamma-ray (^{57}Co) [67]. Figure 4.1 shows the decay scheme of ^{57}Co. Gamma-rays with the energy of 122 keV are mainly emitted. Peaks at 30 keV (characteristic X-ray), 92 keV (escape peak), and 122 keV (full peak) are expected to be observed in the spectrum.

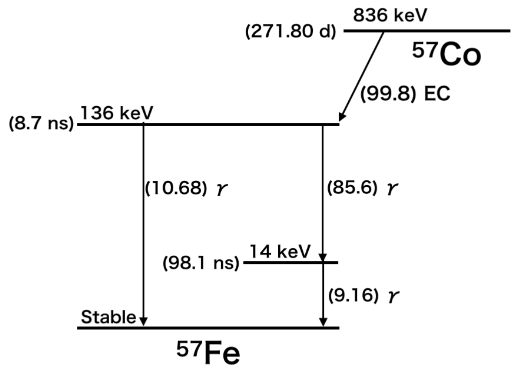

Figure 4.1: Decay scheme of ^{57}Co [68]. The number before an energy represents the probability of that transition (%).

4.2.1 Experimental Condition

Table 4.1 summarizes the condition at this measurement. With 9 kV applied to the cathode electrode and 5.4 kV to the anode electrode, the drift field strength is 100 V/cm/bar and the EL field strength is 2.7 kV/cm/bar. Since the scan of the MPPC bias voltage was not performed, the breakdown voltages and the over voltages are not grasped. The system for gas circulation and purification had not yet been implemented. The gas was purified through the filters only at the timing of introduction. The gamma-ray source, ^{57}Co, is placed on the outer wall of the pressure vessel.

A discriminator module is used as the trigger section shown in Figure 3.47. The threshold is set to the lowest level.

Table 4.1: Condition for 4 bar measurement.

Contents			Reference
Detector		HP10L Version 3	Section 3.1.1
ELCC	configuration	square pattern, 7.5 mm-pitch	Section 3.3.1
	MPPC	VUV-3	Section 3.3.3
Field shaper	type	Ring field shaper	Section 3.4
	size	ϕ9 cm, 9 cm-long	Section 3.4.1
Electric field	Drift region	100 V/cm/bar	Section 3.4.1
	EL region	2.7 kV/cm/bar	Section 3.3.2
Voltage for photo sensors	MPPC	−56.5 V	
	PMT	−800 V	
Gas	Pressure	4 bar	
		w/o circulation and purification	Section 3.7
γ-ray source (^{57}Co)	Activity	1.35×10^4 Bq	

4.2.2 Analysis Overview

The charge of each EL signal is calculated by integrating the waveform after subtracting the baseline, and then converted into the number of detected photons by dividing by the MPPC gain. The MPPC gains are obtained from dark current pulses (Section 4.2.3). Events are selected if the EL signal does not saturate at electronics, scintillation signals are reconstructed well, and tracks are fully-contained in the fiducial region as described in Section 4.2.5. EL gain for each channel is calibrated using 30 keV events. Change of the light yield over time, and the effect of contamination of dark currents in the EL signal are corrected (Section 4.2.7). The performance of the detector is evaluated using the characteristic X-ray peaks (30 keV), escape peak (92 keV), and 122 keV peak (Section 4.2.9).

4.2.3 Processing of the ELCC Signal

A hit channel is selected based on the integration over all ADC samples:

$$S > [\text{Threshold}] = F \times Q_{\text{dark}}, \tag{4.1}$$

where S is the integral after subtracting the baseline, Q_{dark} is expected dark current contribution, and F is a factor to determine a threshold. The baseline is defined as the average of four counts around the mode value of the ADC counts to avoid the effect of the EL signal. The integrated charge is used instead of the pulse height to avoid mis-identification of dark currents as an EL signal. Figure 4.2 shows an example of the distribution of integral values, S. The peak corresponds to the dark current only. In this analysis, the factor F is set to 1.1 for all channels.

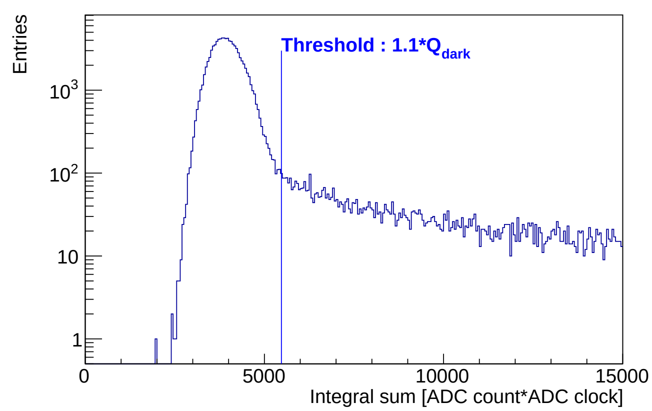

Figure 4.2: Example distribution of integral values over all samples in an event. The threshold (blue line) to select hits is also drawn.

The standard deviation (σ) of the baseline fluctuation multiplied by factor 3, that is, 3σ is used as a threshold to select the EL region.

For each hit channel, the EL region is determined as follows.

1. The waveform is smoothed by averaging over 50 neighboring samples. The maximum point of the smoothed waveform is selected as the starting point to determine the EL region. The reason of smoothing is to avoid selecting dark current signal of the MPPCs as the maximum point. The smoothed waveform is used only to select this starting point.

2. Starting from the point selected in step 1, the points where the waveform falls below the threshold for at least 40 continuous samples are searched for toward both sides. The region between the earlier point (rise time) and the later point (fall time) is defined as the EL region.

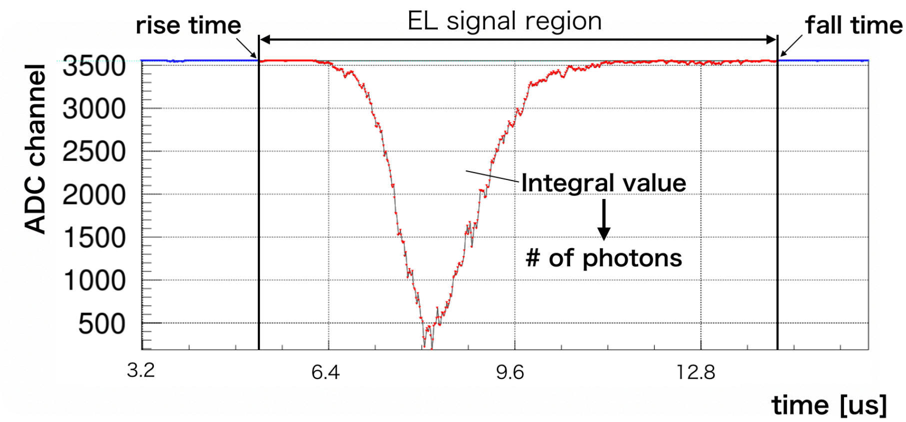

Figure 4.3: Example waveform of an EL signal. The region between two vertical lines is the EL region.

The EL charge is obtained by integrating the EL region after subtracting the baseline, and is converted to the number of photons by dividing the effective gain of the MPPC (see Figure 4.3). The effective gains of MPPCs are calculated by "threshold method" explained in Section 2.3.3. Figure 4.4a shows the obtained effective gain map. MPPCs of two top left channels and one bottom right channel are dead. Figure 4.4b shows its projection to the one dimension histogram. The average and standard deviation of the gains of MPPCs are 33.4 and 2.6 in unit of ADC count, respectively.

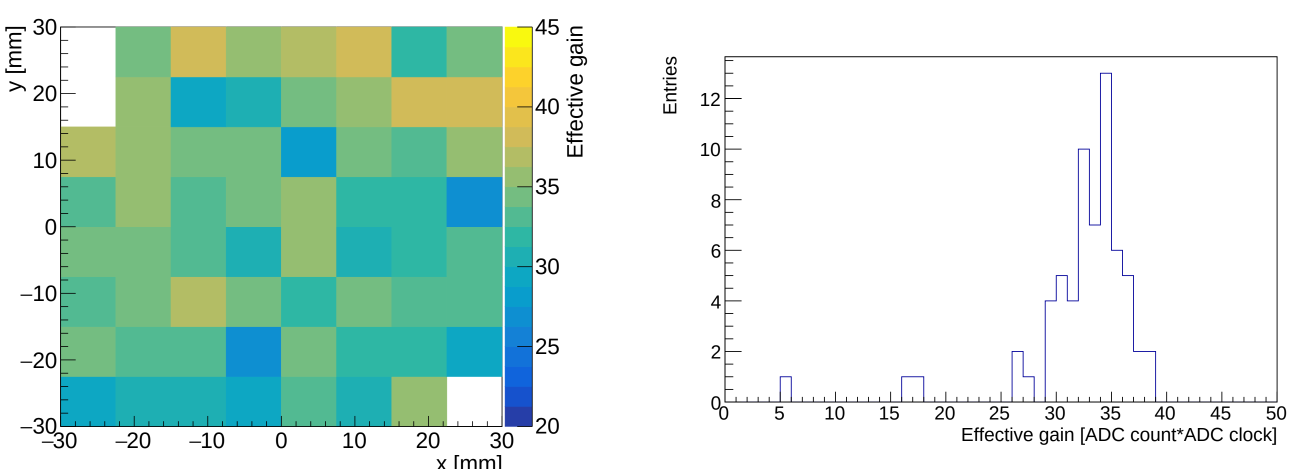

(a) Gain map of each MPPC. One bin corresponds to one channel (MPPC). MPPCs of two top left channels and one bottom right channel are dead.

(b) Distribution of effective gain of MPPCs in unit of ADC count. Three entries below 20 correspond to the dead channels.

Figure 4.4: MPPC effective gain.

Figure 4.5 shows the distribution of the photon count obtained by summing up the photon count of all hit channels before any cuts and corrections. Three peaks corresponding to the characteristic X-rays (∼4500 photons), 90 keV (∼13000 photons), and 122 keV (∼17000 photons), can be seen although they are broad. The rise timing and the fall timing of the combined EL signal are defined as the earliest rise timing of each hit and the latest fall timing among all hits respectively.

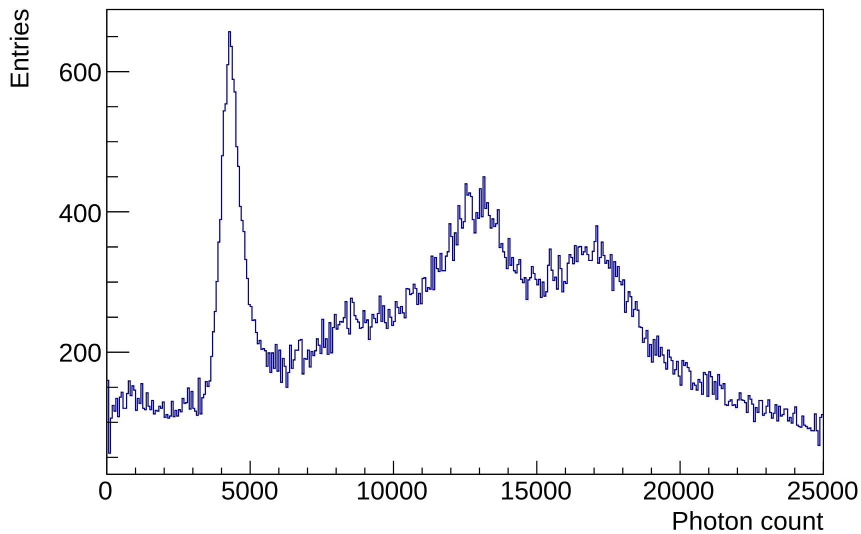

Figure 4.5: Distribution of the photon counts before cuts and corrections.

4.2.4 Processing of the PMT Signal

Figure 4.6 shows example waveforms of the signal from the two PMTs. The earlier 70% region is defined as the scintillation signal region and the later 30% is the EL signal region. Since the EL lights are emitted in various direction, some EL lights go to the PMT side and are detected. The baseline and hit threshold are determined in the same way as the ELCC. For each PMT, signal which exceeds the threshold is searched for in the scintillation region and regarded as a "hit", and the hit with the largest charge is regarded as the scintillation light signal of that PMT. Mean of the scintillation timings of two PMTs is defined as the timing of the scintillation of the event.

4.2.5 Event Selection

Events with missing information, such as signal saturation or events that are not contained within the sensitive region, are cut.

FADC Saturation Cut

Events whose ADC value saturates (0 or 4095 for 12 bit FADC) are cut.

PMT Coincidence Cut

It is required that the timings of scintillation signals of the two PMTs match within 150 ns.

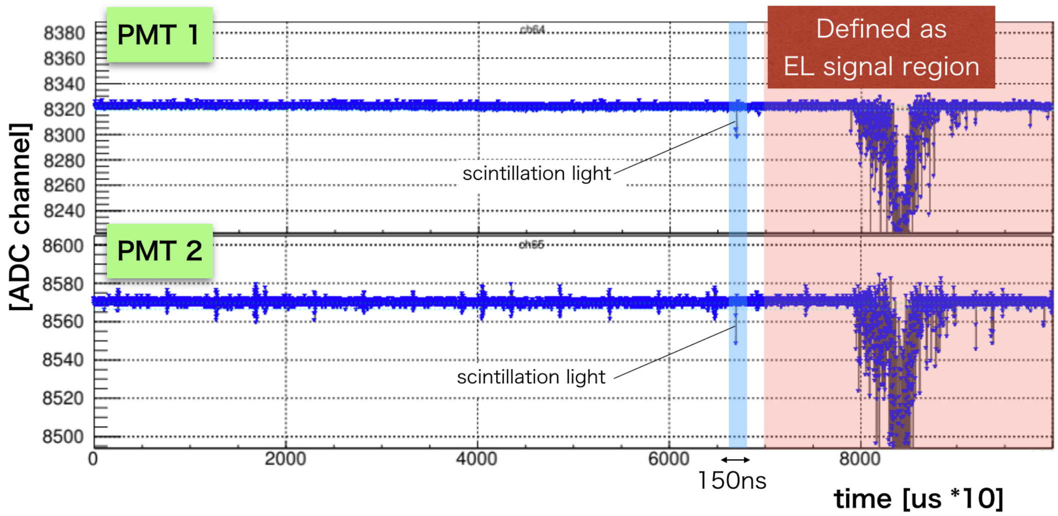

Figure 4.6: Example signal waveforms of the two PMTs. The later 30% is regarded as the EL signal region and is excluded from the search region for scintillation signals.

Fiducial Cut

Fully contained events in the fiducial region are selected. The cut is applied in the xy plane and along the z direction independently.

xy-plane Figure 4.7 shows the fiducial and veto channels. The outermost MPPCs (red painted part) are used as veto. Events which have hits in veto channels are cut. The veto region has irregular shape because the MPPCs at two top-left channels and one bottom-right channel were dead.

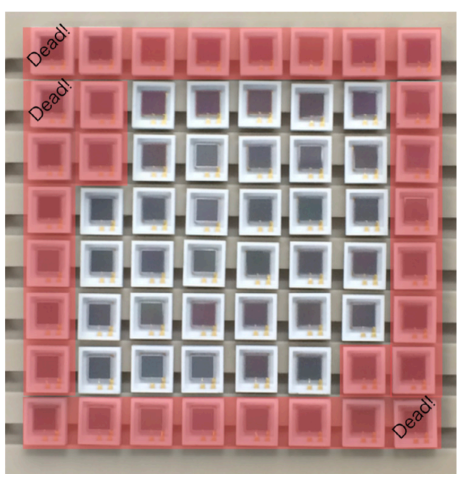

Figure 4.7: MPPCs in red region are used for veto channels and the others are regarded as fiducial channels. Two top left MPPCs behave strangely and the bottom right MPPC has no response, thus these MPPCs (channels) are regarded as dead channel.

z-direction The distributions of timing difference between the EL signal and scintillation signal are shown in Figure 4.8a and Figure 4.8b. The former uses the rise time of the EL signal and corresponds to the drift time of the ionization electrons generated at the track's edge closest to the anode. The later uses the fall time and corresponds to the track's edge farthest to the anode. The red line in Figure 4.8b is the position where the events are 1/10 from peak, and is assigned to $z = 9$ cm, the position of the cathode electrode. Then, the drift velocity is calculated as 0.15 cm/μs. Using this drift velocity, the times are converted to the z positions.

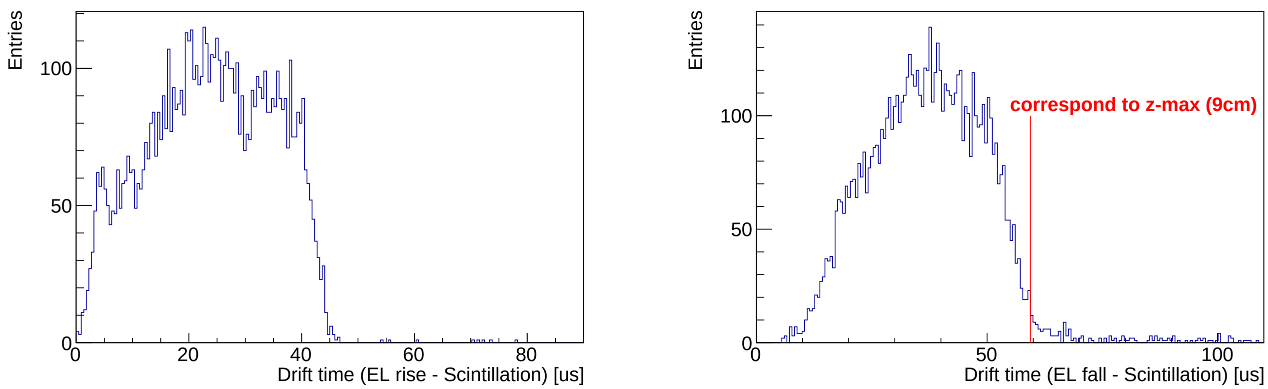

(a) Rise time of the EL signal.

(b) Fall time of the EL signal. The red line is the position which is 1/10 from the peak.

Figure 4.8: Timing distribution of the EL signal measured from the scintillation timing.

Figure 4.9 shows the distributions of the z positions converted from the time differences shown in Figure 4.8. Events less than $z = 2.0$ cm for the anode-side track z position and more than $z = 7.5$ cm for the cathode-side track z position are rejected in the fiducial cut along the z direction.

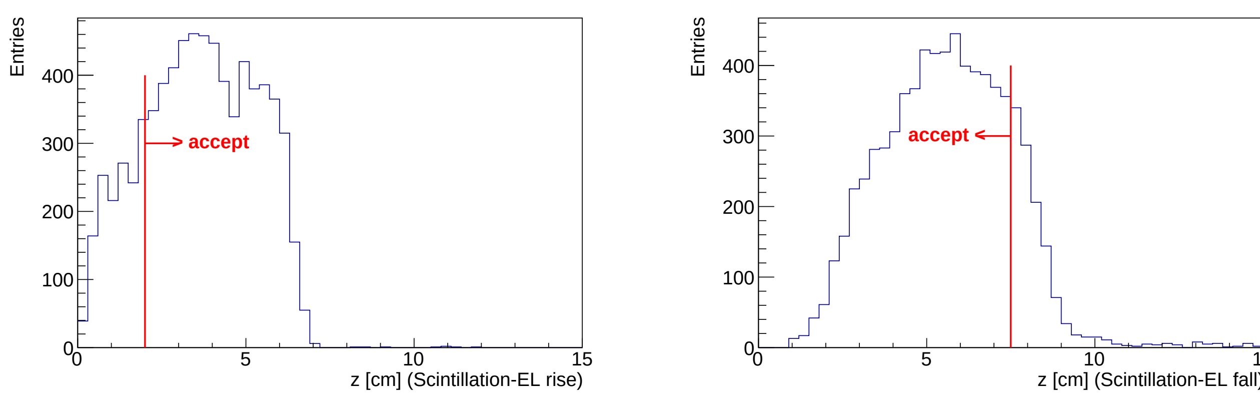

(a) track anode-side z position.

(b) track cathode-side z position.

Figure 4.9: Distribution of the z position converted from the drift time shown in Figure 4.8.

4.2.6 Result of Cuts

Figure 4.10 shows the overlaid photon count spectra for each cut step. The widths of the peaks do not change much by these cuts. The number of events is significantly reduced mainly by the PMT coincidence cut and fiducial cut on the xy plane as shown in Figure 4.11. The reason why the PMT coincidence cut reduced events so much is the low expected number of scintillation lights detected by PMTs. It is calculated to be about 1.7 photons with the Q.E. of 0.3 and the cathode mesh aperture of 0.6 when an event occurs at the center of the sensitive region. In this measurement, veto is not set at the DAQ stage, therefore, a lot of events which have hits at veto channels are also acquired and they are cut at the analysis stage.

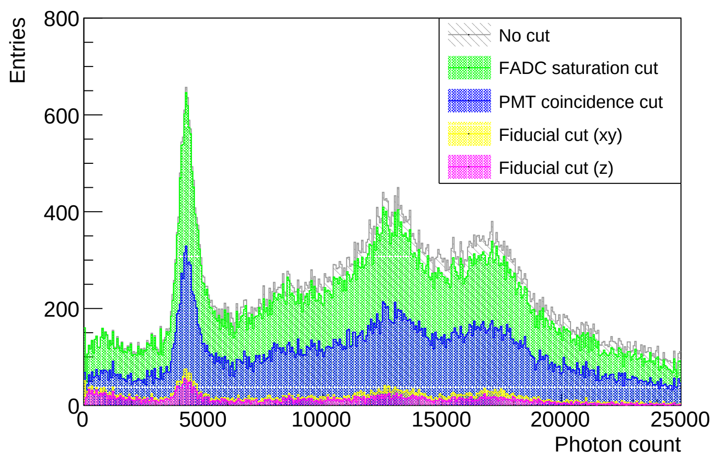

Figure 4.10: Distribution of photon count overlaid for each cut.

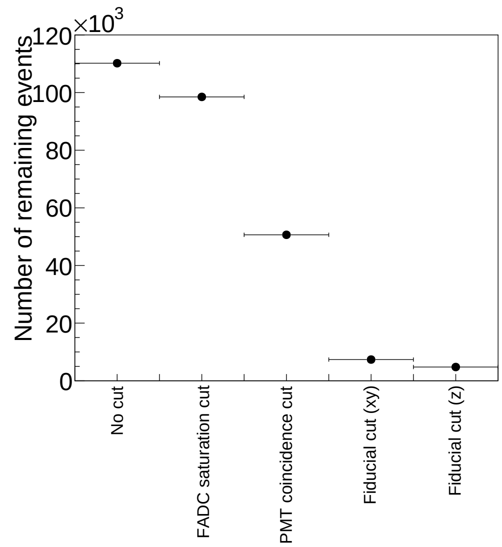

Figure 4.11: Change in the number of events remained after each cut.

4.2.7 Calibration and Corrections

EL Gain Calibration Using K_α Peak

The EL gain varies channel-by-channel because of manufacturing errors of the structures, difference of mesh tension, and difference of the PDE of MPPC. It is calibrated using the K_α peak, which can be regarded point-like event, as follows. For each channel, events are selected if that channel has the largest photon counts among all channels and no channels other than its four nearest neighbors have hit (see Figure 4.12). The distribution of the photon counts obtained by summing the number of photons detected by these channels shows a clear 30 keV characteristic X-ray peak as shown in Figure 4.13. The relative EL gain is obtained by fitting the K_α peak with Gaussian and normalizing by the average value of all channels.

Figure 4.14a shows the map of the normalized EL gains and Figure 4.14b shows its projection. Its standard deviation is 0.045. The photon counts for each channel is corrected by dividing by the normalized EL gain to get uniform response to ionization electrons.

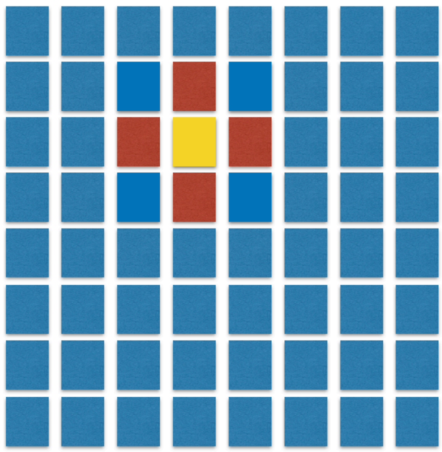

Figure 4.12: Schematic of event selection for EL gain correction. Each block corresponds to channel (MPPC). The yellow cell represents the channel which has the maximum photon counts and the red channels are permitted to have hits.

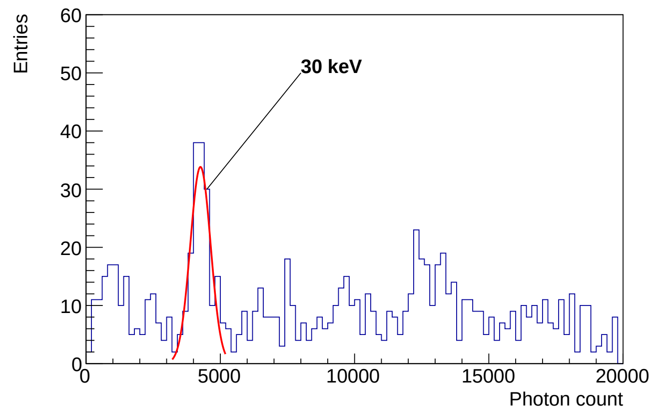

Figure 4.13: Example of the cell gain calibration distribution. Red curve represents the Gaussian fit result.

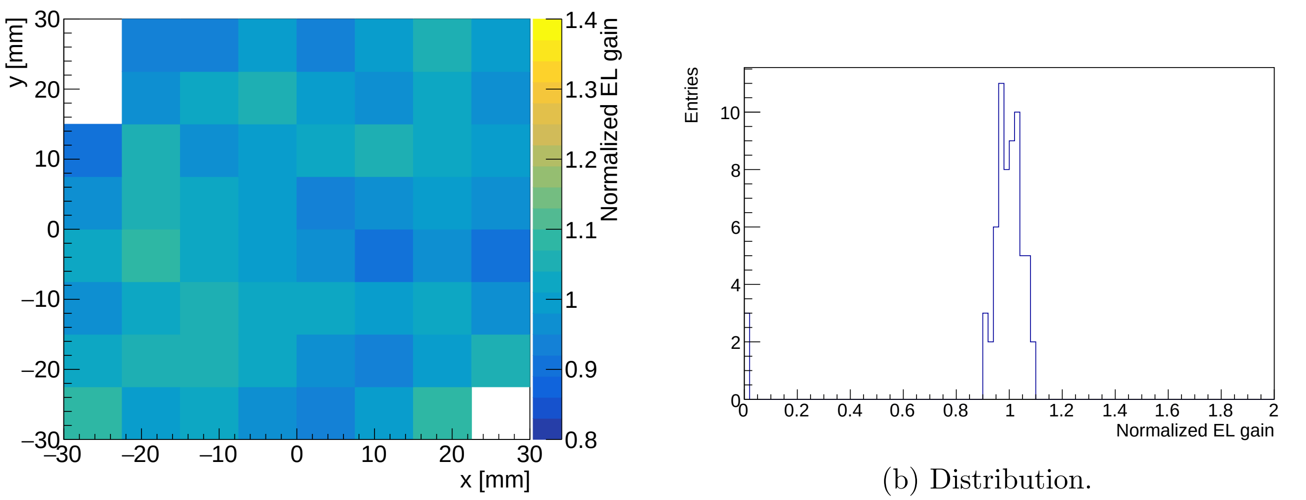

(a) Map.

(b) Distribution.

Figure 4.14: Normalized EL gains.

Correction of Time Dependence

The purity of the xenon gas decreased as time elapsed due to outgas or leak from outside. Figure 4.15a shows the photon counts as a function of the measurement time. The light yield decreased as the time elapsed. A correction is applied with the following equation:

$$N_{\text{photon}} = N_0 \times (1 + \alpha t), \tag{4.2}$$

where N_0 and N_{photon} are the number of detected photons before and after correction, respectively, the t is the time [sec] since the DAQ start, and α is a constant. The optimum value of the correction factor α is determined to get the best resolutions of K_α peak and 122 keV peak. Figure 4.15b shows the plot of photon counts as a function of time after correction with the constant $\alpha = 1.45 \times 10^{-5}$ /sec.

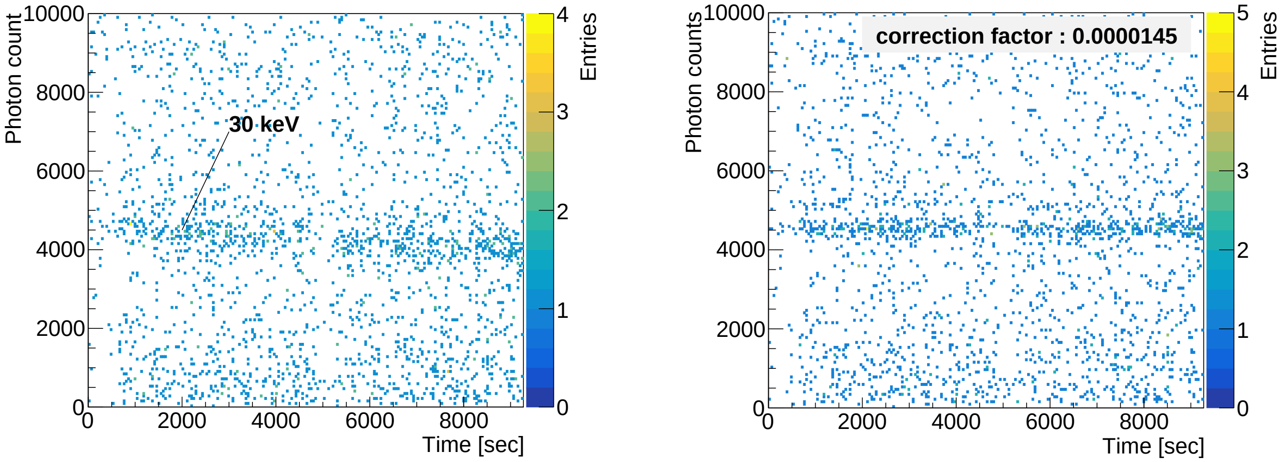

(a) Photon counts as a function of measurement time. The light yield decreased as time passed.

(b) Same as (a), but after the time correction with $\alpha = 1.45 \times 10^{-5}$ /sec.

Figure 4.15: Photon counts as a function of the data taking time.

Dark Current Subtraction

The expected dark current charge in the EL region is calculated and subtracted channel by channel.

4.2.8 Result of Correction

Figure 4.16 shows the photon count spectrum after the corrections. The peaks become very sharp. The K_α, K_β, escape and full peaks are clearly seen. The escape peak is considered as the escape peak of K_α, and a small K_β-like peak can be seen in the left tail. However, since the separation is poor, it is not considered in the analysis hereafter.

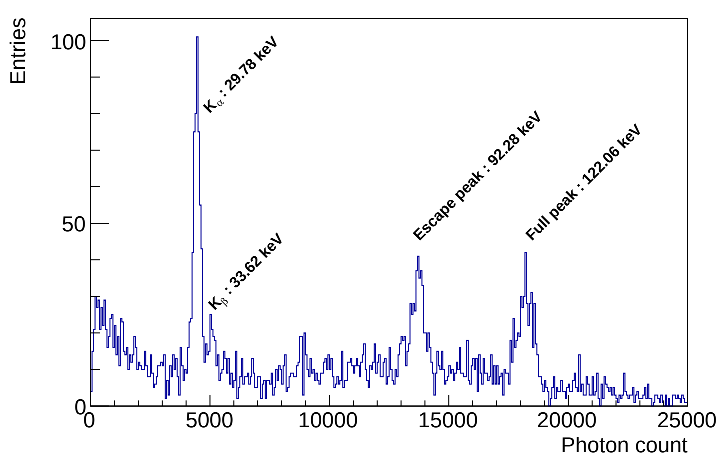

Figure 4.16: Photon count spectrum after the corrections.

4.2.9 Evaluation of the Energy Resolution

Each of the first three peaks (K_α, K_β, and escape) is fitted with a Gaussian and the last peak (full peak) is fitted with "Gaussian+linear function" to include background contribution. Figure 4.17 shows the fit results. The obtained energy resolutions are summarized in Table 4.2. The estimated energy resolutions at the Q-value extrapolated by $1/\sqrt{E}$ are also described.

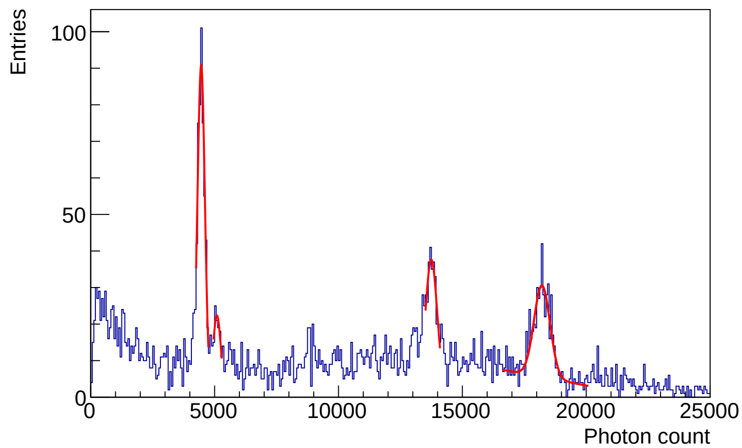

Figure 4.17: Photon count spectrum and fit results

Table 4.2: Energy resolution of each peak. Error is statistical.

Energy	Photon count	Resolution (FWHM)	Resolution at 2458 keV (converted by $1/\sqrt{E}$)
29.78 keV	4457.5±9.1	7.85±0.52%	0.86±0.06%
33.62 keV	5094.0±27.2	7.32±1.83%	0.86±0.21%
92.28 keV	13746.9±25.9	4.16±0.59%	0.81±0.11%
122.06 keV	18214.8±26.1	4.16±0.30%	0.93±0.07%

The expected performance of the prototype at the ^{136}Xe $0\nu\beta\beta$ decay Q-value, 2458 keV, is estimated by fitting the obtained resolutions under two energy-dependence assumptions and extrapolating to 2458 keV. One of the assumptions is that the resolution depends only on the statistical uncertainty, so the fitting function is $A\sqrt{E}$ and the other assumes the additional linear dependence thus the fitting function is $A\sqrt{E + BE^2}$, where E is energy and A, B are fitting parameters. The fit results and extrapolations are shown in Figure 4.18 and summarized in Table 4.3. The estimated energy resolutions at 2458 keV are $0.88 \pm 0.04\%$ (FWHM) with the function $A\sqrt{E}$ and $1.74 \pm 0.16\%$ (FWHM) with the function $A\sqrt{E + BE^2}$.

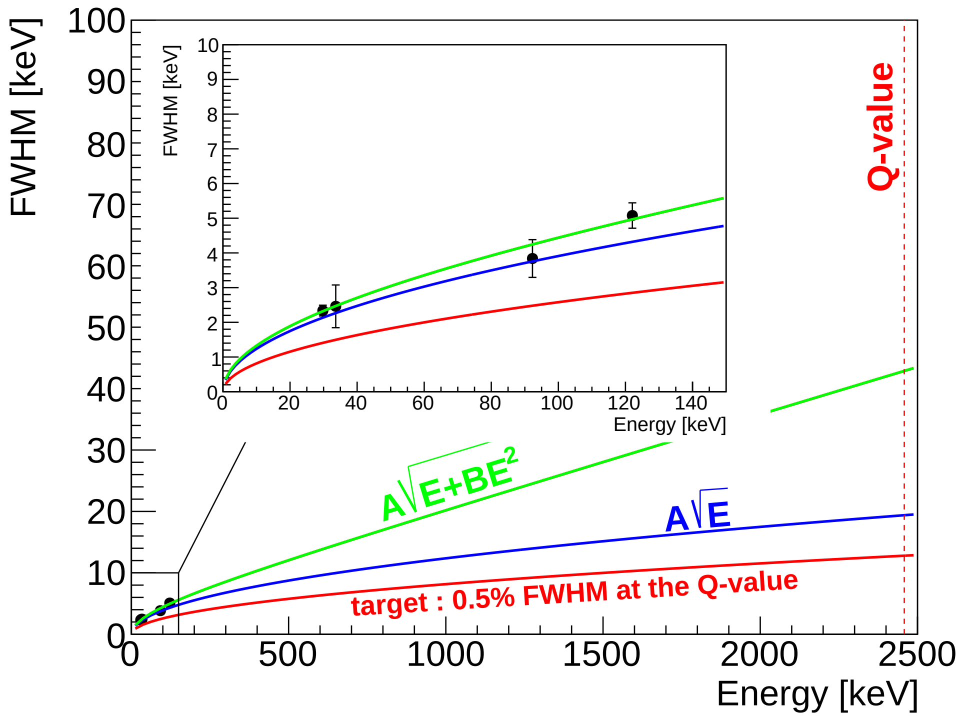

Figure 4.18: Extrapolation of the energy resolution to the ^{136}Xe $0\nu\beta\beta$ decay Q-value

Table 4.3: Energy resolution extrapolated to the ^{136}Xe $0\nu\beta\beta$ decay Q-value.

Fitting function	A	B	Extrapolated resolution at Q-value (FWHM)
$A\sqrt{E}$	0.436±0.020	–	$0.88 \pm 0.04\%$
$A\sqrt{E+BE^2}$	0.417±0.039	0.0013±0.0025	$1.74 \pm 0.16\%$

4.2.10 Summary of the Measurement at 4 bar and Discussion

In this measurement, we have confirmed a good performance of the ELCC by observing sharp peak structures by gamma-rays from ^{57}Co and evaluating the energy resolutions of these peaks. The obtained result showed better energy resolution than that of ongoing $0\nu\beta\beta$ decay search experiments using xenon. However, it does not reach the target energy resolution as shown in Figure 4.18 even in the case of extrapolation by $A\sqrt{E}$. One possible cause to worsen the energy resolution is an incomplete collection efficiency of ionization electrons into the ELCC as mentioned in Section 3.3. In addition, additional component proportional to E seems to exist in the extrapolation. To investigate the cause of that component, evaluations at higher energies are required.

4.3 Evaluation of Performance at 8 bar

The performance of the 10 L prototype Version 3 was evaluated at 8 bar xenon gas with 356 keV gamma-rays from a ^{133}Ba source. The decay scheme of ^{133}Ba is shown in Figure 4.19. Gamma-rays with the energies of 81 keV, 302.8 keV, and 356 keV are mainly emitted. The expected spectrum has peaks at 30 keV, 51 keV (escape peak), 81 keV (full peak), 272 keV (escape peak), 303 keV (full peak), 326 keV (escape peak), and 356 keV (full peak).

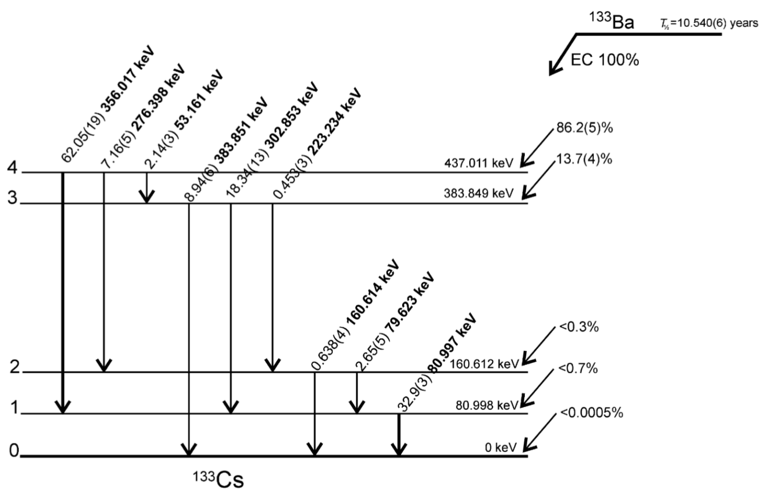

Figure 4.19: Decay scheme of ^{133}Ba [68]. The number before the energy represents the probability of that transition (%).

4.3.1 Experimental Condition

Table 4.4 summarizes the experimental condition. Because of the discharges at the cathode electrode, the electric fields were limited to 2.375 kV/cm/bar for the EL region and 83 V/cm/bar for the drift field. The system for gas circulation was installed and the gas had been purified during the measurement.

There are two types of triggers: high-threshold and low-threshold. The low-threshold triggers are reduced to 1/10 in order not to occupy the whole trigger rate. The low-threshold is set to the lowest value of the discriminator module and the high-threshold is set to the level roughly corresponding to 60 keV.

4.3.2 Analysis Overview

The analysis flow is the same as in Section 4.2. In event selections, events which are not contained in the fiducial region, saturate at the amplifier or ADC, and have multi-site hits are cut (Section 4.3.4). The correction for non-linearity of the MPPC signal is added. Since the gas had been purified during the measurement, decrease of light yield was not seen in this measurement. Details of the corrections are explained in Section 4.3.6. The performance is evaluated using the characteristic X-ray peaks (29.78 keV, 33.62 keV), escape peaks (51 keV, 272 keV, 326 keV), and full peaks (81 keV, 303 keV, 356 keV).

4.3.3 Processing of the ELCC Signal

Hit channel is defined by the integrated charge over all ADC samples as was done in Section 4.2.3. This time, threshold is set to 2.6 sigma above the pedestal, where sigma is standard deviation of

Table 4.4: Condition for 8 bar measurement.

Contents			Reference
Detector		HP10L Version 3	Section 3.1.1
ELCC	configuration	square pattern, 7.5 mm-pitch	Section 3.3.1
	MPPC	VUV-3	Section 3.3.3
Field shaper	type	Ring field shaper	Section 3.4
	size	ϕ9cm, 9 cm-long	Section 3.4.1
Electric field	Drift region	83 V/cm/bar	Section 3.4.1
	EL region	2.375 kV/cm/bar	Section 3.3.2
Voltage for photo sensors	MPPC	-55.0 V	
	PMT	-800 V	
Gas	Pressure	8 bar	
		w/ circulation and purification	Section 3.7
γ-ray source (^{133}Ba)	Activity	4.71×10^5 Bq	

the pedestal.

The algorithm to determine the EL region and to calculate the EL charge, rise timing, and fall timing for each hit channel are the same as that in Section 4.2.3. The MPPC gains are calculated by the “random window method” to more accurately evaluate the effects of after pulse as explained in Section 2.3.3. The obtained MPPC gain map is shown in Figure 4.20a and Figure 4.20b shows its 1-D distribution. The average and the standard deviation of the effective gain in unit of ADC count are 22.61 and 2.12, respectively. As it turned out later, a bug existed in an analysis code for calculating the MPPC gains, thus, the actual gains are about 1.5 times smaller than the obtained values. The mis-calculation of the MPPC gain does not affect to the energy resolution analysis because it is corrected simultaneously during the EL gain calibration. However, the number of detected photons is underestimated. The top right channel and the bottom right channel are dead in this data set.

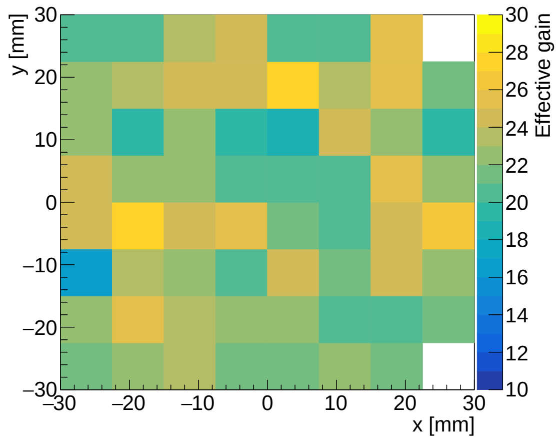

(a) Gain map of each MPPC. One bin corresponds to one cell. The top right channel and the bottom right channel are dead.

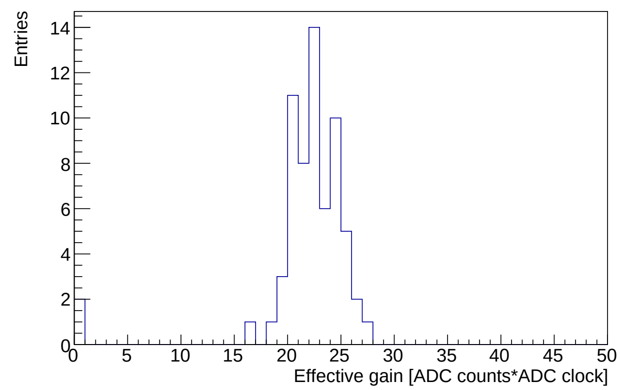

(b) Distribution of effective gain of MPPCs.

Figure 4.20: Effective gain in unit of ADC count.

Figure 4.21 shows the photon count spectrum before applying any cuts and corrections. Peaks of X-rays (30 keV) and photo peak (81 keV) can be seen. Escape peak (50 keV) is also seen between the 30 keV and the 81 keV peaks. Peak structure around 356 keV is not seen in this raw distribution.

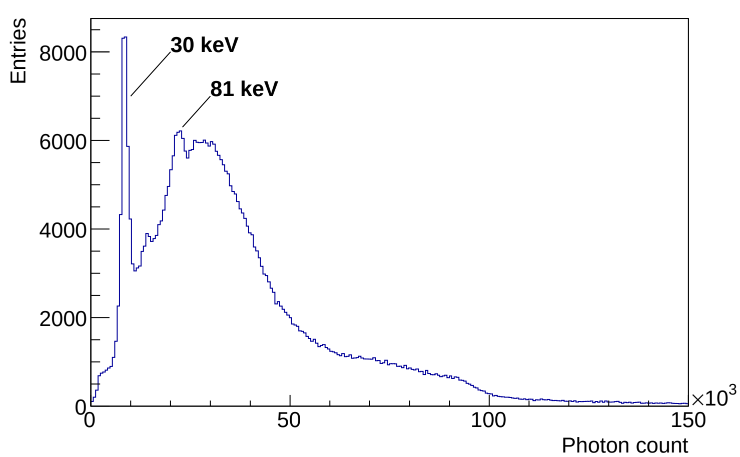

Figure 4.21: Photon count spectrum before cuts and corrections.

4.3.4 Event Selection

Basic Cut

The cuts explained in Section 4.2.5 (ADC saturation cut, PMT coincidence cut, and fiducial cuts in the xy-plane and along the z-direction) are applied. We call these cuts "basic cut" hereafter.

The configuration of fiducial and veto channels is shown in Figure 4.22.

Events contained between $z = 1$ cm and $z = 8$ cm are selected. The z fiducial cut is loosened compared to the 4 bar measurement to increase the statistics.

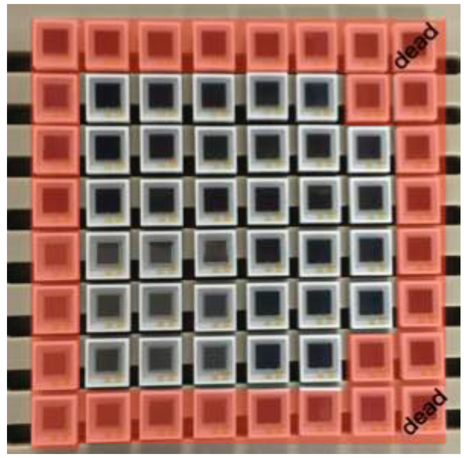

Figure 4.22: MPPCs in red region are used as veto channels.

Figure 4.23 shows the overlaid photon count spectrum before and after the basic cut.

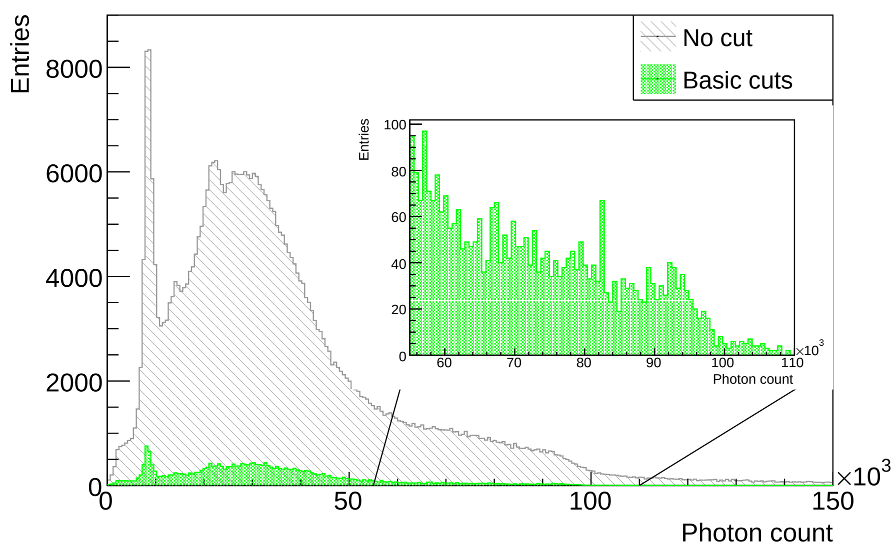

Figure 4.23: Photon count spectrum before and after the basic cut.

Amplifier Saturation Cut

Figure 4.24 shows an example waveform with saturation at the amplifier output. Events whose pulse height goes below ADC count of 100 are rejected.

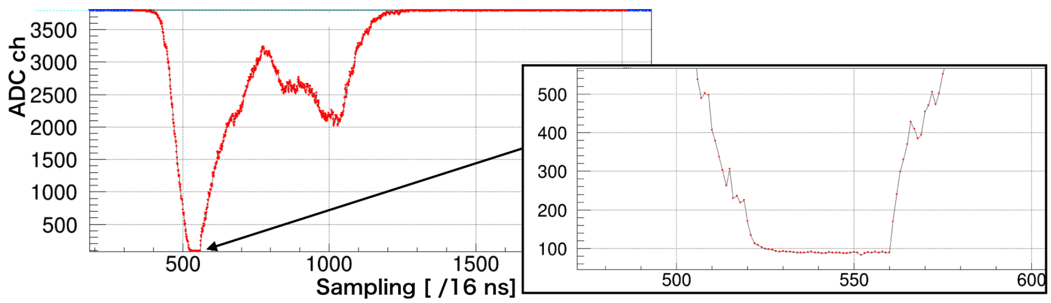

Figure 4.24: Example waveform with a saturation at the amplifier output. The waveform is flat between 520 and 560 sampling because of the saturation.

PMT Signal Width Cut

The z position dependence of the light yield was investigated using the 30 keV events. As a result, the dependence was found to be quite a small and no corrections are needed, but a strange z position distribution was found. The cause was found to be the mis-identification of the EL pulse as scintillation pulse and such events were cut. Details are described below.

The z position of the light intensity centroid (z_{avg}) is calculated. Figure 4.25 shows the z_{avg} distribution of the 30 keV events (selection criteria: $6500 \leq$ Photon counts ≤ 10000). Only in this photon count range, the number of events increases as z_{avg} decreases.

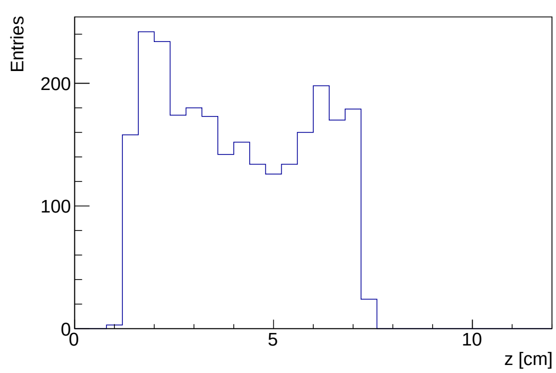

Figure 4.25: Distribution of z_{avg} of 30 keV events (Photon counts: 6500-10000).

An example waveform of the events at $z_{\mathrm{avg}} = 2$ cm is shown in Figure 4.26. The upper one is the sum waveform of 64 MPPC signals, and the lower is the sum waveform of two PMTs. The EL pulse is detected by both MPPCs and PMTs around $t = 0$ μs. In the scintillation region of the PMTs, another EL-like pulse can be seen at around -20 μs. Many such events are found around $z_{\mathrm{avg}} = 2$ cm for the 30 keV events.

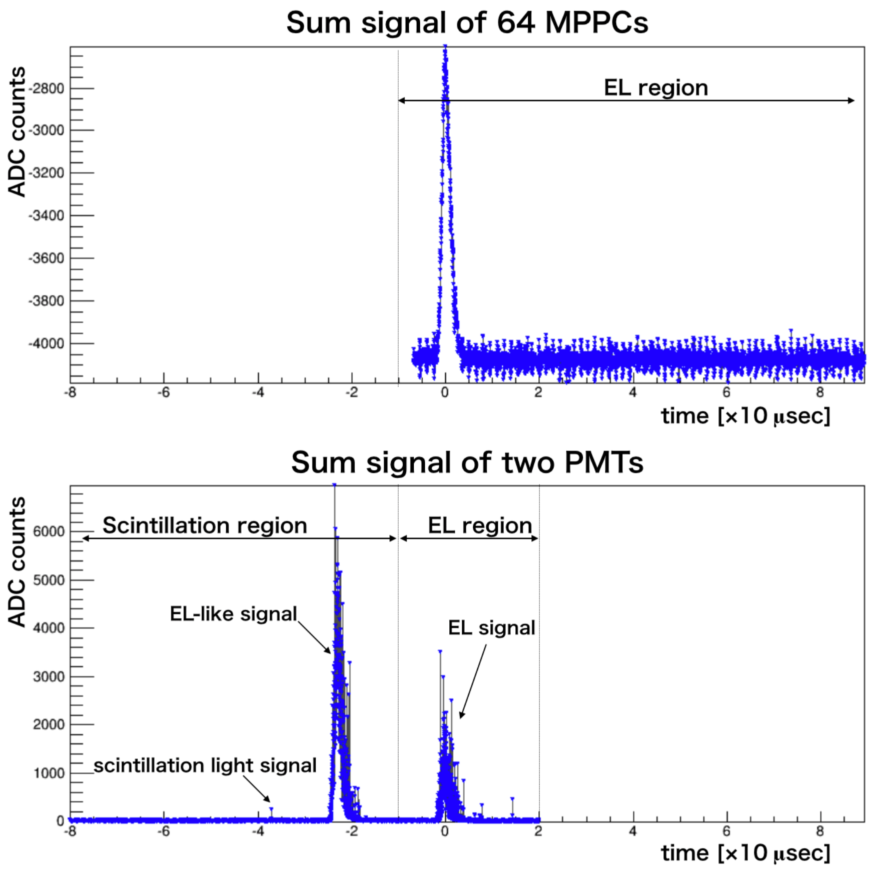

Figure 4.26: Example waveform of sum of the MPPC signals (top) and the PMT signals (bottom) for $z_{\mathrm{avg}} = 2$ cm. An EL-like signal is observed in the scintillation region of the PMT signal. The signals are flipped vertically in these plots.

These events can be interpreted that a γ-ray interacts via photoelectric absorption in the xy veto region and its characteristic X-ray is absorbed in the fiducial region. The trigger is issued by the interaction in the fiducial region, thus the EL signal by the initial photoelectric absorption can be observed outside the EL region as shown in Figure 4.27.

When searching for a scintillation signal candidate in the scintillation region of the PMT waveform, the largest signal is regarded as the scintillation candidate as mentioned in Section 4.2.4. In case of Figure 4.27, the EL signal by the interaction in the veto region is regarded as the scintillation light and is defined as the time zero signal of TPC. Therefore, the z_{avg} position of such events concentrate around the mean free path of 30 keV X-rays in 8 bar xenon, 2.58 cm [45].

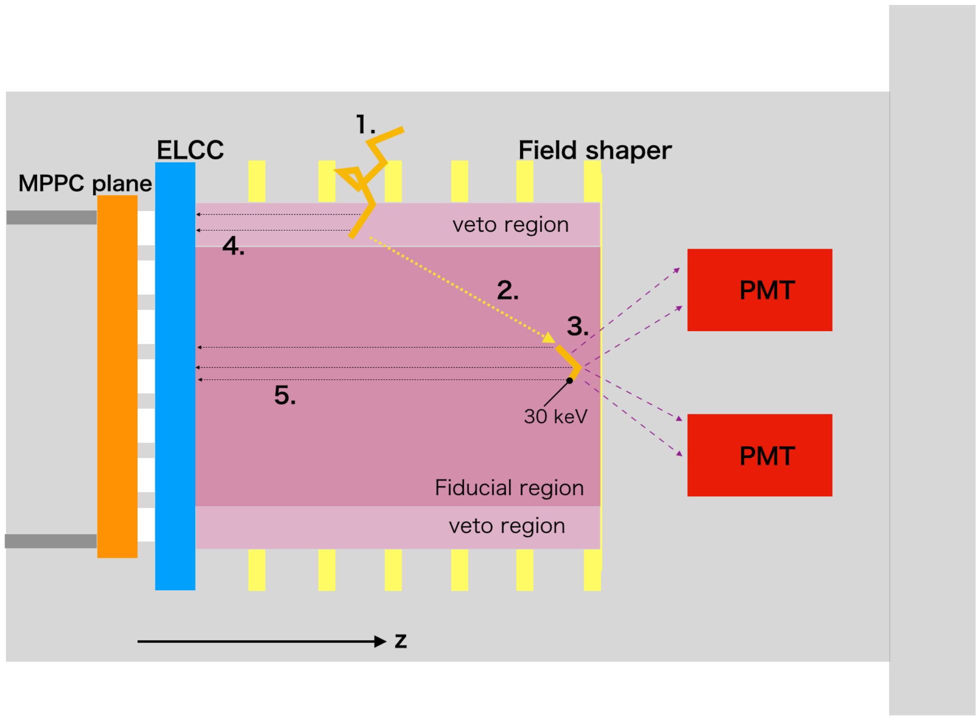

Figure 4.27: Schematic of possible cause of EL-like signal contamination in the scintillation region. Photoelectric absorption occurs in the region covered by veto channels (1.), and a characteristic X-ray is emitted to cathode side of the fiducial region (2.) and interacts there (3.). After that, ionization electrons are drifted to the ELCC in the order of the veto region and the fiducial region then generate EL lights (4. and 5.).

The width of the PMT signal for such EL-like events tends to be large. As shown in Figure 4.28, PMT signals having a width of 30 ADC clocks or more are cut. The peak structure around $z_{\rm avg} = 2$ cm in the 30 keV events disappeared as shown in Figure 4.29 after the cut.

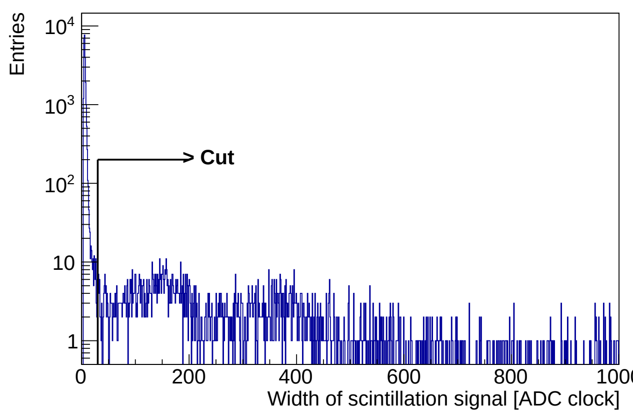

Figure 4.28: Distribution of signal width of scintillation candidates.

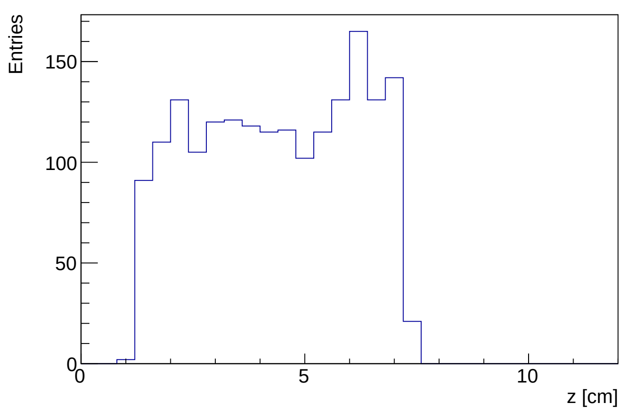

Figure 4.29: Distribution of $z_{\rm avg}$ of 30 keV events (Photon counts : 6500-10000) after the cut of EL-like signals in the scintillation region.

Multi Site Event Cut

Figure 4.30 explains the multi-site cut in the xy plane. A hit cluster is made as a group of neighboring hits. Events with only one cluster are accepted (left in Figure 4.30), and multi-cluster events are excluded (right in Figure 4.30).

Figure 4.31 explains the multi-site cut along the z direction. Events whose waveform sum exceeds a threshold more than once are cut.

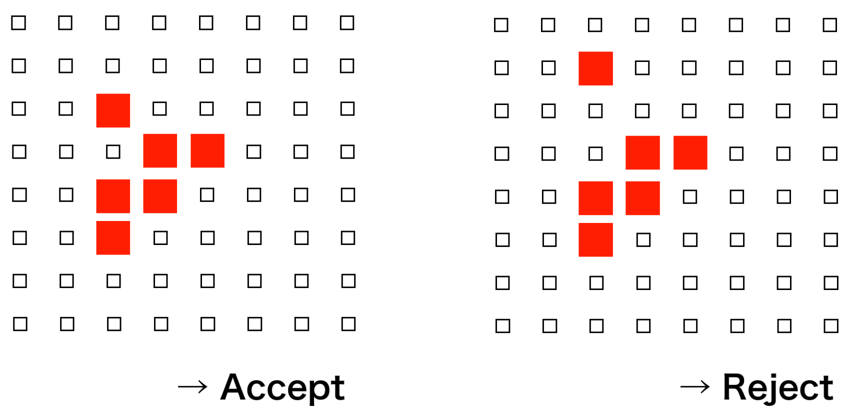

Figure 4.30: Event selection by multi-site cut in the xy plane. Red squares represent the hit channels. Right: all hit channels are adjacent to each other. The event is regarded as a single-site event. Left: the upper left hit channel and the lower cluster are not adjacent and it is regarded as a multi-site event.

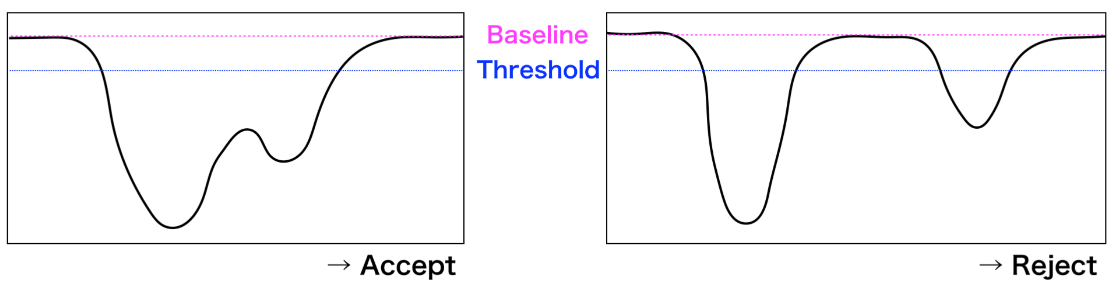

Figure 4.31: Event selection by multi-site cut along the z direction. Right: the sum waveform of the MPPCs exceeds the threshold only once. Left: the sum waveform of the MPPCs exceeds the threshold twice.

4.3.5 Result of Cuts

Figure 4.32 shows the overlaid photon counts spectra for each cut step (whole range in Figure 4.32a and lower range in Figure 4.32b). The number of 30 keV events is reduced by the PMT signal width cut. The multi-site cut reduces events in high energy region. This may be because the probability of Compton scattering increases at higher energy region.

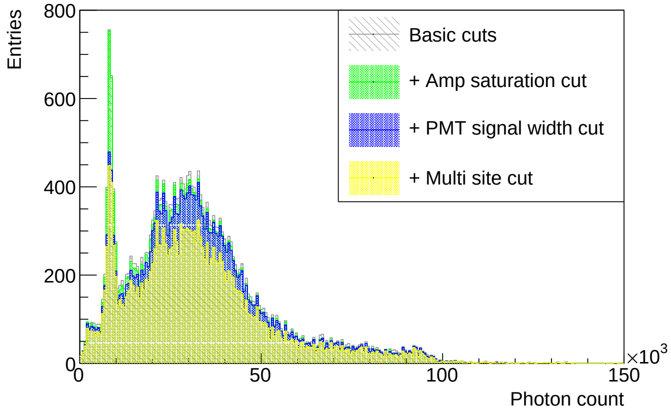

(a) Photon counts for each cut step.

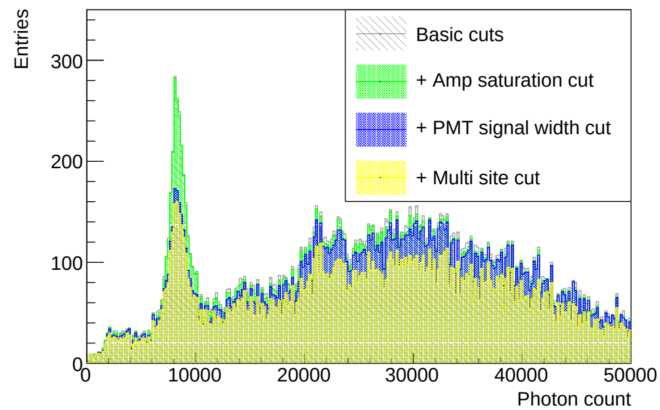

(b) Photon counts for each cut step in lower photon range.

Figure 4.32: Overlaid photon count spectra for each cut

4.3.6 Calibration and Correction

EL Gain Calibration using K_α Peak

The EL gains are calibrated in almost the same way as in Section 4.2.7. In this analysis, to improve the accuracy of calibration, eight channels surrounding the channel in calibration are allowed to have hits instead of four neighboring channels in Section 4.2.7. Data taken with ^{57}Co gamma-ray source just before the ^{133}Ba run are used.

Figure 4.33 shows the map of the relative EL gains (Figure 4.33a) and its projection (Figure 4.33b). The standard deviation is 0.128 and is larger than that in Figure 4.14b, 0.045. This is because the number of permitted channels to have hit surrounding the channel in calibration increased from the case of 4 bar measurement, and the influence of the surrounding channels also increased.

To reduce the effect from surrounding channels, the calibration has to be iterated multiple times. The calibration is repeated five times in this analysis.

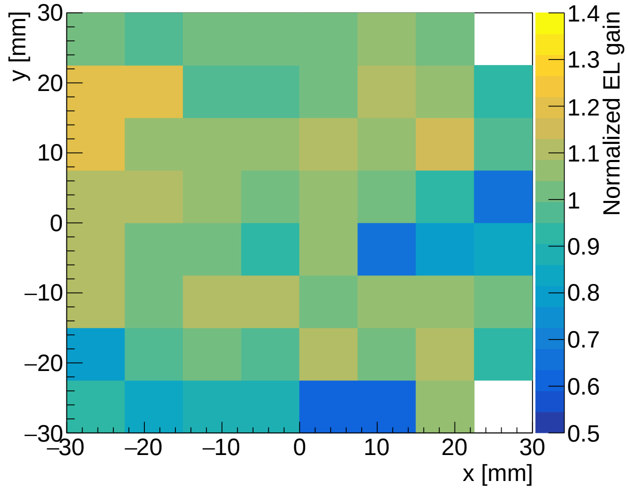

(a) Map.

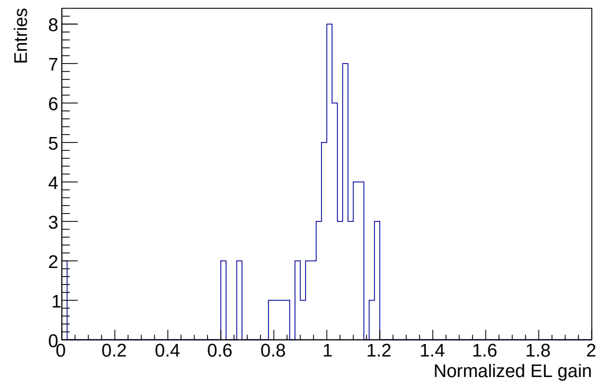

(b) Distribution.

Figure 4.33: Normalized EL gains.

Correction of MPPC non-linearity

To investigate the effect of track density to the detector performance, a parameter “hit volume” is introduced and is defined as

$$\text{hit volume} \equiv \sum_{\text{hit channel}} 7.5^2 \times l_{\text{each hit}}\ [\text{mm}^3], \tag{4.3}$$

where $l_{\text{each hit}}$ [mm] is the length of hit along the z direction of each hit channel. The factor 7.5^2 mm^2 corresponds to the square of the ELCC pitch. Therefore “hit volume” roughly represents the event volume size (Figure 4.34). For a given energy, smaller hit volume means higher density of ionization electrons. Figure 4.35 is a scatter plot of hit volume and photon count. The positive correlation of each peak cluster seen in Figure 4.35 means that the photon count is small when the hit volume is small. We consider that this is caused by the non-linearity of MPPC mentioned in Section 2.3.3. The non-linearity of MPPC is more significant in this measurement as the amount of light increases with higher gas pressure and higher gamma-ray energy.

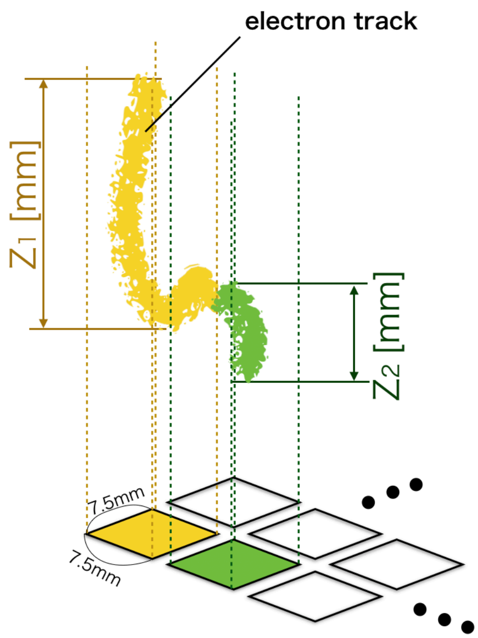

Figure 4.34: Definition of "hit volume". In this case, hit volume is calculated as $7.5^2 \times (z_1 + z_2)$ mm^3.

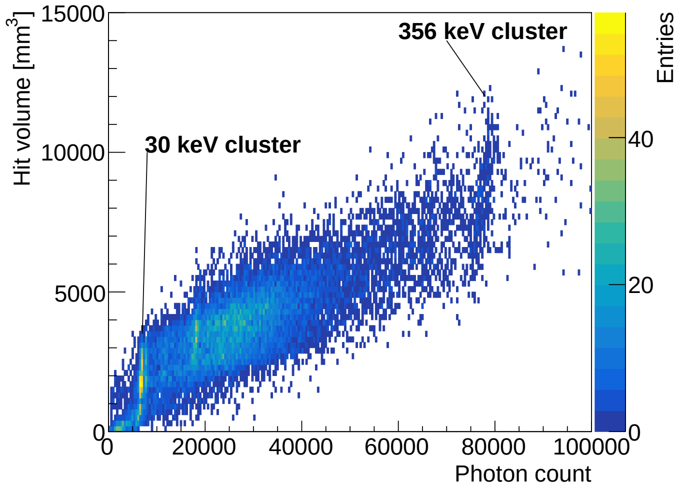

Figure 4.35: Scatter plot of hit volume versus photon count. Positive correlation can be seen.

This inference is supported by the negative correlation observed in the scatter plot of the maximum height of the waveform sum and the photon counts (Figure 4.36). As the maximum height of the waveform increases, the instantaneous maximum light yield increases, then the MPPC signal saturates.

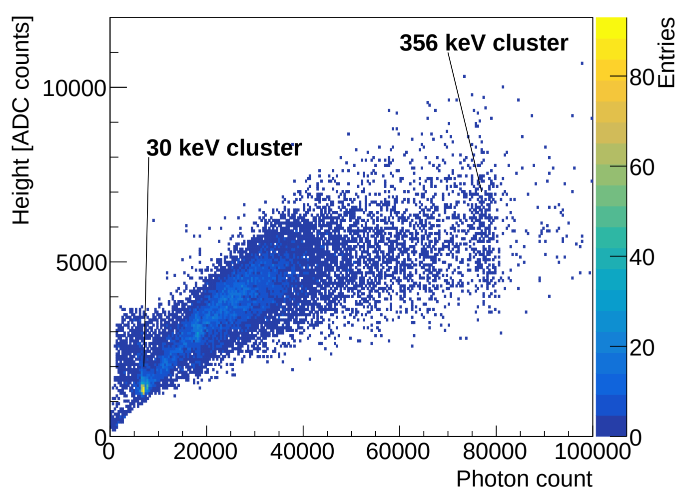

Figure 4.36: Scatter plot of maximum height of sum waveform and photon count. Negative correlation at each gamma-ray peak can be seen.

We measured the response of MPPCs and found that there seem two components in the recovery process. When there are two components, the recovery times, τ_1 and τ_2, are obtained by fitting with the following function:

$$N_{\text{observe}} = \frac{\alpha N_{\text{true}}}{1 + \tau_1/(N_{\text{pixel}} \cdot \Delta t) N_{\text{true}}} + \frac{\beta N_{\text{true}}}{1 + \tau_2/(N_{\text{pixel}} \cdot \Delta t) N_{\text{true}}}, \tag{4.4}$$

where τ_1 and τ_2 satisfy $\tau_1 < \tau_2$ by definition, α and β are fraction of each recovery time component, N_{pixel} is 3,600 pixels as described in section 3.3.3, and the Δt is 240 ns. This is a modified version of Equation (2.20). In principle, sum of α and β should be one, but in this analysis, α and β are treated as free parameters to prioritize the accuracy of the fitting.

Figure 4.37a shows the distribution of τ_1 and τ_2 [69]. Most of MPPCs have recovery time around 80 ns and some have a second component around 500–900 ns. The reason why each recovery time is divided into two clusters is not clearly understood. One possible cause is a systematic error due to a measurement method. The measurement was done with every five MPPCs and they tend to belong to the same cluster depending on the measurement set.

Figure 4.37b shows the distribution of α and β [69]. Since α and β are both free parameters, they are not strictly on the straight line of $\alpha + \beta = 1$, however they are on the line of $\alpha + \beta = 1$ within the errors. The error is estimated by the fitting error, however, it seems to be over estimate because each point is concentrated in a region much smaller than the size of the error bars.

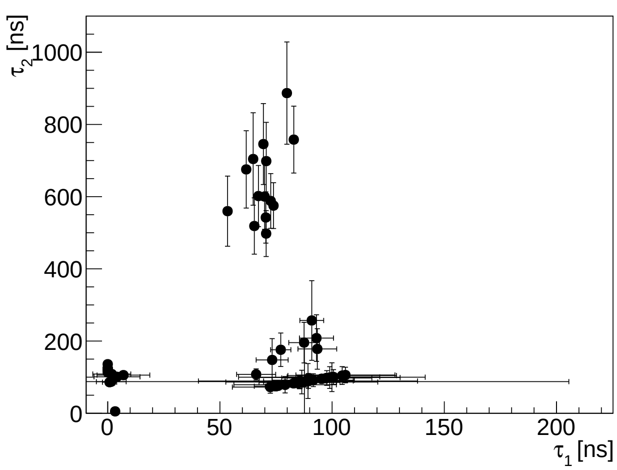

(a) τ_1 versus τ_2.

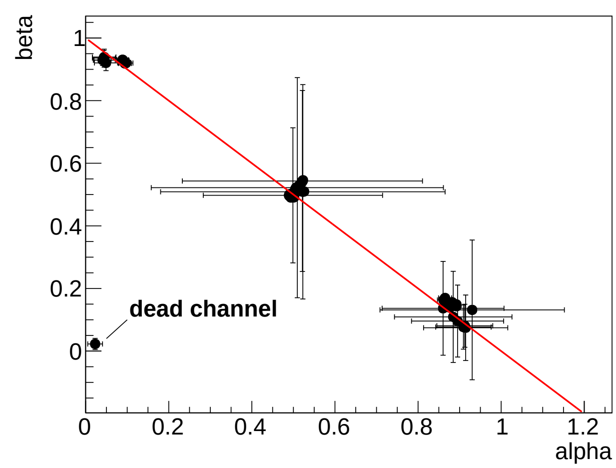

(b) α versus β. Red line represents the line of $\alpha + \beta = 1$.

Figure 4.37: MPPC recovery time [69]

The τ_1 and τ_2 obtained here are substituted into Equation (4.4), and the number of detected photons, N_{observed}, is corrected to the actual incident number of photon, N_{real}.

Dark Current Subtraction

Dark current contribution is subtracted from the EL signal channel by channel.

4.3.7 Result of Correction

Figure 4.38 shows the photon count spectra after the cuts and the corrections. The peaks of characteristic X-ray (K_α : 29.78 keV, K_β : 33.62 keV), full peaks (81.00 keV, 302.85 keV, 356.02 keV), and their escape peaks (47.38 keV, 51.22 keV, 273.07 keV, 326.24 keV) are clearly seen.

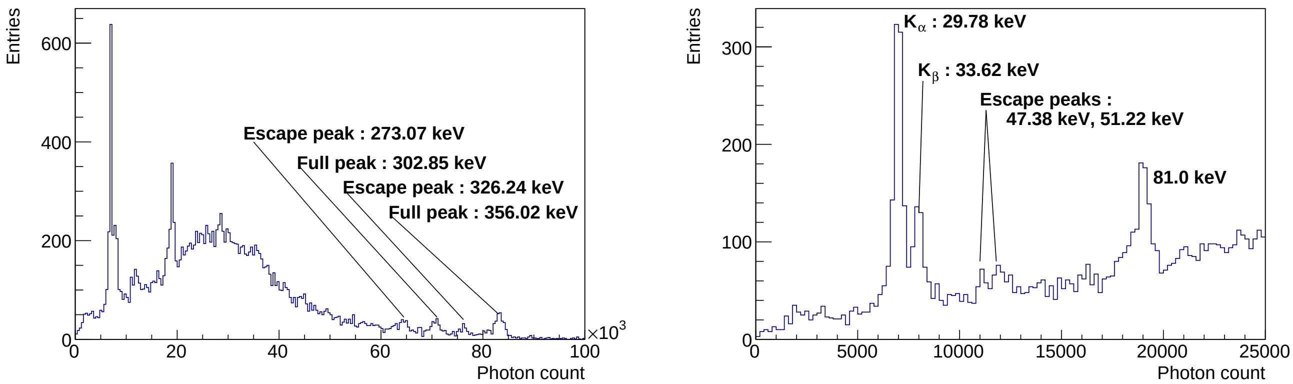

(a) Entire range

(b) Range between 30 keV and 81 keV

Figure 4.38: Distribution of photon count after all cuts and corrections.

4.3.8 Evaluation of the Energy Resolution

The first five peaks (K_α peak, K_β peak, 47.38 keV, 51.22 keV, 81.0 keV) are fitted with "five Gaussians + linear function". The linear term was introduced to model the continuous background contribution. Figure 4.39a shows the fit result. The last four peaks (273.07 keV, 302.85 keV, 326.24 keV, and 356.02 keV) are also evaluated with four Gaussians. The background distribution is fitted with an exponential function instead of a linear function. Figure 4.39b shows the fit result of the last four peaks.

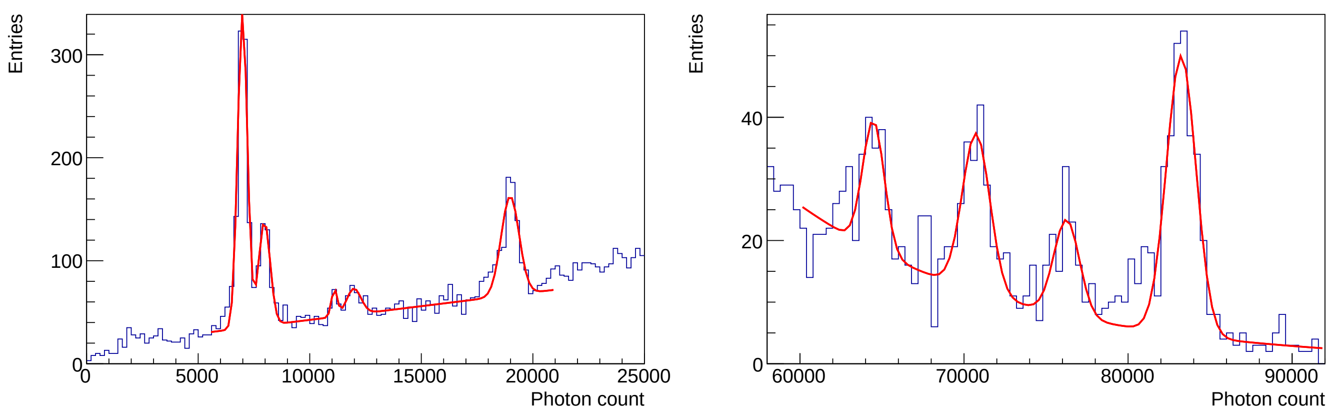

(a) Low photon count range.

(b) High photon count range.

Figure 4.39: Result of fit with Gaussian plus background models.

Table 4.5 is the summary of the position of peak center and the energy resolution obtained by the fitting.

Table 4.5: Energy resolution of each peak. Error is statistical.

Energy	Peak center [photons]	Resolution (FWHM)
29.78 keV	6986.6±9.6	7.25 ± 0.35%
33.62 keV	7967.8±23.3	7.57 ± 0.77%
47.38 keV	11103.3±57.9	2.77 ± 0.74%
51.22 keV	11973.2±86.7	6.31 ± 1.88%
81.00 keV	18979.7±37.0	4.98 ± 0.59%
273.07 keV	64485.2±143.5	2.39 ± 0.54%
302.85 keV	70740.2±117.8	2.78 ± 0.36%
326.24 keV	76256.9±147.0	2.40 ± 0.55%
356.02 keV	83241.9±69.5	2.54 ± 0.20%

Figure 4.40a and Figure 4.40b show the relation between the peak position and energy of gamma-rays and their residuals. The linearity of the detector in this energy region is confirmed.

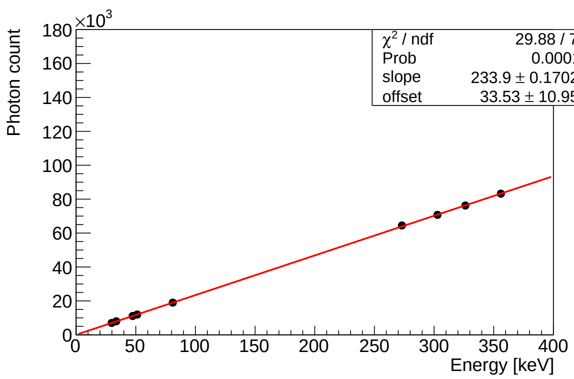

(a) Photon count peak position as a function of gamma-ray energies. Red line represents the fit result with a linear function.

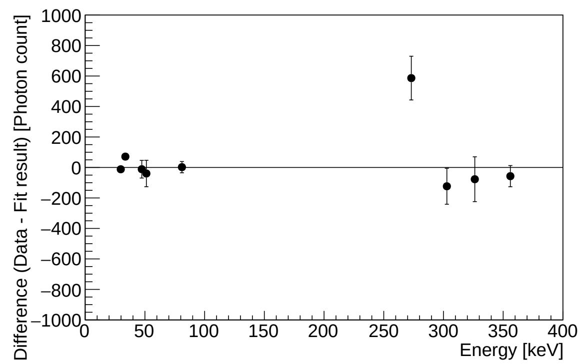

(b) Residual between data and the fit result in Figure 4.40a.

Figure 4.40: Linearity of the detector.

The performance of the detector at 2458 keV is estimated by extrapolating with two kinds of functions as was done in Section 4.2.9. The results are shown in Figure 4.41 and summarized in Table 4.6. The estimated energy resolutions are $0.82 \pm 0.038\%$ with the function $A\sqrt{E}$ and $1.70 \pm 0.084\%$ with the function $A\sqrt{E + B^2}$.

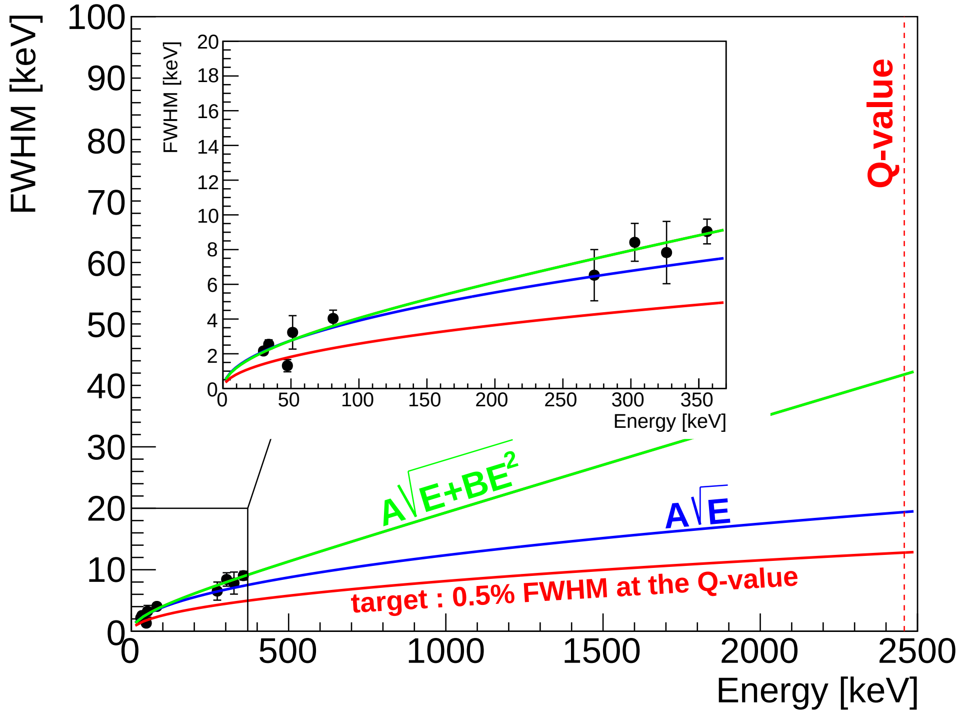

Figure 4.41: Evaluation of energy resolution at Q-value extrapolated by two kind of function : $A\sqrt{E}$ and $A\sqrt{E+BE^2}$, where A and B are fitting parameters.

Table 4.6: Results of evaluation.

Fitting function	A	B	Extrapolated resolution at Q-value (FWHM)
$A\sqrt{E}$	0.405±0.014	–	0.82±0.038%
$A\sqrt{E+BE^2}$	0.376±0.019	0.002±0.0008	1.70±0.084%

4.3.9 Summary of the Measurement at 8 bar and Discussion

In this measurement, as the gas pressure increased from 4 bar to 8 bar and the energy of gamma-rays increased, the EL light yield increased, then, the amplifier output and the MPPC signal began to saturate. Therefore, new cut and correction were introduced for such saturation. The good performance of the ELCC was shown, again. The evaluation at 356 keV was performed and the obtained results are comparable to the measurement at 4 bar, 0.88–1.74% (FWHM) extraplated to the Q-value. The reason why the energy resolution was not improved from the measurement at 4 bar in spite of the increase of photon count may be because of a larger position dependence relative to a cell as described in Section 3.3.

4.4 Evaluation of the Performance with Hexagonal Cell Pattern ELCC

Performance of the ELCC with 13 mm-pitch, 7 mm-hole-diameter, and hexagonal pattern (HP10L Version4) is evaluated at 6 bar. The evaluation was done using the ^{133}Ba gamma-ray source.

4.4.1 Experimental Condition

Table 4.7 summarizes the experimental condition. In this version, the dependence on electric field was studied by applying various electric fields to the EL region. The scanned values of the EL field are 1.5, 1.75, 2.0, 2.25, 2.5, 2.75, and 3.0 kV/cm/bar. The drift field was fixed to 72 V/cm/bar.

In addition to two threshold-level triggers explained in Section 4.3.3, veto signal is generated from the waveform sum of the veto channels in order to collect fully-contained events efficiently.

Table 4.7: Condition for measurement.

Contents			Reference
Detector		HP10L Version 4	Section 3.1.1
ELCC	configuration	hexagonal pattern, 13 mm-pitch	Section 3.3.1
	MPPC	VUV-4	Section 3.3.3
Field shaper	type	Strip field shaper	Section 3.4
	size	ϕ15cm, 10 cm-long	Section 3.4.2
Electric field	Drift region	72 V/cm/bar	Section 3.4.2
	EL region	Various	Section 3.3.2
Voltage for	MPPC	−54.0 V	
photo sensors	PMT	−800 V	
Gas	Pressure	6 bar	
		w/ circulation and purification	Section 3.7
γ-ray source (^{133}Ba)	Activity	4.71×10^5 Bq	

4.4.2 Analysis Overview

The same analysis was performed as was done in Section 4.3. The obtained photon count spectrum after the cuts and corrections showed poor performance. Then, the reason for bad energy resolution was investigated using the K_α peak events. It turned out that the EL gain changes depending on the event position relative to the ELCC cell and it deteriorates the performance. The dependence was reproduced by a simulation and the cause was understood.

4.4.3 Processing of the ELCC signal

The flow of the ELCC signal processing is the same as that in Section 4.3.3. The obtained effective MPPC gain map is shown in Figure 4.42a and Figure 4.42b shows its projection to the 1-D histogram. The mean is 16.7 ADC counts and the standard deviation is 1.6.

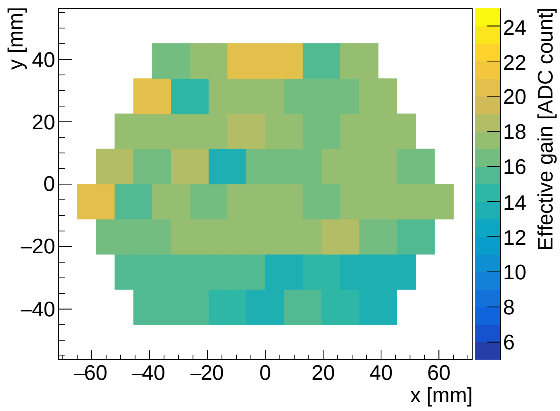

(a) Gain map of each MPPC

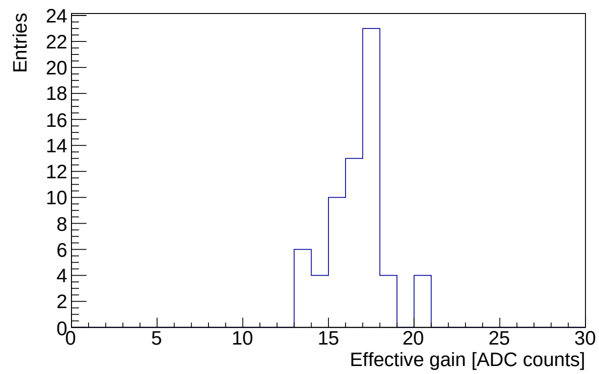

(b) Distribution of effective gain of MPPCs.

Figure 4.42: Effective MPPC gain in unit of ADC count.

4.4.4 Event Selection and Correction

Basic Cut

Basic cut explained in Section 4.3.4 is applied. The configuration of fiducial cut in the xy-plane is shown in Figure 4.43. The central 39 cells are regarded as fiducial channels and their surrounding channels are set to veto channels.

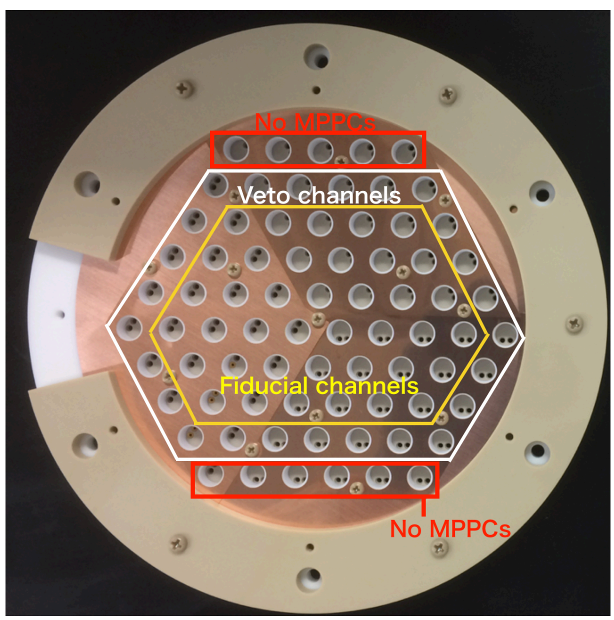

Figure 4.43: Configuration of Cells. The central 39 cells surrounded by yellow lines are regarded as fiducial channels. The outer layer of the fiducial channels is set to veto channels. The cells at the top and bottom lines have no MPPCs. In this picture, MPPCs are not installed in any channels.

The cut criteria along the z-direction are set to 2 cm for the signal edge of the anode side and 8.5 cm for the signal edge of the cathode side.

EL gain Calibration using K_α Peak

EL gains are calibrated in the same way as in Section 4.2.7. Six channels surrounding the channel in calibration are permitted to have hits. The EL gains are determined for each anode voltage setting.

Correction of MPPC non-linearity

Non-linearity of MPPC signal is corrected in the same way as in Section 4.3.6.

Figure 4.44a shows the scatter plot of τ_1 and τ_2 [69]. The values of τ_1 mainly distribute around 50–60 ns and τ_2 around 120–300 ns. In this time, the recovery times are not divided into multi-cluster thanks to an improvement of the measurement method, for example, more speedy measurement. Although an outlier exists at $(\tau_1, \tau_2) = (38.23, 175.61)$, other characteristics such as MPPC gain of that channel are normal, thus that channel is also included in the analysis. Figure 4.44b shows the scatter plot of α and β [69]. The red line represents $\alpha + \beta = 1$. All points are on the line within the errors. These values are used in the MPPC saturation correction for all data set of each EL field.

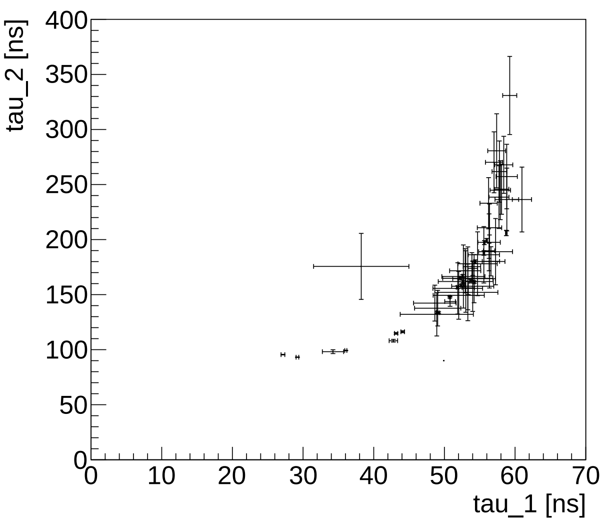

(a) τ_1 versus τ_2

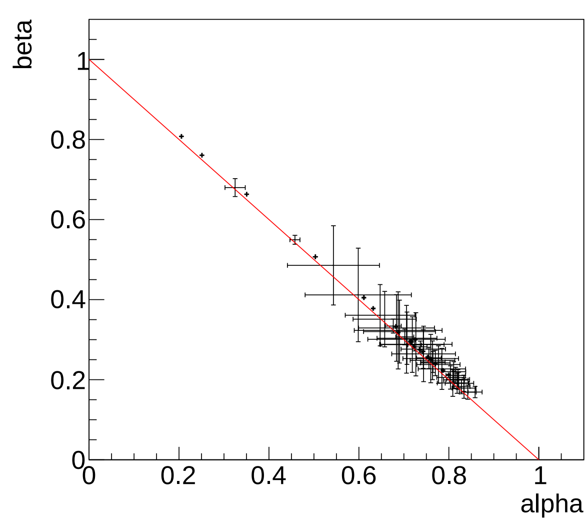

(b) α versus β. Red line represents the line of $\alpha + \beta = 1$.

Figure 4.44: MPPC recovery time [69]

4.4.5 Result of Cuts and Corrections

Figure 4.45 shows the photon count spectrum after all cuts and corrections for the EL field of 3.0 kV/cm/bar. The peaks around 350 keV (at ∼150,000 photons) are not as sharp as Figure 4.38a. Therefore, the energy resolution was not evaluated this time, and instead, the reason why the resolution is worse is discussed hereafter.

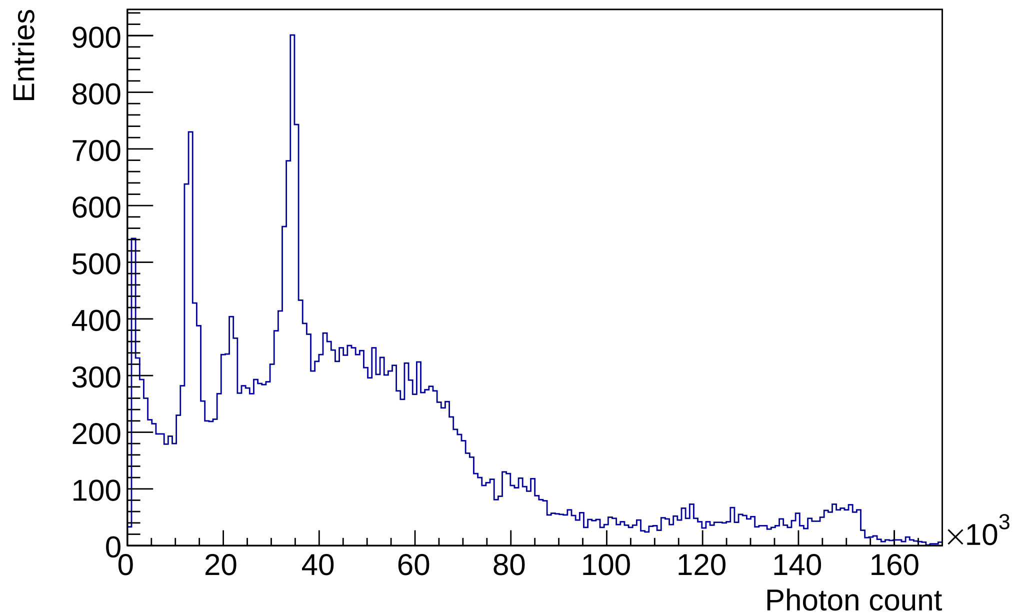

Figure 4.45: Distribution of photon count after all cuts and corrections.

4.4.6 Position Dependence

We found that the EL light yield is different depending on the position relative to the cell. This positional dependence is caused by differences in the length of the path of the drift electrons passing through the region exceeding the EL threshold, the electric field strength thereof, and the solid angle to the MPPC. It could deteriorate the energy resolution. Figure 4.46 shows the distribution of "max-fraction" for 30 keV events. The "max-fraction" is the fraction of photons detected by the channel having the maximum photon count to the total photon count. According to Section 2.1.1, the CSDA range of a 30 keV electron in 6 bar xenon is 0.225 cm. Therefore 30 keV events can be regarded as point-like compared to the cell size. When the ionization electrons reach just above the center of a cell, most of electrons are pulled into that cell and the max-fraction tends to be 1. On the other hand, if initial electrons reach between cells, they are divided and pulled into two or more cells. Thus the max-fraction is small (see Figure 4.47). Therefore, the max-fraction can be used to guess the event position relative to the cell.

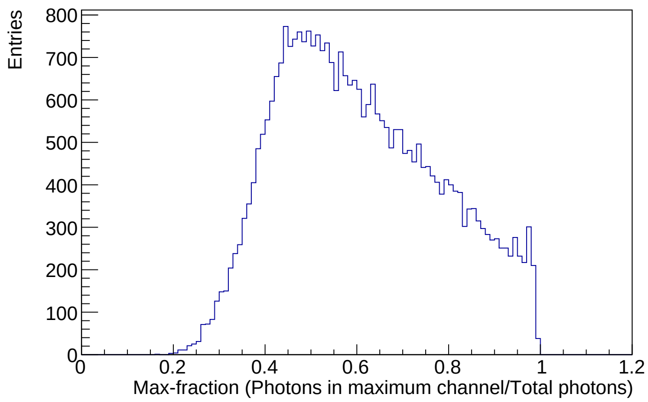

Figure 4.46: Distribution of the max-fraction.

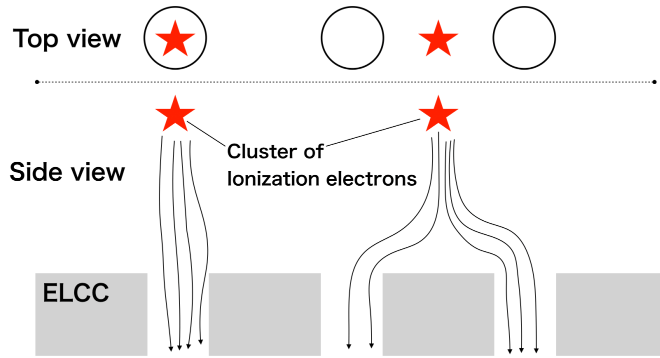

Figure 4.47: Schematic drawing of drifts of the ionization electrons into cells. Left: ionization electrons reach just above the center of a cell and collected into that cell therefore the max-fraction tends to be 1. Right: electrons are divided and collected into more than two cells, thus the max-fraction is small.

Figure 4.48 shows the photon count spectra for various values of the max-fraction. The 30 keV peak position moves to higher photon count at the max-fraction between 0.8 and 1.0, that is, when the event position is close to the center of cells. The K_α peak center for each max-fraction is shown in Figure 4.49. The change is estimated to be 5.14±0.85%.

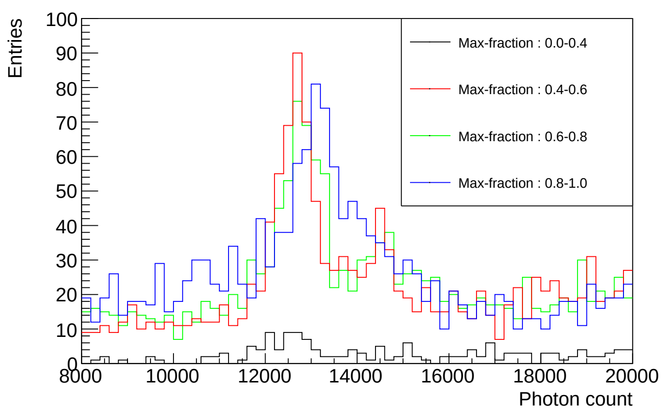

Figure 4.48: Distribution of photon count for each max-fraction.

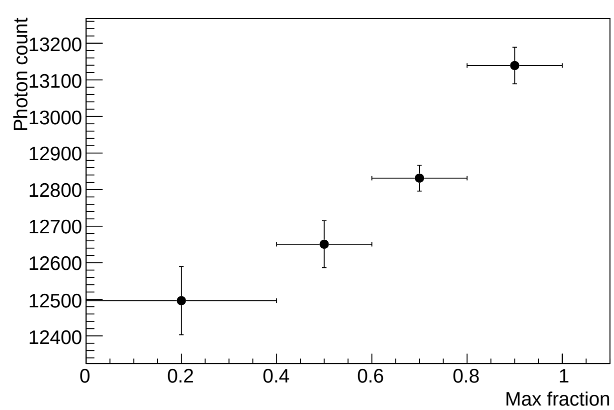

Figure 4.49: Plot of the center of K_α peak for each max-fraction.

4.4.7 Comparison to Simulation

For more understanding, comparison to simulations was performed.

Net EL Gain

The net EL gain of the data is calculated by dividing the photon count at the K_α peak by the number of ionization electrons initially generated. The initial number of electrons is calculated by dividing 29.78 keV (K_α) by the W-value of xenon ionization, 22.1 eV [70]. The net EL gain in the simulation is calculated by the method described in Section 3.3.2 as the number of photons detected by an MPPC when one ionization electron is generated. Figure 4.50 shows the net EL gain as a function of the EL electric field strength for the data and the simulation. The data are well reproduced without tuning. Therefore, it can be said that whole detection processes such as the collection of drift electrons, the EL light emitting, and the transition and reflection of the generated EL lights are well understood.

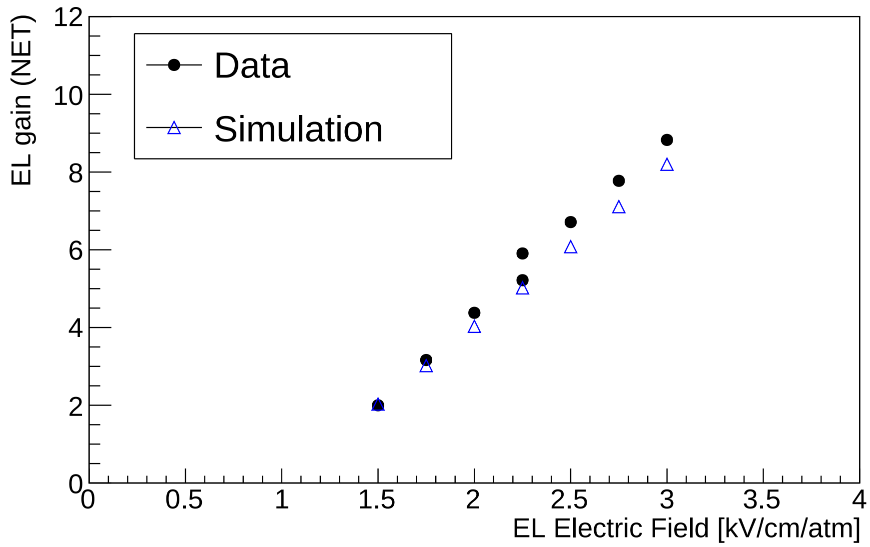

Figure 4.50: Net EL gain as a function of EL electric field strength. The error bars at the data points are statistical and cannot be seen because they are too small. Error bars are not considered at the simulation points.

Energy Resolution at K_α peak

The energy resolution at the K_α peak was estimated by simulation taking into account the position dependence of the EL gain obtained in the simulation in Section 3.3.2. Characteristic X-rays are generated by Geant4 and converted into ionization electrons through photoelectric absorption process. The ionization electrons are drifted to the position at $z = 2$ cm according to the diffusion coefficient in Section 2.3.4. After drifting to the position of $z = 2$ cm, the ionization electrons are converted to the photon count detected by an MPPC taking into account the gain map obtained in the simulation in Section 3.3.2. By repeating the process for all electrons, the total photon count is calculated. The energy resolution is evaluated by fitting the obtained peak with a Gaussian. The energy resolutions of the data were also evaluated by fitting the K_α peak with a Gaussian.

The EL field (E_{EL}) dependence of the energy resolution in the data and the simulation is shown in Figure 4.51. The error of data is the statistic error from fitting. It is possible that the simulation points have large error due to the uncertainty of input parameters to the simulation such as the PDE of the MPPC and the reflectance of PTFE. However, they were not considered here. The data and simulation are in agreement in their tendency. The target value of the resolution, 4.52%, which corresponds to 0.5% at the ^{136}Xe $0\nu\beta\beta$ decay Q-value converted by $1/\sqrt{E}$, is also shown in the same figure. It turned out that the configuration of ELCC with 13 mm pitch hexagonal pattern does not satisfy our requirement. The components to worsen the energy resolution in the simulation are the fluctuation of the number of ionization electrons, electrons which are not collected in cells, and the position dependency. Since the effect of the former two components are very small, it can be said that the main cause of deteriorating the energy resolution is the position dependency.

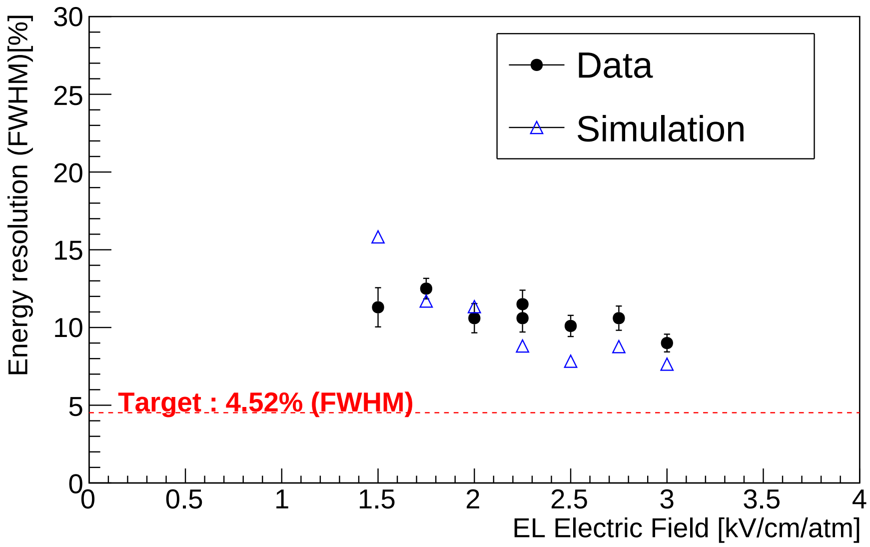

Figure 4.51: Energy resolution at K_{α} peak as a function of EL field.

4.5 Summary and Discussion

The performance of the 10 L prototype detector was evaluated. The constructed 10 L prototype was operated and clear peak structures by gamma-rays were obtained in the photon count spectrum. With the configuration of the 7.5 mm-pitch square pattern cells, the energy resolution was measured at 4 bar with ^{57}Co source and 0.88–1.74% at the ^{136}Xe $0\nu\beta\beta$ decay Q-value was estimated. The principle of the ELCC was verified. Evaluation using ^{133}Ba gamma-ray source at 8 bar shows an energy resolution of $2.54 \pm 0.2\%$ at the energy of 356 keV. The estimated energy resolution at the Q-value is between 0.82% and 1.70%. In addition, the cell configuration was changed to the 13 mm pitch hexagonal pattern in preparing for future larger scale detectors, and the evaluation was performed. It was found that with this cell configuration, the position dependence of the EL gain is problem, and the energy resolution is worse than the previous cell patterns. Detailed simulation method was developed to understand the behavior of the ELCC and the results of the simulation was compared to the obtained data. The simulations and data were in good agreement, therefore the behaivior of the ELCC is now well understood.

These results are important for verifying the principle of ELCC with high pressure xenon gas. However, obtained energy resolutions does not reach the target value, 0.5% FWHM at the ^{136}Xe $0\nu\beta\beta$ decay Q-value. The reason is considered that the designs of ELCC were inappropriate. Collection efficiency of ionization electrons is not 100% for the ELCC with 7.5 mm pitch, 4.0 mm diameter, and square pattern and this may deteriorate the energy resolution. In the case of the 13 mm pitch hexagonal pattern, the collection efficiency is sufficiently high, however, the dependence of EL gain on the initial electron position was found to be too large to achieve the target energy resolution by a detailed simulation. It is necessary to conduct a detailed simulation and determine the optimal ELCC configuration that can have sufficient performance. This was performed for the next larger prototype described in Chapters 5 and 6.

Chapter 5

Design and Construction of a 180 L Size Prototype

5.1 Overview

A larger size prototype is being developed for evaluation of the detector performance at around the ^{136}Xe $0\nu\beta\beta$ decay Q-value, 2458 keV. Establishing the technique to build a large detector is another important purpose of the prototype. The pressure vessel has 180 L volume (Section 5.2), thus, we call the prototype "HP180L" (high pressure 180 L) or "180 L prototype". The ELCC of HP180L is made by assembling units, thus it can be extended easily by adding the units (Section 5.3). A front-end electronics board (FEB) called AxFEB (AXEL Front-end Electronics Board) has been developed to readout the ELCC signal. It has a wide dynamic range from a few photons/μs to $\sim 10^4$ photons/μs and 56 channels in one board (Section 5.4.1). In order to handle larger number of channels, flexible printed circuit (FPC) cables are used for signal transmission and bias voltage supply (Section 5.4.2). The 180 L prototype was also built at Kyoto University.

The design of the full version of the 180 L prototype is described in Section 5.1.1. In the first phase of HP180L, we have constructed a small size TPC whose sensitive volume is 15 cm in diameter and 10 cm in length, and the number of readout channels is 168. From Section 5.2 components of the first phase of the 180 L prototype are explained.

5.1.1 Design of the Full Version of HP180L

Figure 5.1 shows the 3D CAD model of the full version of HP180L. The sensitive volume of the 180 L prototype will be 486 mm in diameter and 500 mm in length. The field shaper is made of aluminium ring electrodes. The aluminium reflects scintillation light of xenon and increases the number of incident photons to PMTs behind the cathode. The voltage required at the cathode electrode is 48.8 kV with the EL electric field of 3.0 kV/cm/bar and the drift electric field of 100 V/cm/bar at 8 bar. To avoid discharges at the feedthrough, AC voltage with 1.5 kVpp and 5 kHz will be introduced into the pressure vessel through the feedthrough, and it is boosted by a Cockcroft-Walton circuit inside the pressure vessel to generate about 50 kV DC. The maximum number of readout channels is 1512 with 27 units of ELCC. The ELCC is designed as hexagonal pattern with 10 mm pitch based on the optimization as will be described in Section 5.3.1, thus, the sensitive area is 982.07 cm^2. The number of outermost channels is 138 and they are treated as veto channels. Therefore, the area of fiducial region in the ELCC plane is 892.44 cm^2. Seven PMTs will be installed at the opposite side of the ELCC plane.

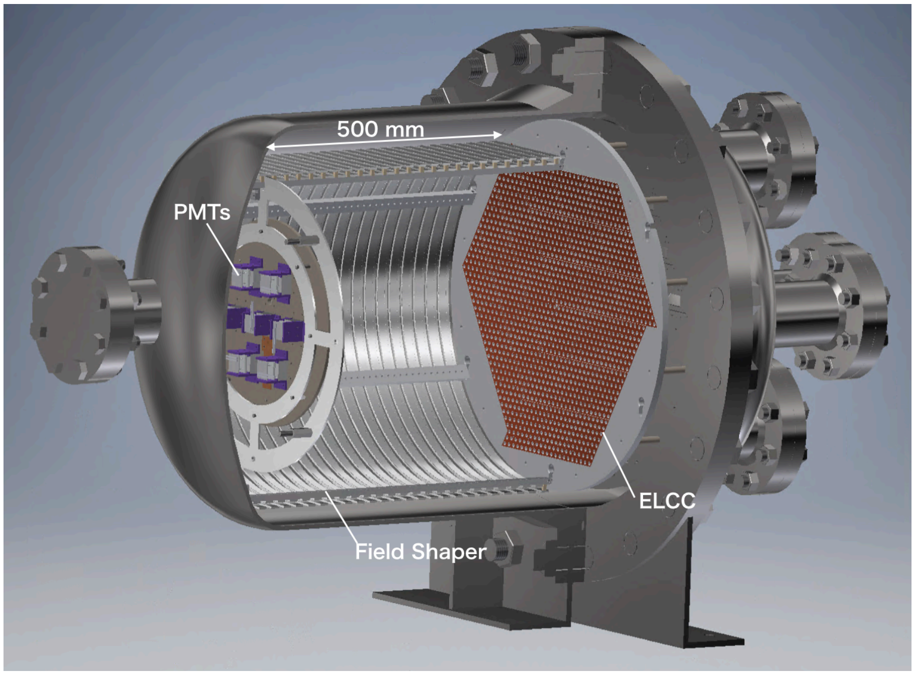

Figure 5.1: CAD model image of the full version of HP180L.

5.2 Pressure Vessel

Figure 5.2 shows the pressure vessel of the 180 L prototype. It is made of stainless steel (SUS304L). The cylindrical part is based on the JIS 550A-sch10 standard and both ends consist of head plates. The vessel can withstand up to 10 bar of gas pressure. The outer diameter is 559 mm, the inner diameter is 547 mm and the length between both ends of the vessel is 834 mm for a total volume of about 180 L. The pressure vessel is separated into two parts, the lid part and the body part, at the straight part of the cylindrical body and they are coupled by JIS 10K550A flanges. The air tightness is kept by an O-ring made of fluorocarbon rubber. The pressure vessel is mounted on a base made of aluminium frames. The body part can be slid on rails to open and close the vessel.

Four JIS 80A-sch10 ports and one JIS 50A-sch10 port are attached at the end of the lid part (Figure 5.3a) and two JIS 80A-sch10 ports are attached at the opposite end (Figure 5.3a).

Eight M8 nuts are welded to the inner end of the lid part and four M8 nuts to the inner end of the body part to fix detector components.

5.2.1 Feedthrough

Three types of feedthrough were produced with epoxy molding.

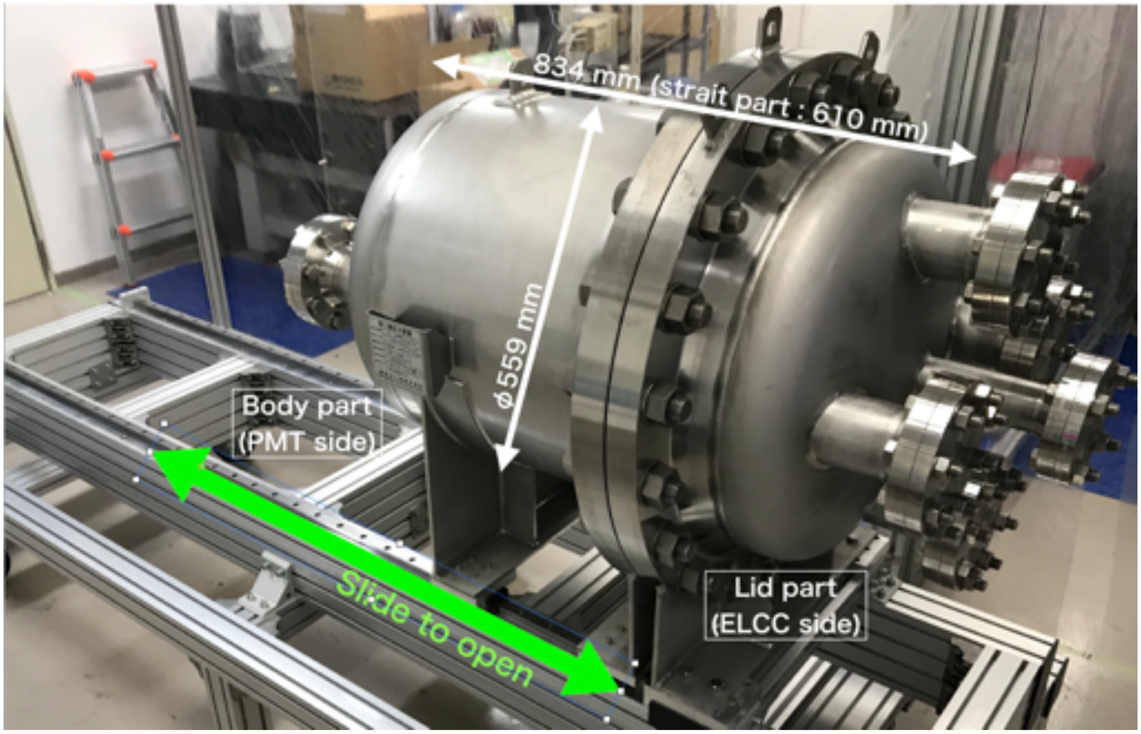

Figure 5.2: Pressure vessel of the 180 L prototype.

Feedthrough for MPPC Signal and Bias

Signal readout and bias voltage supply of each MPPC are done by double-sided FPC-based cables (cable-FPC) explained in Section 5.4.2. Twelve cable-FPCs are passed through a JIS 10K80A standard flange (see Figure 5.4a).

Feedthrough for High Voltage Supply

Three silicon-sleeved cables (SIL12#15F) are passed through a feedthrough on a JIS 10K80A flange to apply high voltages to the anode and cathode electrodes. One Teflon sleeved co-axial cable (RG-188A/U produced by Fujikura inc.) and one Teflon sealed 9-bundles-ribbon-cable (RF28#9) are also passed through the same flange but separate feedthroughs (see Figure 5.4b). The former cable will be used for a Cockcroft-Walton booster for the high voltage to the cathode electrode and the latter is for monitors such as thermometer.

Feedthrough for PMT Signal and High Voltage

Teflon sleeved co-axial cables (RG-188A/U produced by Fujikura inc.) are used to read out the signals from PMTs and apply high voltages to PMTs. Total of 32 cables pass through a feedthrough on a JIS 10K80A flange as shown in Figure 5.4c. Half of them are used as signal lines and the others for HV lines.

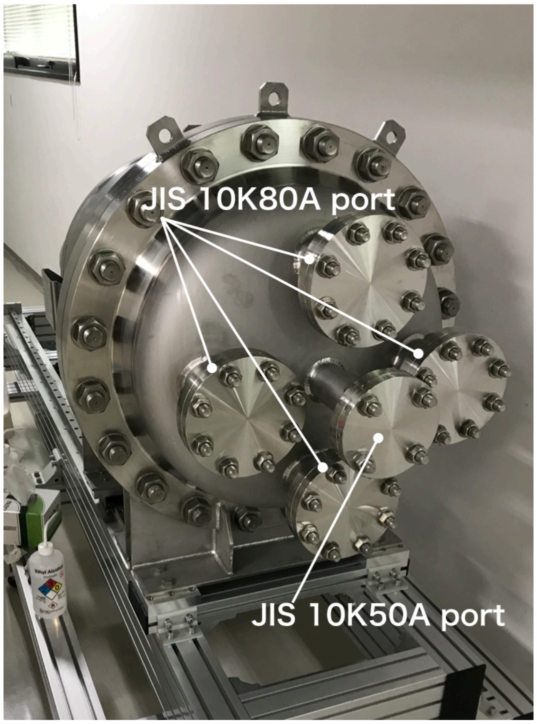

(a) Ports at the ELCC side. Four JIS 80A-sch10 ports and one JIS 50A-sch10 port are attached.

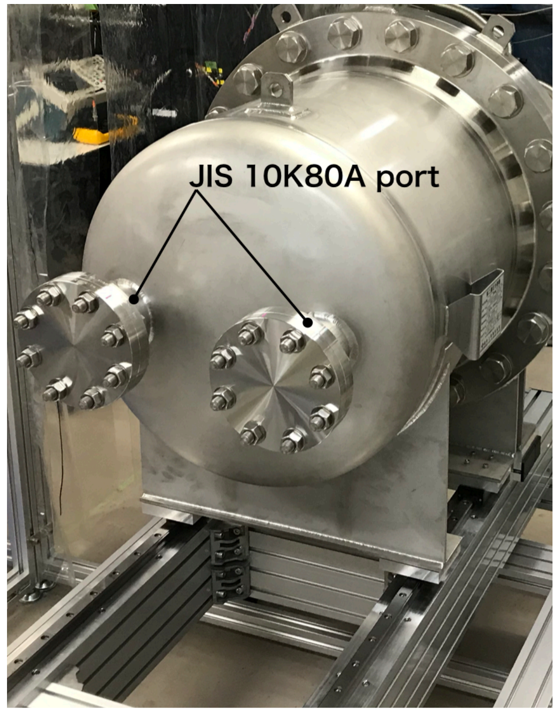

(b) Ports at the PMT side. Two JIS 80A-sch10 ports are attached.

Figure 5.3: Ports attached at the pressure vessel.

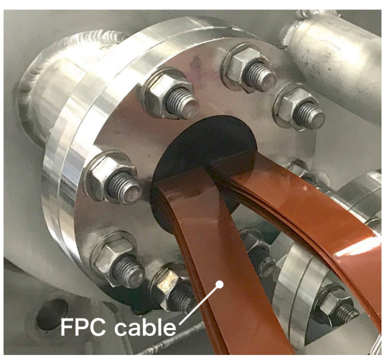

(a) Feedthrough flange for MPPC signal and bias lines.

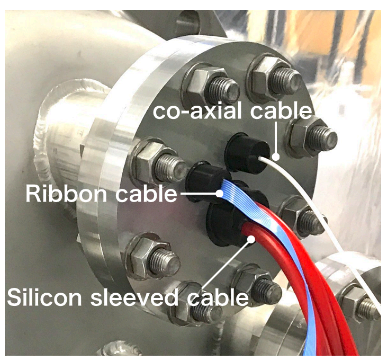

(b) Feedthrough flange for HV supply to the cathode and anode electrodes and other monitors.

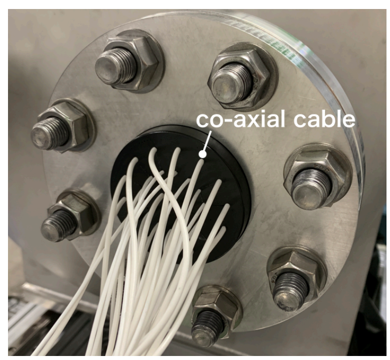

(c) Feedthrough flange for PMT signal and high voltage lines.

Figure 5.4: Feedthrough flanges.

5.3 ELCC

ELCC is redesigned and constructed for the 180 L prototype.

5.3.1 Optimization of ELCC Dimension

The dimension of the ELCC structure is further optimized after the HP10L version. The optimization was done by evaluating the energy resolution of 30 keV peak simulated by Geant4 simulation [47]. The flow of the simulation is the same as that in Section 4.4.7. The electric field strengths are fixed at 3.0 kV/cm/bar for the EL region and 100 V/cm/bar for the drift region and the gas pressure is 8 bar. The hexagonal cell pattern is chosen for the uniform distance to the neighboring cells. The cell pitch and the hole diameter are parameters to be optimized. The depth of the ELCC is fixed at 5 mm. Figure 5.5 shows the estimated energy resolution for 30 keV electrons for various cell dimensions [71]. The vertical axis is "aperture ratio", which is defined as the area of one cell hole divided by the area covered by one channel. In the region where the aperture ratio is less than 0.2, the collection efficiency of ionization electrons into cells is not 100% and the energy resolution deteriorates significantly. For the aperture ratio larger than 0.2, the finer cell pitch and the smaller aperture ratio give better energy resolution. However, too fine pitch increases the number of readout channels and costs a lot. And the region aperture ratio close to 0.2 should be avoided because manufacturing error could affect the performance significantly. For tracking purposes, a pitch of 10 mm is sufficient because the typical diffusion size for 1 m drift is about 12 mm (Figure 2.26b). We adopted 10 mm pitch and 5.5 mm diameter as a condition to satisfy the energy resolution of 4.5% (FWHM), which is our requirement at 30 keV. At this condition, the expected number of detected photons is 1.8×10^4 and contribution from the photon count statistics to the energy resolution is 3.2% (FWHM).

The electric field strength and electric potential are shown in Figure 5.6a and Figure 5.6b, respectively.

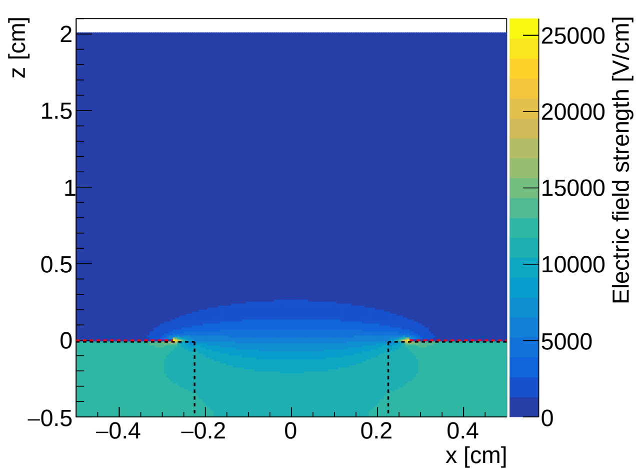

(a) Electric field strength

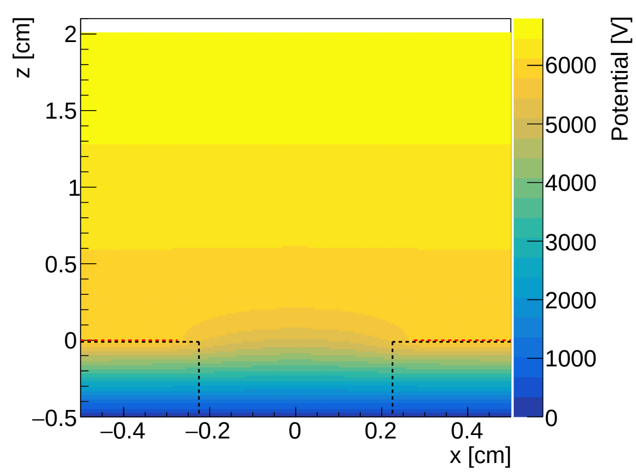

(b) Electric potential

Figure 5.6: Calculated electric field strength and electric potential at 3.0 kV/cm/bar for the EL region and 100 V/cm/bar for the drift region at 4 bar xenon gas.

Figure 5.7a shows the dependence of EL gain on initial position of an electron and Figure 5.7b shows its 1-D projection. The deviation is smaller than that in the case of the 10 L prototype mentioned in Section 3.3.2. In this condition, 9,996 initial electrons out of 10,000 electrons are pulled into ELCC cells; the collection efficiency is 99.96%.

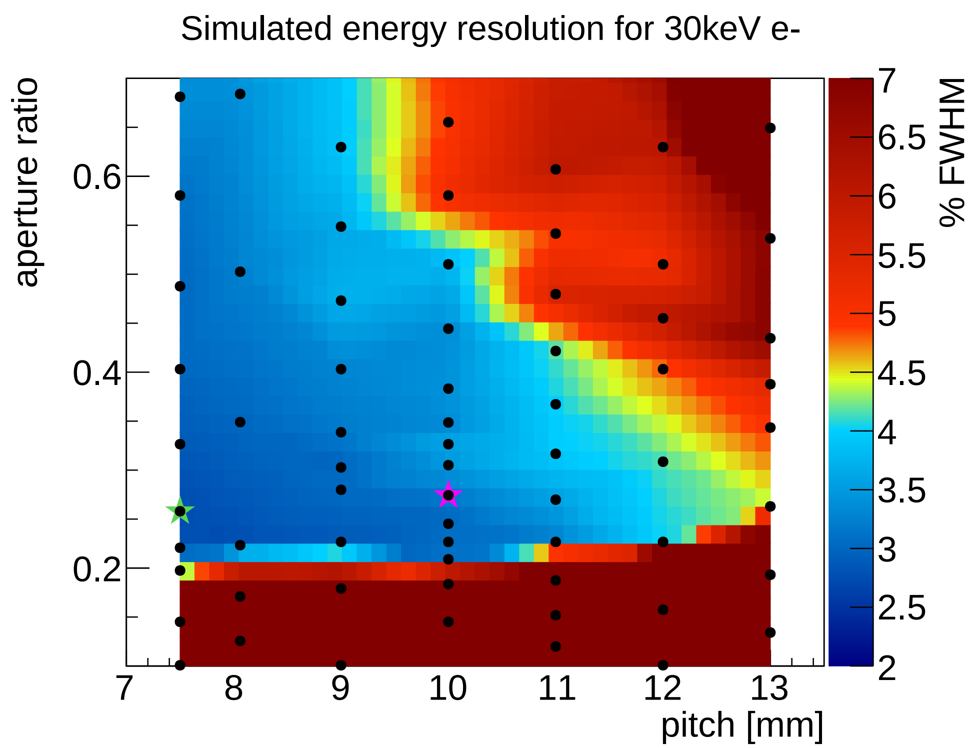

Figure 5.5: Energy resolution for 30 keV electrons for various ELCC configurations estimated by simulation [71]. Black dots represent the simulation points and the color histogram is drawn by interpolating the simulation points. The best condition is found to be 7.5 mm-pitch and 4 mm-diameter, which is shown as the green star. The adopted condition, 10 mm-pitch and 5.5 mm-diameter, is shown as the magenta star.

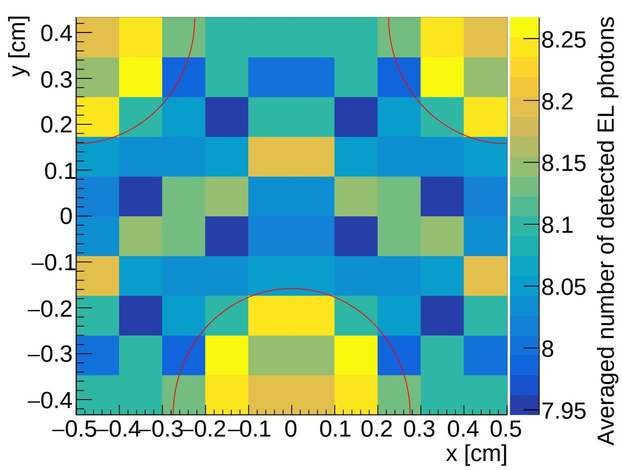

(a) EL gain map for each initial electron position

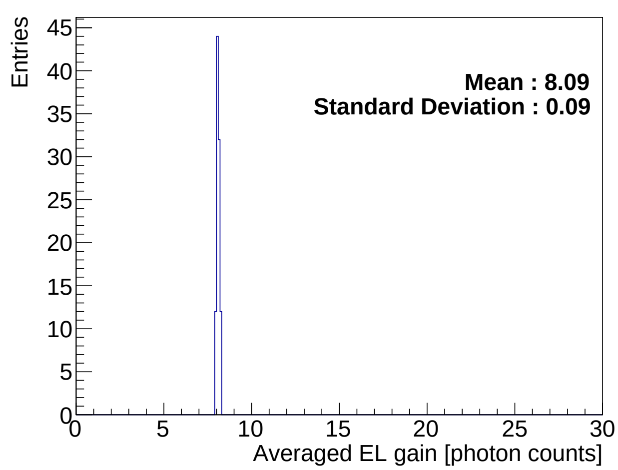

(b) Distribution of EL gain

Figure 5.7: EL gains for various initial position of electrons.

The simulation was also performed for the measurement conditions described in Chapter 6, 4 bar xenon gas, E_{EL} = 3.0 kV/cm/bar, and E_{drift} = 100 V/cm/bar. Figure 5.8 shows the distribution of photon counts obtained by Geant4 [47] simulation considering the position dependence shown in Figure 5.7a. The expected number of detected photons is 10,980 and the energy resolution estimated by fitting the 30 keV peak with Gaussian is 3.46% (FWHM). Although the estimated value of the energy resolution is worse than the estimated value at 8 bar because of the less photon statistics than that at 8 bar, it is better than the target energy resolution at 30=keV, 4.52%.

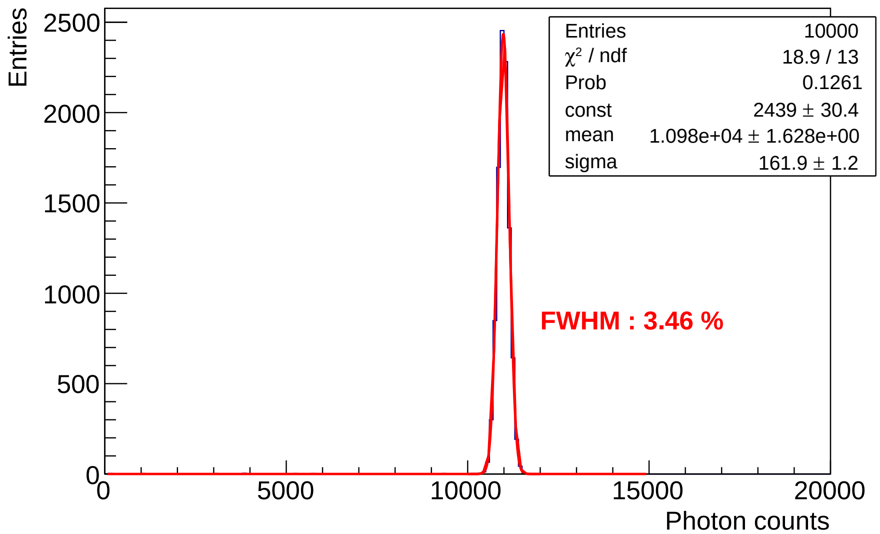

Figure 5.8: Expected distribution of photon counts obtained by simulation and the fitting result with Gaussian with the optimized ELCC at 4 bar.

5.3.2 ELCC Unit

The ELCC for the 180 L prototype is made as the unit style. A 3D CAD model of an ELCC unit is shown in Figure 5.9. A single unit has a trapezoidal shape and 7×8 channels. It consists of a PTFE with cells, a ground mesh electrode, 56 MPPCs, an MPPC base plate made of PEEK, and a flexible printed circuit (FPC) on which MPPC signal and bias lines are printed (see Section 5.3.3). In the first phase of the 180 L prototype, three units are installed, thus, the total number of channels is 168. A single Cu plate covers all units as the anode. The same type of MPPC as the HP10L Version 4, Hamamatsu Photonics K.K., S13370 (VUV-4), is used in the 180 L prototype. As mentioned in Section 5.3.1, the cell pitch is 10 mm, the hole diameter of the anode electrode is 5.5 mm, and the hole diameter of the PTFE body is 4.5 mm, which is 1 mm smaller than that of anode electrode to prevent discharge.

5.3.3 Signal and Bias Voltage Lines by FPC

In order to read out MPPC signals and supply bias voltages, a double-sided FPC called "unit-FPC" is attached to the MPPC base of an ELCC unit. A photograph of a unit-FPC is shown in Figure 5.10. It is connected to the MPPCs electrically via sockets (PD-10, MAC8) and pins (FC-1-4.7, MAC8). A connector (FX11-LA, Hirose electric inc.) is attached at the end of the unit-FPC to connect a cable-FPC described in Section 5.4.2.

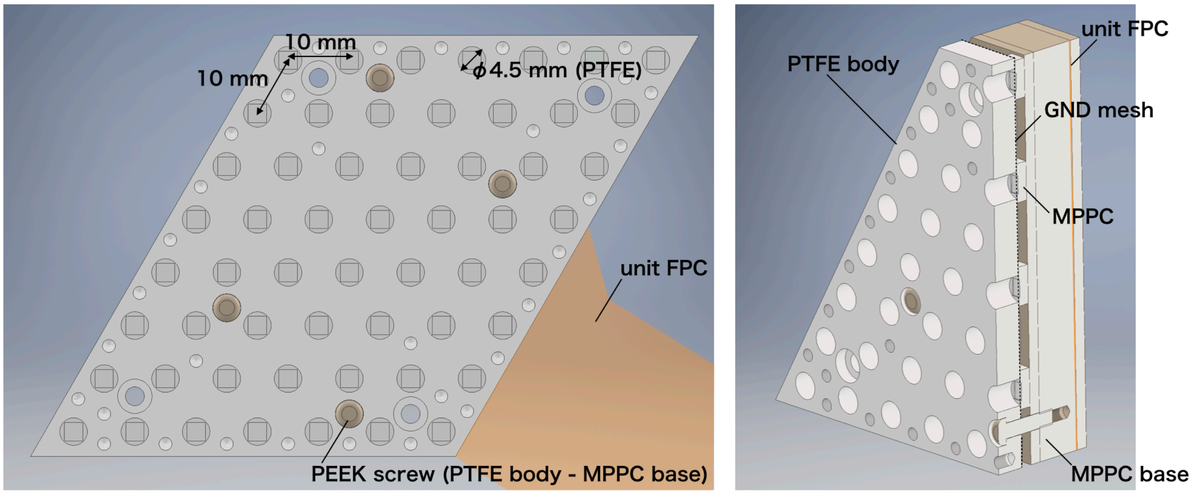

Figure 5.9: 3D CAD model image of an ELCC unit for the 180 L prototype. Front view (left) and cross sectional view (right).

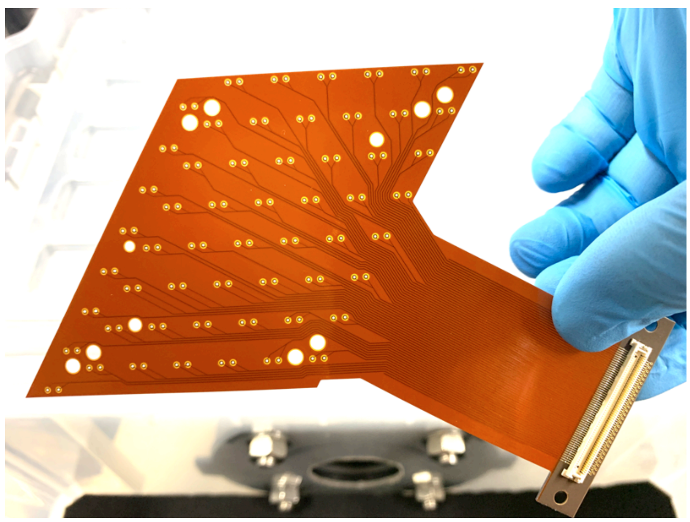

Figure 5.10: Unit-FPC for signal readout and bias voltage application of MPPCs.

5.3.4 Assembling of the ELCC for the 180L Prototype

The procedure of the ELCC assembling is described here. Sockets (WS-1, MAC8) are inserted to a base part made of PEEK (Figure 5.11-①) and a PEEK lid is screwed on to prevent the sockets from coming off (Figure 5.11-②). The lid for sockets has holes that are smaller than the socket head, and larger than the MPPC pin. Thus, MPPCs' pins can pass through the holes and be inserted into the sockets. A unit-FPC is attached to the back side of the base. Electrical connection is done by putting pins (FC-1-4.7, MAC8) to the sockets from the opposite side. A lid is attached on the unit-FPC by PEEK screws in order for the unit-FPC not to fall off (Figure 5.11-③). Figure 5.11-④ shows an assembled MPPC base.

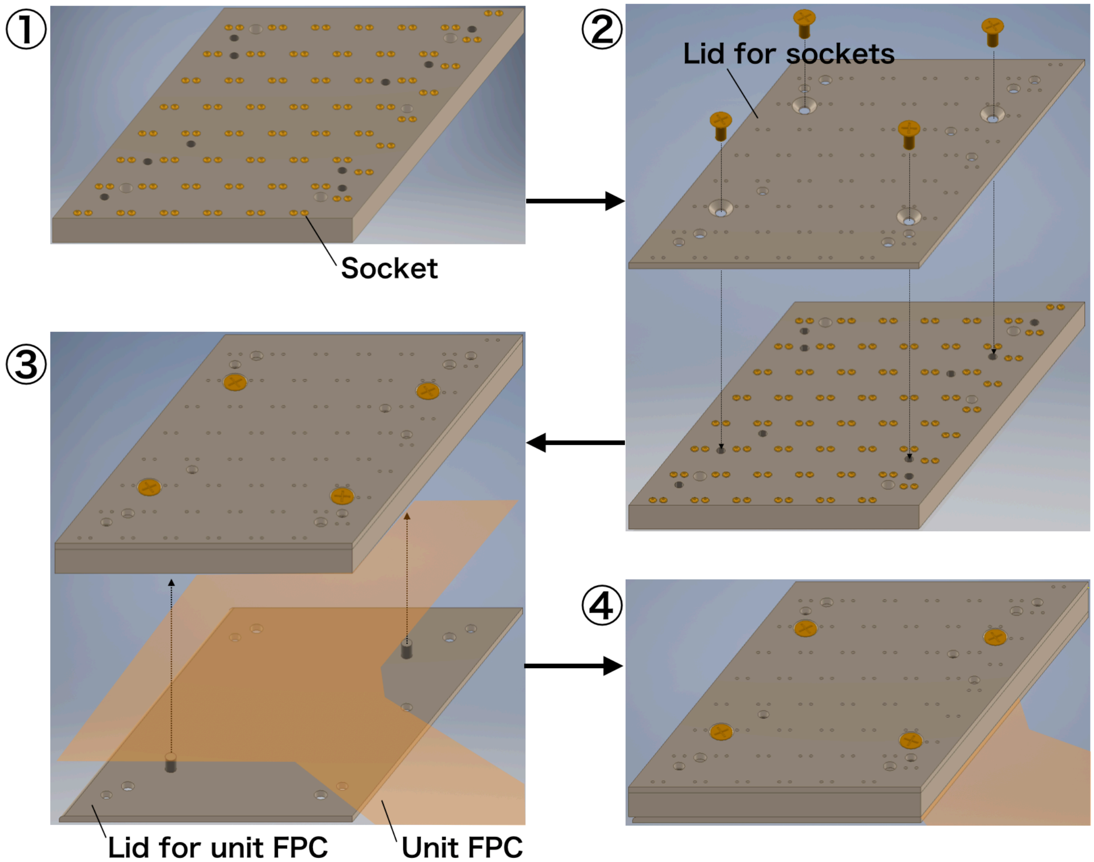

Figure 5.11: Assembling of an MPPC base.

MPPCs are installed on the base as shown in Figure 5.12-⑤. A stainless nail is inserted to the MPPC base to connect the ground mesh electrode to the ground potential electrically. A ground mesh electrode cut to the ELCC unit shape with a margin is sandwiched between a PTFE body and the MPPC base (Figure 5.12-⑥⑦). The edges of the ground mesh are folded on the MPPC base and are fixed with polyimide tapes on the back side of the MPPC base. Figure 5.12-⑧ shows an assembled ELCC unit.

The ELCC unit is attached to the pressure vessel via a conversion ring frame and a two-staged base made of PEEK (Figure 5.13-⑨). The connector of a cable-FPC is fixed to the base frame. After connecting to the cable-FPC, the ELCC unit is fixed to the base frame. Three units are assembled by rotating every 120° as shown in Figure 5.13-⑩. Peripheral plates are mounted around the ELCC units at the same height level as the ELCC surface (Figure 5.13-⑪). On the surface of ELCC units and edge parts, an anode electrode is attached (Figure 5.13-⑫).

Figure 5.14 is a schematic view of the cross section of the ELCC plane. The high voltage to the anode electrode is supplied by a cable via a crimp terminal. The electrodes kept at the ground potential are laid on the base frame, and when the ELCC units are assembled, the stainless nail extending from the GND mesh presses the electrode via a stainless spring to give the ground potential to the GND mesh.

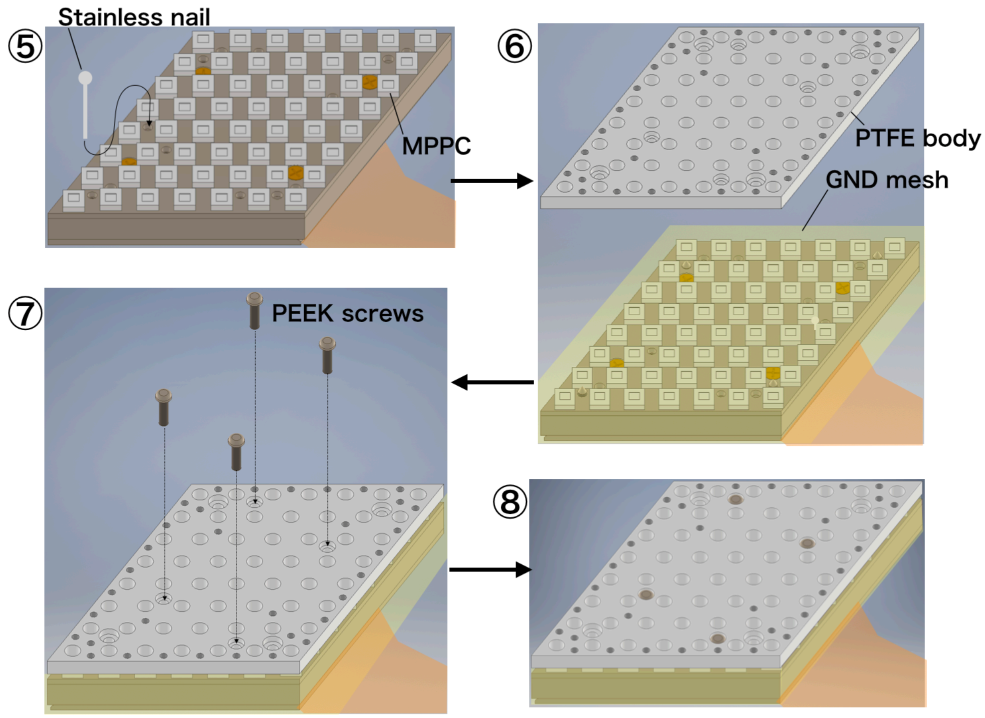

Figure 5.12: Assembling of an ELCC unit.

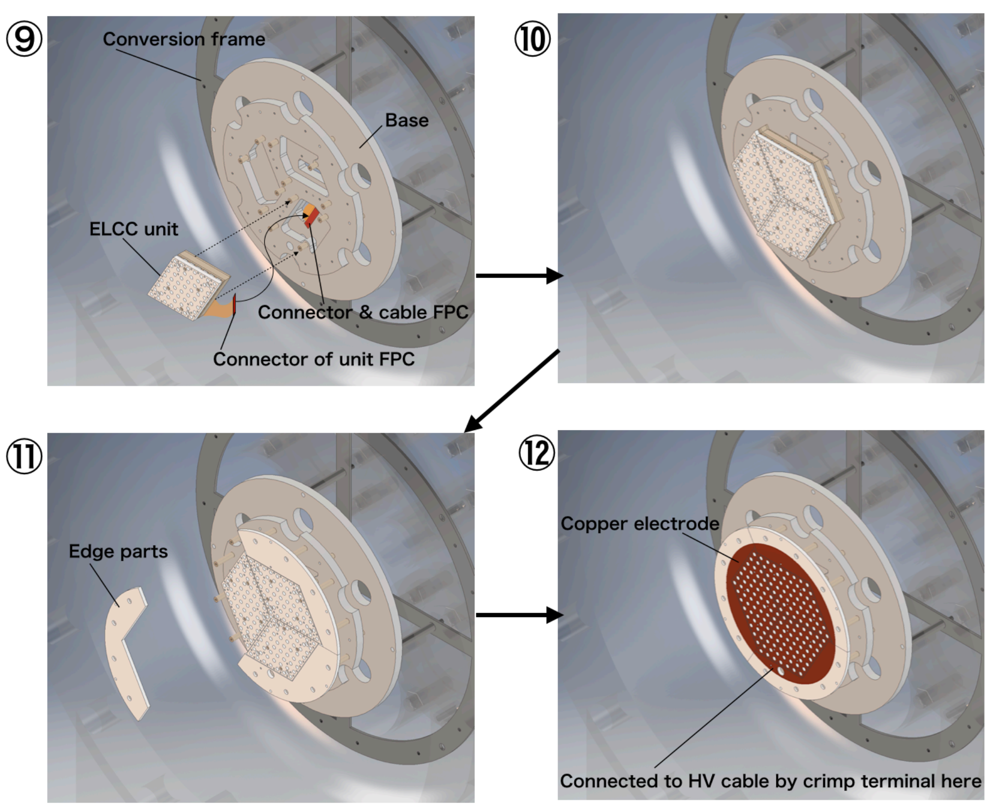

Figure 5.13: Installation of ELCC units to the pressure vessel.

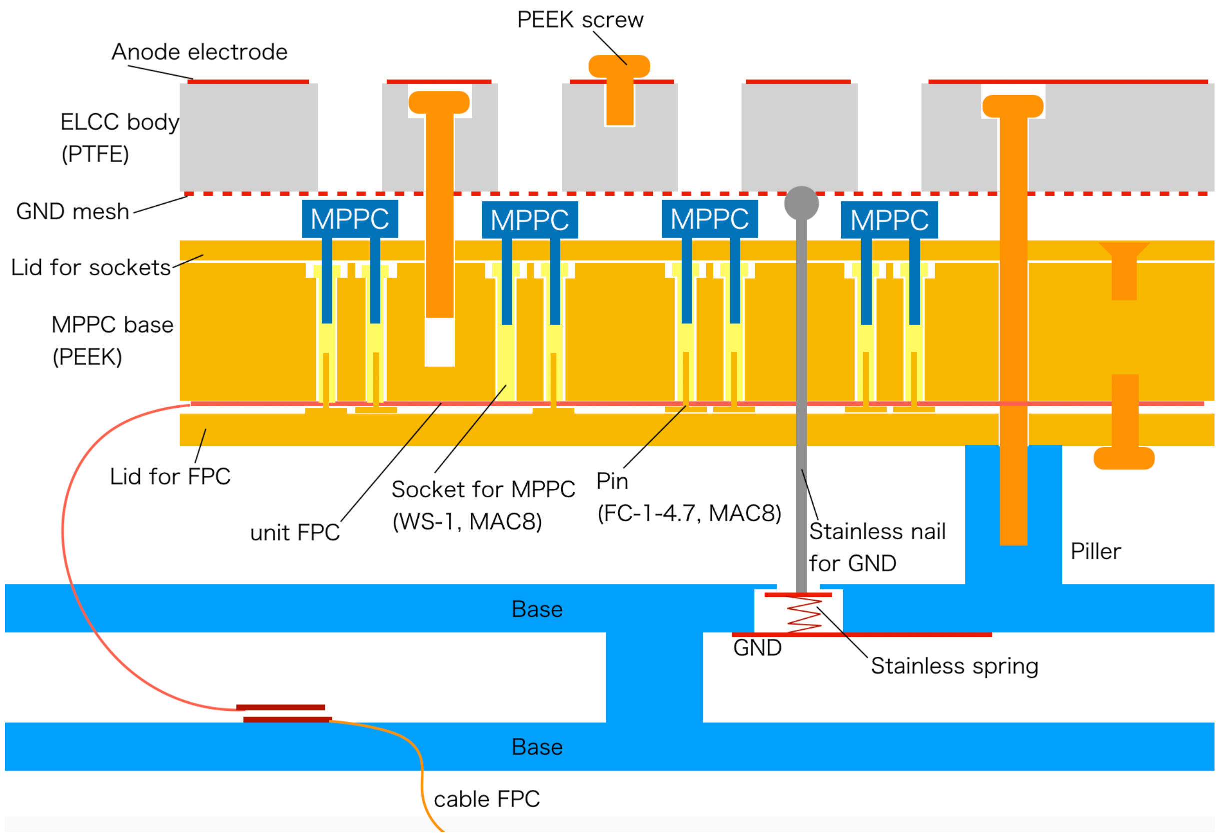

Figure 5.14: Schematic view of the cross section of the ELCC plane.

5.4 Readout of Ionization Signals

5.4.1 Front-End Electronics Board (AxFEB)

We have developed a front-end electronics board (FEB) called "AxFEB" (AXEL FEB). Figure 5.15 is a photograph of AxFEB and Figure 5.16 shows a block diagram of AxFEB. An AxFEB has 56 inputs. It has two types of ADCs with different sampling rate. One is 40 MS/s, 2 V_{pp}, 12 bit ADC with 165 times gain amplifier in front to measure dark current signals (high-gain ADC) and the other is 5 MS/s, 2 V_{pp}, 12 bit ADC with 5 times gain amplifier in front to measure EL signals (low-gain ADC). Every seven channels share one high-gain ADC input via a multiplexer. Power supply for MPPC bias is also implemented on AxFEB. In addition to the common high voltage ($\sim$60 V) power supply for all MPPCs' cathode, digital analog converter (DAC) for finely adjusting the bias voltage of individual MPPC is connected to each MPPC's anode. The offset by this adjustment is cancelled in the succeeding amplifiers. The controls of AxFEB such as high voltage application, data processing, and communication with other modules are done by a field-programmable gate array (FPGA) on the board. Data are send to a PC via Ethernet by SiTCP on the FPGA [72]. More details and performance evaluation of the AxFEB are described in [73].

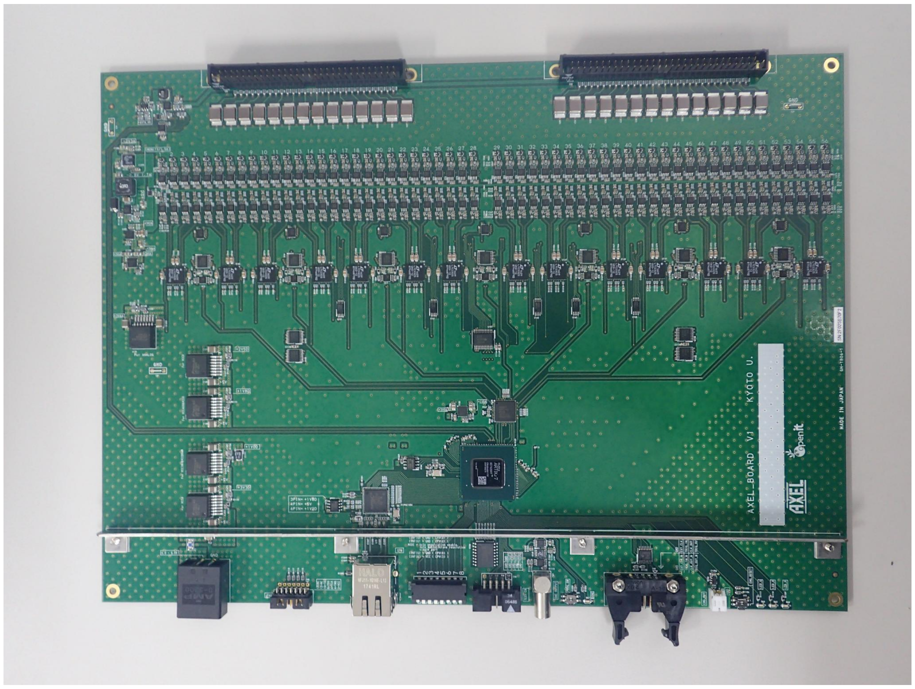

Figure 5.15: AxFEB.

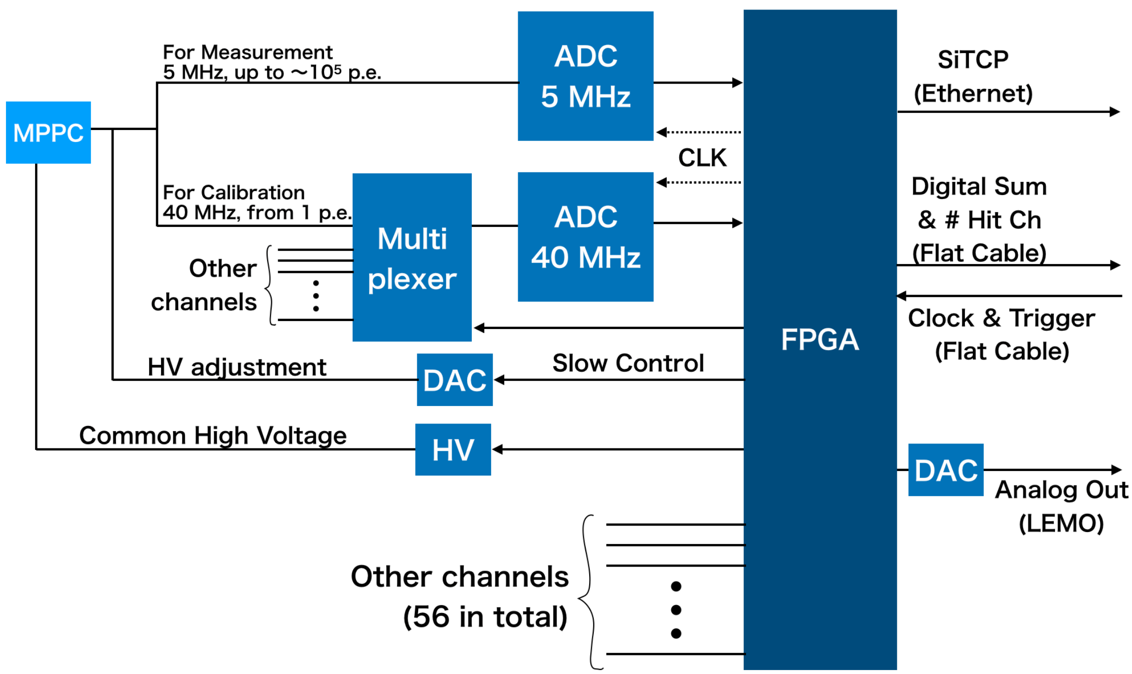

Figure 5.16: Block diagram of AxFEB.

Each AxFEB is connected to an ELCC unit, thus, three AxFEBs are used in the first phase. As will be described in Section 5.5.1, another AxFEB is used to readout the PMT signals. These boards communicate with a general-purposed trigger logic module, Hadron University Logic (HUL), developed by KEK Open-it [74] via flat cables. The ADC sum of all channels for each three clocks is send to the HUL module in LVDS standard signal. HUL further sums up the ADC sums from modules and a trigger is issued when the height of waveform sum exceeds thresholds and is sent to AxFEBs to start data transfer. Waveform data are sent from AxFEB's to a PC via Ethernet. Trigger information and clock information are sent from HUL module to the PC through Ethernet. The schematic diagram is shown in Figure 5.17.

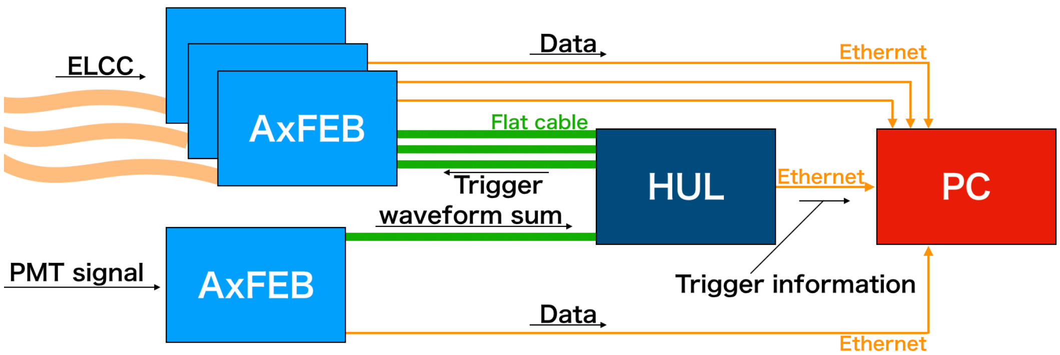

Figure 5.17: Block diagram of DAQ system.

5.4.2 Flexible Printed Circuit for Signal Readout

Signal transmission and bias voltage application between an ELCC unit and an AxFEB are performed through double-sided FPC-based cables (cable-FPC). A picture of cable-FPC is shown in Figure 5.18a. The width of the cable-FPC is 30 mm and the length is 500 mm for cables used inside the pressure vessel (inner cable-FPC) and 400 mm for cables which penetrate the feedthrough flange and extend outward the vessel (outer cable-FPC). Figure 5.18b shows a schematic cross sectional view of a cable-FPC. It consists of a base made of polyimide (25 μm), adhesive (20 μm), copper trace (33 μm), adhesive (35 μm), and polyimide coverlay (50 μm) on both side symmetrically. A single cable-FPC has 56 signal lines on one side and 56 bias voltage lines on the opposite side. The signal line and bias line of one channel are overlaid to suppress attenuation of the signal and crosstalk from neighboring lines. The width of 0.1 mm and pitch of 0.5 mm in each signal and bias lines also prevent the crosstalk. The basic design of the cable-FPC is based on the FPC developed by the NEXT experiment [75]. Stiffening plates and connectors (FX11-LA, Hirose electric inc.) are attached at the both ends of the cable-FPC.

A schematic view of cable connections are shown in Figure 5.19. The unit-FPC, the inner cable-FPC, the outer cable-FPC, and a conversion board are connected by FX11-LA connectors of Hirose electric. In the conversion board, a connector is converted from FX11-LA to a flat cable connector (XG4C-6031, Omron inc.), then, the conversion board is connected to AxFEB.

5.5 PMT

Two PMTs, Hamamatsu Photonics K.K. R8520-406MPDASSY, are installed with the same configuration as the 10 L prototype described in Section 3.5. Signal lines from PMT's are connected to co-axial cables described in Section 5.2.1 by LEMO connectors (HUBER&SUHNER 11 QLA-01-1-8) and high voltage lines are connected by SHV standard connectors (SHV-50-3-1/133).

(a) Photograph of cable-FPC.

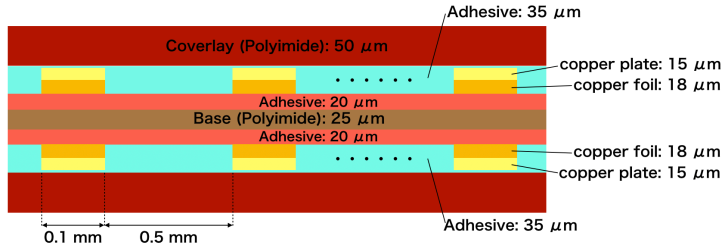

(b) Schematic cross sectional view of cable-FPC.

Figure 5.18: Cable-FPC.

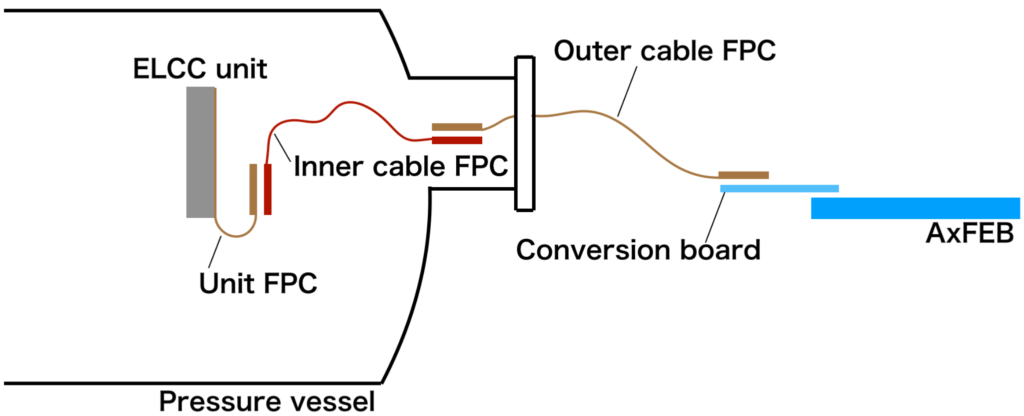

Figure 5.19: Schematic of cable connections.

5.5.1 Block Diagram for Acquisition of PMT Signal

Timing signals of scintillation light detected by PMTs are acquired by AxFEB. Due to the limitation of the pre-trigger window of AxFEB, the scintillation light signal cannot be obtained. Therefore, the timing signals are input to AxFEB after delay of 140 μs by the NIM logic circuit as shown in Figure 5.20. Coincidence of two PMT signals is required to suppress accidental backgrounds.

5.6 Field Shaper

In the first phase of the 180 L prototype, the strip field shaper, which was used in the HP10L, was used (Figure 5.21). Since the length along the drift direction is 10 cm, the required maximum high voltages are 12 kV for the anode electrode with the EL field of 3 kV/cm/bar and 20 kV for the cathode electrode with the drift field of 100 V/cm/bar at 8 bar. The power supplies for the anode and cathode electrodes are the same as those used for the 10 L prototype described in Section 3.6.1.

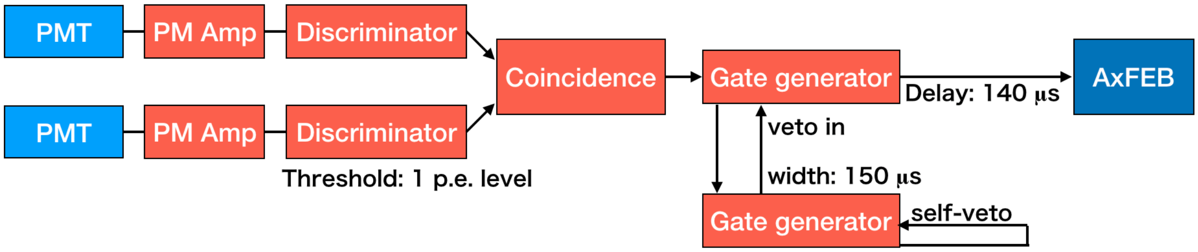

Figure 5.20: Block diagram for PMT signal timing.

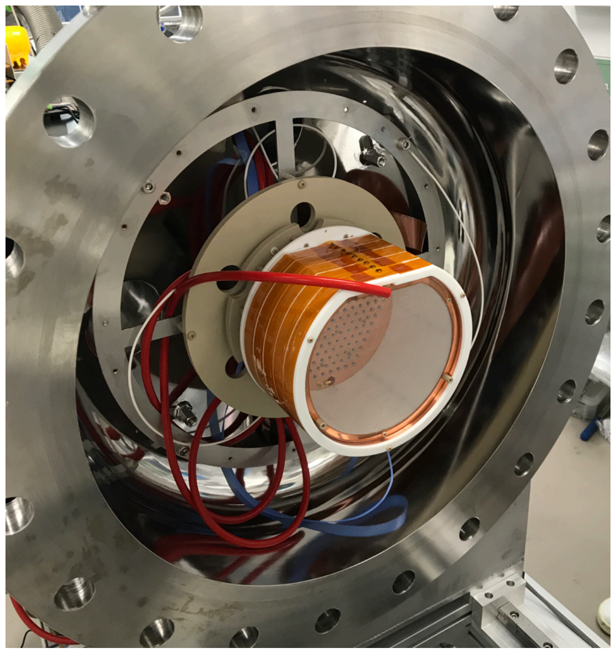

Figure 5.21: Field shaper of the first phase HP180L.

5.7 Gas System

Figure 5.22 shows a schematic diagram of the gas system for the 180 L prototype. The xenon gas is stored in five 47 L cylinders in the gaseous phase up to 10 bar and in a 300 mL cylinder in solid phase by soaking the cylinder in liquid nitrogen. This storage system can store a total of 2,100 nominal liters of xenon. The xenon gas is introduced to the pressure vessel by a compressor (MB-601HPAL, IBS). The gas is circulated also by the same compressor and purified by the molecular-sieve and the getter as explained in Section 2.5.2 during the data acquisition. The mass flow meter (F-111CM-40K-AAD-88-K, BRONKHORST inc.) monitors the gas flow and the dew point transmitter (PURA, MICHELL Instruments) monitors the water concentration. The pressure vessel and the gas line are evacuated prior to gas introduction. The pressure vessel is connected to the vacuum pump by NW50 standard pipes and tubes via a high pressure tolerable valve with JIS 25A standard, CARTEN inc. HFC25A-PC2FSM. By using this valve, the conductance to the vacuum pump is significantly improved compared to the VCR valve, whose size is limited to 1/2 inch. A photograph of HFC25A-PC2FSM is shown in Figure 5.23.

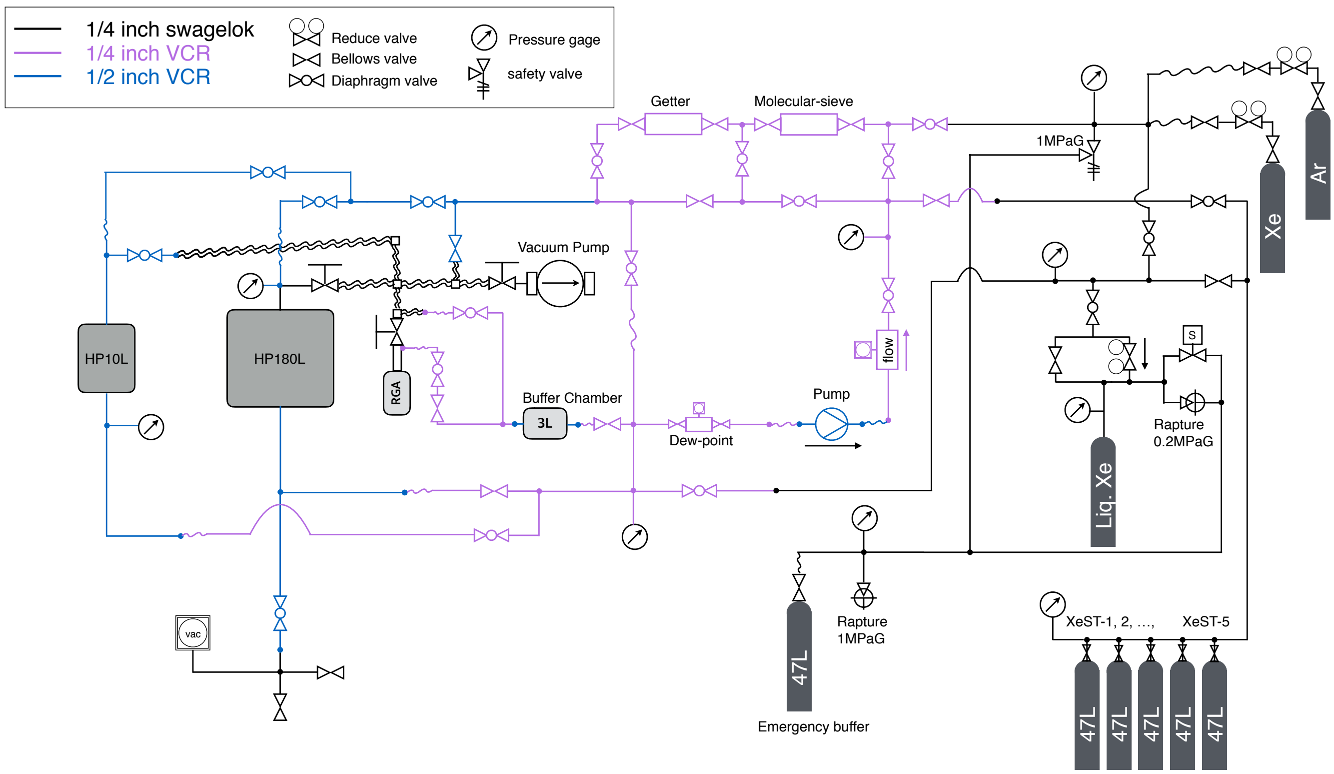

Figure 5.22: Gas system for the 180 L prototype.

Figure 5.23: High pressure tolerable valve with JIS 25A standard, CARTEN inc. HFC25A-PC2FSM.

Chapter 6

Performance of the 180 L Size Prototype

The performance of the first phase HP180L was evaluated at 4 bar using 511 keV annihilation gamma-rays from ^{22}Na β^{+}-ray source placed on the pressure vessel. The decay scheme of ^{22}Na is shown in Figure 6.1. The main decay channel is β^{+} decay accompanied by a 1274.5 keV gamma-ray emission. Because of the limitation of detector size, 1274.5 keV events are not confined within the fiducial region. The emitted β^{+}-ray stops in stainless steel of the vessel and annihilates with an electron to emit two 511 keV gamma-rays back-to-back.

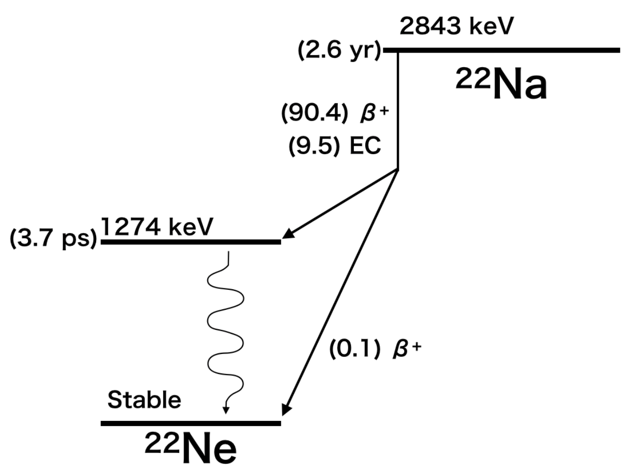

Figure 6.1: Decay scheme of ^{22}Na [68]. Numbers written before decay modes are the probability of that transition (%).

6.1 Purpose and Target

The purpose and target of the 180 L prototype are as follows:

- To achieve a long term operation stably
- To evaluate the performance at higher energy region than that of the 10 L prototype
- To demonstrate a good energy resolution, 0.5% (FWHM) at the Q-value
- To observe track patterns of gamma-rays.

6.2 Experimental Condition

Table 6.1 summarizes the condition at this measurement. The EL field strength is 3.0 kV/cm/bar and the drift field strength is 100 V/cm/bar with 6.0 kV and 10.0 kV applied to the anode and cathode electrodes. During the measurement, the gas has been circulated at 10 L/min and purified.

The trigger is issued by HUL when the height of the waveform sum of the inner fiducial channels exceeds a threshold and the veto channels have no hits. We had intended to veto the outermost channels (see Figure 6.2a), however, because of a bug in the firmware of AxFEB, some channels were swapped in the trigger setting as shown in Figure 6.2b. Although the incorrect veto setting decreases the efficiency of acquiring high energy events, it may not affect the energy resolution significantly. Complete veto is applied in the analysis as described in Section 6.6. The threshold level is set high, roughly corresponds to 130 keV. In addition to the high-level threshold trigger, a trigger with low-level threshold, roughly corresponds to 10 keV, is adopted to acquire 30 keV events for the EL gain calibration explained in Section 6.7. The triggers by low-level threshold are reduced to 1/100 not to dominate the trigger rate. This trigger does not have the veto setting.

Waveform data are recorded for 1,024 samples (204.8 μs) with the post-trigger of 128 samples (25.6 μs).

Table 6.1: Experimental setup for the data.

Contents			Reference
Detector		HP180L first phase	Section 5.1
ELCC	configuration	hexagonal pattern, 10 mm-pitch	Section 5.3.1
	MPPC	VUV-4	Section 5.3.2
Field shaper	type	Strip field shaper	Section 5.6
	size	ϕ15 cm, 10 cm-long	Section 5.6
Electric field	Drift region	100 V/cm/bar	
	EL region	3.0 kV/cm/bar	
Voltage for photo sensors	MPPC	-56.0 V	
	PMT	-760 V	
Gas	Pressure	4 bar	
		w/ circulation and purification	Section 5.7
γ-ray source (^{22}Na)	Activity	7.0×10^5 Bq	

The data were acquired for four days in December 2019. In total, 8,061,016 events are acquired. Among those, about 1,000,000 events are used as sample data to determine cut criteria and establish the correction algorithm.

The gas pressure, EL field strength, drift field strength, and water concentration were monitored during the measurement and Figure 6.3 shows these trends. The xenon gas pressure was monitored at 4.0±0.6 bar. The large error comes from a systematic uncertainty of the pressure gauge (ZT67, Nagano Keiki), however, the actual pressure seemed to be more stable as will be shown in Section 6.7.3. The electric fields in the EL and drift regions were also stable except for some spikes. The spikes are due to discharges happened mostly between the GND mesh and the anode electrode of the ELCC once per six hours on average. When a discharge occurs, an interlock system cut and reset high voltage immediately. At around 12:00, 3rd December (JST), the values

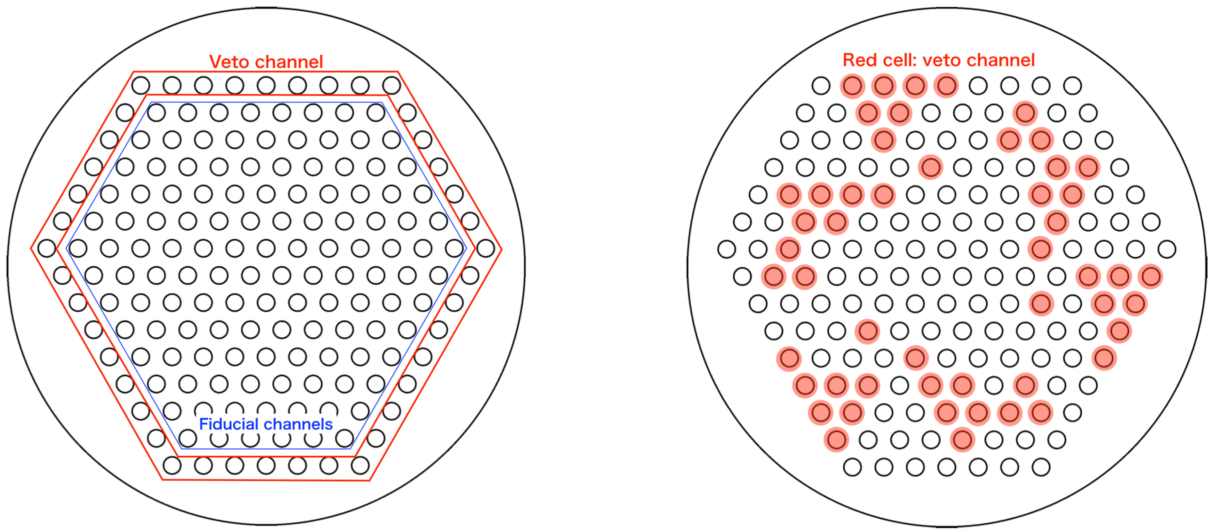

(a) Designed setting of fiducial and veto channels.

(b) Actual fiducial and veto settings.

Figure 6.2: Configuration of fiducial and veto channels. The strange veto setting in Figure 6.2b is due to a bug in the firmware of the AxFEB.

of the electric fields were changed due to a setting error. Data during this period was not used. The water concentration was slightly decreased by the purification but its variation was smaller than the systematic error of the dew point transmitter: 0.1±0.1 ppm.

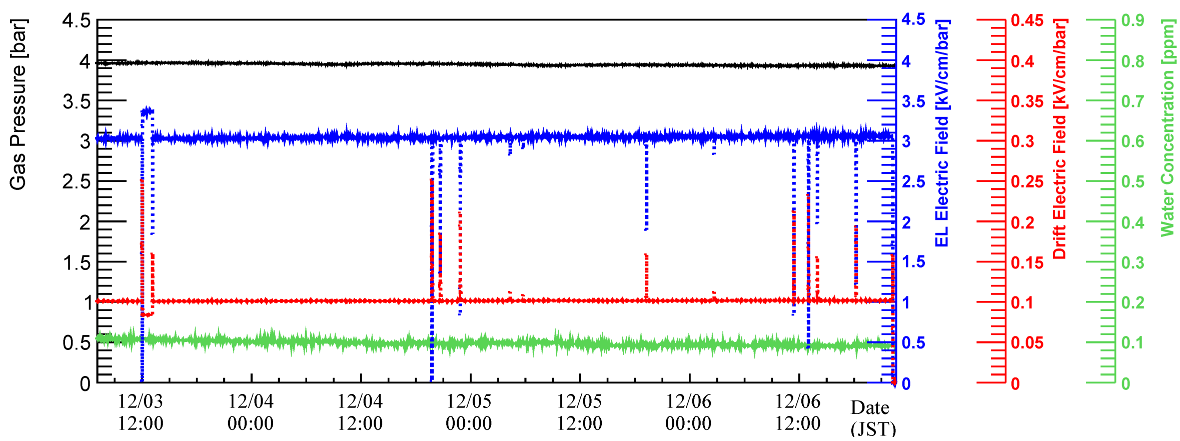

Figure 6.3: Slow monitor trends during the data acquisition. The black line shows the gas pressure, the blue line is EL field strength, the red line is drift field, and the green line is the water concentration. Spikes in the electric field lines are due to anode-voltage discharges and trips.

6.3 Analysis Overview

The analysis flow is the same as that in Section 4.4.2. Fully-contained events are selected. In addition to the EL gain calibration and the correction for MPPC non-linearity, change of the light yield over time and z position dependence are corrected. To avoid the effect of the EL gain variation depending on the ionization electron position relative to the cell, events close to the ELCC are cut. The detector performance is evaluated using events by the characteristic X-rays and 511 keV full peak.

6.4 Processing of the ELCC Signals

Typical waveform recorded by AxFEBs is shown in Figure 6.4. Of the acquired waveform data, the first 650 samples are defined as signal window. For each signal window, regions whose pulse height exceeds an analysis threshold are regarded as hits. The analysis threshold is set to 3.5 ADC counts away from a baseline. If the waveform exceeds the threshold multiple times, each region is regarded as a hit separately. The algorithms to calculate the EL charge, the rise timing, and the fall timing for each hit are the same as those in Section 4.2.2. The effective gains of MPPCs are calculated by the "threshold method" described in Section 2.3.3 and are shown in Figure 6.5. Mean of the gain is 1.89 in unit of ADC counts with the standard deviation of 0.11.

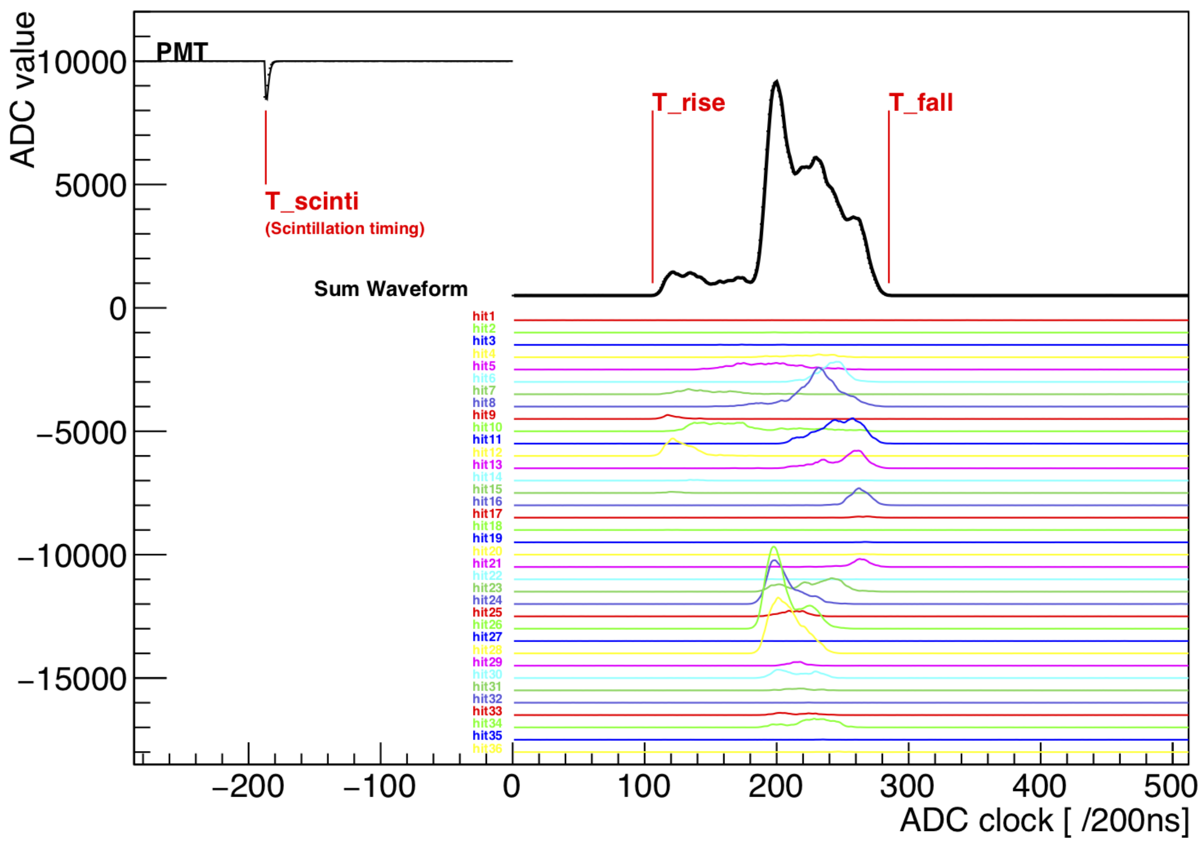

Figure 6.4: Typical waveform and definition of parameters. Waveform drawn in black line is the sum of ELCC hit channels. Individual waveforms are drawn as colored lines.

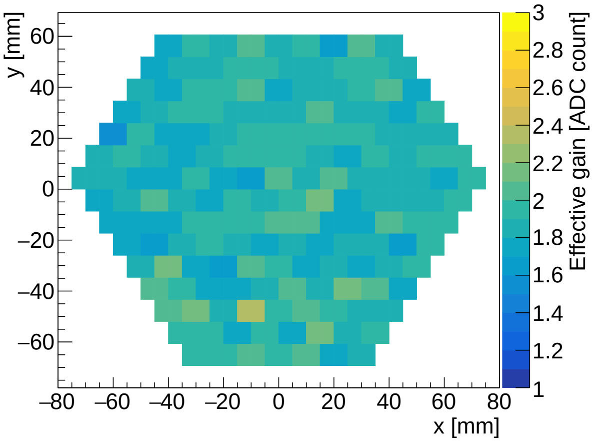

(a) Gain map of each MPPC.

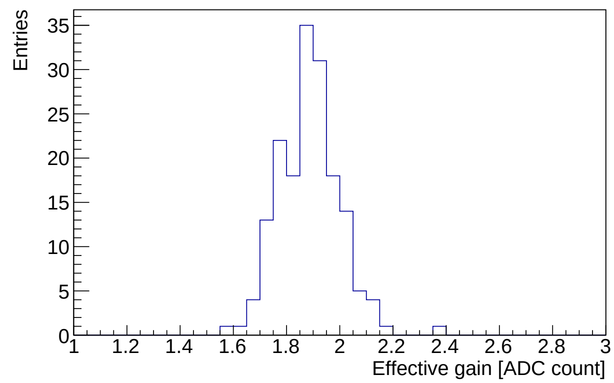

(b) Distribution of effective gain of MPPCs in unit of ADC count.

Figure 6.5: MPPC effective gain of the sample data set.

Figure 6.6a shows a distribution of the event fall timing which is defined as the last fall timing among hits. The left peak corresponds to the proper EL signals, which have the rise timing of 128 ADC clock and typically the width of 5–100 ADC clocks (1–20 μs). The peak around 570–630 ADC clocks consists of the hits about 10 cm away from the first hit among all hits. Almost all of these hits are isolated from other hit cluster. The photon count spectrum of such isolated hits at the peak around 570–630 ADC clocks is shown in Figure 6.6b. They have about 10 photons, which corresponds to EL photons by a single electron. Accordingly, these hits are considered to be due to secondary electrons generated at the cathode stainless electrode by the EL lights. Hence, hits whose fall timing is in the range of 570–630 ADC clocks and photon count is less than 10 are eliminated from the analysis.

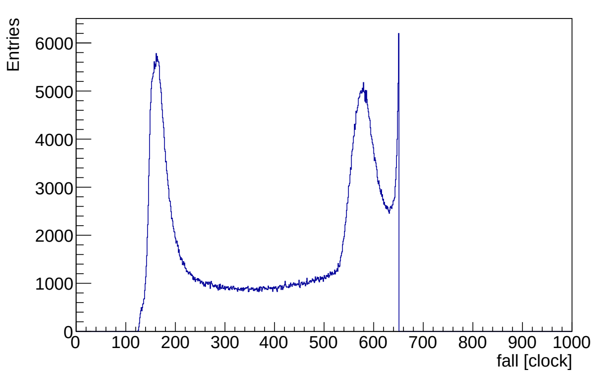

(a)

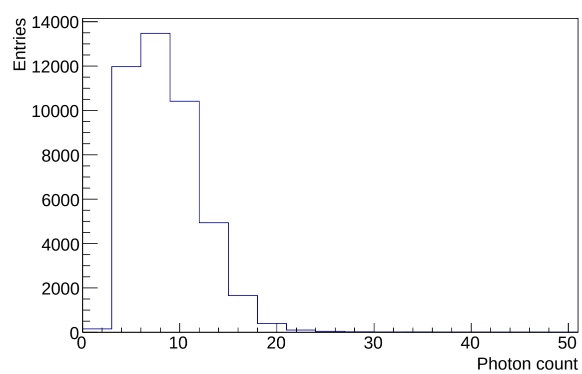

(b)

Figure 6.6: (a) distribution of the event fall timing and (b) photon count spectrum of the hits with the fall timing between 570 and 630 ADC clocks.

6.5 Processing of the PMT Timing Signal

Figure 6.7 shows the timing distribution of the PMT signal. Because only the timing information is acquired and waveform is not recorded as explained in Section 5.5.1, the scintillation signal and the EL signal cannot be distinguished. The peak at 800 ADC clock corresponds to the EL signal timing. About 20% entries are such mis-identified events. This timing is used for matching with the timing of ELCC signals. The region between 350 and 790 ADC clocks is regarded as scintillation signal region. The flat distribution below 350 ADC clock is due to contamination of accidental hits.

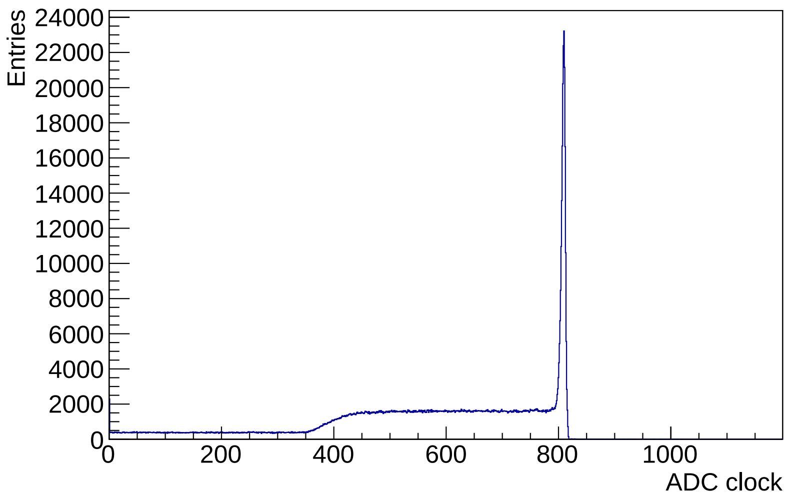

Figure 6.7: Timing distribution of PMT signal. The peak at 800 ADC clock corresponds EL timing. The flat distribution below 350 ADC count is due to accidental hits.

6.6 Event Selection

6.6.1 Fiducial Cut

As explained in Section 6.2, the outer veto was not properly applied in the trigger. Events which have hits in the proper veto channels are cut at analysis. The fiducial and veto channels are set as Figure 6.2a.

Figure 6.8a shows the distribution of the timing difference between the EL rise timing and timing signal from PMTs after the fiducial channel cut. The peak at 0 μs corresponds to events that PMTs misidentified the EL signal as a scintillation signal or events in which the track hits the anode electrode. Figure 6.8b is the distribution of time interval between the EL fall timing and the scintillation signal. The right peak in Figure 6.8b corresponds to events that crossed the cathode electrode. To select fully-contained events along the drift direction, events are selected if the time interval between the rise (fall) timing and the scintillation timing is more (less) than 5.0 (80) μs. Figure 6.9 shows the distributions of time differences after the cut. It is considered that the reason why the number of events having larger time intervals in Figure 6.9b, that is, the events closer to the cathode are large, is that the detection efficiency of the scintillation light by the PMTs is higher when they are closer to the cathode.

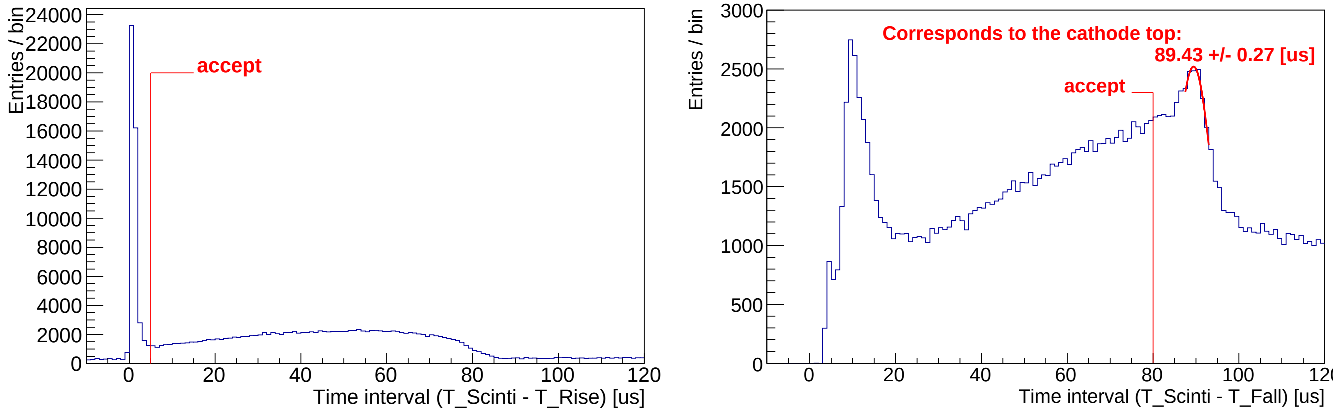

(a) Time interval between scintillation timing and rise timing.

(b) Time interval between scintillation timing and fall timing.

Figure 6.8: Distribution of time interval between the scintillation signal and EL signal.

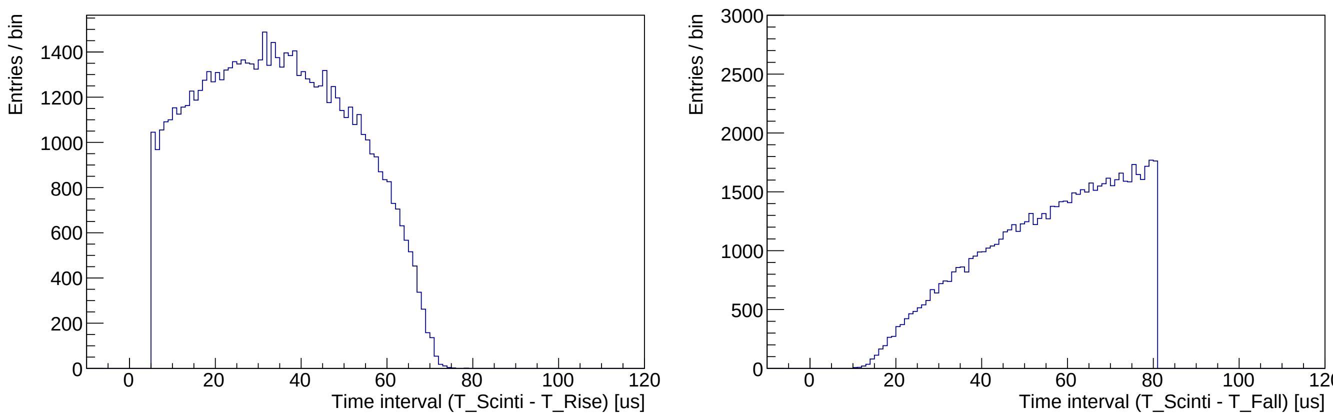

(a) Time interval between scintillation timing and rise timing after the fiducial cut.

(b) Time interval between scintillation timing and fall timing after the fiducial cut.

Figure 6.9: Distribution of time interval between the scintillation signal and EL signal after the fiducial cut.

The drift velocity of electrons can be calculated using the timing of the cathode ($z = 10$ cm) crossing events. The timing of events crossing the cathode electrode is obtained by fitting the right peak in Figure 6.8b with a Gaussian. The fitting yields 89.43 ± 0.27 μs as the cathode timing and thus the drift velocity is 0.11 cm/μs. The obtained value is comparable to the previous study [40]. The width of the peak estimated as 1σ of the Gaussian fitting is 6.39 μs and corresponds to 0.70 cm at the drift velocity of 0.11 cm/μs. The spread of the peak is caused by diffusion during drift and means that the reconstructed z position has at most a 0.70 cm uncertainty.

6.7 Calibration and Correction

6.7.1 EL gain Calibration using K_α Peak

The EL gains are calibrated in almost the same way as in Section 4.2.7 except that two layers of channels surrounding the channel in calibration are allowed to have hits for more statistics (see Figure 6.10). The calibration is repeated multiple times considering the effect from the gains of surrounding channels. In this analysis, the EL gain calibration is repeated five times for all channels and, after that, four more times for the fiducial channels only.

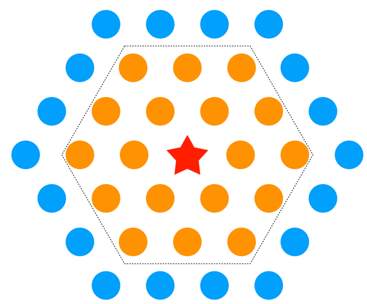

Figure 6.10: Selection of events for the EL gain calibration. The central red star is the channel in calibration and has to have the largest photon count. Only two layers of surrounding channels represented as orange circle are permitted to have hits.

6.7.2 Correction of MPPC Non-linearity

Unlike the case of HP10L, the response of MPPCs are modeled using the following function:

$$N_{\text{observed}} = \frac{aN_{\text{true}}}{1 + \tau/(N_{\text{pixel}} \cdot \Delta t)N_{\text{true}}}, \tag{6.1}$$

where the notations are the same as that in Equation (2.20) and a is another free parameter for more accurate fitting, in particular, at low photon count region. The N_{pixel} is 3,600 and Δt is 200 ns, which corresponds to one clock of the ADC. The recovery time is measured for each MPPC. Figure 6.11 shows the distribution of the measured recovery time of MPPCs. The mean is 137.38 ns and its standard deviation is 15.40 ns. Actually, the measured MPPC recovery times have a systematic error of about 10 ns because of the measurement method. The effect of this systematic error is discussed in Chapter 7.

6.7.3 Correction of Time Dependence

The light yield change during the data taking was seen as shown in Figure 6.12a. This may be caused by an improvement of gas purity and fluctuation of the gas density during the measurement. The period of data taking is divided into 50 bins and correction for the time dependence is applied (Figure 6.12b).

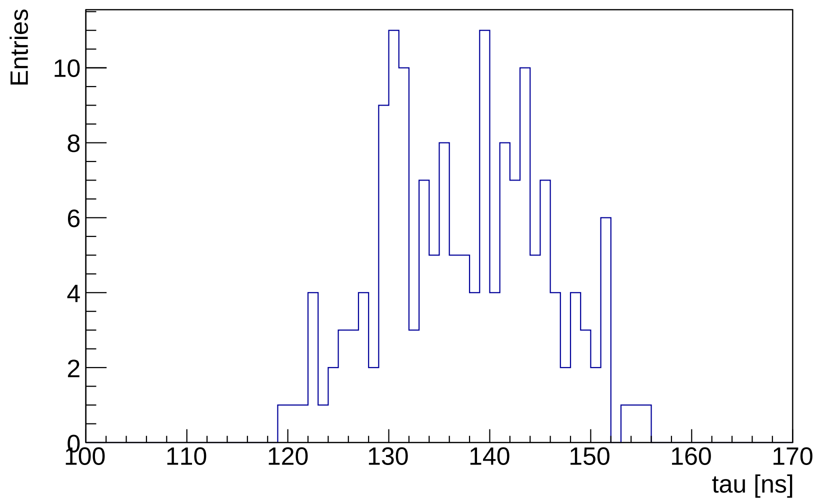

Figure 6.11: Distribution of MPPC recovery time.

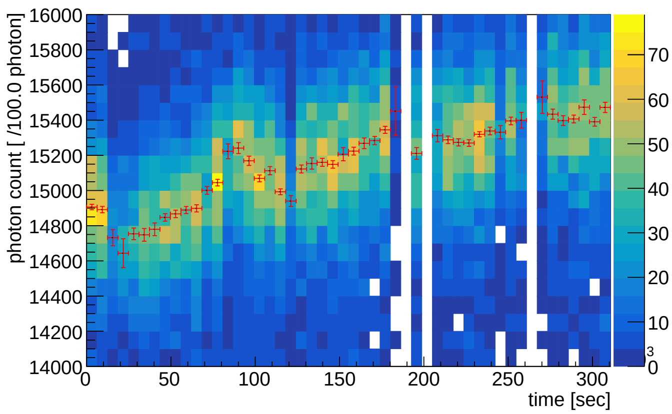

(a) Before correction.

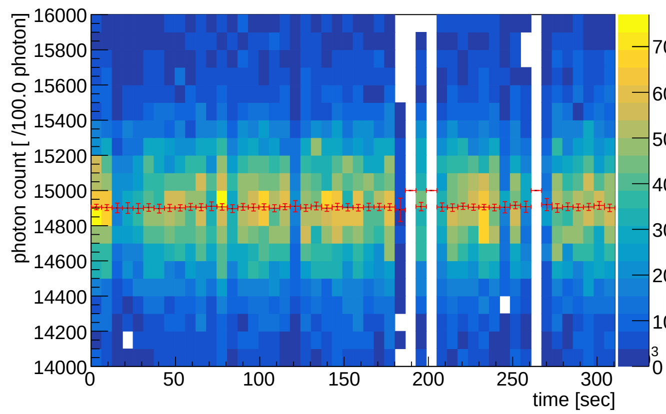

(b) After correction.

Figure 6.12: Variation of light yield as a function of the data taking time. Red crosses represent the K_α peak center and its fitting errors. The empty bins are the timing of run switching or troubles of DAQ.

6.7.4 Correction of z Position Dependence

Figure 6.13 shows the photon count at the K_α peak center as a function of the z-position. The z position here is defined as the weighted average of the light amount. The light yield decreases as the distance from the ELCC increases. This may be caused by loss of ionization electrons during drift due to capture by impurities such as oxygen.

The z-position dependence in 3 cm$\leq z \leq$10 cm is fitted with a linear function. Then, the dependence was corrected with the following equation:

$$\mathrm{Photon}(z) = \mathrm{Photon}_0(z) \times (1 + az), \tag{6.2}$$

where $\mathrm{Photon}_0(z)$ and $\mathrm{Photon}(z)$ are the photon count at z before and after the correction, and $a = 0.000437 \pm 0.00012$ calculated from the fitting result. The correction was performed for every

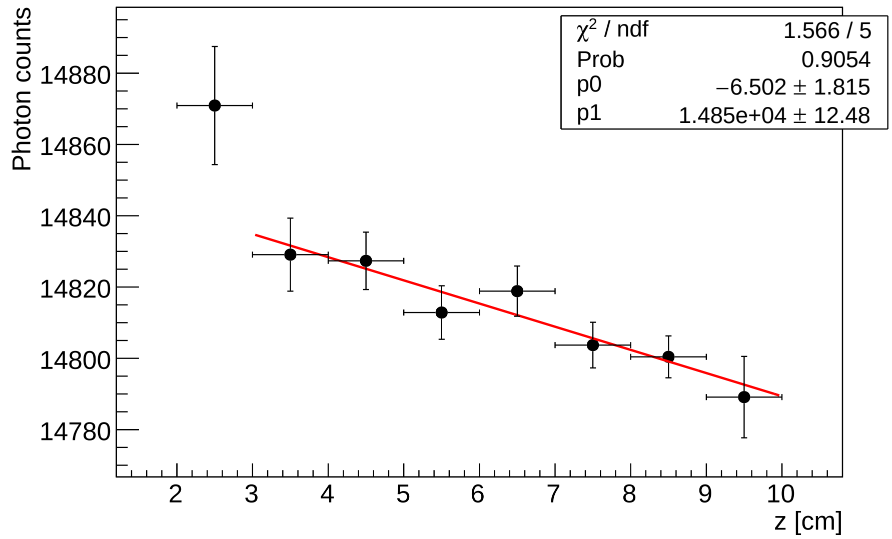

Figure 6.13: Photon count of K_α events as a function of z position.

sampling point of the 5 MS/s ADC.

In the region below 3 cm, the light yield increases non-linearly. In this region, non-uniformity of the light yield depending on the event position relative to the cell position is also observed as the case in Section 4.4.6. For checking the effect of the position dependence, the photon count spectra for various max-fraction around characteristic X-ray peaks are shown in Figure 6.14a. The definition of max-fraction is described in Section 4.4.6. The K_α peak photon count of each max-fraction is plotted in Figure 6.14b. A variation of peak center is seen in large max-fraction and is calculated to be 0.97±0.45%. This value is smaller than that in Section 4.4.6 thanks to the optimization of the cell configuration.

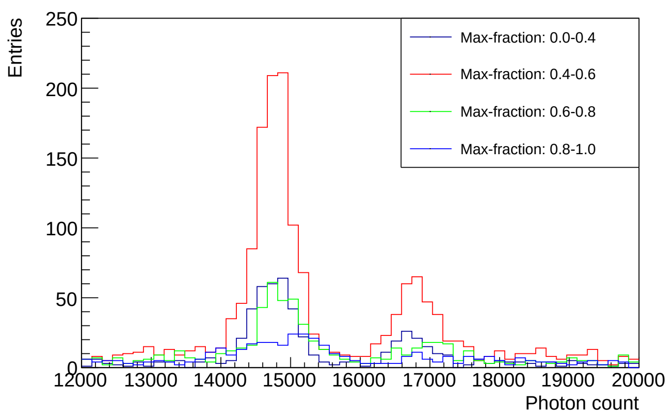

(a) Photon count spectra for each max-fraction.

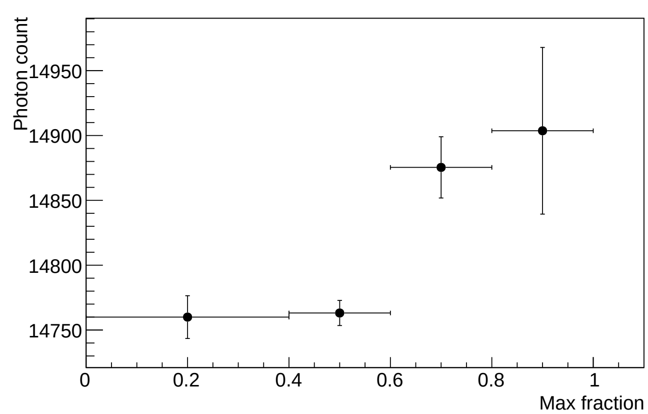

(b) K_α peak center for each max-fraction.

Figure 6.14: Position dependence relative to cell.

As mentioned in Section 5.3.1, the dependence on the initial electron position 2 cm above the ELCC is also reproduced by a simulation at 4 bar and its variation is 1.1%, which is comparable to the value from the data within the error.

6.8 Additional Event Selection

6.8.1 Additional z Cut

As mentioned in Section 6.7.4, non-uniformity depending on the position relative to the cell position was seen for events close to the ELCC. Since the effect of position dependence above $z = 2$ cm is well understood by simulation and is small enough as explained in Section 5.3.1, events whose event edge at the ELCC side is larger than $z = 2$ cm should be selected. Considering the uncertainty of reconstruction of z-position, 0.7 cm, events whose z-position at the signal rise is less than 2.7 cm are cut.

6.9 Result of Cut and Correction

The change of the energy spectrum after the fiducial channel cut and the fiducial cut along the z direction is shown in Figure 6.15.

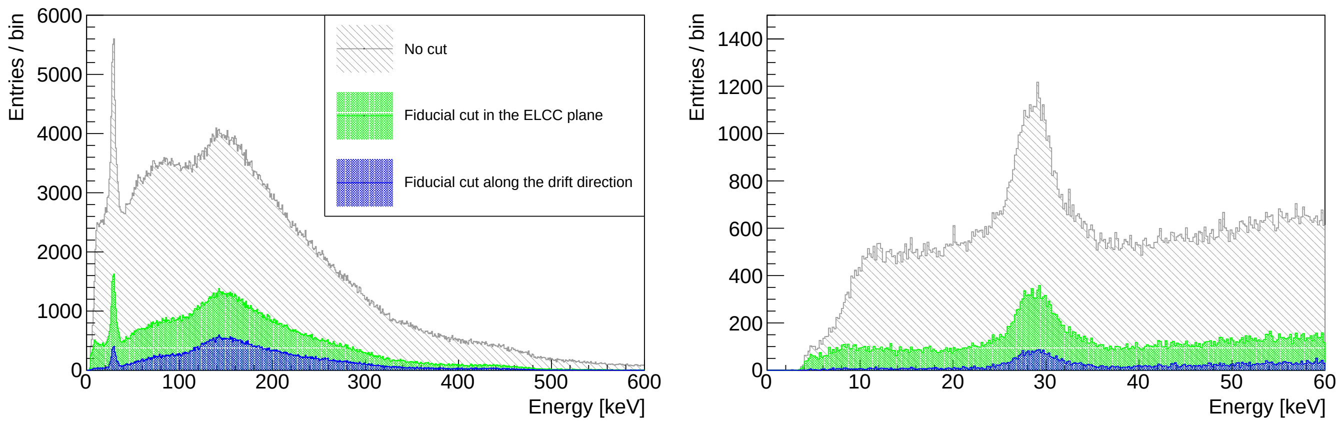

Figure 6.15: Change of the energy spectrum by each fiducial cut for sample data set. The right figure is shown around 30 keV with finer binning.

The change of the energy spectrum after the corrections and the additional z cut for the whole data set is shown in Figure 6.16. After these corrections and cuts, peak structures at 511 keV and its escape peaks are clearly seen. In these energy spectra, the energy scale is calibrated using the photon count of K_α, K_β (29.78 keV, 33.62 keV) and the 511 keV peak.

6.10 Evaluation of the Performance

6.10.1 EL yield

The total photon counts of K_α and 511 keV events are 14,896.3±3.4 and 259,77.7±57.6, respectively. The expected photon count for 30 keV events at 4 bar was 10,980 by simulation as mentioned in Section 5.3.1 thus the inconsistency during the data and the simulation exists. Dark current data for calculating the MPPC gains were acquired by high gain ADC then converted into unit of ADC count of low gain ADC by the specification value of each ADC. However, there can be an

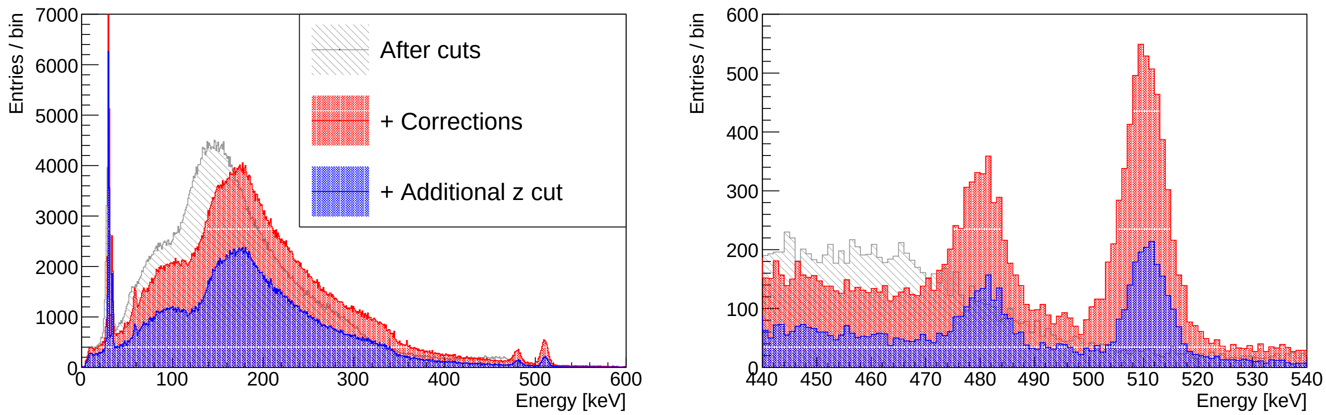

Figure 6.16: Change of the energy spectrum by corrections and the additional z cut for whole data set. The right figure is shown around 511 keV with finer binning.

additional factor, whereby a systematic error in the calculation of the MPPC gain may cause the inconsistency. The causes of the inconsistency may also be due to the incorrect input parameters to the simulation such as MPPC detection efficiency, the reflectivity of PTFE, and the angular dependence of incident photons relative to GND mesh.

6.10.2 Energy Resolution

The energy spectrum around the characteristic X-rays and their fit results with two-Gaussian plus constant are shown in Figure 6.17. The obtained energy resolutions are 4.50±0.05% (FWHM) and 4.03±0.10% (FWHM) for the K_α and K_β peaks, respectively. Figure 6.18 shows the energy spectrum at around the 511 keV peak. The peak at around 480 keV consists of the escape peaks of K_α (481.22 keV) and K_β (477.38 keV). Thus, the peak was fitted with a double-Gaussian with the peak positions of the fitting function fixed to each energy and with the condition that the widths of two peaks are the same. The 511 keV peak was fitted with a Gaussian. The continuum component is modeled by a linear function. The obtained energy resolutions are 1.59±0.09% (FWHM) for 481.2 keV and 1.49±0.04% (FWHM) for 511 keV, which corresponds to 0.68±0.02% (FWHM) at the ^{136}Xe $0\nu\beta\beta$ decay Q-value when extrapolated by $\sqrt{E}$.

The energy resolution at the Q-value is estimated with additional energy dependency term, that is, the function of $A\sqrt{E + BE^2}$, where A and B are free parameters. The energy resolutions at K_α, K_β, 481.2 keV, and 511 keV peaks are used for the estimation with this function. The fitting result is shown in Figure 6.19 and summarized in Table 6.2. The extrapolated energy resolution to the Q-value, 2458 keV, is estimated to be 1.18±0.01% (FWHM). This value is worse than that obtained by conversion with $1/\sqrt{E}$, since the peak resolutions at 481 keV and 511 keV are worse than the resolution of the characteristic X-ray peaks. Possible reasons are discussed in the next chapter.

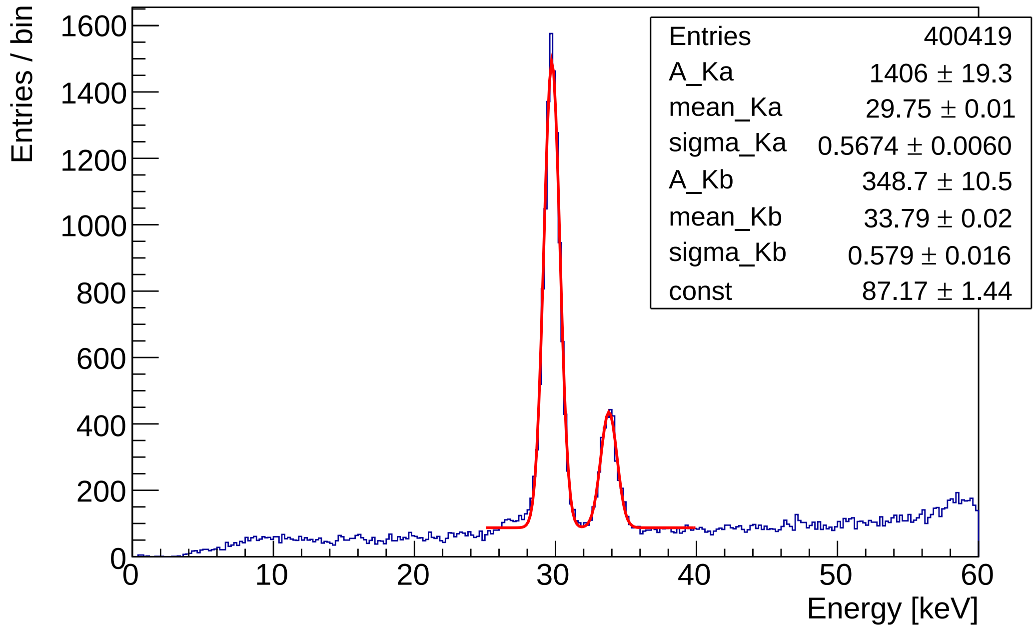

Figure 6.17: Energy spectrum at around 30 keV and the fit result with two Gaussian plus constant.

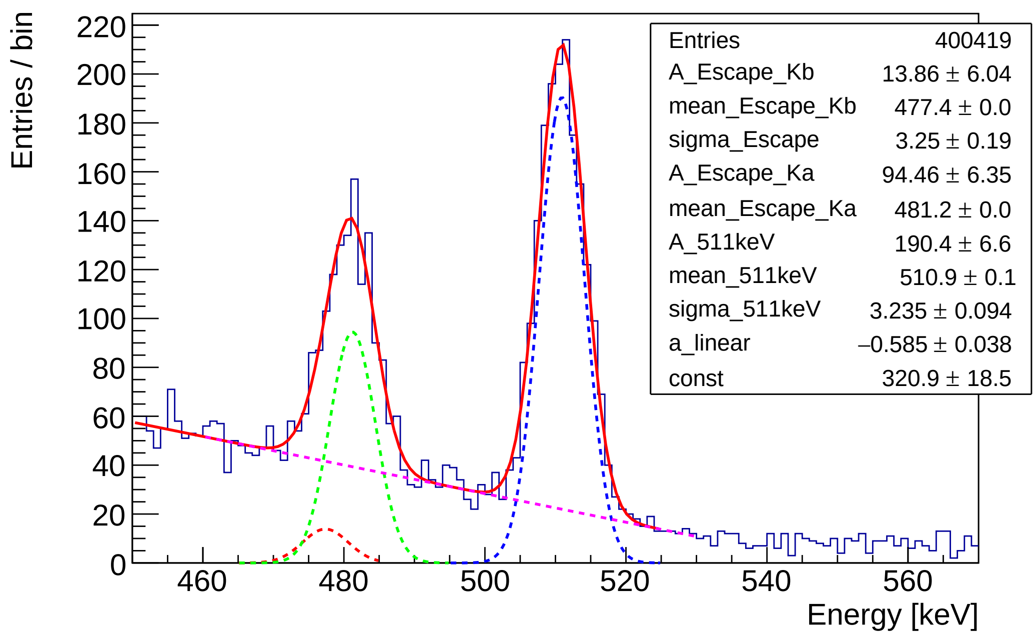

Figure 6.18: Energy spectrum at around 511 keV. The peak at 480 keV consists of two escape peaks (the K_α escape and the K_β escape). The escape peaks are fitted with two Gaussians and the 511 keV peak with a Gaussian. The continuum component is fitted with a linear function.

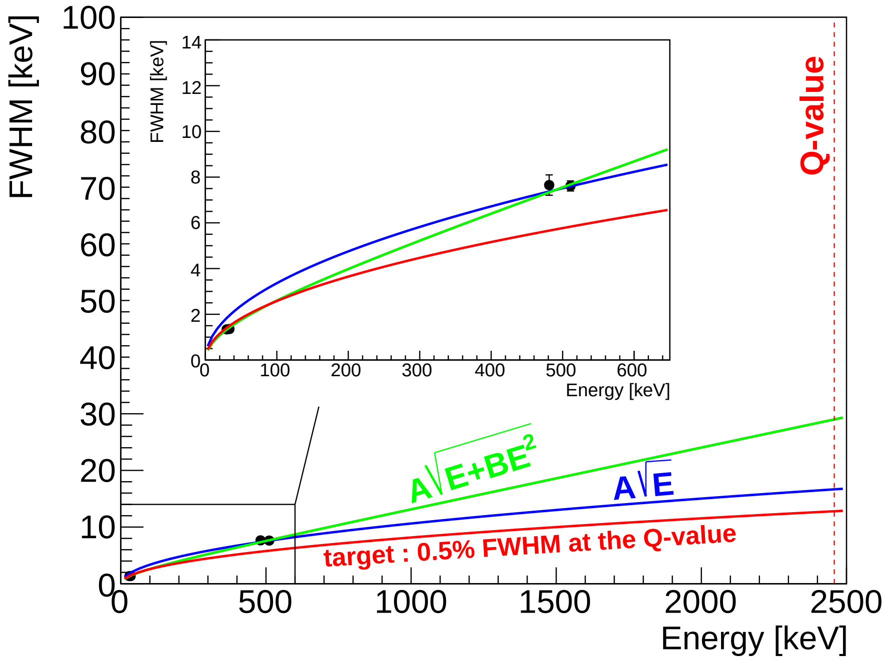

Figure 6.19: Extrapolation to ^{136}Xe $0\nu\beta\beta$ decay Q-value with two types of function: $A\sqrt{E}$ and $A\sqrt{E+BE^2}$, where E is energy and A, B are free parameters. The evaluation is performed with the resolution at 511 keV only for $A\sqrt{E}$ (blue curve) and with the resolutions at K_α, K_β, and 511 keV peaks for $A\sqrt{E+BE^2}$.

Table 6.2: Results of evaluation.

Fitting function	A	B	Extrapolated resolution at Q-value (FWHM)
$A\sqrt{E+BE^2}$	0.236±0.003	0.003±0.0002	1.18±0.01%

6.11 Event Topology

An example event display of a 511 keV event is shown in Figure 6.20. The bin of z direction is set to every 0.22 mm, which corresponds to one ADC clock. Figure 6.21 shows an event display of the same event, but the bin of z direction is roughened to every 5 mm for easy viewing. A blob structure which corresponds to the track endpoint can be clearly seen at (x, y, z)=(5 mm, -10 mm, 60 mm). Eye scan shows that about one-half of the events have a clear blob structure at their track endpoint. The result that clear blob structures were seen gives a persuasive power to the estimation of event selection by deep leaning using track pattern. Eight more event displays at 511 keV are shown in Figures 6.22-6.29.

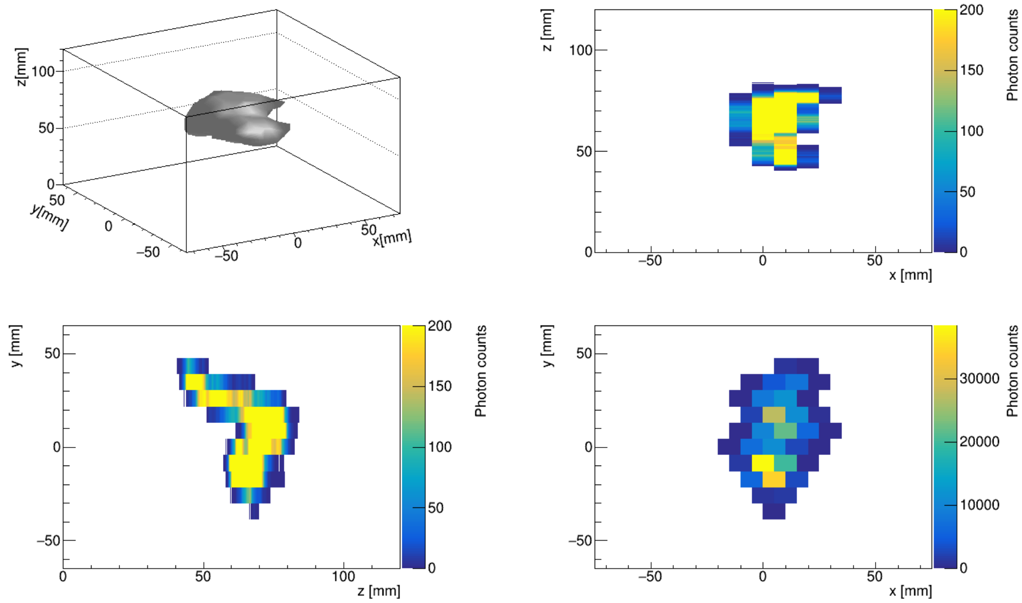

Figure 6.20: Event display of a 511 keV event

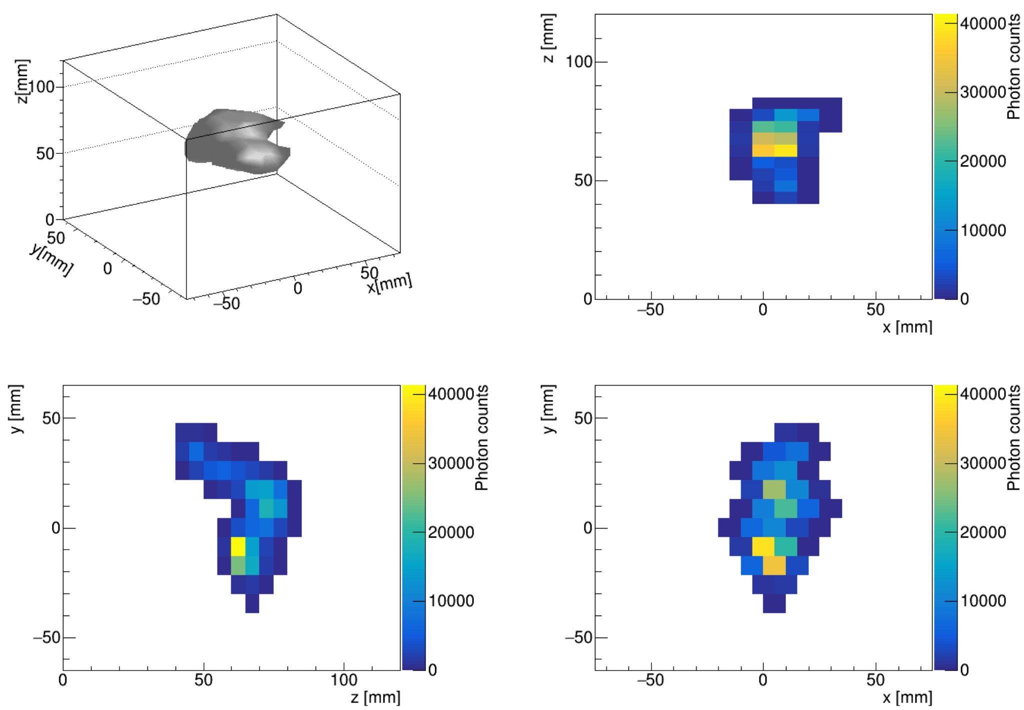

Figure 6.21: Event display of the same event as Figure 6.20. The sampling of z direction is merged to 5 mm for easy viewing.

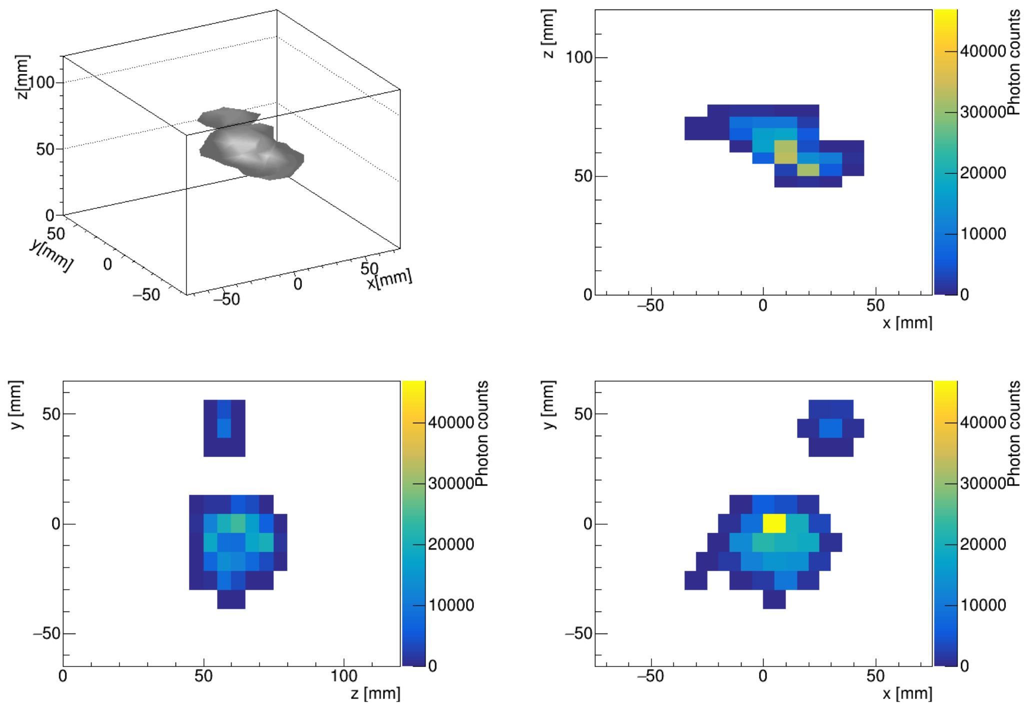

Figure 6.22: Event display of a 511 keV event.

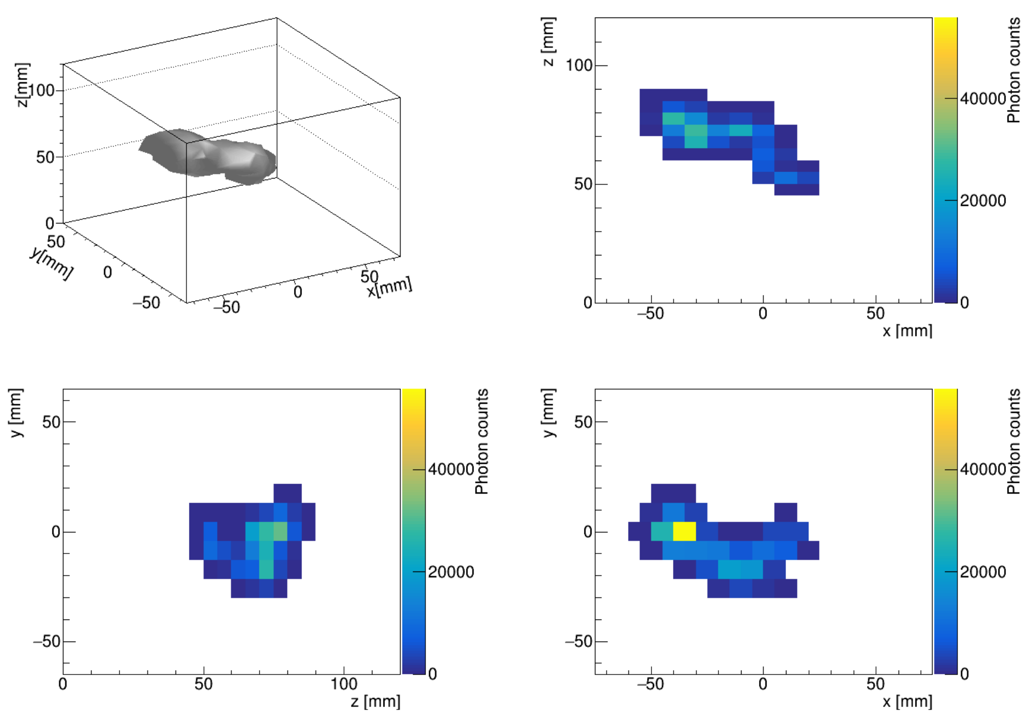

Figure 6.23: Event display of a 511 keV event.

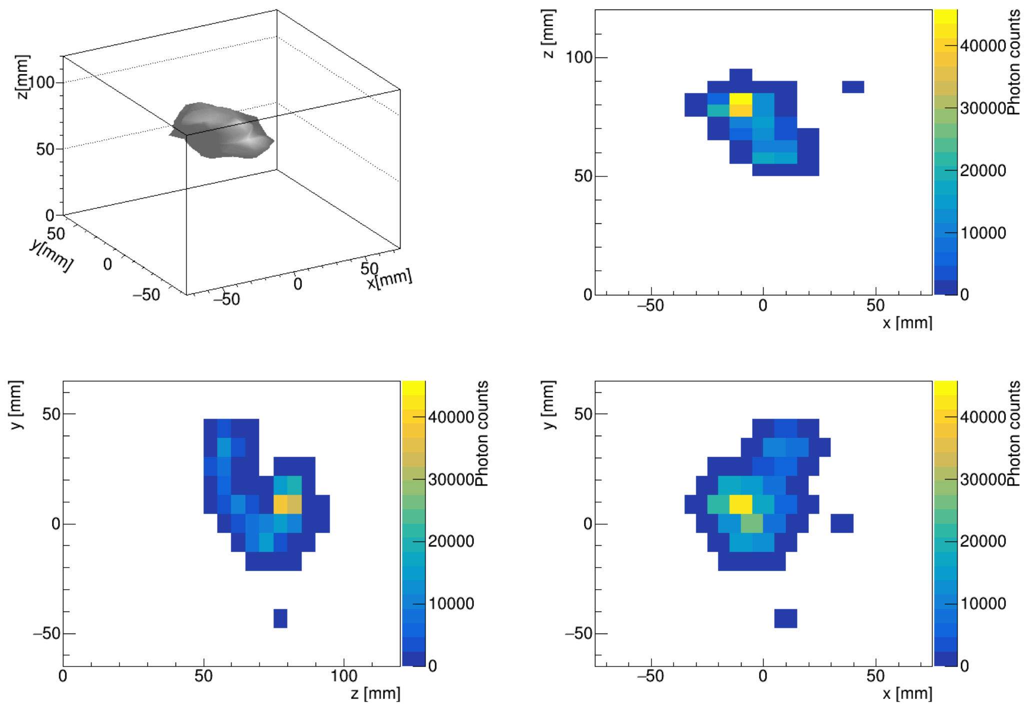

Figure 6.24: Event display of a 511 keV event.

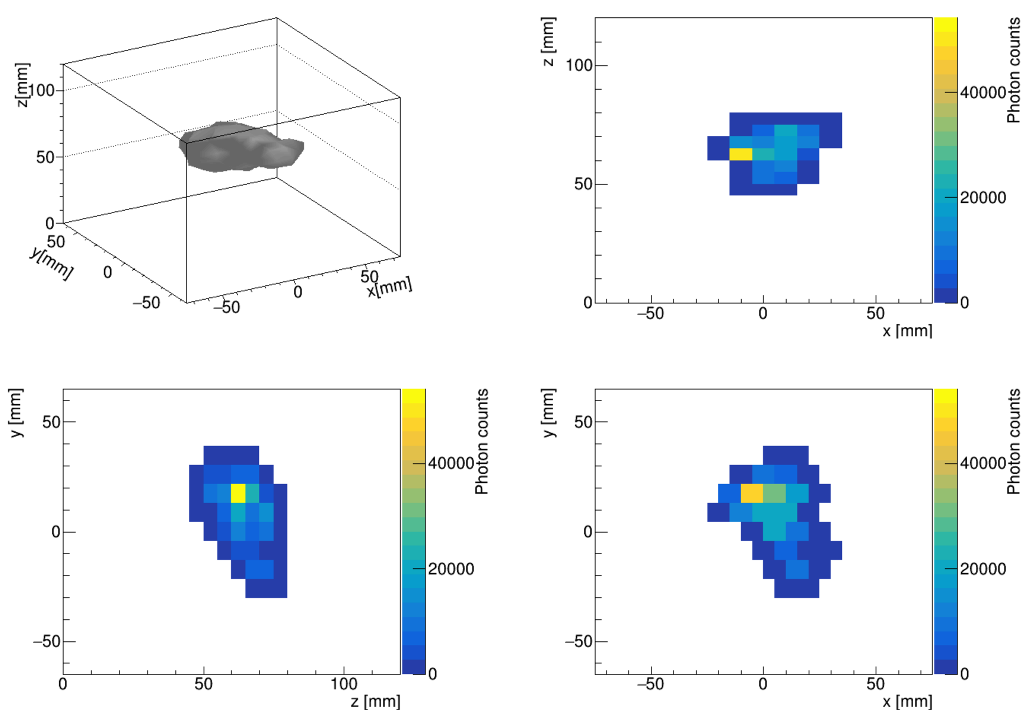

Figure 6.25: Event display of a 511 keV event.

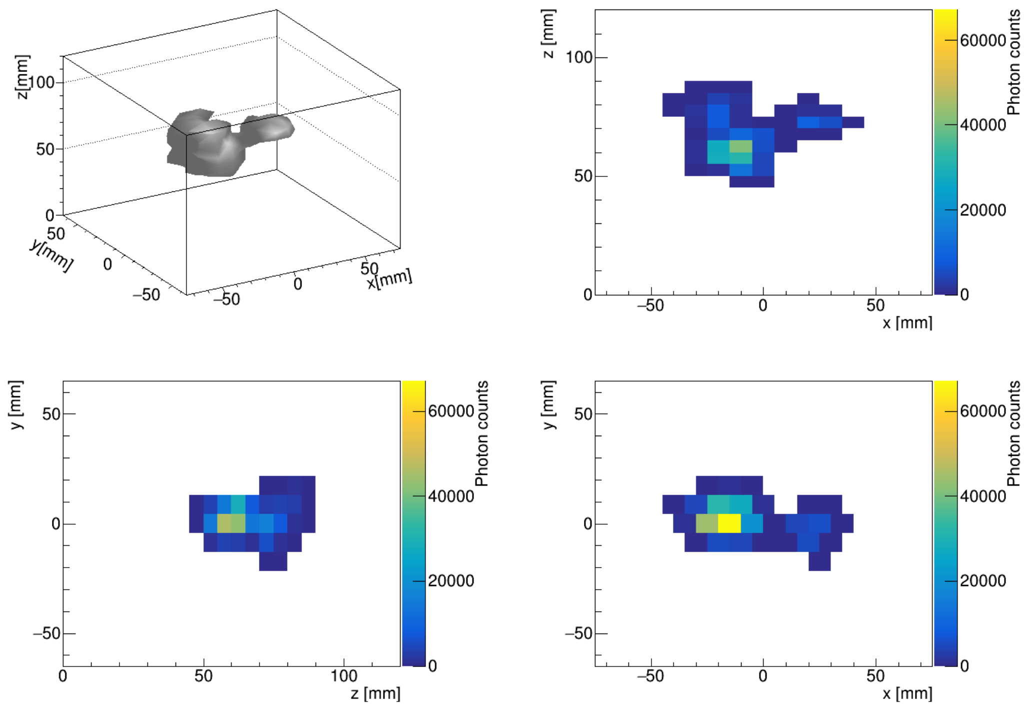

Figure 6.26: Event display of a 511 keV event.

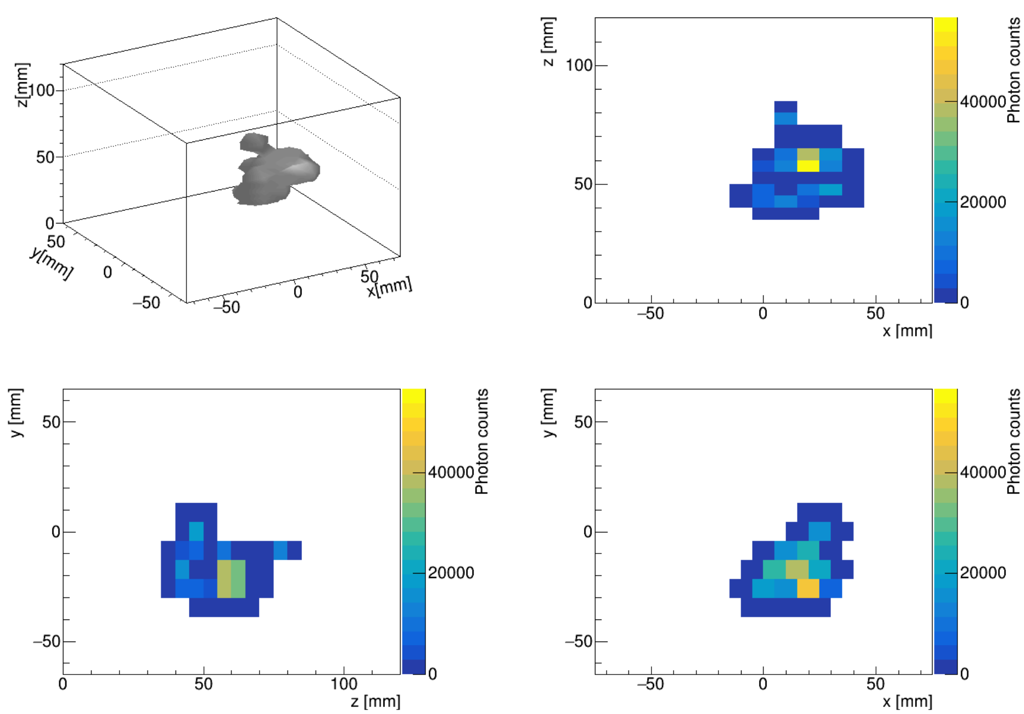

Figure 6.27: Event display of a 511 keV event.

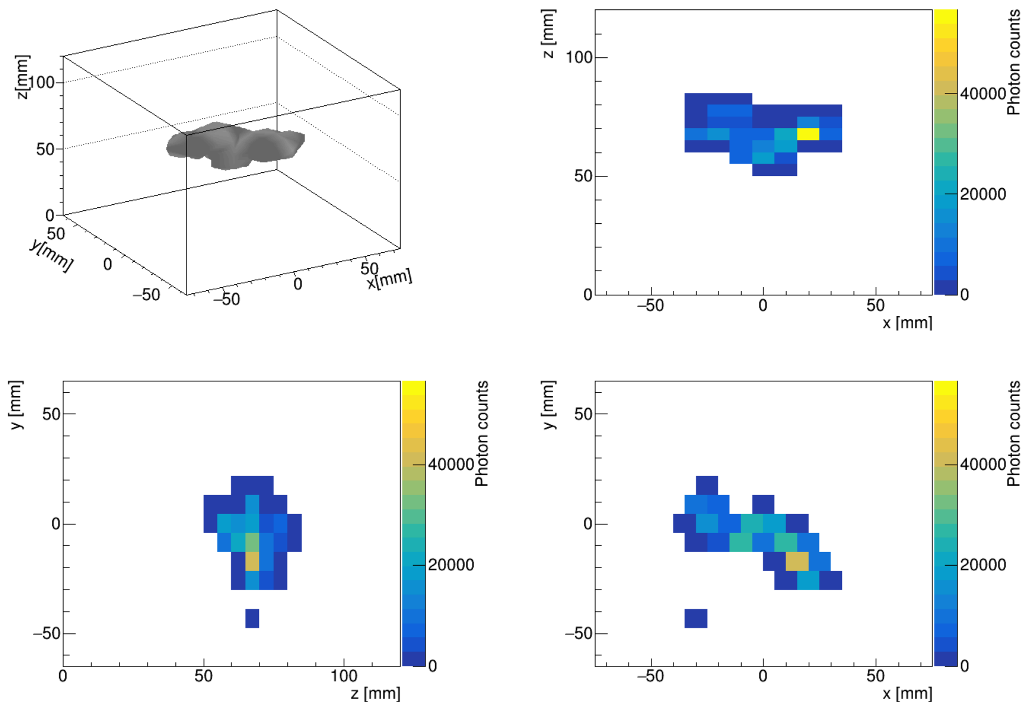

Figure 6.28: Event display of a 511 keV event.

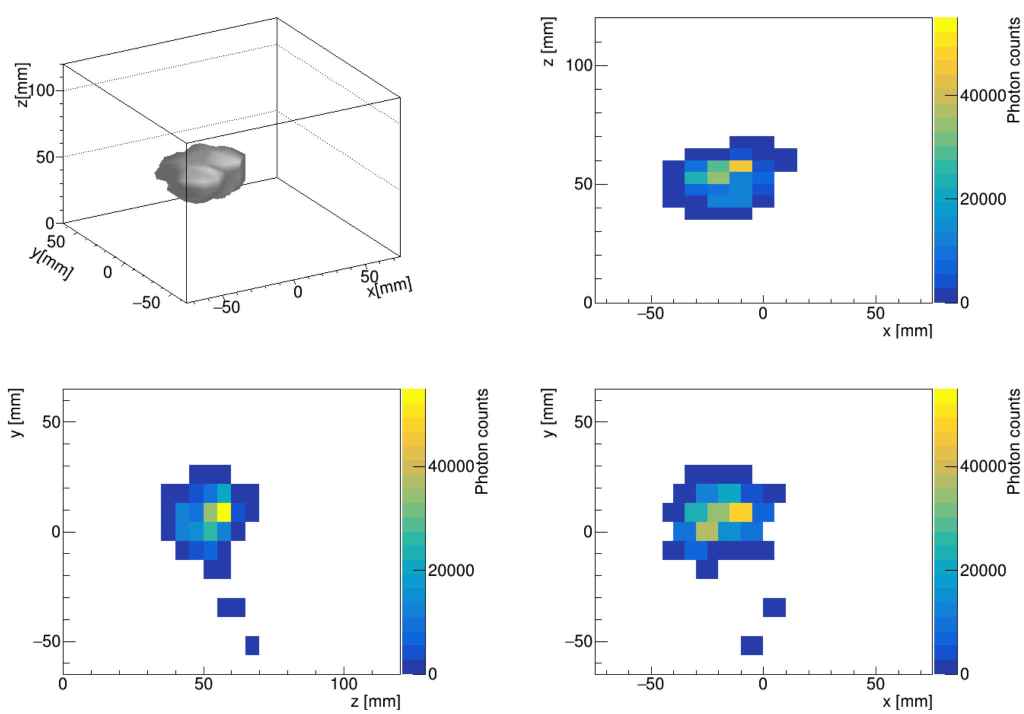

Figure 6.29: Event display of a 511 keV event.

6.12 Summary

The construction and evaluation of the first phase 180 L prototype were done. The stable operation for four days was achieved thanks to the slow monitors and interlock system for discharges. The performance was evaluated using 511 keV gamma-rays. The achieved energy resolution, 0.68% (FWHM), is comparable to the best energy resolution in the $0\nu\beta\beta$ decay search experiments using xenon. We succeeded to observe track patterns with the clear blob structure with the energy of 511 keV. In spite of the successful results above, the obtained energy resolution does not reach the target value, 0.5% (FWHM). The cause and detail of the obtained result are discussed in Chapter 7.

Chapter 7

Discussion and Future Prospects

7.1 Contamination of Backgrounds

$2\nu\beta\beta$ decay background

The background rate from the $2\nu\beta\beta$ decay is calculated by Equation (2.3). With the estimated energy resolution, 1.18% (FWHM) at the Q-value, obtained from the 180 L prototype, the fraction of 1.1×10^{-10} of $2\nu\beta\beta$ decay events is mixed in the $0\nu\beta\beta$ decay peak. With 1 ton of ^{136}Xe, 2×10^6 of $2\nu\beta\beta$ decay will occur in one year with $T^{2\nu}_{1/2} = 2.21 \pm 0.02(\text{stat}) \pm 0.07(\text{syst}) \times 10^{21}$ year. Therefore, the contamination of $2\nu\beta\beta$ decay background will be 2.2×10^{-4} events/year with the achieved energy resolution and it is negligible.

Gamma-ray background from ^{214}Bi

Figure 7.1 shows the simulated energy spectra of the ^{136}Xe $0\nu\beta\beta$ decay (red line) and the gamma-ray backgrounds from ^{214}Bi (blue line) with the energy resolution of 1.18% (FWHM). The ^{136}Xe $0\nu\beta\beta$ decay half-life of 10^{28} years and 10 tons of pressure vessel made of oxygen-free copper as the background source are assumed. The region of interest (ROI) defined as one FWHM range around the Q-value is also drawn in Figure 7.1. About 14 times more gamma-ray backgrounds compared to the $0\nu\beta\beta$ signals contaminate in the ROI. The algorithm of event selection with deep learning described in Section 2.2.3 reduces the gamma-ray background by 1/20. However, the algorithm uses the energy information, thus, the reduction might be less efficient.

7.2 Breakdown of the Obtained Energy Resolution

Sources determining the energy resolution at 511 keV, 1.49% (FWHM) are discussed here.

Intrinsic Fluctuation

Intrinsic fluctuation exists because of the statistical effect of the ionization electrons. It does not obey the simple Poisson distribution because the ionization process of each atom is not completely independent, instead, additional factor, so-called "Fano factor" is multiplied. The number of

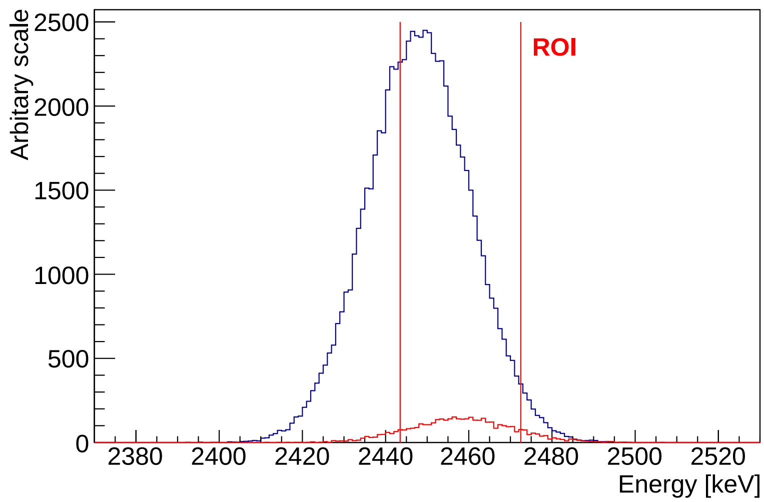

Figure 7.1: Expected energy spectrum around the ^{136}Xe $0\nu\beta\beta$ decay Q-value. The histogram drawn with red line represents $0\nu\beta\beta$ decay events. The blue histogram is for the ^{214}Bi gamma-ray background from a pressure vessel made of oxygen-free copper.

ionization electrons is estimated to be 511 keV/22.1 eV=24,333 electrons, where 22.1 is the W-value of ionization for xenon [49]. The fluctuation is calculated as

$$2.35 \times \sqrt{\frac{0.17}{24333}} = 0.0062, \tag{7.1}$$

where 0.17 is the Fano factor of xenon [49] and 2.35 is the factor to convert a standard deviation to FWHM.

Fluctuation of EL multiplication

Amplification fluctuation in the EL process causes deterioration of the energy resolution. Since the EL gain is 10.67, the amplification fluctuation is calculated as follows:

$$2.35 \times \sqrt{\frac{1}{24333} \cdot \frac{1}{10.67}} = 0.0046. \tag{7.2}$$

Normalized EL Gain

Errors of the normalized EL gain can cause the deterioration of the energy resolution. Figure 7.2 shows a distribution of the fitting errors of the fiducial channels. The mean of the distribution is 0.00927. Figure 7.3a shows the scatter plot of the photon count and the number of hits. The number of hits increases as the photon count increases. Figure 7.3b is the distribution of the number of hit channels at around 511 keV (505–520 keV). The mean number of hit channel for 511 keV events is 48. Among this, 99.8% of photons are detected by 30 channels on the average. Therefore, the contribution to the energy resolution is roughly calculated to be

$$2.35 \times \frac{0.00927}{\sqrt{30}} = 0.0040. \tag{7.3}$$

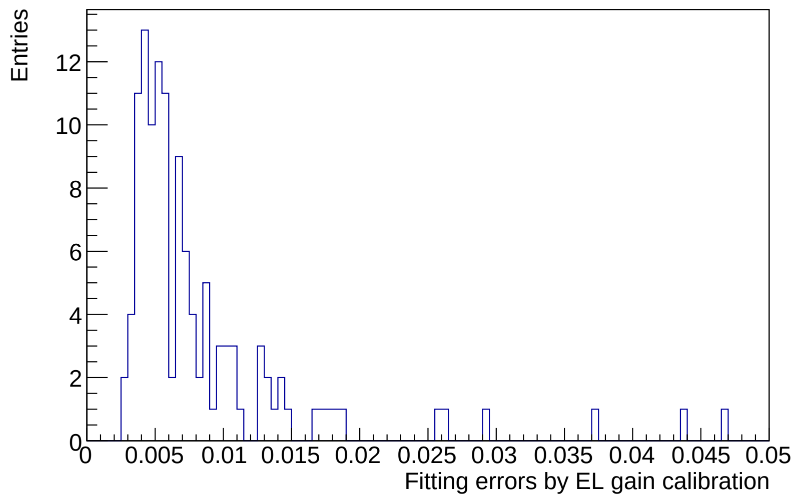

Figure 7.2: Distribution of fitting errors of normalized EL gains.

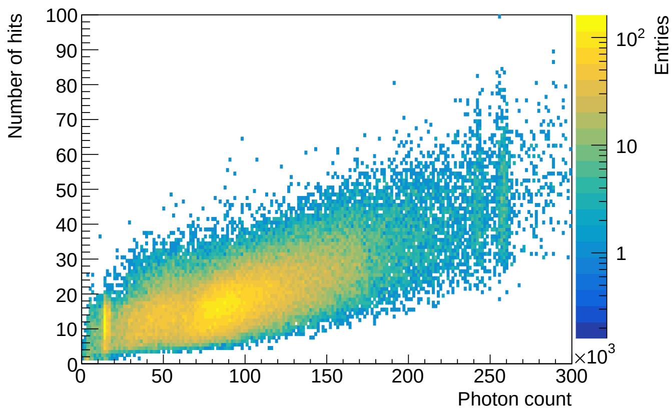

(a) Number of hits versus photon count of HP180L data.

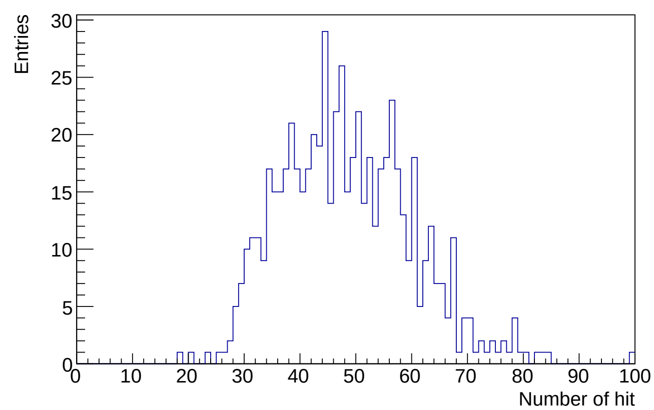

(b) Distribution of number of hits at around the 511 keV peak. Events with the energy between 505–520 keV are selected.

Figure 7.3: Number of hits.

Systematic Error of MPPC Recovery Time

The MPPC recovery times shown in Figure 6.11 have a systematic error of about 10 ns. A previous study has shown that the effect of this systematic error on the energy resolution is 0.0014 for ^{136}Xe $0\nu\beta\beta$ decay (2458 keV). Because we do not have a dedicated simulation study at 511 keV, here, the effect is estimated by assumptions. The value is converted to 0.0031 at 511 keV if it scales according to $1/\sqrt{E}$ [69].

Since the MPPC saturation correction mainly contributes to positions where the deposit energy is large, the MPPC saturation correction effect would be large at the track end blob. The blob's energy is considered to be almost constant regardless of the total deposit energy of an event. Considering that there are two blobs in the $0\nu\beta\beta$ decay and one blob in the gamma ray event, the effect of the systematic error of MPPC saturation correction is estimated to be

$$0.0014 \times \frac{2458}{511} \times \frac{1}{\sqrt{2}} = 0.0048. \tag{7.4}$$

Therefore, the contribution of the systematic error of MPPC saturation correction is evaluated as 0.0031–0.0095. Note that this component is proportional to $\sqrt{E}$ for the former and to $1/E$ for the latter.

Effect of Position Dependence

The dependence on the position relative to the cells is estimated to be 1.1% at 30 keV as described in Section 5.3.1. As discussed above, the mean number of effective hits at 511 keV is about 30 channels. The fluctuation is calculated as

$$2.35 \times 0.011 \times \frac{1}{\sqrt{30}} = 0.0047. \tag{7.5}$$

Error in the Correction of Time Dependency

Figures 7.4a and 7.4b show the distribution of the relative EL gain and the fitting error obtained by fitting the K_α peak for each time bin after the time dependency correction, which are represented by the red crosses in Figure 6.12b.

The standard deviation of the relative EL gain is 0.0017, which corresponds to 0.0037 (FWHM). This residual fluctuation may deteriorate the energy resolution.

In addition, the precision of the determination of the correction factor, that is, the fitting error can also worsen the energy resolution. The average fitting errors in Figure 7.4b is about 50 photons. The effect at 511 keV is estimated as follow:

$$\frac{50}{259,761} \times \frac{511}{29.78} = 0.0033, \tag{7.6}$$

where 259,761 is the average photon count at the 511 keV peak.

Combining these, the contribution of the time dependence correction is calculated to be

$$\sqrt{0.0037^2 + 0.0033^2} = 0.0050. \tag{7.7}$$

As expressed in Equation (7.6), this component is expected to affect the energy resolution depending on the energy linearly.

Error in the Correction of z Position

The inaccuracy of the correction factor of the z position dependency may deteriorate the energy resolution depending on the energy linearly. As shown in Section 6.7.4, the correction factor is $a = 0.00044 \pm 0.00012$. In order to estimate the impact of this error, the energy resolution was evaluated at the upper and lower limits with the error, respectively. The obtained energy resolutions at 511 keV are 1.53% (FWHM) with $a = 0.000315$ and 1.54% (FWHM) with $a = 000559$. The contribution from this error is roughly estimated as $0.0154 - 0.0153 = 0.0001$ (FWHM), which is negligible compared to the obtained energy resolution, 1.53%, and also negligible compared to the component proportional to E, 0.012.

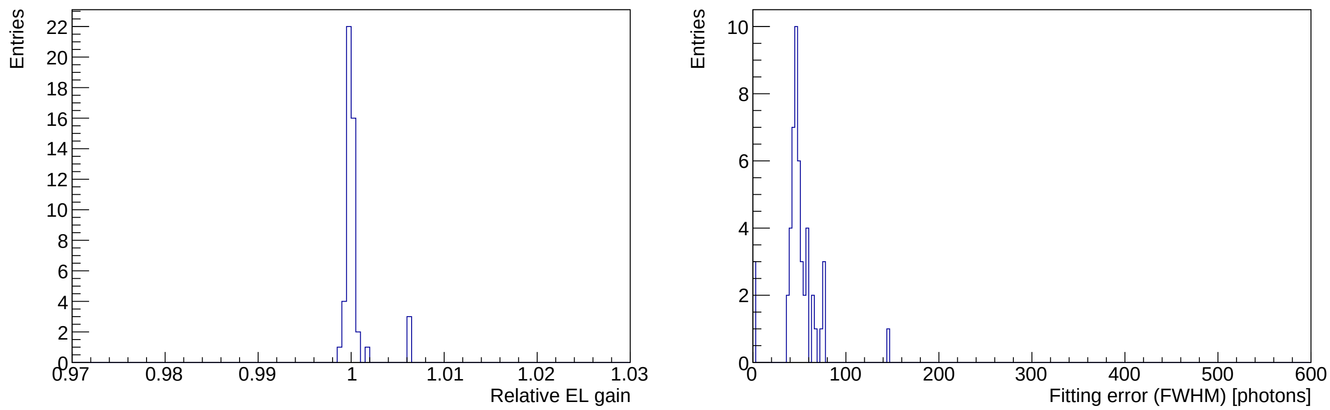

(a) Distribution of relative EL gain after the time dependence correction.

(b) Distribution of fitting errors at the K_α peak after the time dependence correction.

Figure 7.4: Effect of time correction.

Analysis Threshold

Another possible cause of the deterioration of the energy resolution, in particular, on the high energy side is the influence of the regions that are not regarded as hits due to the analysis threshold. Because the hit threshold in analysis is set to be 3.5 ADC counts above the baseline and the MPPC gain is about 2 ADC count, a cluster whose photon count is below 2.5 photons may not be regarded as a hit. Roughly, same order of missing hits may exist. Thus, there can be about 100 photon number fluctuation with the variation of number of hits as shown in Figure 7.3b. The contribution to the energy resolution (FWHM) is

$$\sim 100/259,761 \times 2.35 = 0.00090. \tag{7.8}$$

The obtained value is very small compared to the component proportional to E of 0.012, thus the influence of the analysis threshold is negligible.

Summary of the Breakdown of the Energy Resolution

The component of energy resolution which is proportional to $\sqrt{E}$ is calculated as

$$\sqrt{(0.62)^2 + (0.46)^2 + (0.40)^2 + (0.0\text{–}0.31)^2 + (0.47)^2} = 0.98\text{–}1.03\% \text{ (FWHM)}, \tag{7.9}$$

and the component which is proportional to E ($1/E$) is 0.50% (0.0–0.48%). The total energy resolution is estimated as

$$\sqrt{(0.62)^2 + (0.46)^2 + (0.40)^2 + (0.31\text{–}0.48)^2 + (0.47)^2 + (0.50)^2} = 1.15\text{–}1.21\% \text{ (FWHM)}. \tag{7.10}$$

Comparing to this estimation with the obtained energy resolution, 1.49%, it is found that the contribution of 0.88–0.95% (FWHM) exists as an unknown factor. One possibility of unknown factor is fluctuation of recombination rate of ionization electrons. The drift electric field was not completely uniform because of the distortion of the cathode electrode, and the recombination rate changes depending on the event position. To estimate this effect, it is necessary to measure the non-uniformity of the drift electric field.

The breakdown of the obtained energy resolution at 511 keV mentioned above is summarized in Table 7.1.

Table 7.1: Breakdown of the obtained energy resolution at 511 keV (FWHM).

Components	$\propto \sqrt{E}$	$\propto E$	$\propto 1/E$
Intrinsic fluctuation	0.62%	–	–
EL multiplication	0.46%	–	–
EL gain calibration	0.40%	–	–
MPPC recovery time	0.31%	or	0.48%
Position dependence	0.47%	–	–
Time correction	–	0.50%	–
Total of each component	0.98–1.03%	0.50%	0–0.48%
Unknown factor		0.88–0.95%	
Total		1.49%	

Prospect for Improvement of the Energy Resolution

In spite of the rough estimations by hand calculations discussed above, it is meaningful in terms of estimating what kinds of components determine the detector performance. For more precise estimation of each component, Monte-Carlo simulations should be performed. After more detailed estimation of the breakdown, we aim to improve correction methods for components that have large contributions for better energy resolution. As an idea of improved correction method, for example, K_β peak or 80 keV peak from ^{133}Ba gamma-ray source can be used for the EL gain calibration and time dependence correction in addition to the K_α peak.

7.3 Future Plan and Prospects

7.3.1 180 L prototype

For more understanding of energy resolution, it is important to perform several measurements at higher energies. Phased enlargements of the sensitive region are planned for the 180 L prototype. The number of ELCC units will be increased to 12 units and then to 27 units, which is the designed full version as shown in Figure 7.5. The field shaper will be replaced to that made of aluminium electrodes with the diameter of 40 cm as explained in Section 5.1.1. Challenges for the full detector are, for example, handling of higher voltages using a Cockcroft–Walton booster and establishing an efficient data transfer with larger number of channels. By expanding the sensitive region, it is possible to evaluate the detector at higher energy. We plan to evaluate the prototype with 1.1 MeV and 1.3 MeV gamma-rays from ^{60}Co, and 1.8 MeV gamma-rays from ^{88}Y. Detailed study of event topology will be possible in addition to the evaluation of the energy resolution with the full detector.

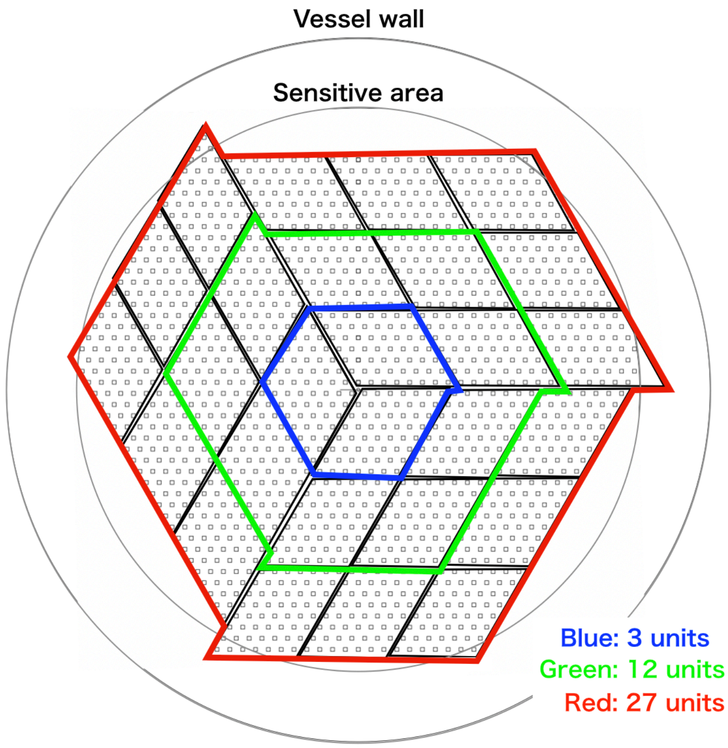

Figure 7.5: Plan for enlargements of the 180 L prototype. As a next step of the three units evaluation, operation with 12 units is planned (green line). The full version 180 L prototype will have 27 units ELCC represented by red line.

7.3.2 For $0\nu\beta\beta$ Decay Search

As discussed in Section 2.2.4, the original target sensitivity of the AXEL project is $\langle m_{\beta\beta}\rangle = 20$ meV, which covers all the region of inverted hierarchy of the neutrino mass ordering. However, recent results of oscillation experiments favor the normal mass ordering as mentioned in Section 1.3.2. To reach a sensitivity of the normal ordering region within 10 years, zero background is required with ton-scale $\beta\beta$-decay target mass. Thus, more powerful background rejection methods are required in addition to high energy resolution and track pattern recognition.

Tagging of the ^{136}Xe $0\nu\beta\beta$ decay daughter, ^{136}Ba^{++}, would be a strong evidence of the signal. The nEXO and NEXT experiments have been developing single barium ion tagging methods [76] [77]. We also started developing a single ^{136}Ba^{++} detection method. Figure 7.6 shows a possible configuration of the AXEL detector with a single ion detection scheme. Cells made of glass are placed behind the cathode electrode. Each cell has an electrode cooled to about 100 K by liquid nitrogen and liquid and solid xenon is formed in each cell. When a $\beta\beta$-decay occurs, the generated ^{136}Ba^{++} ion is drifted toward the cathode, collected into a cell, and trapped in solid xenon. The trapped barium ion is excited by irradiating a laser through the glass, then the de-excitation lights are observed, thereby the generation of a barium ion is confirmed [76]. To place the barium ion detection structure, PMTs for the primary scintillation photons are placed at the side wall of the vessel behind the field shaper. This configuration is possible because both of the energy and track pattern measurements are done at one side by ELCC. This ^{136}Ba tagging idea has just been proposed and needs to be verified.

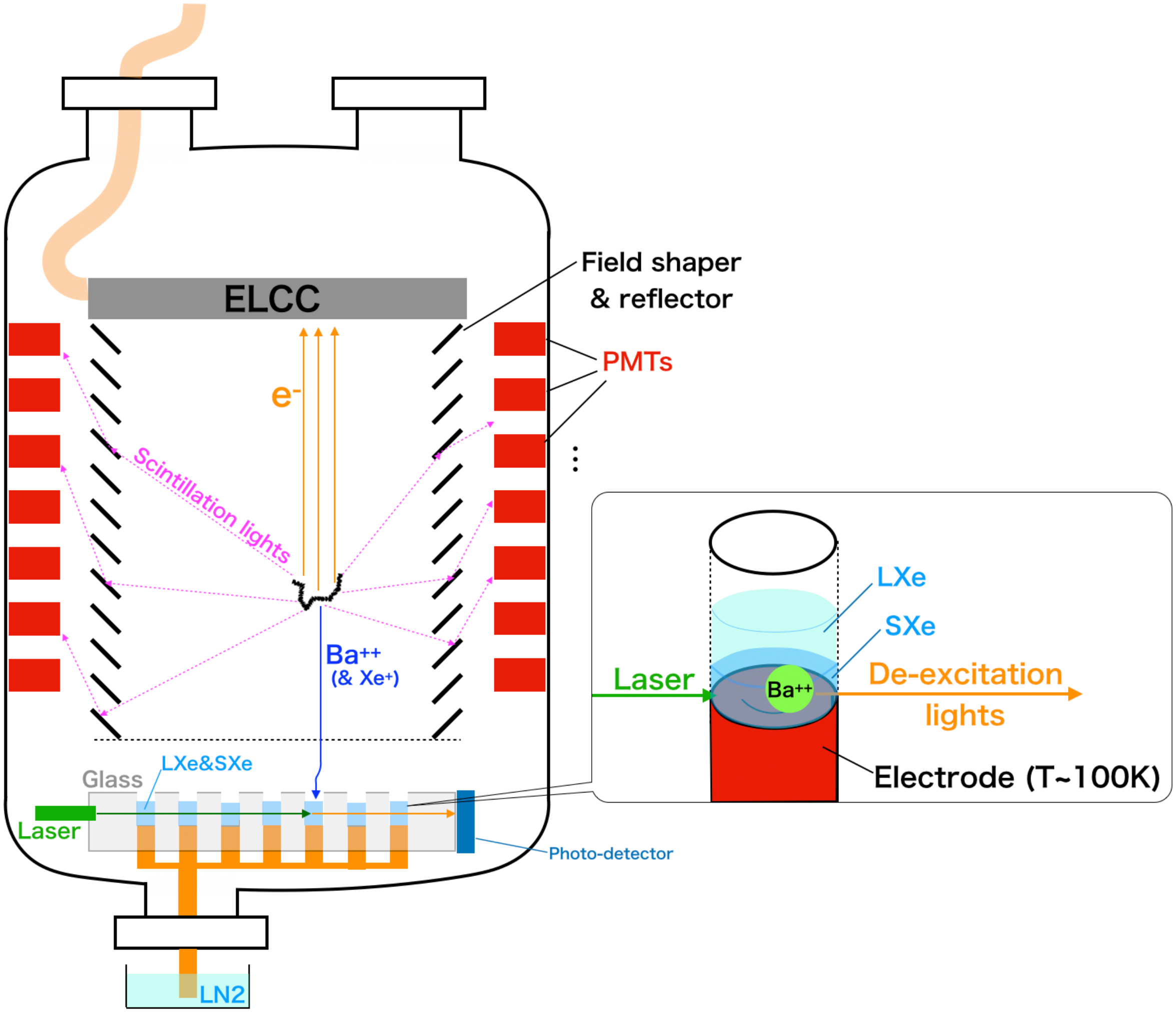

Figure 7.6: Schematic of the AXEL detector with a barium tagging scheme.

Chapter 8

Conclusion

Searching for neutrinoless double-beta ($0\nu\beta\beta$) decay is important to reveal the mysteries of neutrino. Observation of $0\nu\beta\beta$ decay would confirm that neutrinos are Majorana particles. Unnaturally light neutrino masses may be explained by the seesaw mechanism if neutrinos are Majorana particle. The origin of the matter-antimatter asymmetry in the universe may also be explained by right handed Majorana neutrinos via leptogenesis. The current limit of the half life of $0\nu\beta\beta$ decay is given, for example, for ^{136}Xe by KamLAND-zen experiment as $T^{0\nu}_{1/2} > 1.07 \times 10^{26}$ years (90% C.L.). It is extremely rare process even if it occurs. To detect such rare decay events, ton-scale target masses and extremely low background environment are required. Good energy resolution is important not only to distinguish external background, but also to distinguish the intrinsic background of $2\nu\beta\beta$ decay.

We proposed a new high pressure xenon gas TPC employing a unique cellular structure to collect ionization electrons and detect electroluminescence (EL) light, named "A Xenon ElectroLuminescence (AXEL)". The EL process does not accompany an avalanche multiplication process, thus good energy resolution can be obtained by utilizing this process. We expect 0.5% (FWHM) energy resolution at the ^{136}Xe $0\nu\beta\beta$ decay Q-value, 2458 keV. Three-dimensional track pattern can be reconstructed from the information of hit timing and pattern. The track pattern can be used to reject alpha-ray and gamma-ray backgrounds.

The project is now in a R&D phase prior to the $0\nu\beta\beta$ decay search. Since the ionization detection method is brand-new, proof of principle and establishment of the detector technology are necessary. Two prototypes, 10 L prototype and 180 L prototype, have been constructed for that purpose.

Many problems happened to make the 10 L prototype operational, especially, discharges occurred in various places. During the course of solving these problems, discharge-resistant design has been established. The performance was evaluated using 122 keV gamma-rays at 4 bar and 356 keV gamma-rays at 8 bar with the 10 L prototype. The analysis flow with waveform processing, event selections, and correction methods has been established. The energy resolution of 4.16±0.30% (FWHM) is achieved at 122 keV at 4 bar. Other peaks (the K_α, K_β and escape peaks) were also evaluated. From the obtained results, the energy resolution at the Q-value is estimated to be 0.88±0.04% (FWHM) assuming the statistical fluctuation ($\propto E$) only and 1.74±0.16% (FWHM) with additional component proportional to the deposit energy, E. At 8 bar, the achieved energy resolution is 2.54±0.20% (FWHM) at 356 keV and the estimated energy resolution is 0.85±0.028% (FWHM) by extrapolation by $\sqrt{E}$ and 1.70±0.084% (FWHM) with additional term proportional to E. The principle of the ELCC was confirmed from these results. The achieved energy resolutions are quite high, however, these results do not reach the target resolution, 0.5% (FWHM). It turned out that the collection efficiency of ionization electrons in ELCC is less than 100%. It may be a cause of the component proportional to E and may deteriorate the energy resolution. The ELCC configuration was changed to hexagonal pattern with 13 mm-pitch and 7 mm-diameter. The simulation shows the collection efficiency of drift electrons is almost 100% for this configuration. However, the performance with this cell configuration is not good and a detailed ELCC simulation shows the position dependence of the EL gain which worsen the energy resolution.

Based on the detailed simulation, the dimensions of ELCC were optimized and adopted to the 180 L prototype. ELCC for the 180 L prototype is made as unit style, thus, it is easy to expand by assembling multiple units. As a first phase of the 180 L prototype, the field shaper for the 10 L prototype was installed. The number of readout channel is 168. The gas circulation and purification system and interlock system for discharges have been established. The detector had been stably operated for four days thanks to the monitoring system and the interlock systems. The performance was evaluated using 511 keV gamma-ray at 4 bar. The peak at 511 keV and its escape peak were clearly seen with this prototype for the first time in our experiment. The achieved energy resolutions are 4.50±0.05% (FWHM) at the K_{α} peak and 1.49±0.04% (FWHM) at 511 keV. The estimated energy resolution is 1.18±0.01% (FWHM) at Q-value assuming the statistical fluctuation and the additional dependence on energy linearly. The result is improved compared to that of the 10 L prototype and now is comparable to the best energy resolution in $0\nu\beta\beta$ decay search experiments using xenon. The track patterns with the characteristic blob structure were also observed. We foresee that the energy resolution will be improved and become close to the target value with more careful treatment of EL gain calibration and z position correction.

For the future 180 L prototype, we plan to expand the detector and evaluate its performance at higher energies, in particular, at around the ^{136}Xe $0\nu\beta\beta$ decay Q-value. A $0\nu\beta\beta$ search will start with a 1000 L size detector and about 40 kg ^{136}Xe enriched xenon gas after the evaluation of the detector performance and the investigation of backgrounds by the 180 L prototype. A physics run aiming to cover all the region of the inverted neutrino mass ordering is planed with a ton-scale detector. Furthermore, we have started a study of a single barium ion tagging as a powerful background rejection method. A ton-scale detector with a barium tagging scheme is expected to reach the sensitivity of $\langle m_{\beta\beta} \rangle$ =1 meV.

Appendix A

Previous Works of Prototypes

A.1 HP10L Version 1

A.1.1 Detector

As the first phase of the 10 L prototype, we developed a TPC with 32 channels ELCC and a ring field shaper whose diameter is 9 cm and length is 6 cm. Figure A.1 shows the configuration of MPPCs. The pitch of MPPCs is 7.5 mm. The MPPCs (type number: S12572-025C, Hamamatsu Photonics K.K.) used in HP10L Version 1 do not sensitive to VUV lights, thus the wavelength of xenon EL lights is converted to visible light by WLS plate as shown in Figure A.2 on the MPPCs. On the MPPCs and WLS plate, the ELCC is assembled as shown in Figure A.3. Then the field shaper is installed (Figure A.4).

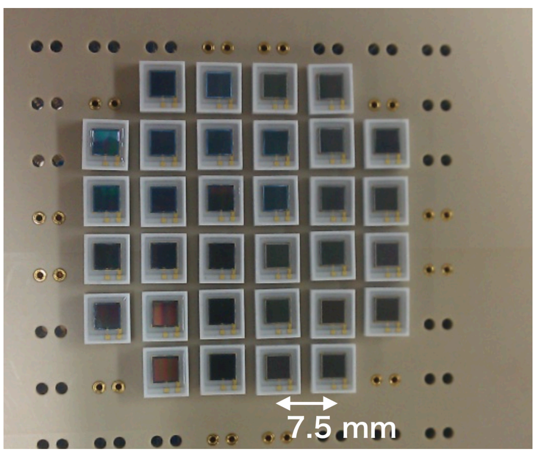

Figure A.1: MPPCs.

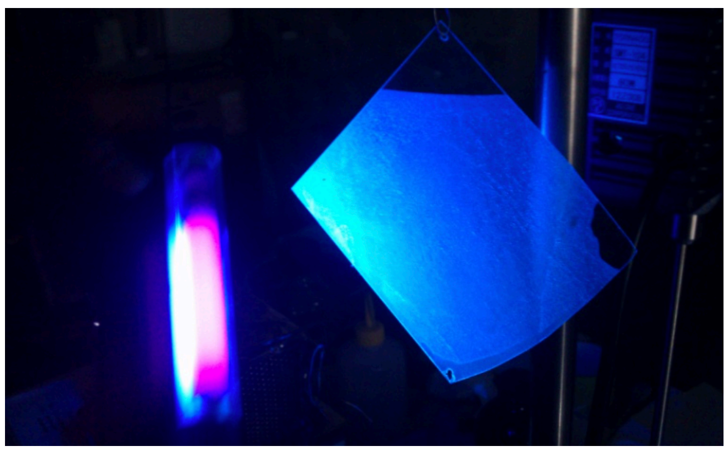

Figure A.2: Plate that wave length shifter is coated. It scintillates by irradiated UV lights from left.

A.1.2 Experimental Condition

Measurements with the 10 L prototype Version 1 was done using 4 bar xenon gas. The gas circulation system was not introduced at this time, the gas was installed through a molecular-sieve

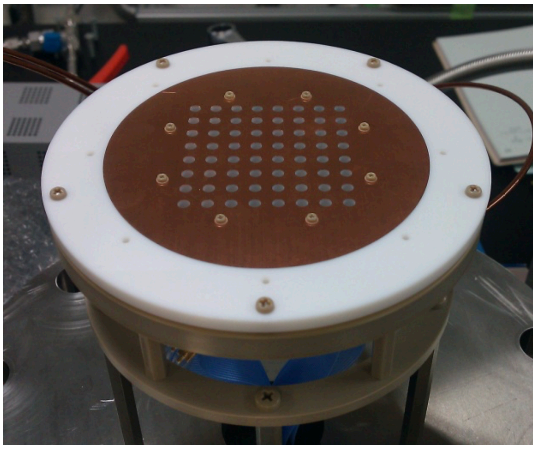

Figure A.3: Picture of ELCC.

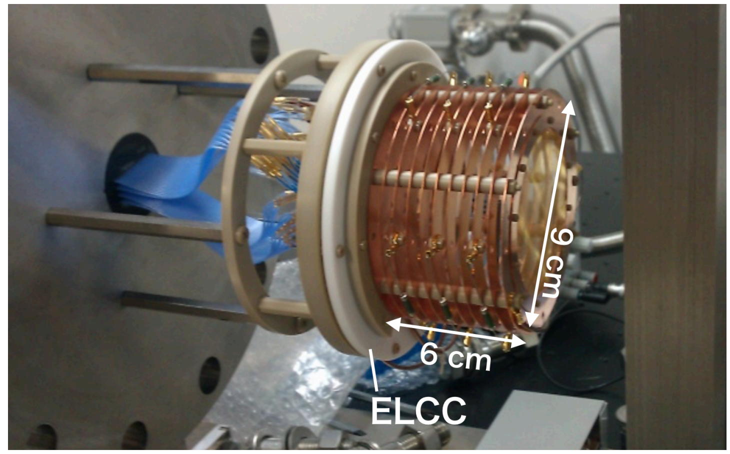

Figure A.4: Picture of whole detector.

filter once and sealed during the measurement. Various electric field strengths were applied to the anode and the cathode electrodes. The set electric fields are summarized in Table A.1. A ^{57}Co gamma-ray source was used for evaluations.

Table A.1: Data set.

Data	E_{EL} [kV/cm/bar]	E_{EL} [V/cm/bar]	Data	E_{EL} [kV/cm/bar]	E_{EL} [V/cm/bar]
Data 1	2.25	23.25	Data 6	2.25	93.25
Data 2	2.25	46.75	Data 7	2.25	116.75
Data 3	2.25	58.25	Data 8	2.25	140.0
Data 4	2.25	70.0	Data 9	1.92	40.0
Data 5	2.25	80.0	Data 10	1.60	33.25

A.1.3 Analysis

The MPPC gains were obtained using the "threshold method". The algorithm for EL waveform processing is the same as that in Section 4.2.3. Fully contained events were selected by rejecting the events that have hits at the outer most cells. Since PMTs were not installed, fiducial cut along z direction was not applied. The EL gain was calibrated using 30 keV peak.

Figure A.5 shows a photon count spectrum of Data 4, which shows the best energy resolution among the data set in Table A.1, after the fiducial cut and EL gain calibration. Three peaks are clearly seem at $\sim$ 650 photons (characteristic X-ray, 30 keV), $\sim$ 2100 photons (escape peak, 90 keV), and $\sim$ 2900 photons (full peak, 120 keV). The number of photons at 30 keV, 650 photons, is very small compared to that with HP10L Version 3 and Version 4. This may be because the purity of the gas was poor and the luminous efficiency of the WLS is not high.

A.1.4 Evaluation of the Performance

The fit results in Figure A.5 are summarized in Table A.2. The energy resolutions are poor compered to that with HP10L Version 3 and Version 4. This is because of the poor photon

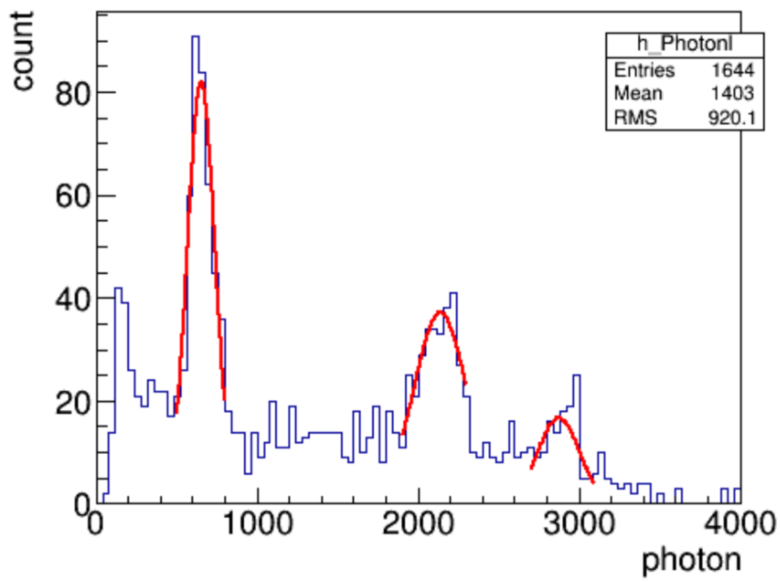

Figure A.5: Photon count spectrum of Data 4. Fit results with Gaussian for 30 keV, 90 keV, and 120 keV peaks are also shown.

statistics.

Table A.2: Fit results of each peak.

Energy	Photon count at peak center	Energy resolution (FWHM) [%]
30 keV	653.6	30.6
90 keV	2138.5	17.8
120 keV	2874.4	10.5

The light yield dependence on the drift field is studied and shown in Figure A.6. The maximum exists at around 70 V/cm/bar. In the region below the drift field of 70 V/cm/bar, the drift velocity decreases and attachment because of impurities in the gas may be serious. In the region above 70 V/cm/bar, collection efficiency of the electric field lines, thus, the drift electrons into cells gets worse. The tendency of the electric field lines above $E_{\mathrm{drift}} = 70$ V/cm/bar was reproduced by a simulation as shown in Figure A.6b.

The light yield dependence on the EL field is shown in Figure A.7. It increases linearly as the EL field increases. This dependence agrees Equation (2.7).

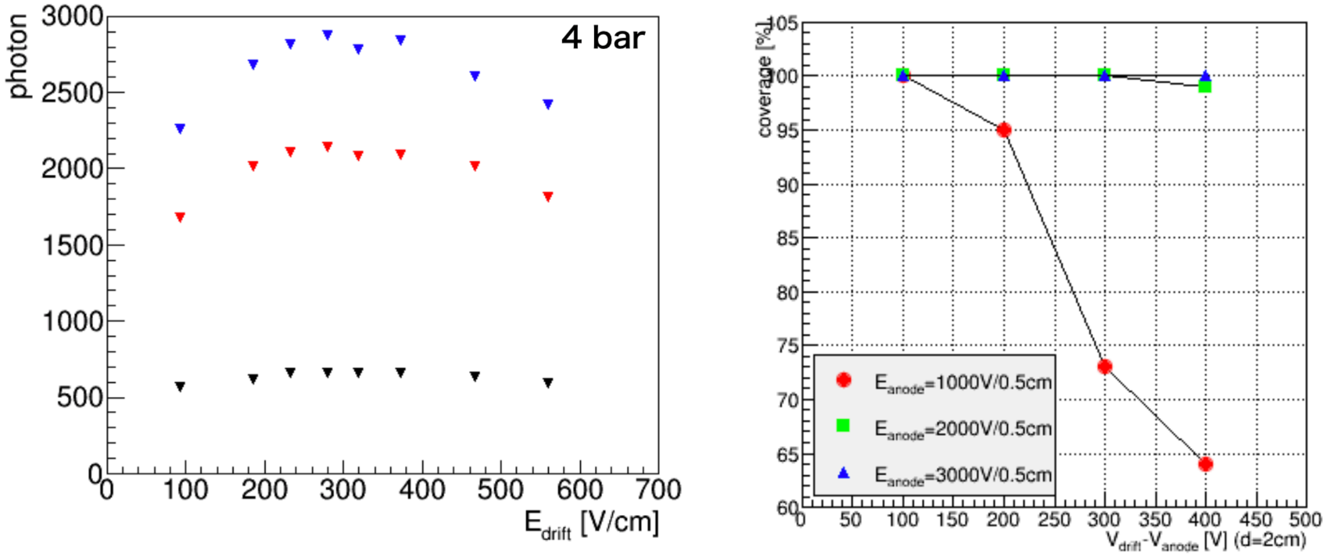

(a) Light yield as a function of the drift field. Black points represent the 30 keV, red points the 90 keV, and blue points the 120 keV peaks.

(b) Light yield as a function of the drift field by simulation.

Figure A.6: Light yield dependence on the drift electric fields.

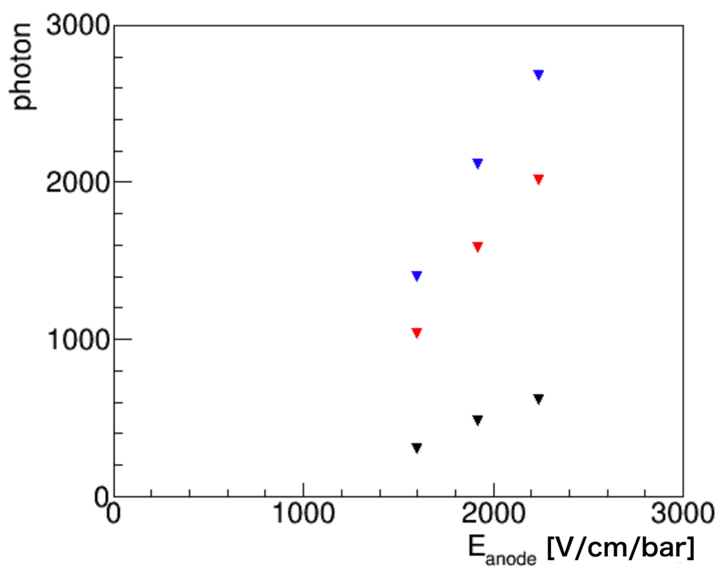

Figure A.7: Light yield as a function of the EL field. Black points represent the 30 keV, red points the 90 keV, and blue points the 120 keV peaks.

A.1.5 Summary and Discussion

The first evaluation of the 10 L size prototype was performed with 32 channels ELCC and at 4 bar. Peak structures can be seen at 30 keV, 90 keV, and 120 keV, however, their photon counts are very low compared to the measurements in Chapter 4 because of the impurities in the gas or low luminous efficiency of the WLS. The performance of HP10L Version 1 was evaluated. The best energy resolution is 10.5% (FWHM) at 120 keV corresponding to 2.32% at the ^{136}Xe $0\nu\beta\beta$ decay Q-value converted by $\sqrt{E}$. The electric field dependence was also investigated and the tendencies were understood.

For the better performance, purification of the xenon gas is needed and a production method of WLS should be improved.

A.2 HP10L Version 2: WLS plate

A.2.1 Detector

In the 10 L prototype Version 2, the number of MPPCs increased from 32 to 64. The field shaper is the same as that of Version 1. One PMT is installed in this phase. However, signals from PMT were not used in analysis in this time. The assembled detector is shown in Figure A.8. The WLS plate is renewed with more transparent acrylic plate and better composition (Figure A.9).

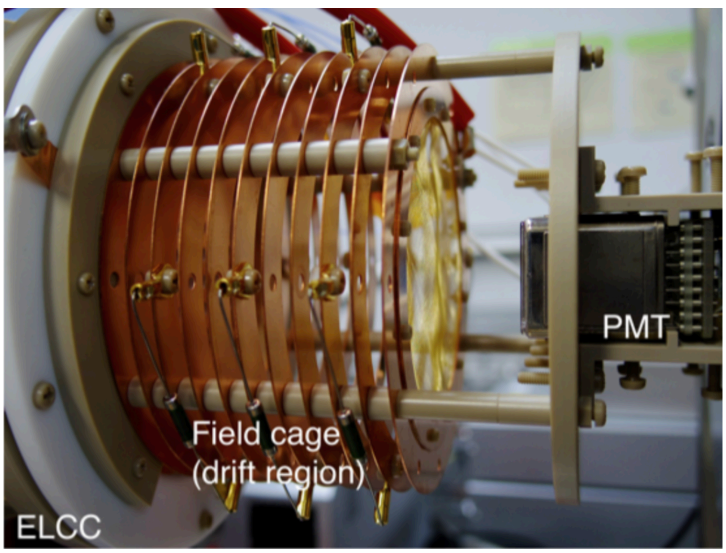

Figure A.8: Detector.

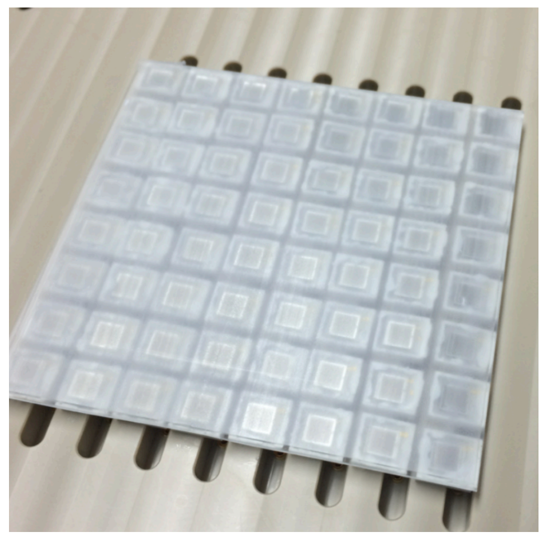

Figure A.9: MPPCs and plate that WLS is coated.

A.2.2 Experimental Condition

Measurements with Version 2 was done at 4 bar. The gas was installed through the molecular-sieve filter and sealed during the measurement. The EL field was 2.4 kV/cm/bar and the drift field was 50 V/cm/bar. The EL field was limited by discharges and with set EL field, the drift field was set to the value that collection efficiency of electric field lines is estimated to be 100% by simulation. A ^{57}Co gamma-ray source was used for the evaluation.

A.2.3 Analysis

The analysis flow is the same with that of Version 1. Figure A.10 shows the photon count spectrum after the cuts and EL gain calibration. The peaks of K_α and K_β are separated thanks to the improved resolution. The 90 keV and 120 keV peaks are also clearly seen. The photon count at each peak increases significantly compared to Version 1 thanks to improvement of WLS sheet.

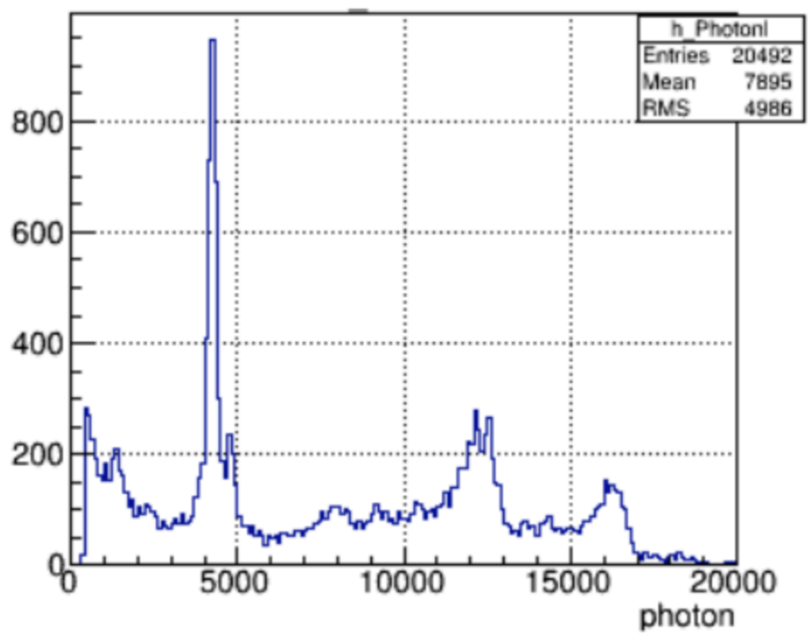

Figure A.10: Photon count spectrum after cuts and EL gain calibration. K_α and K_β peaks are separated and 90 keV, 120 keV peaks are also clearly seen.

A.2.4 Evaluation of the Performance

The performance of Version 2 was evaluated by fitting each peak with a Gaussian. The fit results are summarized in Table A.3. The obtained energy resolutions are much better than that of Version 1 thanks to improved photon statistics. The energy resolutions of each peak were fitted with the function: $A\sqrt{E} + BE$ and extrapolated to 2458 keV to estimate the performance at the Q-value. The obtained results are $A = 0.324 \pm 0.559$ and $B = 0.040 \pm 0.058$. With these values, the energy resolution at the Q-value is estimated to be 4.64% (FWHM).

Table A.3: Fit results of each peak.

Energy	Photon count at peak center	Energy resolution (FWHM) [%]
29.78 keV	4245.1	7.2
33.62 keV	4791.4	8.8
90 keV	12256.8	9.9
120 keV	16221.2	5.7

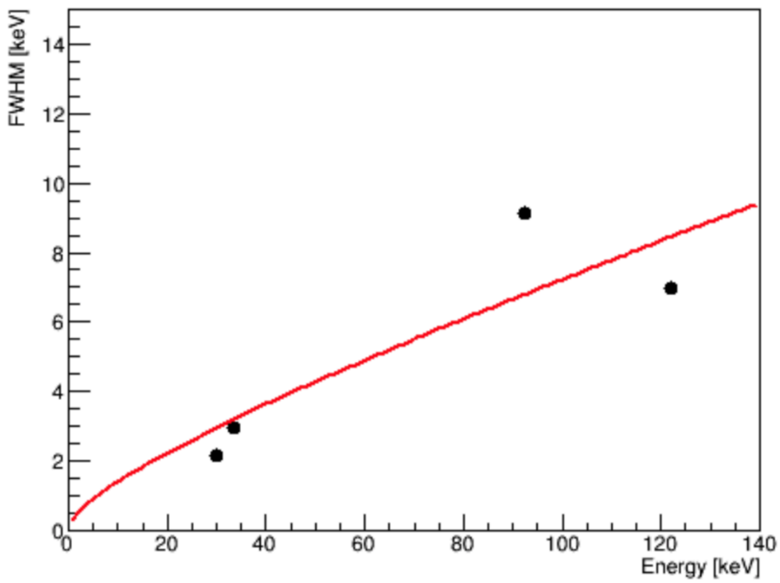

Figure A.11: Fit result of the energy resolution of each peak with the function: $A\sqrt{E} + BE$.

A.2.5 Summary and Discussion

The photon statistics was greatly improved compared to HP10L Version 1 because of the improvement of the WLS plate. Hence, the energy resolution was also improved and the estimated energy resolution at the Q-value is 4.64% (FWHM). The obtained result is an order of magnitude worse than the target resolution. It is considered that a crosstalk of EL lights between multi cells and a loss of EL lights inside the WLS plate worsen the energy resolution. For more good resolution, the method using one WLS plate is rejected,

A.3 HP10L Version 2: WLS coated on SiPMs

A.3.1 Detector

To avoid the crosstalk and loss of the EL photons in the WLS plate, WLS was directly coated on the MPPC surface as shown in Figure A.12. The light yield is expected to be increased.

A.3.2 Experimental Condition

The 10 L prototype Version 2 with WLS coated on the MPPC surface was evaluated at 4 bar using 122 keV gamma-ray. The gas was again installed through the molecular-sieve filter and sealed during the measurement. The EL field was 2.4 kV/cm/bar and the drift field was 50 V/cm/bar.

A.3.3 Analysis

The analysis flow is almost same with that of Version 1. In addition, the light yield dependence on data taking time was seen because of impurities in the gas as shown in Figure A.13a. This dependence was corrected.

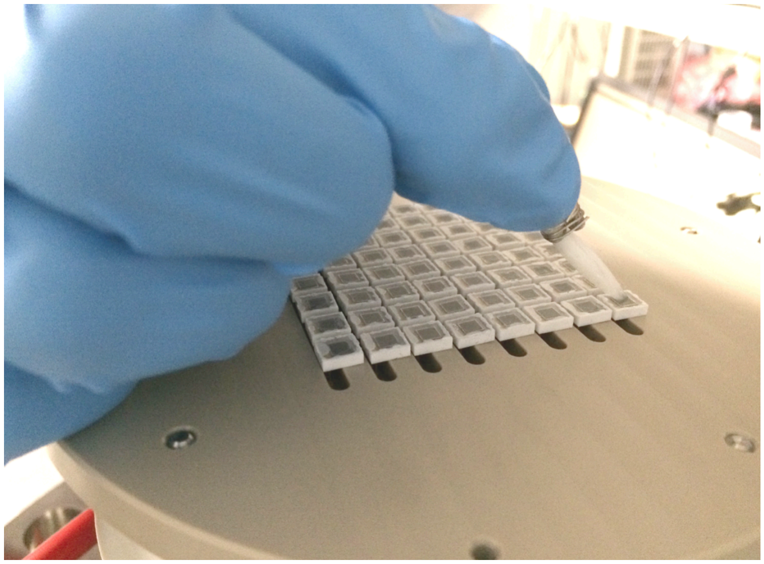

Figure A.12: MPPCs directly coated by WLS.

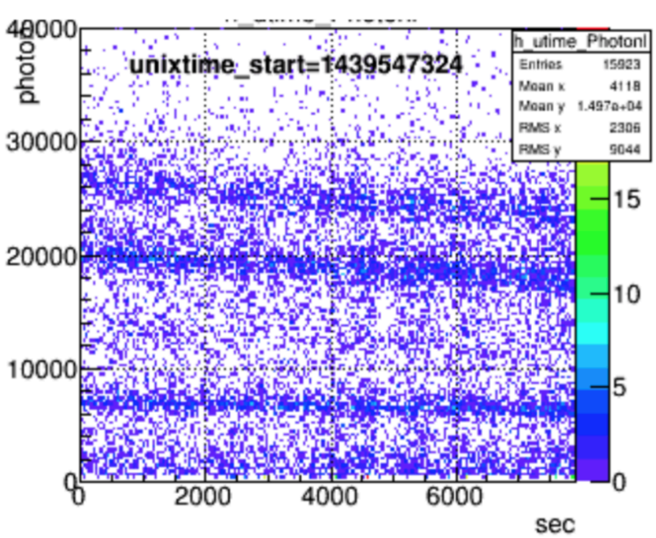

(a) Photon count as a function of time. The light yield decreases because of impurities in the gas.

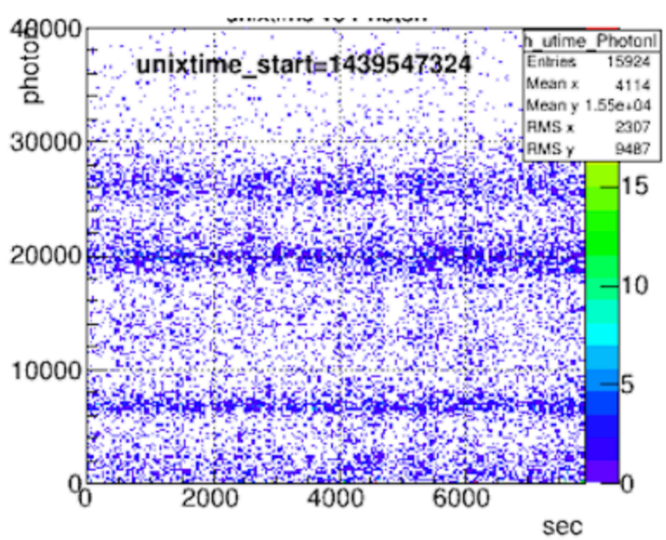

(b) Photon count as a function of time after correction.

Figure A.13: Light yield as a function of the data taking time.

Furthermore, positive correlations of "hit volume" were seen for each peak cluster as shown in Figure A.14a. Now, we know the cause of this correlation is due to the saturation of MPPC signal. However, during the analysis, the cause was still unknown. Therefore, the correction for the positive correlation is directly applied. The plot of photon count and the hit volume after the correction is shown in Figure A.14b.

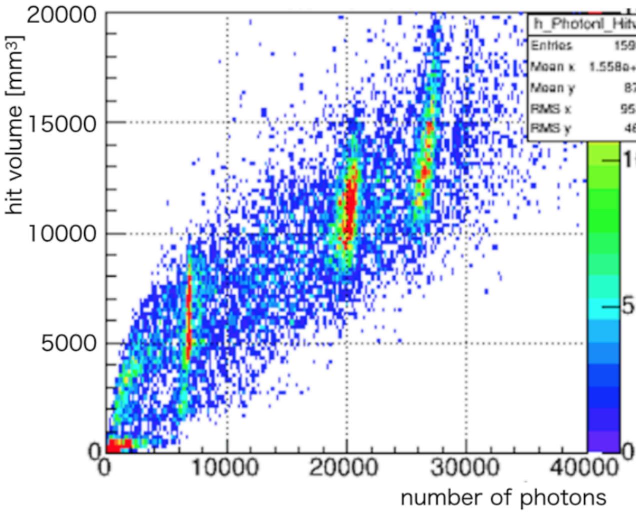

(a) Photon count versus hit volume. Positive correlations at each peak cluster are seen.

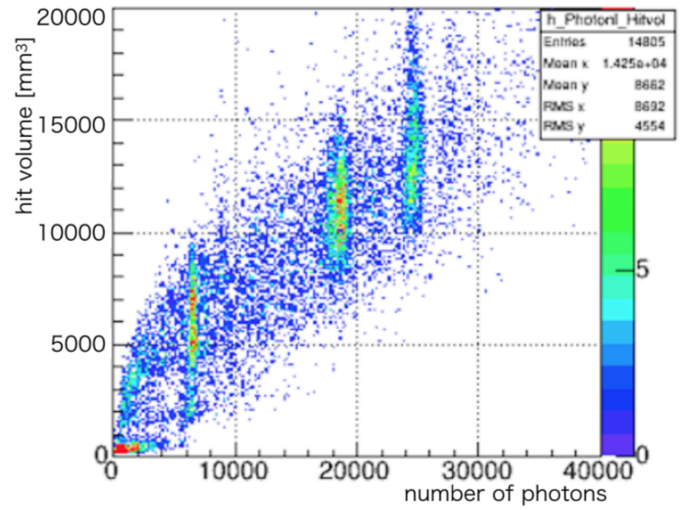

(b) Photon count versus hit volume after correction.

Figure A.14: Photon count versus hit volume.

A.3.4 Evaluation of the Performance

The photon count spectrum after the cuts and all corrections is shown in Figure A.15. The performance was again evaluated by fitting each peak with a Gaussian. The fit results are summarized in Table A.4. The light yield further increases compared to the previous measurement. The energy resolutions of each peak were fitted with the function: $A\sqrt{E} + BE$ and the fit results are $A = 0.423 \pm 0.070$ and $B = 0.0097 \pm 0.0073$ (see Figure A.16). The energy resolution at the Q-value is estimated to be 1.82% (FWHM).

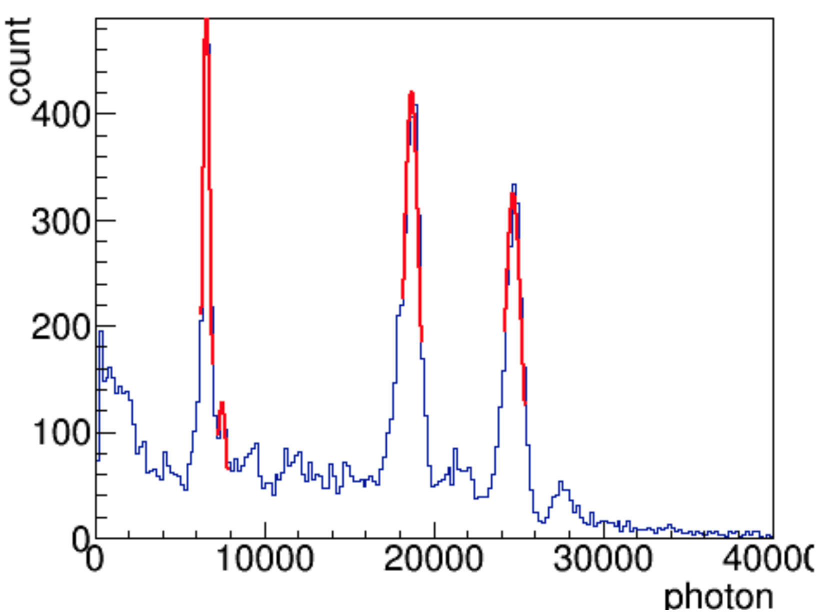

Figure A.15: Photon count spectrum after cuts and corrections.

Table A.4: Fit results of each peak.

Energy	Photon count at peak center	Energy resolution (FWHM) [%]
29.78 keV	6604.6	7.9
33.62 keV	7516.2	8.7
90 keV	18711.4	5.6
120 keV	24710.2	4.7

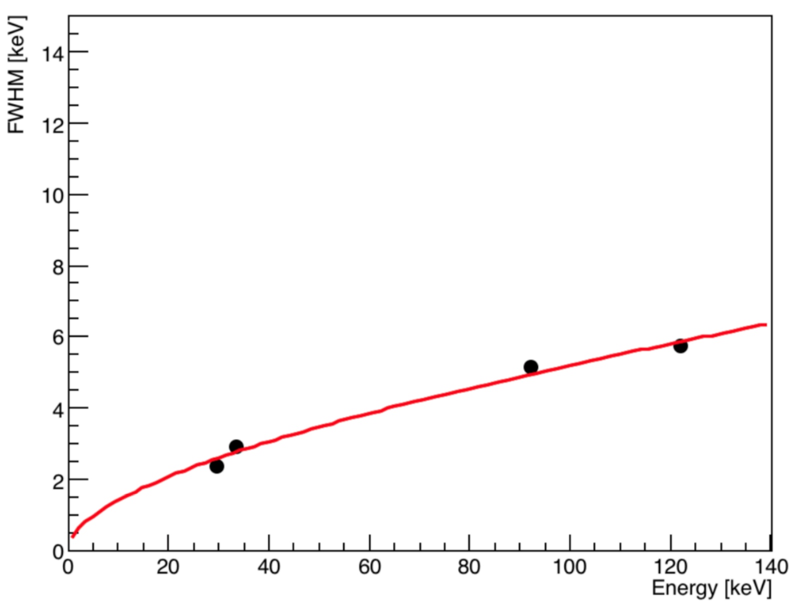

Figure A.16: Fit result of the energy resolution of each peak with the function: $A\sqrt{E} + BE$.

List of Figures

List of Tables

Bibliography

[1] W. Pauli. *Letter of 4 December to L.Meitner et al.*, 1930.

[2] E. Fermi. *Z. Phys*, 88(3):161 – 177, 1934.

[3] F. Reines, C. L. Cowan, F. B. Harrison, A. D. McGuire, and H. W. Kruse. Detection of the free antineutrino. *Phys. Rev.*, 117:159–173, Jan 1960.

[4] G. Danby, J-M. Gaillard, K. Goulianos, L. M. Lederman, N. Mistry, M. Schwartz, and J. Steinberger. Observation of high-energy neutrino reactions and the existence of two kinds of neutrinos. *Phys. Rev. Lett.*, 9:36–44, Jul 1962.

[5] K. Kodama et al. Observation of tau neutrino interactions. *Phys. Lett.*, B504:218–224, 2001.

[6] S. Schael et al. Precision electroweak measurements on the Z resonance. *Phys. Rept.*, 427:257–454, 2006.

[7] John N. Bahcall and Raymond Davis. Solar neutrinos: A scientific puzzle. *Science*, 191(4224):264–267, 1976.

[8] Y. Fukuda et al. Atmospheric $\nu_\mu \nu_e$ ratio in the multi-gev energy range. *Physics Letters B*, 335(2):237 – 245, 1994.

[9] Y. Fukuda and others. Evidence for oscillation of atmospheric neutrinos. *Phys. Rev. Lett.*, 81:1562–1567, Aug 1998.

[10] Q. R. Ahmad et al. Measurement of the rate of $\nu_e + d \rightarrow p + p + e^-$ interactions produced by ^{8}b solar neutrinos at the sudbury neutrino observatory. *Phys. Rev. Lett.*, 87:071301, Jul 2001.

[11] M. Tanabashi et al. Review of particle physics. *Phys. Rev. D*, 98:030001, Aug 2018.

[12] K. Abe et al. Atmospheric neutrino oscillation analysis with external constraints in super-kamiokande i-iv. *Phys. Rev. D*, 97:072001, Apr 2018.

[13] Ivan Esteban, M. C. Gonzalez-Garcia, Alvaro Hernandez-Cabezudo, Michele Maltoni, and Thomas Schwetz. Global analysis of three-flavour neutrino oscillations: synergies and tensions in the determination of θ_{23}, δ_{CP}, and the mass ordering. *JHEP*, 01:106, 2019.

[14] G. Drexlin, V. Hannen, S. Mertens, and C. Weinheimer. Current direct neutrino mass experiments. *Adv. High Energy Phys.*, 2013:293986, 2013.

[15] M. Aker et al. Improved upper limit on the neutrino mass from a direct kinematic method by katrin. *Phys. Rev. Lett.*, 123:221802, Nov 2019.

[16] N. Aghanim et al. Planck 2018 results. VI. Cosmological parameters. 2018.

[17] A. Gando et al. *Phy. Rev. Lett.*, 117:082503, 2016.

[18] Sacha Davidson, Enrico Nardi, and Yosef Nir. Leptogenesis. *Phys. Rept.*, 466:105–177, 2008.

[19] A. D. Sakharov. Violation of CP Invariance, C asymmetry, and baryon asymmetry of the universe. *Pisma Zh. Eksp. Teor. Fiz.*, 5:32–35, 1967. [JETP Lett.5,24(1967); Sov. Phys. Usp.34,no.5,392(1991); Usp. Fiz. Nauk161,no.5,61(1991)].

[20] Y. Aoki, F. Csikor, Z. Fodor, and A. Ukawa. The end point of the first-order phase transition of the su(2) gauge-higgs model on a 4-dimensional isotropic lattice. *Phys. Rev. D*, 60:013001, May 1999.

[21] Patrick Huet and Eric Sather. Electroweak baryogenesis and standard model cp violation. *Phys. Rev. D*, 51:379–394, Jan 1995.

[22] Georges Aad et al. Search for squarks and gluinos in final states with same-sign leptons and jets using 139 fb^{-1} of data collected with the ATLAS detector. 2019.

[23] Albert M Sirunyan et al. Search for supersymmetry in events with a photon, jets, b -jets, and missing transverse momentum in proton–proton collisions at 13 TeV. *Eur. Phys. J.*, C79(5):444, 2019.

[24] M. Fukugita and T. Yanagida. Baryogenesis Without Grand Unification. *Phys. Lett.*, B174:45–47, 1986.

[25] T. Asaka, K. Hamaguchi, M. Kawasaki, and T. Yanagida. Leptogenesis in inflaton decay. *Physics Letters B*, 464(1):12 – 18, 1999.

[26] Hitoshi Murayama and T. Yanagida. Leptogenesis in supersymmetric standard model with right-handed neutrino. *Physics Letters B*, 322(4):349 – 354, 1994.

[27] T. Asaka, Masaaki Fujii, K. Hamaguchi, and T. Yanagida. Affleck-dine leptogenesis with an ultralight neutrino. *Phys. Rev. D*, 62:123514, Nov 2000.

[28] Masaaki Fujii, K. Hamaguchi, and T. Yanagida. Reheating-temperature independence of cosmological baryon asymmetry in affleck-dine leptogenesis. *Phys. Rev. D*, 63:123513, May 2001.

[29] E. Kh. Akhmedov, V. A. Rubakov, and A. Yu. Smirnov. Baryogenesis via neutrino oscillations. *Phys. Rev. Lett.*, 81:1359–1362, Aug 1998.

[30] Erasmo Recami. Majorana, the neutron, and the neutrino: Some elementary historical remarks. 2017.

[31] Frank T. Avignone, Steven R. Elliott, and Jonathan Engel. Double beta decay, majorana neutrinos, and neutrino mass. *Rev. Mod. Phys.*, 80:481–516, Apr 2008.

[32] J. J. Gómez-Cadenas and Justo Martín-Albo. Phenomenology of neutrinoless double beta decay. *PoS*, GSSI14:004, 2015.

[33] M. Agostini et al. Probing majorana neutrinos with double-β decay. *Science*, 365(6460):1445–1448, 2019.

[34] C. Alduino et al. First results from cuore: A search for lepton number violation via $0\nu\beta\beta$ decay of ^{130}Te. *Phys. Rev. Lett.*, 120:132501, Mar 2018.

[35] E. Andreotti et al. 130Te Neutrinoless Double-Beta Decay with CUORICINO. *Astropart. Phys.*, 34:822–831, 2011.

[36] K. Alfonso et al. Search for neutrinoless double-beta decay of ^{130}Te with cuore-0. *Phys. Rev. Lett.*, 115:102502, Sep 2015.

[37] O. Azzolini et al. Final result of cupid-0 phase-i in the search for the ^{82}Se neutrinoless double-β decay. *Phys. Rev. Lett.*, 123:032501, Jul 2019.

[38] G. Anton et al. Search for neutrinoless double-β decay with the complete exo-200 dataset. *Phys. Rev. Lett.*, 123:161802, Oct 2019.

[39] J. B. Albert et al. Sensitivity and Discovery Potential of nEXO to Neutrinoless Double Beta Decay. *Phys. Rev.*, C97(6):065503, 2018.

[40] V Álvarez et al. Ionization and scintillation response of high-pressure xenon gas to alpha particles. *Journal of Instrumentation*, 8(05):P05025–P05025, may 2013.

[41] J. Renner et al. Initial results on energy resolution of the NEXT-White detector. *JINST*, 13(10):P10020, 2018.

[42] P. Novella et al. Radiogenic Backgrounds in the NEXT Double Beta Decay Experiment. *JHEP*, 10:051, 2019.

[43] J. Martín-Albo et al. Sensitivity of NEXT-100 to Neutrinoless Double Beta Decay. *JHEP*, 05:159, 2016.

[44] Japan Isotope Association, editor. *Handbook of Isotopes*. Japan Isotope Association, 10 edition, 2002.

[45] Nist physical reference data. https://www.nist.gov/pml/productsservices/physical-reference-data.

[46] Steven R. Elliott and Petr Vogel. Double beta decay. *Annual Review of Nuclear and Particle Science*, 52(1):115–151, 2002.

[47] S. Agostinelli et al. Geant4—a simulation toolkit. *Nuclear Instruments and Methods in Physics Research Section A: Accelerators, Spectrometers, Detectors and Associated Equipment*, 506(3):250 – 303, 2003.

[48] S. Tanaka. Private communication.

[49] Elena Aprile, Aleksey E. Bolotnikov, Alexander I. Bolozdynya, and Tadayoshi Doke. *Noble Gas Detectors*. Wiley-VCH, 2006.

[50] R. E. Huffman, J. C. Larrabee, and Y. Tanaka. Rare gas continuum light sources for photoelectric scanning in the vacuum ultraviolet. *APPLIED OPTICS*, 4(12):1581, 1965.

[51] C.M.B.Monteiro L.M.P.Fernandes J.A.M.Lopes L.C.C.Coelho J.F.C.A.Veloso J.M.F. dos Santos K.Giboni E.Aprile. *Revista do Detua*, VOL.4, N°7:849, 2007.

[52] Christophe Geuzaine and Jean-Francois Remacle. Gmsh: A 3-d finite element mesh generator with built-in pre- and post-processing facilities. *International Journal for Numerical Methods in Engineering*, 79(11):1309–1331, 2009. http://gmsh.info/.

[53] M. Malinen and Peter Raback. Elmer. https://www.csc.fi/web/elmer/.

[54] Kim Baraka et al. Garfield++ – simulation of tracking detectors. https://garfieldpp.web.cern.ch/garfieldpp/.

[55] Web page of hamamatsu photonics k.k. https://www.hamamatsu.com/us/en/product/optical-sensors/mppc/mppc_mppc-array/index.html.

[56] Hamamatsu photonics k.k.

[57] *MPPC and MPPC module for precision measurement*.

[58] Technical document for apds and mppcs by hamamatsu photonics k.k. (in japanese). https://www.hamamatsu.com/resources/pdf/ssd/03_handbook.pdf.

[59] S. Yanagita. Master's thesis, 2015. https://www-he.scphys.kyoto-u.ac.jp/theses/master/yanagita_mt.pdf (in Japanese).

[60] S. Biagi. Magboltz - transport of electrons in gas mixtures. 1995. http://magboltz.web.cern.ch/magboltz.

[61] et al. L. Serra. An improved measurement of electron-ion recombination in high-pressure xenon gas. *JINST*, 10:P03025, 2015.

[62] Y. Ishiyama. Master's thesis, 2016. https://www-he.scphys.kyoto-u.ac.jp/theses/master/ishiyama_mt.pdf (in Japanese).

[63] T. D. Bonifield, F. H. K. Rambow, G. K. Walters, M. V. McCusker, D. C. Lorents, and R. A. Gutcheck. Time resolved spectroscopy of xenon excimers excited by synchrotron radiation. *The Journal of Chemical Physics*, 72(5):2914–2924, 1980.

[64] M. Hirose A. K. Ichikawa Y. Ishiyama A. Minamino K. Miuchi T. Nakaya H. Sekiya S. Tanaka K. Ueshima K. D. Nakamura, S. Ban. Angular dependence of columnar recombination in high pressure xenon gas using time profiles of scintillation emission. *JINST*, 13:P07015, 2018.

[65] A. Bolotnikov and B. Ramsey. *Nucl. Instr. and Meth. A*, 396:360–370, 1997.

[66] D. C. Meeker. Finite element method magnetics, version 4.2. 2018. https://www.femm.info/wiki/HomePage.

[67] S. Ban, K. D. Nakamura, M. Hirose, A. K. Ichikawa, A. Minamino, K. Miuchi, T. Nakaya, H. Sekiya, S. Tanaka, K. Ueshima, S. Yanagita, Y. Ishiyama, and S. Akiyama. Electroluminescence collection cell as a readout for a high energy resolution xenon gas tpc. *Nuclear Inst. and Methods in Physics Research, A*, 875:185–192, 2017.

[68] Richard B. Firestone and Virginia S. Shirley. *Table of Isotopes*. John Wiley & Sons Inc, 1996.

[69] K. Z. Nakamura. Private communication.

[70] Steven P. Ahlen. Theoretical and experimental aspects of the energy loss of relativistic heavily ionizing particles. *Rev. Mod. Phys.*, 52:121–173, Jan 1980.

[71] K. D. Nakamura. Private communication.

[72] T. Uchida. Hardware-Based TCP Processor for Gigabit Ethernet. *IEEE transactions on nuclear science*, 55(3):1631–1637, jun 2008.

[73] K. Z. Nakamura, S. Ban, A. K. Ichikawa, M. Ikeno, K. D. Nakamura, T. Nakaya, S. Obara, S. Tanaka, T. Uchida, and M. Yoshida. Front-end-Electronics for the SiPM-readout gaseous TPC for neutrinoless double beta decay search. *IEEE transactions on nuclear science*, 2019. (Submitted to IEEE transactions on nuclear science).

[74] R. Honda. Hadron universal logic module. http://openit.kek.jp/project/HUL (in Japanese).

[75] V Álvarez et al. NEXT-100 technical design report (TDR). executive summary. *Journal of Instrumentation*, 7(06):T06001–T06001, June 2012.

[76] C. Chambers et al. Imaging individual barium atoms in solid xenon for barium tagging in nEXO. *Nature*, 569(7755):203–207, 2019.

[77] B.J.P. Jones, A.D. McDonald, and D.R. Nygren. Single molecule fluorescence imaging as a technique for barium tagging in neutrinoless double beta decay. *Journal of Instrumentation*, 11(12):P12011–P12011, dec 2016.